



Dynamical Modelling of the Human Larynx in Phonation

Author:

Adam Graham APOSTOLI

THESIS SUBMITTED IN FULFILLMENT OF THE
REQUIREMENTS FOR THE DEGREE OF

Doctor of Philosophy

SCHOOL OF PHYSICS AND ASTRONOMY
THE UNIVERSITY OF EDINBURGH
2012

Abstract

Producing an accurate model of the human voice has been the goal of researchers for a very long time, but is extremely challenging due to the complexity surrounding the way in which the voice functions. One of the more complicated aspects of modelling the voice is the fluid dynamics of the airflow, by which the process of self-oscillation of the vocal folds is sustained. This airflow also provides the only means by which the ventricular bands (two vocal fold-like structures located a short distance above the vocal folds) are driven into self-oscillation. These have been found to play a significant role in various singing styles and in voice pathologies. This study considers the airflow and flow-structure interaction in an artificial up-scaled model of the human larynx, including self-oscillating vocal folds and fixed ventricular bands. As the majority of any significant fluid-structure interaction takes place between structures found within the larynx, this thesis is limited only to examining this component of the voice organ.

Particle Image Velocimetry (PIV) has been used to produce full field measurements of the flow velocity for the jet emerging from the oscillating vocal folds. An important advance in this study is the ability to observe the glottal jet from the point at which it emerges from the vocal folds, thus permitting a more complete view of the overall jet geometry within the laryngeal ventricle than in previous work.

Ensemble-averaged PIV results are presented for the experimental model at different phase steps, both with and without ventricular bands, to examine their impact on the dynamics of the human larynx and the glottal jet. Finally, the three-dimensional nature of the glottal jet is considered in order to further understand and test currently held assumptions about this aspect of the jet dynamics. This was achieved by undertaking PIV in a plane perpendicular to that already considered. It is shown that the ventricular bands have an impact on the flow separation point of the glottal jet and on the deflection of the jet centreline. Furthermore, the dynamics of the vocal folds alters when ventricular bands are present, but the glottal jet is found to exhibit similar three-dimensional behaviour whether or not ventricular bands are present.

Declaration

I do hereby declare that this thesis was composed by myself and that the work described within is my own, except where explicitly stated otherwise. I declare also that this work has not been submitted for any other degree or professional qualification.

Adam G. Apostoli

August 2012

Acknowledgements

The last 4 years have been some of the most difficult and yet the most rewarding of my life so far. The people to whom I owe the most and who have been with me through all of this, providing unstinted support regardless of my state of mind are my parents and sister. Thank-you for your patience and support particularly towards the end whilst I've been writing up. I wish to thank my supervisors, Dr Will Hossack, Prof. Murray Campbell, and Prof. Clive Greated for their support and encouragement over the years and for reading the endless stream of drafts for either papers or thesis chapters.

A big thank-you is due to Andrew Downie and Derek Low from the Mechanical Workshop in the School of Physics and Astronomy. Without your help and guidance none of the experimental apparatus used in this study (most of which had to be built specially) would have come to fruition. My sincere thanks are also due to technicians Andrew Garrie and Les Russell, who further supported my work either through building tricky glass vocal tracts or complicated electronics; and to Dr Gordon Findlater, the University Anatomist, for sharing some of his vast knowledge and expertise and for the stunning photographs of the cadaver. A debt of thanks also is due to Richard Taylor and Hunter Scullion in the Electronics Workshop for helping me design, build, and fix electronic equipment used throughout my PhD, and to Dr Frank Mill in the School of Engineering for taking the time to teach me how to use Solid Edge and create the drawings shown in this thesis.

I would like to thank my officemates and colleagues: Shona, Lisa, Alan, and Darren, for their support. It's been great to share some of my successes and mishaps over the years and to know that I'm not going through the experience on my own.

Finally, I would like to thank some of the organisations who have supported my work. I would like to thank the Engineering and Physical Sciences Research Council for their financial support. I would also like to thank DantecDynamics for the use of their Dynamic Studio software, without which the PIV undertaken in this work would have been much more challenging to acquire. The financial support of COST Action 2103 is gratefully appreciated in facilitating a Short-term Scientific Mission to the Institut National Polytechnique de Grenoble in Grenoble, France.

*To Amanda, George,
and Georgina*

Contents

Abstract	2
Declaration	4
Acknowledgements	5
Contents	8
List of Figures	12
List of Tables	29
1 Introduction	31
1.1 Introduction and Context	31
1.2 Terminology	33
1.3 Aims	35
1.4 Content Outline	35
2 Review of Vocal Anatomy and Previous Modelling Attempts	38
2.1 Introduction	38
2.2 Anatomy of the Human Larynx	39
2.3 Previous Studies	44
2.3.1 <i>Ex vivo</i> Studies using Canine Larynges	44
2.3.2 <i>In vitro</i> Studies using Rigid Vocal Fold Models	47
2.3.3 <i>In vitro</i> Studies using Driven Mechanical Vocal Fold Models	49
2.3.4 <i>In vitro</i> Studies using Self-Oscillating Vocal Fold Models	53
3 Physics and Fluid Dynamics in Models of the Human Larynx	58
3.1 Introduction	58
3.2 Fundamental Aerodynamic Theory	59
3.2.1 Dimensionless Fluid Mechanical Measures	63
3.2.2 Flow Separation and Jet Formation	66
3.3 Modelling Complex Laryngeal Anatomy and Physiology	67
3.3.1 Principles of Vocal Fold Oscillation	68

3.3.2	The Vocal Tract and Vowel Production	70
3.4	<i>In vitro</i> Models of the Human Larynx	73
3.4.1	Using Scaled Models	73
3.4.2	Construction of the <i>in vitro</i> Model of the Human Larynx . . .	74
3.5	Mechanical Response	78
3.5.1	Principles of Mechanical Response Measurement	80
3.5.2	Experimental Apparatus and Procedure	82
3.5.3	Analysis and Application of Results	86
3.6	Model Open Height and Area using a High-Speed Camera	87
3.6.1	Experimental Apparatus and Procedure	87
3.6.2	Analysis and Application of Results	89
3.7	Physical Models	91
3.7.1	Two-Mass Model without Ventricular Bands	92
3.7.2	Two-Mass Model with Ventricular Bands	94
3.7.3	Fluid Flow Models	97
3.7.4	Models of the Glottal Jet	101
3.7.5	Physical Models and High-throughput Distributed Computing	104
4	Particle Image Velocimetry Applied to <i>in vitro</i> Models of the Larynx	109
4.1	Introduction	109
4.2	Background Theory to PIV	110
4.3	Experimental Apparatus	114
4.3.1	Seeding Particle Size	117
4.3.2	Seeding Particle Delivery System	118
4.3.3	Phase Stepping Mechanism and Image-Pair Acquisition . . .	119
4.4	PIV Data Analysis Methods	125
4.4.1	PIV Flow Field Data Calculation Routine	125
4.4.2	Velocity Magnitude, Standard Deviation, and Ensemble-Averaging	128
4.4.3	Vorticity	129
4.4.4	Jet Centreline	130
4.4.5	Dimensional Analysis Parameters	132
5	Vocal Fold and Glottal Jet Dynamics within Models of the Human Larynx	137
5.1	Introduction	137

5.2	Basic Structure of the Glottal Jet	139
5.3	Results for the <i>in vitro</i> Model in the Free Jet Control Case	141
5.3.1	Characterisation of the Jet	148
5.3.2	Jet Deflection and Centreline Calculation	148
5.3.3	Expansion of the Jet	151
5.3.4	Dimensional Analysis	152
5.3.5	Summary	155
5.4	Results of Experiments Undertaken Prior to Self-Sustained Oscillation	155
5.4.1	Mechanical Response for the <i>in vitro</i> Model	156
5.4.2	‘Bowling’ and the Impact of Initial Observations	158
5.5	Results for the <i>in vitro</i> Model without Ventricular Bands	160
5.5.1	Phase Stepping and Ensemble-Averaging	161
5.5.2	Vocal Fold Open Height through High-Speed Camera Analysis	163
5.5.3	Characterisation of the Jet	165
5.5.4	Vorticity Flow Field Data	172
5.5.5	Jet Deflection and Centreline Calculation	175
5.5.6	Expansion of the Glottal Jet	177
5.5.7	Dimensional Analysis	178
5.5.8	Summary	183
5.6	Results for <i>in vitro</i> Model with Rigid Ventricular Bands	184
5.6.1	Vocal Fold Open Height through High-Speed Camera Analysis	186
5.6.2	Characterisation of the Glottal Jet	189
5.6.3	Jet Deflection and Centreline Calculation	200
5.6.4	Expansion of the Glottal Jet	204
5.6.5	Dimensional Analysis	204
5.6.6	Summary	208
5.7	Results from Computational Physical Model Simulations	209
5.7.1	Impact of Sampling Rate in Simulations	210
5.7.2	Impact of Ventricular Bands in Simulations	211
5.7.3	Impact of Empirical Aerodynamic Observations in Simulations	214
5.7.4	Comparison Between Simulation and Experiment	217
5.7.5	Summary	222

6	Three-dimensional Glottal Flow within Models of the Human Larynx	224
6.1	Results for the <i>in vitro</i> Model without Ventricular Bands	224
6.1.1	Calculated Vorticity Flow Field Data	231
6.1.2	Jet Major Axis-Switching	234
6.1.3	Summary	236
6.2	Results for <i>in vitro</i> Model with Rigid Ventricular Bands	236
6.2.1	Calculated Vorticity Flow Field Data	247
6.2.2	Jet Major Axis-Switching	252
6.2.3	Summary	254
7	Conclusions and Future Work	255
7.1	Conclusions	255
7.1.1	Construction of a New <i>In vitro</i> Model of the Human Larynx and PIV of the Complete Glottal Jet	256
7.1.2	Impact of the Ventricular Bands on the Glottal Jet in the <i>In- vitro</i> Model of the Human Larynx	257
7.1.3	Investigation of the Three-dimensional Dynamical Nature of the Glottal Jet	258
7.1.4	Further Develop an Existing State-of-the-art Computational Model in order to Investigate the Relationship between Jet Behaviour and Vocal Fold Oscillation	259
7.2	Possible Future Work	260
7.2.1	Further Work on the Ventricular Bands	260
7.2.2	Using <i>in vitro</i> Models for Pathological Comparative Studies .	260
	Bibliography	262
A	Published Papers	278
A.1	Conference Papers	278
B	Additional Results	279
B.1	Vorticity Flow Field Data	279
B.2	Jet Major Axis-Switching	284
C	Experimental Drawings	291

List of Figures

1.1	Schematic representation of the human voice.	32
1.2	A diagram showing the interdependency of disciplines required in the human voice.	32
1.3	Schematic diagram showing the locations of the sagittal, coronal, and transverse planes.	33
2.1	A mid-coronal section of a horse larynx with labels.	39
2.2	Labelled illustration showing a coronal section through one of the vocal folds.	41
2.3	Series of images of the human head and larynx either from plastic models or from human cadavers. Anatomical labels for Roman numerals shown in (a) are included.	43
3.1	Schematic diagram showing the <i>boundary layer</i> and <i>bulk flow</i> regions in pipe flow.	61
3.2	Schematic diagram of the vocal folds and glottis showing the glottal centreline open height h_{vf} , and the glottal open width W_{vf}	63
3.3	A schematic diagram showing the boundary layer separation from a flow boundary, with S marking the point of flow separation. Streamlines are shown as continuous lines with arrows.	67
3.4	A diagram showing changes in the shape of the vocal folds and the geometry of glottis through a phonatory cycle.	69
3.5	Image showing subglottal and supraglottal geometrical changes from high-speed camera filming of the <i>in vitro</i> model of the human larynx with a vocal tract but without ventricular bands in self-sustained oscillation through a side window. In each image in this figure the flow moves from left to right.	71
3.6	Mid-sagittal plane view of a human head showing the vocal tract shape for two different vowels using Magnetic Resonance Imaging (MRI).	72
3.7	A diagram of one of the vocal fold blocks (including stud) with key dimensions labelled.	74
3.8	A labelled diagram showing the <i>in vitro</i> model of the human larynx once constructed.	77

3.9	Plots of the magnitude of the acoustic input impedance for an <i>in vitro</i> model of the human larynx with and without a model of the lungs attached.	79
3.10	A diagram showing the setup used for undertaking a mechanical response measurement on the <i>in vitro</i> model of the vocal folds. Note, the acoustic cavity was only used as part of the mechanical response apparatus and is much smaller than the model lung discussed earlier. .	82
3.11	A diagram showing the setup used for undertaking a mechanical response measurement on the <i>in vitro</i> model of the vocal folds.	83
3.12	The magnitude (<i>upper</i>) and phase (<i>lower</i>) plots for the frequency response function for the Brüel and Kjær type 4192 microphone with a short probe attachment.	84
3.13	A plot showing the photodiode calibration relating the open width of a rectangular opening to the voltage across the photodiode caused by an expanded laser beam shining through the opening. The red dashed line is the straight line fitted to the blue data points.	85
3.14	A schematic diagram of the experimental setup used for the high-speed camera.	88
3.15	A diagram showing the extraction of the glottal open area using a thresholding program in MATLAB. To provide a sense of scale, from one side of the glottis to the other side measures 20 mm.	90
3.16	A schematic diagram showing the computational model of the human larynx with the vocal folds modelled as a physical two-mass model and without ventricular bands.	92
3.17	Schematic diagram illustrating the programming logic for computational physical model of the <i>in vitro</i> model of the human larynx. . . .	95
3.18	A schematic diagram showing the computational model of the human larynx with the vocal folds modelled as a physical two-mass model and with rigid ventricular bands.	96
3.19	Diagram illustrating the uniform jet expansion hypothesis, where h_0 is the width of the trachea, h_{vf} is the minimum glottal opening, h_{s1} is the point of flow separation, h_R is the point of flow reattachment, and h_{vb} is the minimum ventricular band separation.	101

3.20	Diagram illustrating the laminar jet expansion hypothesis, where h_{s1} is the point of flow separation and h_R is the point of flow reattachment.	102
3.21	Diagram illustrating the turbulent jet expansion hypothesis, where h_{s1} is the point of flow separation, h_R is the point of flow reattachment, and θ_{jet} is the half-angle of the jet expansion.	103
3.22	Schematic diagram illustrating the Condor system.	105
4.1	Schematic diagram summarising the basic principles of PIV.	110
4.2	Cross-correlation plane and constituent interrogation areas from which the correlation peak can be extracted and a velocity vector calculated.	112
4.3	Oxford Lasers Fibresheet optical delivery unit.	114
4.4	Labelled setup of the <i>in vitro</i> model in preparation for an image pair acquisition.	115
4.5	Schematic diagram of the laser light sheet planes used during PIV. Light sheet configuration 1 (relating to results discussed in Chapter 5) is the red plane and is perpendicular to the glottal open width. Light sheet configuration 2 (relating to results discussed in Chapter 6) is the green plane and is parallel to the glottal open width.	116
4.6	Schematic diagram of the seeding particle delivery system.	119
4.7	Plot showing the upstream acoustic signal and the filtered upstream acoustic signal.	120
4.8	Diagram summarising the triggering process used to undertake phase-stepped PIV (not to scale).	122
4.9	Plot showing upstream acoustic signal synchronised with the measured open area of the vocal folds.	124
4.10	Plot showing an example of the areas used for the jet core (shown by a horizontal thick magenta line) and pre-turbulent region (shown by a black square) used in the dimensional analysis marked on an ensemble-averaged velocity magnitude and standard deviation map. The calculated centreline is shown as a vertical magenta line on both maps, and plots showing the jet centreline velocity and phase step position are included on the right hand side.	132

5.1	Ensemble-averaged velocity magnitude data and standard deviation for a free jet with the key elements of the jet labelled.	139
5.2	Ensemble-averaged velocity magnitude data (<i>top left</i>), standard deviation (<i>bottom left</i>), and vorticity (<i>bottom right</i>), together with an instantaneous velocity flow field (<i>top right</i>) from a static <i>in vitro</i> model of the human larynx with no vocal tract attached at subglottal pressure (P_{sub}) = 258 Pa.	142
5.3	Ensemble-averaged velocity magnitude data (<i>top left</i>), standard deviation (<i>bottom left</i>), and vorticity (<i>bottom right</i>), together with an instantaneous velocity flow field (<i>top right</i>) from a static <i>in vitro</i> model of the human larynx with no vocal tract attached at subglottal pressure (P_{sub}) = 430 Pa.	143
5.4	Ensemble-averaged velocity magnitude data (<i>top left</i>), standard deviation (<i>bottom left</i>), and vorticity (<i>bottom right</i>), together with an instantaneous velocity flow field (<i>top right</i>) from a static <i>in vitro</i> model of the human larynx with no vocal tract attached at subglottal pressure (P_{sub}) = 600 Pa.	144
5.5	Ensemble-averaged velocity magnitude data (<i>top left</i>), standard deviation (<i>bottom left</i>), and vorticity (<i>bottom right</i>), together with an instantaneous velocity flow field (<i>top right</i>) from a static <i>in vitro</i> model of the human larynx with no vocal tract attached at subglottal pressure (P_{sub}) = 900 Pa.	145
5.6	Ensemble-averaged velocity magnitude data (<i>top left</i>), standard deviation (<i>bottom left</i>), and vorticity (<i>bottom right</i>), together with an instantaneous velocity flow field (<i>top right</i>) from a static <i>in vitro</i> model of the human larynx with no vocal tract attached at subglottal pressure (P_{sub}) = 1100 Pa.	146
5.7	Ensemble-averaged velocity magnitude data (<i>top left</i>), standard deviation (<i>bottom left</i>), and vorticity (<i>bottom right</i>), together with an instantaneous velocity flow field (<i>top right</i>) from a static <i>in vitro</i> model of the human larynx with no vocal tract attached at subglottal pressure (P_{sub}) = 1300 Pa.	147

5.8	Histogram plots of the deflection angle of the centreline of the glottal jet across all subglottal pressures used for a static <i>in vitro</i> model of the human larynx with no vocal tract attached.	150
5.9	Parametric non-dimensionalised flow parameter plots showing the jet core turbulence (T_{core}), normalised jet core velocity (u_{norm}), and jet flow resistance (Z_{core}) against either subglottal pressure or jet core Reynolds number (Re_{core}) across all subglottal pressures used for a static <i>in vitro</i> model of the human larynx with no vocal tract attached.	154
5.10	Plots showing the mechanical response for a self-oscillating <i>in vitro</i> model of the human larynx with no ventricular bands highlighting the change caused by the presence of a flow. The upper plot in each subfigure shows the calibrated amplitude against frequency and the lower plot shows the phase difference between the opening of the vocal folds and the acoustic driving signal. The purple asterisks indicate detected resonance peak frequencies.	157
5.11	Plot showing the mechanical response for a self-oscillating <i>in vitro</i> model of the human larynx with no ventricular bands. The red lines indicate the fitted resonance functions from which the quality factors (Q_0) are extracted, and the numbers relate to the detected peak numbers.	158
5.12	Image illustrating the lines of analysis in high-speed camera filming used to calculate the degree to which the <i>in vitro</i> model of the human larynx is bowed in its initial state and its initial opening.	159
5.13	Plots illustrating the image pair acquisition times aligned to the phonatory cycle using the phase windowing and phase stepping techniques for a self-oscillating <i>in vitro</i> model of the human larynx.	161
5.14	Several kymographs taken either <i>in vivo</i> or from an <i>in vitro</i> model of the human larynx without ventricular bands.	164
5.15	Plot showing the measured open height of the vocal folds in the centre and at two lines either side equidistant to the centreline for an <i>in vitro</i> model without ventricular bands.	164

5.16	Ensemble-averaged velocity magnitude data for phase steps 1 - 5 on an <i>in vitro</i> model of the human larynx with no ventricular bands . The positions of the phase steps in relation to the centreline open height of the vocal fold model are included. $P_{sub} = 813$ Pa.	168
5.17	Ensemble-averaged velocity magnitude data for phase steps 6 - 10 on an <i>in vitro</i> model of the human larynx with no ventricular bands . The positions of the phase steps in relation to the centreline open height of the vocal fold model are included. $P_{sub} = 813$ Pa.	169
5.18	Standard deviation of the ensemble-averaged velocity magnitude data for phase steps 1 - 5 on an <i>in vitro</i> model of the human larynx with no ventricular bands . The positions of the phase steps in relation to the centreline open height of the vocal fold model are included. $P_{sub} = 813$ Pa.	170
5.19	Standard deviation of the ensemble-averaged velocity magnitude data for phase steps 6 - 10 on an <i>in vitro</i> model of the human larynx with no ventricular bands . The positions of the phase steps in relation to the centreline open height of the vocal fold model are included. $P_{sub} = 813$ Pa.	171
5.20	Vorticity ensemble-averaged PIV data for phase steps 1 - 5 on an <i>in vitro</i> model of the human larynx with no ventricular bands . The positions of the phase steps in relation to the normalised open area of the vocal fold model are included. $P_{sub} = 813$ Pa.	173
5.21	Vorticity ensemble-averaged PIV data for phase steps 6 - 10 on an <i>in vitro</i> model of the human larynx with no ventricular bands . The positions of the phase steps in relation to the normalised open area of the vocal fold model are included. $P_{sub} = 813$ Pa.	174
5.22	A series of histograms showing the jet deflection angle against the total percentage of measured jet centrelines, organised by phase step, for an <i>in vitro</i> model of the larynx without ventricular bands	176
5.23	Non-dimensional flow parameter parametric plots illustrating changes in turbulence and the Reynolds number across established phase steps for a self-oscillating <i>in vitro</i> model of the human larynx with no ventricular bands . Phase steps 2, 4, and 9 are highlighted.	180

5.24	Non-dimensional flow parameter parametric plots illustrating changes in jet speed and flow admittance and resistance across established phase steps for a self-oscillating <i>in vitro</i> model of the human larynx with no ventricular bands . Phase steps 2, 4, and 9 are highlighted. .	181
5.25	Kymograph lines taken from an <i>in vitro</i> model of the human larynx with and without ventricular bands.	187
5.26	Plots showing the measured open height of the vocal folds in the centre and at two lines either side equidistant to the centreline for an <i>in vitro</i> model with ventricular bands 16 mm downstream and either 8 mm or 3 mm apart.	188
5.27	Ensemble-averaged velocity magnitude data for phase steps 1 - 5 on an <i>in vitro</i> model of the human larynx with rigid ventricular bands placed 16 mm downstream of the vocal folds with an 8 mm separation . The positions of the phase steps in relation to the centreline open height of the vocal fold model are included. $P_{sub} = 802$ Pa. Only the top of the ventricular bands are shown in these plots, the reported separation is the minimum constriction formed by the bands further downstream.	192
5.28	Ensemble-averaged velocity magnitude data for phase steps 6 - 10 on an <i>in vitro</i> model of the human larynx with rigid ventricular bands placed 16 mm downstream of the vocal folds with an 8 mm separation . The positions of the phase steps in relation to the centreline open height of the vocal fold model are included. $P_{sub} = 802$ Pa. Only the top of the ventricular bands are shown in these plots, the reported separation is the minimum constriction formed by the bands further downstream.	193

5.29	Standard deviation of the ensemble-averaged velocity magnitude data for phase steps 1 - 5 on an <i>in vitro</i> model of the human larynx with rigid ventricular bands placed 16 mm downstream of the vocal folds with an 8 mm separation . The positions of the phase steps in relation to the centreline open height of the vocal fold model are included. $P_{sub} = 802$ Pa. Only the top of the ventricular bands are shown in these plots, the reported separation is the minimum constriction formed by the bands further downstream.	194
5.30	Standard deviation of the ensemble-averaged velocity magnitude data for phase steps 6 - 10 on an <i>in vitro</i> model of the human larynx with rigid ventricular bands placed 16 mm downstream of the vocal folds with an 8 mm separation . The positions of the phase steps in relation to the centreline open height of the vocal fold model are included. $P_{sub} = 802$ Pa. Only the top of the ventricular bands are shown in these plots, the reported separation is the minimum constriction formed by the bands further downstream.	195
5.31	Ensemble-averaged velocity magnitude data for phase steps 1 - 5 on an <i>in vitro</i> model of the human larynx with rigid ventricular bands placed 16 mm downstream of the vocal folds with a 3 mm separation . The positions of the phase steps in relation to the centreline open height of the vocal fold model are included. $P_{sub} = 805$ Pa. Only the top of the ventricular bands are shown in these plots, the reported separation is the minimum constriction formed by the bands further downstream.	196
5.32	Ensemble-averaged velocity magnitude data for phase steps 6 - 10 on an <i>in vitro</i> model of the human larynx with rigid ventricular bands placed 16 mm downstream of the vocal folds with a 3 mm separation . The positions of the phase steps in relation to the centreline open height of the vocal fold model are included. $P_{sub} = 805$ Pa. Only the top of the ventricular bands are shown in these plots, the reported separation is the minimum constriction formed by the bands further downstream.	197

5.33	Standard deviation of the ensemble-averaged velocity magnitude data for phase steps 1 - 5 on an <i>in vitro</i> model of the human larynx with rigid ventricular bands placed 16 mm downstream of the vocal folds with a 3 mm separation . The positions of the phase steps in relation to the centreline open height of the vocal fold model are included. $P_{sub} = 805$ Pa. Only the top of the ventricular bands are shown in these plots, the reported separation is the minimum constriction formed by the bands further downstream.	198
5.34	Standard deviation of the ensemble-averaged velocity magnitude data for phase steps 6 - 10 on an <i>in vitro</i> model of the human larynx with rigid ventricular bands placed 16 mm downstream of the vocal folds with a 3 mm separation . The positions of the phase steps in relation to the centreline open height of the vocal fold model are included. $P_{sub} = 805$ Pa. Only the top of the ventricular bands are shown in these plots, the reported separation is the minimum constriction formed by the bands further downstream.	199
5.35	A plot showing the measured width of the glottal jet and the opening of the vocal folds for a self-oscillating <i>in vitro</i> model of the human larynx with no ventricular bands (<i>left</i>), a model with ventricular bands 16 mm downstream of the vocal folds with an 8 mm separation (<i>centre</i>), and a model with ventricular bands 16 mm downstream of the vocal folds with a 3 mm separation (<i>right</i>).	200
5.36	A series of histograms showing the jet deflection angle against the total percentage of measured jet centrelines, organised by phase step, for an <i>in vitro</i> model of the larynx with ventricular bands placed 16 mm downstream of the vocal folds with an 8 mm separation	202
5.37	A series of histograms showing the jet deflection angle against the total percentage of measured jet centrelines, organised by phase step, for an <i>in vitro</i> model of the larynx with ventricular bands placed 16 mm downstream of the vocal folds with a 3 mm separation	203

5.38	Non-dimensional flow parameter parametric plots illustrating changes in turbulence and the Reynolds number across established phase steps for a self-oscillating <i>in vitro</i> model of the human larynx with no ventricular bands and with rigid ventricular bands placed 16 mm downstream of the vocal folds with 8 mm and 3 mm separations. Phase steps 2, 4, and 9 are highlighted.	206
5.39	Non-dimensional flow parameter parametric plots illustrating changes in jet speed and flow admittance and resistance across established phase steps for a self-oscillating <i>in vitro</i> model of the human larynx with no ventricular bands and with rigid ventricular bands placed 16 mm downstream of the vocal folds with 8 mm and 3 mm separations. Phase steps 2, 4, and 9 are highlighted.	207
5.40	Results from a set of physical model simulations using Condor with the values which are considered to exhibit unphysical behaviour shaded in grey. Jitter and shimmer are defined within Section 3.7.5	210
5.41	Results from a set of Condor simulations for the physical model using a Bernoulli steady flow model with Poiseuille losses, no jet pressure losses, and either a sampling rate of 20 kHz or 40 kHz.	212
5.42	Results from a set of Condor simulations for the physical model using a Bernoulli steady flow model with Poiseuille losses, no jet pressure losses, and either a sampling rate of 60 kHz or 80 kHz.	213
5.43	Results from a set of Condor simulations for the physical model with ventricular bands separated by 3 mm, placed 16 mm downstream using a Bernoulli steady flow model with Poiseuille losses, no jet pressure losses, and with a sampling rate of 100 kHz.	214
5.44	Results from a set of Condor simulations for the physical model with ventricular bands separated by 3 mm, placed 16 mm downstream using a Bernoulli steady flow model with Poiseuille losses, no jet pressure losses, and with a sampling rate of 20 kHz but with the number data points increased by a factor of 5 using spline interpolation.	215
5.45	Results from two sets of Condor simulations for the physical model using a Bernoulli steady flow model with Poiseuille losses, and no jet pressure losses.	216

5.46	Results from a set of Condor simulations for the physical model with no ventricular bands using a Bernoulli steady flow model with Poiseuille losses, and no jet pressure losses.	217
5.47	Results from two sets of Condor simulations for the physical model using a Bernoulli steady flow model with Poiseuille losses, no jet pressure losses, and the turbulent jet expansion hypothesis.	218
5.48	Results from a set of Condor simulations for the physical model with ventricular bands placed 16 mm downstream with a 3 mm separation using a Bernoulli steady flow model with Poiseuille losses, no jet pressure losses, and the turbulent jet expansion hypothesis with $\theta_{jet} = 26^\circ$	219
5.49	Comparison between the measured jet width from PIV data and that from a physical model without ventricular bands using a Bernoulli steady flow model with Poiseuille losses, no jet pressure losses, and the turbulent jet expansion hypothesis with $\theta_{jet} = 21^\circ$	220
5.50	Comparison between the measured jet width from PIV data and that from a physical model with ventricular bands placed 16 mm downstream with a 8 mm separation using a Bernoulli steady flow model with Poiseuille losses, no jet pressure losses and the turbulent jet expansion hypothesis with $\theta_{jet} = 21^\circ$	221
5.51	Comparison between the measured jet width from PIV data and that from a physical model with ventricular bands placed 16 mm downstream with a 3 mm separation using a Bernoulli steady flow model with Poiseuille losses, no jet pressure losses, and the turbulent jet expansion hypothesis with $\theta_{jet} = 26^\circ$	222
6.1	Ensemble-averaged velocity magnitude data for phase steps 1 - 5 on an <i>in vitro</i> model of the human larynx with no ventricular bands . The positions of the phase steps in relation to the centreline open height of the vocal fold model are included. $P_{sub} = 800$ Pa.	227
6.2	Ensemble-averaged velocity magnitude data for phase steps 6 - 10 on an <i>in vitro</i> model of the human larynx with no ventricular bands . The positions of the phase steps in relation to the centreline open height of the vocal fold model are included. $P_{sub} = 800$ Pa.	228

6.3	Standard deviation of the ensemble-averaged velocity magnitude data for phase steps 1 - 5 on an <i>in vitro</i> model of the human larynx with no ventricular bands . The positions of the phase steps in relation to the centreline open height of the vocal fold model are included. $P_{sub} = 800$ Pa.	229
6.4	Standard deviation of the ensemble-averaged velocity magnitude data for phase steps 6 - 10 on an <i>in vitro</i> model of the human larynx with no ventricular bands . The positions of the phase steps in relation to the centreline open height of the vocal fold model are included. $P_{sub} = 800$ Pa.	230
6.5	Vorticity ensemble-averaged PIV data for phase steps 1 - 5 on an <i>in vitro</i> model of the human larynx with no ventricular bands . The positions of the phase steps in relation to the normalised open area of the vocal fold model are included. $P_{sub} = 800$ Pa.	232
6.6	Vorticity ensemble-averaged PIV data for phase steps 6 - 10 on an <i>in vitro</i> model of the human larynx with no ventricular bands . The positions of the phase steps in relation to the normalised open area of the vocal fold model are included. $P_{sub} = 800$ Pa.	233
6.7	Two plots showing the distance downstream of the vocal folds whereby jet major axis-switching take place across phase steps 2 - 9 for a self-oscillating <i>in vitro</i> model of the human larynx with no ventricular bands.	234
6.8	Ensemble-averaged velocity magnitude data for phase steps 1 - 5 on an <i>in vitro</i> model of the human larynx with rigid ventricular bands placed 16 mm downstream of the vocal folds with an 8 mm separation . The positions of the phase steps in relation to the centreline open height of the vocal fold model are included. $P_{sub} = 800$ Pa.	239
6.9	Ensemble-averaged velocity magnitude data for phase steps 6 - 10 on an <i>in vitro</i> model of the human larynx with rigid ventricular bands placed 16 mm downstream of the vocal folds with an 8 mm separation . The positions of the phase steps in relation to the centreline open height of the vocal fold model are included. $P_{sub} = 800$ Pa.	240

6.10	Standard deviation of the ensemble-averaged velocity magnitude data for phase steps 1 - 5 on an <i>in vitro</i> model of the human larynx with rigid ventricular bands placed 16 mm downstream of the vocal folds with an 8 mm separation . The positions of the phase steps in relation to the centreline open height of the vocal fold model are included. $P_{sub} = 800$ Pa.	241
6.11	Standard deviation of the ensemble-averaged velocity magnitude data for phase steps 6 - 10 on an <i>in vitro</i> model of the human larynx with rigid ventricular bands placed 16 mm downstream of the vocal folds with an 8 mm separation . The positions of the phase steps in relation to the centreline open height of the vocal fold model are included. $P_{sub} = 800$ Pa.	242
6.12	Ensemble-averaged velocity magnitude data for phase steps 1 - 5 on an <i>in vitro</i> model of the human larynx with rigid ventricular bands placed 16 mm downstream of the vocal folds with a 3 mm separation . The positions of the phase steps in relation to the centreline open height of the vocal fold model are included. $P_{sub} = 804$ Pa.	243
6.13	Ensemble-averaged velocity magnitude data for phase steps 6 - 10 on an <i>in vitro</i> model of the human larynx with rigid ventricular bands placed 16 mm downstream of the vocal folds with a 3 mm separation . The positions of the phase steps in relation to the centreline open height of the vocal fold model are included. $P_{sub} = 804$ Pa.	244
6.14	Standard deviation of the ensemble-averaged velocity magnitude data for phase steps 1 - 5 on an <i>in vitro</i> model of the human larynx with rigid ventricular bands placed 16 mm downstream of the vocal folds with a 3 mm separation . The positions of the phase steps in relation to the centreline open height of the vocal fold model are included. $P_{sub} = 804$ Pa.	245

6.15	Standard deviation of the ensemble-averaged velocity magnitude data for phase steps 6 - 10 on an <i>in vitro</i> model of the human larynx with rigid ventricular bands placed 16 mm downstream of the vocal folds with a 3 mm separation . The positions of the phase steps in relation to the centreline open height of the vocal fold model are included. $P_{sub} = 804$ Pa.	246
6.16	Vorticity data ensemble-averaged PIV data for phase steps 1 - 5 on an <i>in vitro</i> model of the human larynx rotated by 90° with rigid ventricular bands placed 16 mm downstream of the vocal folds with an 8 mm separation . The positions of the phase steps in relation to the normalised open area of the vocal fold model are included. $P_{sub} = 800$ Pa.	248
6.17	Vorticity data ensemble-averaged PIV data for phase steps 6 - 10 on an <i>in vitro</i> model of the human larynx rotated by 90° with rigid ventricular bands placed 16 mm downstream of the vocal folds with an 8 mm separation . The positions of the phase steps in relation to the normalised open area of the vocal fold model are included. $P_{sub} = 800$ Pa.	249
6.18	Vorticity data ensemble-averaged PIV data for phase steps 1 - 5 on an <i>in vitro</i> model of the human larynx rotated by 90° with rigid ventricular bands placed 16 mm downstream of the vocal folds with a 3 mm separation . The positions of the phase steps in relation to the normalised open area of the vocal fold model are included. $P_{sub} = 804$ Pa.	250
6.19	Vorticity data ensemble-averaged PIV data for phase steps 6 - 10 on an <i>in vitro</i> model of the human larynx rotated by 90° with rigid ventricular bands placed 16 mm downstream of the vocal folds with a 3 mm separation . The positions of the phase steps in relation to the normalised open area of the vocal fold model are included. $P_{sub} = 804$ Pa.	251

6.20	Two plots showing the distance downstream of the vocal folds whereby jet major axis-switching take place across phase steps 2 - 9 for a self-oscillating <i>in vitro</i> model of the human larynx with rigid ventricular bands 16 mm downstream with an 8 mm separation.	253
6.21	Two plots showing the distance downstream of the vocal folds whereby jet major axis-switching take place across phase steps 2 - 9 for a self-oscillating <i>in vitro</i> model of the human larynx with rigid ventricular bands 16 mm downstream with a 3 mm separation.	253
B.1	Vorticity ensemble-averaged PIV data for phase steps 1 - 5 on an <i>in vitro</i> model of the human larynx with rigid ventricular bands placed 16 mm downstream of the vocal folds with an 8 mm separation. The positions of the phase steps in relation to the normalised open area of the vocal fold model are included. $P_{sub} = 802$ Pa. Only the top of the ventricular bands are shown in these plots, the reported separation is the minimum constriction formed by the bands further downstream.	280
B.2	Vorticity ensemble-averaged PIV data for phase steps 6 - 10 on an <i>in vitro</i> model of the human larynx with rigid ventricular bands placed 16 mm downstream of the vocal folds with an 8 mm separation. The positions of the phase steps in relation to the normalised open area of the vocal fold model are included. $P_{sub} = 802$ Pa. Only the top of the ventricular bands are shown in these plots, the reported separation is the minimum constriction formed by the bands further downstream.	281
B.3	Vorticity ensemble-averaged PIV data for phase steps 1 - 5 on an <i>in vitro</i> model of the human larynx with rigid ventricular bands placed 16 mm downstream of the vocal folds with a 3 mm separation. The positions of the phase steps in relation to the normalised open area of the vocal fold model are included. $P_{sub} = 805$ Pa. Only the top of the ventricular bands are shown in these plots, the reported separation is the minimum constriction formed by the bands further downstream. .	282

B.4	Vorticity ensemble-averaged PIV data for phase steps 6 - 10 on an <i>in vitro</i> model of the human larynx with rigid ventricular bands placed 16 mm downstream of the vocal folds with a 3 mm separation . The positions of the phase steps in relation to the normalised open area of the vocal fold model are included. $P_{sub} = 805$ Pa. Only the top of the ventricular bands are shown in these plots, the reported separation is the minimum constriction formed by the bands further downstream. .	283
B.5	Measured glottal jet widths in two perpendicular planes, signifying the point of jet major axis-switching, for phase steps 1 - 5 on an <i>in vitro</i> model of the human larynx with no ventricular bands . The positions of the phase steps in relation to the centreline open height of the vocal fold model are included. $P_{sub} = 813$ Pa.	285
B.6	Measured glottal jet widths in two perpendicular planes, signifying the point of jet major axis-switching, for phase steps 6 - 10 on an <i>in vitro</i> model of the human larynx with no ventricular bands . The positions of the phase steps in relation to the centreline open height of the vocal fold model are included. $P_{sub} = 813$ Pa.	286
B.7	Measured glottal jet widths in two perpendicular planes, signifying the point of jet major axis-switching, for phase steps 1 - 5 on an <i>in vitro</i> model of the human larynx with rigid ventricular bands placed 16 mm downstream of the vocal folds with an 8 mm separation . The positions of the phase steps in relation to the centreline open height of the vocal fold model are included. $P_{sub} = 802$ Pa.	287
B.8	Measured glottal jet widths in two perpendicular planes, signifying the point of jet major axis-switching, for phase steps 6 - 10 on an <i>in vitro</i> model of the human larynx with rigid ventricular bands placed 16 mm downstream of the vocal folds with an 8 mm separation . The positions of the phase steps in relation to the centreline open height of the vocal fold model are included. $P_{sub} = 802$ Pa.	288

B.9	Measured glottal jet widths in two perpendicular planes, signifying the point of jet major axis-switching, for phase steps 1 - 5 on an <i>in vitro</i> model of the human larynx with rigid ventricular bands placed 16 mm downstream of the vocal folds with a 3 mm separation . The positions of the phase steps in relation to the centreline open height of the vocal fold model are included. $P_{sub} = 805$ Pa.	289
B.10	Measured glottal jet widths in two perpendicular planes, signifying the point of jet major axis-switching, for phase steps 6 - 10 on an <i>in vitro</i> model of the human larynx with rigid ventricular bands placed 16 mm downstream of the vocal folds with a 3 mm separation . The positions of the phase steps in relation to the centreline open height of the vocal fold model are included. $P_{sub} = 805$ Pa.	290
C.1	Schematic drawing for zero-triggering device developed at the University of Edinburgh (drawing created by R. Taylor)	292
C.2	Technical drawing for the trachea used in the <i>in vitro</i> model of the human larynx.	293
C.3	Technical drawing for the body plate used in the <i>in vitro</i> model of the human larynx.	294
C.4	Technical drawing for the block of the vocal fold assembly used in the <i>in vitro</i> model of the human larynx.	295
C.5	Technical drawing for the stud of the vocal fold assembly used in the <i>in vitro</i> model of the human larynx.	296
C.6	Technical drawing for the front plate used in the <i>in vitro</i> model of the human larynx.	297
C.7	Technical drawing for the glass vocal tract used in the <i>in vitro</i> model of the human larynx.	298
C.8	Technical drawing for the holder used to secure the glass vocal tract in place in the <i>in vitro</i> model of the human larynx.	299
C.9	Technical drawing for the artificial ‘lung’ replica used in the <i>in vitro</i> model of the human larynx.	300

List of Tables

2.1	Table containing measurements of the thickness and composition of the layers of the vocal folds, summarised from data shown in [Titze 94].	40
2.2	Table containing the physiological measurements of a human larynx typical for that of an adult male in speech and singing [Bailly 09]. . .	42
3.1	Table comparing physiological characteristics of an adult male voice in speech and singing with geometrical and dynamical measures of the replica larynx model [Bailly 08]. The <i>in vitro</i> data is that for the model used in this study.	74
3.2	A table showing typical non-dimensional numbers observed <i>in vivo</i> and <i>in vitro</i> and subsequent flow assumptions.	75
4.1	Table summarising the timings for the triggering mechanism used to undertake phase-stepped PIV.	123
4.2	Table summarising the optimum and maximum displacements and velocities for four different sizes of interrogation area for this study using PIV.	126
4.3	Table summarising the settings used in the adaptive correlation function in Dantec Dynamics' DynamicStudio v2.30.	127
5.1	Table showing the range of velocity magnitudes of the jet core (u_{core}), half-width expansion angles (θ_{jet}) of the jet, and the coefficient of determination for the line fitted (R^2) at 6 different subglottal pressures (P_{sub}) in PIV runs using a static <i>in vitro</i> model of the human larynx with no vocal tract attached.	151
5.2	Table containing the amplitude, frequency, and quality factor values extracted from mechanical response plots in Figure 5.10.	156
5.3	Table showing the mean and standard deviation of image pair acquisition times for each phase step in PIV runs using an <i>in vitro</i> model of the human larynx with no ventricular bands.	163
5.4	Table containing the mean minimum ($\overline{h_{min}}$) and maximum ($\overline{h_{max}}$) open heights for the left hand, centre, and right hand lines of analysis for an <i>in vitro</i> model without ventricular bands.	165

5.5	Table showing the half-width expansion angles (θ_{jet}) of the jet and the regression coefficient for the line fitted (R^2) across phase steps 2 - 9 in PIV runs using a self-oscillating <i>in vitro</i> model of the larynx without ventricular bands	177
5.6	Table showing the mean and standard deviation of image pair acquisition times for each phase step in PIV runs using an <i>in vitro</i> model of the human larynx with rigid ventricular bands placed 16 mm downstream of the vocal folds with an 8 mm separation	185
5.7	Table showing the mean and standard deviation of image pair acquisition times for each phase step in PIV runs using an <i>in vitro</i> model of the human larynx with rigid ventricular bands placed 16 mm downstream of the vocal folds with a 3 mm separation	185
5.8	Table containing the mean minimum ($\overline{h_{min}}$) and maximum ($\overline{h_{max}}$) open heights for the left hand, centre, and right hand lines of analysis for an <i>in vitro</i> model with ventricular bands 16 mm downstream and either 8 mm or 3 mm apart.	189
5.9	Table showing the half-width expansion angles (θ_{jet}) of the jet and the regression coefficient for the line fitted (R^2) across phase steps 2 - 9 in PIV runs using a self-oscillating <i>in vitro</i> model of the larynx with rigid ventricular bands placed 16 mm downstream of the vocal folds with an 8 mm and 3 mm separation respectively.	204

*“Since singing is so good a thing, I
wish all men would learne (sic.) to
sing.”*

(William Byrd)

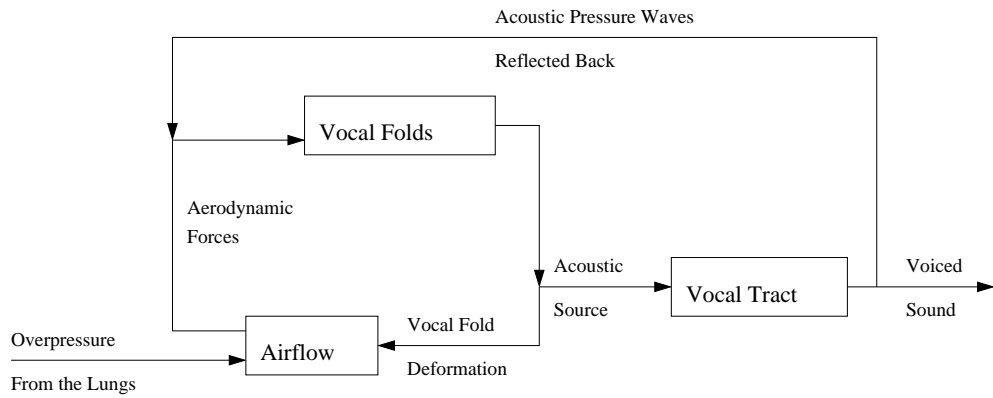


Introduction

1.1 Introduction and Context

Our voices are remarkable instruments, used everyday in today’s world without even a thought, but which are rarely fully appreciated until they one day stop functioning. From seemingly rudimentary speech to high art, the voice is an incredibly versatile tool playing an important role in our society and in our perception of what it is to be human. Indeed, Titze notes that “In combination with our face and hands, it [the voice] signals who we are, what we want, and how we feel” [Titze 94]. The voice also furnishes us with the capability to communicate with others in a way which is not possible by any other means and plays an important role in representing our humanity, something which resonated throughout the recent Opening Ceremony at the Olympic Games in London earlier this month. With our voices being so strongly associated with our character and personality and our constant reliance on its function in either everyday speech or in singing, it is important for us to understand how this instrument works and how to make corrections in pathological cases.

The basic function of human voice can be represented schematically as in Figure 1.1. In this representation, the main mechanism by which sound is produced is through the vocal folds deforming, interacting with the airflow caused by an overpressure from the lungs and then again deforming. A loop also exists whereby the acoustic pressure waves reflected within the vocal tract interact with the vocal folds, meaning that forces additional to the aerodynamic forces act on the vocal folds causing them to deform further. In this study, we will concern ourselves with the first loop and not the acoustic loop but the non-linear nature of the interaction between the vocal folds and



Source: Adapted from [Ruty 07a, Cisonni 08a, Pelorson 08]

Figure 1.1: Schematic representation of the human voice.

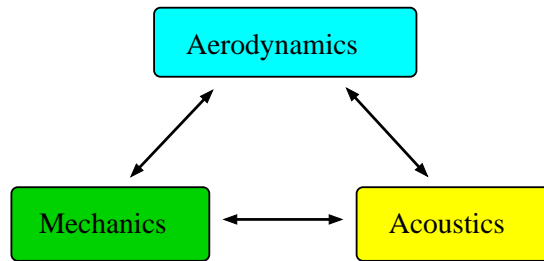


Figure 1.2: A diagram showing the interdependency of disciplines required in the human voice.

the acoustic pressure field within the vocal tract is the subject of other studies.

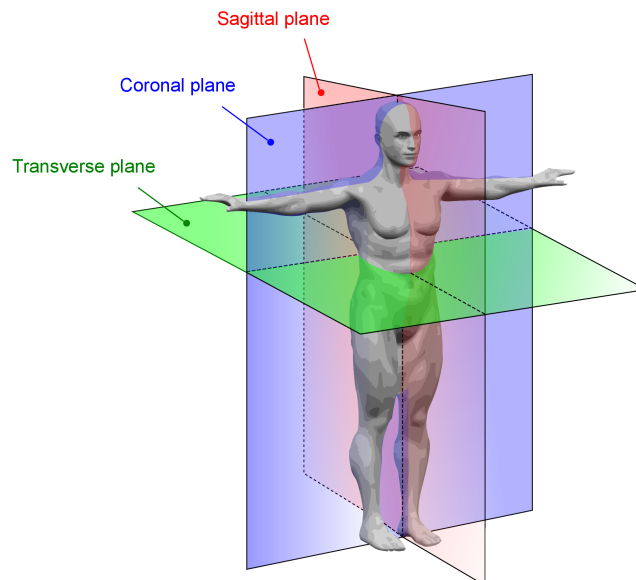
Noting the various elements required in order to produce voice sounds or *phonate*, it is clear that three different disciplines are required in order to produce a full model of the voice. These three disciplines are: acoustics, in order to model the propagation of sound waves within the vocal tract; aerodynamics, to model the behaviour of air within the larynx and its interaction with the vocal folds and ventricular bands; and mechanics, so that the response of the complex biological tissues to elastic deformation by the airflow and acoustic field can be predicted and simulated. Due to the non-linear nature of the behaviour of structures that constitute the voice, these three disciplines are all inter-reliant on each other.

This study considers the airflow and flow-structure interaction in an artificial upscaled model of the human larynx, including self-oscillating vocal folds and fixed

ventricular bands. Experimental measurements are compared with a two-dimensional physical model where the vocal folds are modelled as a two-mass system and ventricular bands as rigid structures. As the majority of any significant fluid-structure interaction takes place between structures found within the larynx, this thesis is limited only to examining this component.

1.2 Terminology

There are a few terms used in this study which are particular to this field of research and need clarifying in order to avoid ambiguity.



Source: After [wik 12b]

Figure 1.3: Schematic diagram showing the locations of the sagittal, coronal, and transverse planes.

In vivo

When the term *in vivo* (meaning ‘in the living’) is used in the context of this study, it refers to the vocal apparatus within living subjects. For example, a study conducted *in vivo* might be completed on a living human being.

Ex vivo

When the term *ex vivo* (meaning ‘out of the living’) is used in the context of this study, it refers to experiments where the vocal apparatus has been removed from living subjects. For example, a study conducted *ex vivo* might be completed on the excised larynx of a subject which is not now living.

In vitro

When the term *in vitro* (meaning ‘in glass’) is used in the context of this study, it refers to experimental apparatus which is not conducted using either living or dead human or animal tissue.

Sagittal Plane

Referring to Figure 1.3 the sagittal plane is one which runs from the front to the back (e.g. a mid-sagittal plane might run from the nose through to the centre of the spinal column).

Coronal Plane

Referring to Figure 1.3 the coronal plane is one which runs from the one side to the other (e.g. a mid-coronal plane might run from the centre an ear on one side of the head to the centre of the ear on the other side of the head).

Phonatory Cycle

The phonatory cycle (also known as the vibratory or mucosal cycle) is described as the process over which the vocal folds are forced apart, reach their maximum opening displacement, are draw back together, and then reach the same geometry that they assumed at the start of the cycle. When phonatory cycles are repeated then sound is produced which is described as phonation.

1.3 Aims

The primary objectives of this thesis are:

1. To construct an *in vitro* model of the human larynx on which it is possible to perform PIV and acquire full flow-field data up to the vocal folds, thereby exposing the complete glottal jet.
2. To include ventricular bands suitable for PIV within the *in vitro* model of the human larynx and analyse the effect of these constrictions on the vocal folds and glottal jet.
3. To investigate the three-dimensional dynamical nature of the glottal jet through the analysis of flow-field data acquired on the same *in vitro* model of the human larynx.
4. To further develop an existing state-of-the-art computational, low-order, lumped-element, physical model of the human larynx in order to investigate the relationship between jet behaviour and vocal fold oscillation.

1.4 Content Outline

This study is constructed from three main parts: a consideration of the dynamical nature of an experimental *in vitro* model of the human larynx with rigid ventricular bands using a high-speed camera, a study of the behaviour of the glottal jet in the experimental model in two perpendicular planes using a technique called Particle Image Velocimetry (PIV), and a comparison between measurements made with experiments and simulations using a state-of-the-art simplified computational physical model. The outline to the content of these three parts and the associated background and theory is summarised below.

Chapter 2 presents a brief description of the anatomy and physiology of the human larynx as is relevant to this study, which is then followed by a critical review of previous attempts at modelling the human larynx.

Chapter 3 begins with a derivation of the assumptions that are made regarding the fluid flow in the *in vitro* model and in the computational physical model along with

non-dimensional numbers, which are used as a measure of the dynamic similarity of the fluid. An explanation of and justification for the simplified models created which models complex vocal anatomy follows this with a discussion of the principles of voice production. The *in vitro* model and its construction is discussed along with detailed descriptions of the mechanical response and high-speed camera experiments used to study the *in vitro* model. Finally, the computational physical model is described, along with models for the expansion of the glottal jet and the implementation of the physical model using a distributed computing paradigm.

Chapter 4 provides a description of the PIV system used in this study to produce full flow-field measurements of the glottal jet and surrounding fluid. In this chapter the background theory to PIV is outlined together with a detailed view of the experimental apparatus and software used. The last part of the chapter details the methods and algorithms used to analyse and interpret the PIV flow-field data in later chapters.

Chapter 5 is the first of the two results chapters and can be divided into five parts. The first part of this chapter discusses the basic structure of the glottal jet and an analysis of the ensemble-averaged PIV results for a control free jet case is presented. The second part presents results of studies made using the mechanical response and high-speed camera setups before self-oscillation of the vocal folds begins.

The third part presents ensemble-averaged PIV results and the results of measurements using the high-speed camera setup for the *in vitro* model without ventricular bands. The fourth part presents ensemble-averaged PIV results and the results of measurements using the high-speed camera setup for the *in vitro* model with ventricular bands and considers the impact of their presence on the glottal jet and oscillation of the vocal folds. The final part of this chapter presents the results of simulations made using the computational physical model, with comparisons made between these results and those from earlier in the chapter.

Chapter 6 is the second of the two results chapters and presents ensemble-averaged PIV results for the *in vitro* model with and without ventricular bands for the PIV plane perpendicular to that used in the previous chapter. As for Chapter 5, these results can be split into those for the *in vitro* model with ventricular bands and those without. The impact of the ventricular bands on the glottal jet in this plane is considered and a comparison is made between the PIV results in this plane and those from the plane used in Chapter 5.

Chapter 7 provides the conclusions for this work in line with the original aims of this study. Possible future work is also presented and discussed. Finally, in the appendices can be found a list of publications associated with the study, sets of additional results, and detailed drawings of the experimental apparatus used.

*“Some books are to be tasted, others
to be swallowed, and some few to be
chewed and digested.”*

(Francis Bacon)

2

Review of Vocal Anatomy and Previous Modelling Attempts

2.1 Introduction

*“There is no algorithm nor implementation of a non-human voice
production system that could compete with a human singer with respect
to beauty or versatility today.” [Kob 04]*

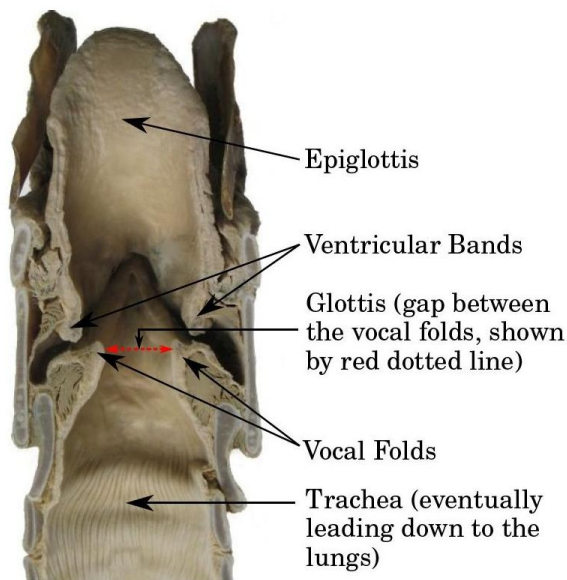
The singing voice is one of the most expressive, dramatic, and emotionally moving of all musical instruments. The ability of the professional singer, particularly if engaged in Western opera, to repeatedly fill large performance venues and typically be heard over orchestras producing ten times the sound power [Campbell 98] is truly remarkable. With strong similarities existing between the dynamics of a brass player’s lips and that of the vocal folds of a singer [Campbell 04], scientific interest into the principles that govern the way in which we speak and sing can be traced back initially to von Helmholtz’s investigations into the physics of brass and woodwind instruments [von Helmholtz 54]. However, pre-dating Helmholtz’s work Kob records in his survey [Kob 04] that the origin of physical voice synthesis dates back as far as the 18th century to von Kempelen’s *speaking machine* of 1769.

The field of speech and phonation research is highly developed with many journal papers, conference papers, and books published annually. Initially the majority of this research was focused on synthesising the voice using computational methods developed from electrical engineering using the principle of equivalent electrical

circuits. With the continual increase in computing power available, efforts by researchers are now being directed towards modelling phonation from a more physical perspective.

2.2 Anatomy of the Human Larynx

To fully understand any attempts to model phonation it is important first to understand something of the anatomy of the complex biological structures involved. A brief account of this is presented here; however, a more detailed description can be found in [Zemlin 68, Shearer 79, Sundberg 87, Titze 94, Stevens 98]. The vocal apparatus required for speech and singing, in acoustical terms, consists of a voice source (the larynx), a passive resonator (the vocal tract, composed of the pharynx and upper respiratory ducts), and an airflow supply (the lungs).



Source: Adapted from [wik 12a]

Figure 2.1: A mid-coronal section of a horse larynx with labels.

Figure 2.1 shows a labelled diagram of the larynx for a horse, where all the constituent elements are clearly visible. At the head of the larynx is a cartilage called the *epiglottis*. During swallowing, the larynx is raised causing the *oesophagus* to sit against the *epiglottis* in order to stop food and fluids from entering the lungs. The *vocal folds* can be seen clearly within the larynx as the structures producing the narrowest constriction. These are also known as the vocal cords, but due to their appearance being more like folds than stretched strings they shall be called the vocal folds throughout this study. A section

through the vocal folds is shown in Figure 2.2, illustrating their complex and intricate structural composition. The vocal folds are created from a muscle layer

2.2. ANATOMY OF THE HUMAN LARYNX

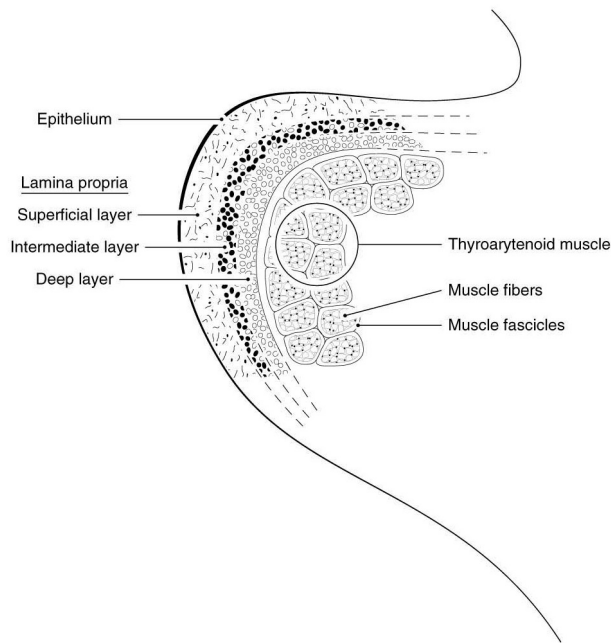
Layer	Typical Thickness	Composition
Epithelium	0.05 - 0.10 mm	Stratified squamous epithelium
Superficial layer	0.5 mm	Elastin fibres
Intermediate layer	} 1 - 2 mm	Homogenous elastin fibres and some collagen fibres
Deep layer		Collagen fibres
Thyroarytenoid muscle	7 - 8 mm	Muscle fibres organised into fascicles

Table 2.1: Table containing measurements of the thickness and composition of the layers of the vocal folds, summarised from data shown in [Titze 94].

(the *thyroarytenoid muscle*) which is then covered by a trilaminar surface (called the *lamina propria*), the individual layers for which are composed of varying mixtures of collagen and elastin fibres. Covering the *lamina propria* is a very thin layer of soft, fluid-like tissue called the *epithelium* [Titze 94]. Typical thicknesses and composition of the layers of the vocal folds are summarised in Table 2.1. This construction inevitably leads to a complex interaction between these various layers and with the air flow during phonation. The gap between the vocal folds is called the *glottis*.

The mechanism by which the vocal folds are brought together in order to oscillate and separated is called *adduction* and *abduction* (respectively). These processes are caused by muscles pulling on the *arytenoid cartilage*, attached to which are the vocal folds. The other end of the vocal folds are attached to the much larger *thyroid cartilage*, with the length of the vocal folds (and therefore the tension across them) controlled by the angle formed by the this cartilage. Sundberg [Sundberg 87] observes that in order for the vocal folds to undergo *adduction* the *lateral cricoarytenoid* and *interarytenoid muscles*, attached to the anterior process of the *arytenoid cartilage*, are contracted. Similarly, in order to undergo *abduction* the *posterior cricothyroid muscles*, attached to the lateral process, are contracted pulling the vocal folds apart. It is also noted that although other muscles are involved in vocal fold *adduction* and *abduction*, these are the muscles with the greatest contribution to these processes.

Above the vocal folds at a distance of between 3.7 mm and 7.5 mm for men or 2.3 mm and 5.7 mm for women [Agarwal 03, Agarwal 04] lie the ventricular bands,



Source: Figure 1.13 from *Principles of Voice Production*, Titze [Titze 94]. Reproduced with permission.

Figure 2.2: Labelled illustration showing a coronal section through one of the vocal folds.

also known as the ‘false vocal folds’. These are like the vocal folds but have been observed to have a lower stiffness and be more viscous, thereby making them poor oscillators [Agarwal 04]. Found between the vocal folds and ventricular bands lies a region of space called the laryngeal ventricle (also known as the *ventricle of Morgagni* [Baer 75]), within which a jet of air formed by the glottis (called the *glottal jet*) is observed.

In other studies, the ventricular bands have been seen to play an important role in some musical styles in particular Mongolian and Tibetan throat singing [Fuks 98, Lindestad 01] and Sardinian *cantu a tenore* [Henrich 06a]. However, their effect during singing and speech is surprisingly still not fully understood [Bailly 08]. An effect called *period doubling*, where the ventricular bands oscillate with half the frequency of the vocal folds, has been observed during endoscopic studies of singers from these specialist musical traditions [Fuks 98, Bailly 08, Bailly 09, Bailly 10]. The

2.2. ANATOMY OF THE HUMAN LARYNX

	Range of Values	Average Value
Diameter of the vocal folds d_{vf}	3 - 9 mm	4 mm
Diameter of the ventricular bands	1.1 - 10.6 mm	5 mm
Glottal width (z -axis) W_{vf}	14 - 22 mm	20 mm
Ventricular band width (z -axis) W_{vb}	-	20 mm
Glottal height h_{vf}	0 - 3 mm	1 mm
Ventricular band separation h_{vb}	0 - 9 mm	5 mm
Length of the laryngeal ventricle, L_{vent}	3.3 - 7.5 mm	5 mm
Height of the laryngeal ventricle, h_{vent}	9.6 - 23 mm	16 mm
Height of the trachea, $h_{trachea}$	18 - 22 mm	20 mm

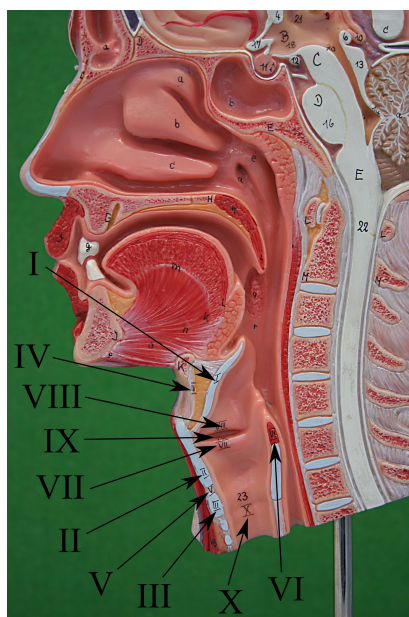
Table 2.2: Table containing the physiological measurements of a human larynx typical for that of an adult male in speech and singing [Bailly 09].

oscillation of the ventricular bands have also been observed in pathological cases; Nasri *et al.* [Nasri 96] note that the ventricular bands participating during phonation can cause the vocal folds to not oscillate normally. They also state that this disorder, called *ventricular dysphonia*, remains poorly understood.

Figure 2.3 shows three different images: one of which is of a labelled model of a mid-sagittal section through a human head; one of which is the same only for a cadaver, thereby showing the likeness between a model and a cadaver; and the final image is a median sagittal section through the posterior wall of the larynx and trachea from a cadaver in order to see the elements of the larynx already discussed on a human subject. Labels for elements of the larynx within the image taken of the model are included in this figure. As this study is not concerned with the structures outwith those already discussed (some of which appear in Figure 2.3), a more detailed consideration of the laryngeal anatomy can be found in the sources already highlighted.

Shown in Table 2.2 are the physiological measures for a human larynx typically found in an adult male. The table has been reproduced and adapted from [Bailly 09] who quotes several different studies as sources for the data shown. These physiological measurements are important values and will be used later to compare with similar measurements determined for deciding the scaling of the *in vitro* model.

2.2. ANATOMY OF THE HUMAN LARYNX



(a) Plastic model of the human head in the mid-sagittal plane.



(b) Human head in the mid-sagittal plane from a cadaver.

- I - Epiglottis
- II - Thyroid cartilage
- III - Cricoid cartilage
- IV - Hypoepiglottic ligament
- V - Cricothyroid ligament
- VI - Arytenoid muscle
- VII - Vocal fold (containing the *thyroarytenoid muscle*)
- VIII - Ventricular band
- IX - Laryngeal ventricle (between VII and VIII)
- X - Trachea



(d) Median sagittal section through the posterior wall of the larynx and trachea from a human cadaver exposing the tongue, epiglottis, vocal folds, and ventricular bands.

Figure 2.3: Series of images of the human head and larynx either from plastic models or from human cadavers. Anatomical labels for Roman numerals shown in (a) are included.

2.3 Previous Studies

It is very clear from even glancing briefly at the intricate anatomy discussed in this study so far that the physics governing phonation is highly complex. As a result of this, various models and methods for understanding and exploring this problem have appeared in published studies, with researchers having different opinions and justifications for their individual approaches. In this section, a critical examination will be made of the different approaches to studying the larynx, with the advantages and limitations of each study highlighted. As this study is performed using an *in vitro* model of the vocal folds, the following section will be focused on studies concerned with models of this type. However, a brief consideration of *ex vivo* studies on canine larynges will be made with the aim of placing *in vitro* studies in context.

2.3.1 *Ex vivo* Studies using Canine Larynges

Ex vivo studies have been conducted in an attempt to understand vocal fold oscillation and the nature of the glottal jet for many years. Indeed, Berke *et al.* [Berke 87] record one of the earliest studies involving excised human and canine larynges as dating back to 1746 [Ferrein 46]. Canine larynges have been used for this purpose because there is a sufficient degree of similarity between the size, geometry, and tissue properties of the human larynx and that of dogs [Drechsel 07], and because they are more easily obtainable.

One of the most substantial early works to adopt this approach is that of Baer [Baer 75]. Continuing much of the same work undertaken by van den Berg [van den Berg 57b, van den Berg 57a, van den Berg 58, van den Berg 60], Baer uses excised canine larynges, seen as simplified versions of the human larynx, to better understand the shape of the glottis during phonation. This is achieved through viewing windows and the use of a stereoscopic microscope, with the samples placed under stroboscopic illumination. Observations are also made of gross responses to any changes in the subglottal pressure and tissue velocity.

Some of the advantages of this approach over more artificial models discussed in the thesis are that no approximation of the intricate tissue structures is required, and that any results can be directly related to modifications made to the anatomical structure. For example, Baer notes that by removing the vocalis muscle from his

samples he was able to sustain a close to normal chest register but not a falsetto sound, leading him to then consider the exact role of this muscle in phonation. It is noted, however, that Baer does not include a vocal tract in his work, thereby allowing the glottal jet to exit into the laboratory, which is hence described as a free jet. This will have an impact on any results gained as, has been shown in later studies, the presence of a vocal tract does alter the pressure at which the vocal folds begin to self oscillate (known as the *phonatory threshold pressure* (PTP)) as shown by results in [Newton 09, Bailly 09] and so must influence the glottal jet to an extent.

One of the first attempts to quantify the airflow through the glottis was undertaken by Berke *et al.* [Berke 89]. This study used hot-wire anemometry to measure volume velocities at five different points along the mid-line of the glottis with the aim of building particle velocity profiles for the sub- and supra-glottal airflows. Also considered as part of this study was the effect of vocal fold configuration on the particle velocity profiles. The results from this study demonstrated that the flow through the glottis may not be uniform, forming a jet, and that canine larynx studies were feasible for examining the flow during phonation.

One of the major limitations of this study is the use of hot-wire anemometry. Hot-wire anemometry is not ideal because velocity data is collected with a single probe, thereby providing information at only one point in the flow. Also, the presence of the probe disturbs the flow, which may have an impact on the results. Finally, using hot-wire anemometry it is not possible to gather any information on the direction of the flow being considered. Neubauer *et al.* [Neubauer 07] also identify that hot-wire anemometry assumes that velocities are non-zero only in one direction and that no negative velocities can be measured.

Three more recent studies by Khosla *et al.* [Khosla 07, Khosla 08a, Khosla 09] use a number of different canine larynges (3, 5, and 6 respectively) with quasi phase-locked particle image velocimetry in order to study vortices in the velocity flow fields downstream of the supraglottal exit. The PIV image pairs were synchronised to the vocal fold oscillation using a microphone signal and then phase-averaged using images captured by a high-speed camera. The data from [Khosla 07] recorded that the frequency of oscillation for the vocal folds was 200-235 Hz; however, oscillation frequencies are not provided in [Khosla 08a, Khosla 09] although the volumetric flow rates in [Khosla 08a] are within the range of those seen in [Khosla 07].

Two interesting observations in [Khosla 07, Khosla 08a] is the report of very stable oscillation, with jitter measured between 0.03 and 0.06%, and symmetric oscillation from high-speed camera footage. A point to note at this stage, however, is that the vocal fold oscillation frequency appears to be quite high considering that the frequency in 8 out of 10 canine larynges from an earlier study [Berke 87] were between 80 and 110 Hz. Berke *et al.* do mention though that they did encounter frequencies up to 340 Hz; however, this was recorded for particularly high levels of recurrent and superior nerve stimulation. Asymmetric oscillation is reported in [Khosla 09] with jitter values below 0.1%.

Using PIV instead of hot-wire anemometry is a major improvement on previous studies. PIV allows for the quantification of the full velocity flow field at a certain point in the phonatory cycle rather than having to build this up from repeated measurements taken with the hot-wire probe. Additionally, as PIV is an optical technique the flow is not disturbed, which is not the case when using hot-wire anemometry. The results from [Khosla 07] demonstrated that vortical structures are apparent above the supra-glottal exit and that the shape of these is consistent at the same point in the phonatory cycle. This leads to the conclusion that these vortical structures must be important to vocal fold vibration and sound production. Indeed [Khosla 09] concludes that vortices during vocal fold closure are very important to the nature of the closing phase and subsequently to sound production. Limitations to all three of these studies are that no vocal tract or supra-glottal laryngeal structures were attached as part of the model, thereby only allowing the free jet case to be considered. Furthermore, only one subglottal pressure, the PTP, is considered. Finally, a further limitation is the time the larynx can be used for phonation. As has been mentioned in [Drechsel 07], this has lead to too few averages being taken at the 30 different phase points in the phonatory cycle.

Due to the increased interest in the role of the ventricular bands in phonation and the attempts of researchers to replicate observed behaviour in singers, several papers over the last four years have been published to look at the effects of the ventricular bands in excised canine larynges. A very recent and highly interesting study completed by Alipour and Scherer [Alipour 12] uses *ex vivo* canine larynges to investigate the role of the ventricular bands in these models. Following on from earlier studies [Alipour 07, Finnegan 09], this study uses excised dog larynges in order to study the effects of the

ventricular bands on the pressures measured within the ventricle. The experiment used seven different dog larynges and a pressure transducer, a pump system providing a static subglottal pressure with the electroglottograph signal (as a measure of vocal fold separation), subglottal pressure, flow rate, acoustic, and ventricular pressures all recorded. A high-speed camera also was used to record the motion of the vocal folds and later produce kymographs.

Two interesting results come out of this study. The first is that the ventricular bands can be found to oscillate at phases which are not necessarily in-phase with the oscillation of the vocal folds and at subharmonics. Alipour and Scherer note that they were not able to find the underlying cause for this, which is common within these studies due to the significant number of uncontrolled variables involved and is one of the unfortunate problems of using this approach. The second is that during ventricular band oscillation, as the gap between the ventricular bands narrows a positive pressure is observed for the pressure in the ventricle. This of course indicates that the ventricular bands do interact with the flow upstream and this work provides results with which it is possible to make comparisons with using *in vitro* and computational models.

2.3.2 *In vitro* Studies using Rigid Vocal Fold Models

Some of the first *in vitro* studies using rigid vocal fold models assumed that the flow through the vocal folds was steady. Being the simplest of all the *in vitro* models, this type is the one most unlike the actual vocal folds. One of the first studies to use this model was [van den Berg 57b]. In an effort to measure the pressure distribution across the glottis, van den Berg *et al.* took a plaster cast of the human vocal folds. This was then modified so that the glottis was rectangular and the diameter adjustable. A series of holes were made in the cast with a diameter of 0.1 mm, through which the pressure was measured using a water manometer. It was noted that for pressure measurements in the glottis, where the diameter was less than 0.8 mm the size of the pressure measurement holes, became an issue and a correction was necessary. Above a critical volume velocity, it was found that the resistance becomes dependant upon the volume velocity due to the formation of vortices. A smooth-walled metal model was created to test volume velocities up to 700 cm³/s.

Results from this study show that a pressure drop is apparent through the glottis and that, neglecting losses due to turbulence and friction, this is broadly in-line with

modelling based on the Bernoulli equation. Van den Berg *et al.* also concludes that a negative intra-glottal pressure may bring the vocal folds together and be partly responsible for vocal fold closure. A further observation was that vortical flow was not confined to the glottis, thereby taking place in the vocal tract further upstream. This view has not been up-held in later studies.

A considerable number of later studies by Scherer *et al.* [Scherer 81, Scherer 83, Scherer 01, Scherer 02] continued the work of van den Berg using static, steady-pressure models. In these studies, Plexiglas models with different configurations were used to investigate the pressure distribution through the glottis. With the model being up-scaled to 7 times life size, this experimental study, coupled with computational fluid dynamic (CFD) models (using a package called FLUENT), aimed to further explain the aerodynamics of the glottal jet. The results from these studies illustrate that obliquely angled vocal folds with a uniform glottal channel exhibit intra-glottal pressure differences. This is an important result, as we are not only able to accurately model the situation using CFD, but the observation of negative intra-glottal pressures at particular points indicates the role of aerodynamics in glottal closure and the presence of possible vortices in the flow. An obvious limitation to these studies is how closely this situation relates to the dynamic motion of actual vocal folds. Respectively, this issue is considered in the discussion element of [van den Berg 57b].

A significant improvement to the static flow models was achieved by Pelorson *et al.* [Pelorson 94] by revising the fluid mechanical description of the flow through the glottis to include a moveable flow separation point. The reason for the introduction of a non-stationary flow separation point being so significant is that the flow separation point is used to determine the volume velocity and hydrodynamic forces exerted by the flow on the vocal fold tissues. Describing the fixed flow separation point model as unrealistic and other effects such as: flow separation at the entrance of the glottis, flow reattachment at the glottal outlet, and asymmetry in the flow due to the Coandă effect, being regarded as irrelevant to phonation, this study takes the traditional two-mass model (comprising of two square-shaped masses on springs with dampers representing each of the vocal folds) and replaces each of the square masses with round masses with smooth transitions between the two. Pelorson *et al.* also validate this experimentally with flow measurements, which are mainly steady in nature. The results presented show a significant improvement on the previous flow model of Ishizaka and Flanagan

[Ishizaka 72]. A good correlation is observed between the glottal volume velocity time derivatives for a numerical simulation using the smooth model and inverse filtering of real speech, which serves to confirm the validity of this flow model in comparison to actual data. Further research, however, to improve the ‘realism’ of this work is identified.

Extensions to this study were published by a similar team in [Pelorson 95]. In this work Pelorson *et al.* add further complications by considering unsteady-flow conditions and more realistic vocal fold geometries. The unsteady flow is created by introducing a valve at the start of the tracheal tube, just after the air supply. The simple valve construction consisted of a sliding metal door connected to a spring. Four different glottal models were used, which consisted of: a straight model with a rounded glottal entrance; a wide-angled ($\alpha = 20^\circ$)¹ diverging glottal model; a narrow-angled ($\alpha = 10^\circ$) diverging glottal model; and a continuously diverging glottal model, rounded at both the glottal entrance and exit (very similar to the lips of a brass player). The model was up-scaled so that it was three times life size. Flow visualisation, pressures, and flow velocities were measured and compared to theoretical predictions and other studies. The results confirm that flow separation does not take place at the supra-glottal exit but within a divergent glottal channel. Also, it is shown that the transition from a laminar to a turbulent flow is shown to take place after the supra-glottal exit. This was also shown to take place at a distance from the point of exit. Finally, it was remarked that the Coandă effect was not to be considered in relation to voiced sound as, although present in steady-flow models, its presence in unsteady-flow models was not apparent. This was attributed to the idea that the Coandă effect required a significant amount of time to become established.

2.3.3 *In vitro* Studies using Driven Mechanical Vocal Fold Models

One of the limitations identified in most of the previous studies concerned with static vocal fold models was the lack of dynamic motion in the vocal folds altering the flow. The natural progression from these studies is to introduce movement into the vocal fold models. However, the motion assumed in these models is forced, therefore the full effects of the aerodynamic interaction of the glottal jet with the vocal fold tissue cannot be fully examined. The earliest two studies considered in this part ([Shadle 91]

¹Where α denotes the angle between the lines formed by the glottal walls.

and [Mongeau 97]) are also discussed in [Drechsel 07]. Some of the points which Drechsel identifies are summarised here, but are also expanded upon.

One of the first studies to use a driven mechanical vocal fold model was [Shadle 91]. In the second part of their study, Shadle *et al.* use a dynamic life-size model with simple Teflon shutters to represent the vocal folds, a rectangular glottis, and a square duct representing both the vocal tract and the trachea. One of the shutters was attached to a motor, which was then driven in a sinusoidal motion to represent the oscillation of the vocal folds. Although this action replicates the pathological condition where one of the vocal folds becomes paralysed, unlike in the pathological case the vocal folds in this study close fully. It should be noted that this is not the only study to be concerned with the flow of air through pathological vocal fold cases, other studies to include discussion of this are [Steinecke 95, Story 95, Kob 04, Triep 05, Khosla 08b]. This number is not surprising, as one of the main incentives for undertaking research in vocal fold modelling is to contribute to the easing of pathological conditions and the prediction of the outcome of surgery. An 8.3 cm vocal tract tube and non-oscillating ventricular bands were also part of the model. The observations from this work, using flow visualisation, recorded that the presence of the vocal tract when compared to the case without caused the glottal jet to expand more slowly. Another observation was that the ventricular bands had the effect of focusing the glottal jet, keeping it along the glottal mid-line even when the glottis was asymmetric. A limitation of this work is that the geometry of the ventricular bands was not specified explicitly and that no detailed fluid mechanical examination is undertaken.

Mongeau *et al.* [Mongeau 97], in an attempt to verify the legitimacy of the quasi-steady air flow assumption, built a more realistic *in vitro* model than that of [Shadle 91]. Another aim of the study was to verify the one-dimensional monopole model for predicting the sound pressure generated by a pulsating jet. The driven mechanical model had rubber vocal fold moulds with more realistic geometries modelled on the convergent shape, with a deformable rubber larynx. Flow visualisation, mean flow measurements, time-averaged pressure measurements across the glottis, and flow velocity measurements were made. Cigarette smoke was used to seed the flow upstream of the glottis to allow laser illumination for flow visualisation. The data from this work appear to be in good agreement with that recorded in [Scherer 81] for a static laryngeal model, and those recorded in [Alipour 95] for an *ex vivo* canine laryngeal

study. It was concluded that the quasi-steady assumption was valid, but only outside of the jet-formation stage (which corresponds to 1/5 of the overall glottal cycle). A limitation of this study was that the model had no vocal tract, meaning that only the free jet case was considered. Also, it is noted that no attempt was made to replicate the transition between the trachea and the larynx.

In a recent study [Triep 05], Triep *et al.* used high-speed PIV measurements on a mechanically driven model of the vocal folds to undertake a detailed analysis of unsteady vortical structures downstream of the glottis. The three times life-size model used consisted of two rotating cams covered with a silicone membrane. Each of the cams is designed such that a realistic glottal profile is assumed as they turn, as illustrated in [Hofmans 98]. An advantage of this approach is the ease within which pathological conditions can be modelled, having only to change the cams involved. A square perspex vocal tract is attached along with static ventricular bands, also manufactured from perspex. Mid-way along the vocal tract, a 45° bend is inserted to allow for additional optical access and to reduce pressure wave reflections. However, it is noted that at low frequencies this bend will not be that effective against pressure reflections. It should also be considered that, unlike all other studies mentioned so far, this work was undertaken in water. Although, it is evident that careful consideration has been given to the all-important dimensionless parameters which characterise the flow, ensuring that these are the same as those used for experiments in air. An advantage of undertaking this study underwater is that the frequencies and flow velocities are reduced, making PIV easier and allowing a high spatial and temporal resolution.

The results from this study include PIV images at instantaneous points through the glottal cycle and phase-averaged images at those points with and without ventricular bands. An interesting observation is the appearance of the Coandă effect in unsteady flow, only seen previously in steady flows. Triep *et al.* postulate that the presence of this effect could be important in the oscillation of the ventricular bands. Whether this is true or not is difficult to assess, particularly as the ventricular bands modelled here are rigid. Conclusions to this study include the fact that the emerging jet appears to attach itself to one of the ventricular bands at an early stage. It was interesting to note that large differences are observed at the same phase points in the glottal cycle between the model with and without ventricular bands. However, one of the key results from this

experiment was that the flow was observed as being highly three-dimensional, thereby bringing into question any glottal flow measurements solely in two dimensions.

An interesting study by Krane *et al.* [Krane 07] uses PIV and a dynamic vocal fold model which is ten-times life size in water in order to study unsteady flow effects in the larynx. This work has been built on a previous theoretical study [Krane 06] where some interesting findings were made, but which left questions regarding assumptions about the glottal flow. The reason for water being used in [Krane 07] as the working fluid is the same as that discussed in [Triep 05], where the fluid flow speeds required are much lower in order to achieve dynamic similarity with the life-size scenario. In addition, the frequency of oscillation of the vocal fold model was 15 Hz which, combined with the increased size of the model, greatly improved the spatial and temporal aspects of this experiment. A slightly asymmetric vocal fold opening function was used and the model is shown to be used without ventricular bands. Krane *et al.* observe a glottal jet in their results which occasionally flaps from side-to-side which they attribute to the Coandă effect. One of the most interesting results to come from this study is the maximum axial velocity component measured at the glottal exit. Across the phonatory cycle, the flow speeds are shown to be asymmetric with the speeds being noticeably higher during the closing phase than the opening phase showing that the glottal jet accelerates and that inertial effects are most likely responsible for this. A follow-on paper [Krane 10] takes this observed asymmetry further and considers time variance of this acceleration coming to the conclusion that inertial effects at the end of the phonatory cycle cannot be ignored.

Finally, a further study [Triep 10] followed their previous study using the same model and setup as in [Triep 05]. This study extends the previous work by specifically considering the three-dimensional nature of the glottal jet. Triep and Brücker use both flow visualisation and particle image velocimetry to study the flow in the model both with and without ventricular bands present. Triep and Brücker perform their experiments in two planes (both parallel and perpendicular to the open width of the glottis), which is the same practice as is used in this study. Although it is not possible to see the impact of the ventricular bands in vocal fold oscillation, it is interesting to see that the shape of the glottal jet changes when the ventricular bands are added. Due to the differences in shape and positioning of the ventricular bands, it will not be possible to make any direct comparisons with results presented here. Finally, a very interesting

observation made was that the jet expansion angle was influenced by the change in subglottal pressure. This would be an interesting point to test in a self-oscillating *in vitro* model, which may change the way in which results between papers using similar models are compared.

2.3.4 *In vitro* Studies using Self-Oscillating Vocal Fold Models

The final type of *in vitro* study to be considered in this review is the vocal fold models that self-oscillate. With the goal of all research into human phonation being the reproduction of the self-oscillating vocal structure, this model represents one of the most recent developments in the field. Over the years, two very distinct opinions have developed as to how to approach modelling the self-oscillating vocal folds. One of these, favoured by those who work along similar lines as Ingo Titze, involves modelling the vocal folds with as much anatomical detail as possible. Another approach, favoured by those who work along similar lines as Avraham Hirschberg and Xavier Pelorson, involves considering the model from a fluid mechanical perspective, using simpler computational models which are then validated through experiment. Although these models are considerably more simple, they still demonstrate all of the observed phenomena of the more complex models at a first approximation [Hirschberg 96].

One of the first studies to mention an *in vitro* self-oscillating vocal fold model is [Titze 95]. In this work, Titze *et al.* attempt to replicate the complicated layered structure of the vocal folds using what will later be known as the ‘body-cover’ model. Using a hemi-larynx setup, the life-size model is built from a rigid stainless steel body and a cover made from a silicone dispersion liquid. A rectangular Plexiglas section 2.7 cm in width and of unspecified length is used with a hole cut out where the vocal fold is to be inserted. Between the body and cover layers, and representing the superficial layer of the *lamina propria*, is a layer of liquids of varying viscosity. Together the body (known anatomically as the *epithelium*) and aqueous layers constitute what is known as the *mucosa* [Titze 94]. The shape of the glottis in this study was rectangular. Their aim was to use the body-cover model vocal fold to study the effect of glottal width and fluid viscosity on the PTP. Using a water manometer to measure the pressure, the conclusions found that glottal width and fluid layer viscosity had the effect on the PTP predicted in earlier work on small amplitude oscillation. Other effects observed were that the lowest value for the PTP was recorded when the glottal width was greater than

zero. A further observation made was that the PTP was higher when subglottal pressure was increased than decreased, thereby creating a hysteresis effect. A limitation of this study is that no vocal tract is incorporated into the model, which has been shown in studies to have a direct effect on the PTP for self-oscillating models [Newton 09, Bailly 09].

An important study in the use of simplified models of the vocal folds was undertaken by Rutty *et al.* [Rutty 07b]. In this work, Rutty *et al.* consider the use and accuracy of low-order models in light of the criticism that the physics they use is too crude. Taking two theoretical models, including one two-mass model used in previous studies [Pelorson 94, Pelorson 95], and an *in vitro* self-oscillating vocal fold model made from latex and water, fluid mechanical, mechanical, and acoustical analyses are run on the theoretical models together with mechanical response and pressure measurements on the experimental model. Finally, linear stability analysis was undertaken on the theoretical models to examine whether they conform with what was observed from experimental data. Unsurprisingly, the conclusions from this work indicate that qualitatively the low-order models are comparable in terms of acoustic coupling, the fundamental frequency, and pressure threshold evolution as a function of the internal pressure of the replica. What was highlighted as being difficult to capture with the one- and two-mass models was the three-dimensional movement of the initial vocal fold oscillation, which made the quantitative errors on the PTP large. A final remark made was that this study did not consider the hystereses observed in other works; however, it is mentioned that this point has been clarified in other low-order model studies.

A recent study to investigate the near field flow for a silicone mono-layered vocal fold model was undertaken by Neubauer *et al.* [Neubauer 07]. Using PIV and flow visualisation, this study aimed to quantify the structure of the glottal flow of the self-oscillating physical model, with the goal of improving the discrepancy previously seen between theory and experiment [Hofmans 03]. The manufacturing details of this model are reported as being in [Thomson 04, Thomson 05]. As Neubauer *et al.* have noted, other studies have also considered the three-dimensional nature of the glottal jet [Barney 99, Hirschberg 92, Hofmans 98, Hofmans 01, Krane 05, McGowan 88, Shadle 99, Zhang 02a]. Indeed, in [Hirschberg 96] it is stated that a prediction of the point of flow separation and glottal jet area cannot be made without a full knowledge

of the near field structures downstream of the glottis. One of the problems with using self-oscillating vocal fold models and PIV is timing the laser pulses and the camera such that images can be taken at exactly the same phase points in the phonatory cycle. Usually, if the sound source is driven (as in the case of a loudspeaker) this is not a problem, as the phase information is known and the equipment can be synchronised; however, with self-oscillating vocal folds this is not the case. A sensible approach taken by Neubauer *et al.* was to record the far field sound pressure and trigger signal generated for each laser pulse and then correlate this with the phonatory cycle based on the harmonic content present in the far field pressure. This approach is indicated as producing ‘quasi phase-locked’ PIV images.

The equipment used for this study include a double-headed Nd:YAG laser, producing approximately 5 - 10 mJ per laser pulse, and a double shutter camera. The reported laser pulse time interval was 5 μ s. Using commercial software, the PIV cross-correlation analysis regime included a multi-pass algorithm consisting of two passes with 64×64 and one with a 32×32 interrogation window. The interrogation window overlap was reported as being 50%. The frequencies of oscillation for the vocal folds were 100 - 122 Hz (typical frequencies of phonation for males) and the flow rates recorded were 480 - 630 ml/s. Presenting flow visualisations and PIV images for various points during the phonatory cycle, the resulting PIV images were analysed to numerically extract the coherent flow structures.

The key conclusions to emerge from this study are that further confirmation is given of the three-dimensional nature of the downstream glottal jet. In addition, vortex generation, vortex convection, and jet flapping were observed. A limitation of this study lies in the presence of a semi-vocal tract. Having the dimensions $25.4 \text{ cm} \times 12.7 \text{ cm} \times 12.7 \text{ cm}$ and assumed to be up-scaled by a factor of five in terms of a real vocal tract, the effects of the walls of the vocal tract model on the jet are reported in the work to be neglected. A further limitation of this work is the exclusion of ventricular bands, which have been proven in earlier works to have a significant effect on the flow dynamics. Finally, it is noted that only 51 pairs of quasi phase-locked flow visualisation and 50 pairs of PIV images were presented for analysis. This is much lower than would typically be expected.

A recent and very interesting collaborative study between Lucie Bailly [Bailly 09] and Michael Newton [Newton 09] considered the aerodynamic interaction of the

ventricular bands and vocal folds in a two-mass model. Using a replica model three times life-size with upstream acoustic damping, static ventricular bands, and a duct representing the vocal tract, theoretical predictions were validated using results obtained from PIV and flow visualisation data. The results from three different *in vitro* experimental setups were presented. These setups included the free jet (used as a test case), a realistic implementation of the ventricular bands (VB - A), and the case where the ventricular bands are considered impeding (VB - B). A useful table comparing the dimensions of salient aspects of the *in vitro* model and those from *in vivo* studies is presented in [Bailly 09]. Having similar problems with synchronising PIV images with defined phase points along the phonatory cycle, Bailly and Newton implement a similar solution to Neubauer *et al.* [Neubauer 07] and separate their results into phase windows. The data collected from the PIV measurements was synchronised with the open height of the vocal folds after the experiment was completed. A full description of this technique is provided in [Newton 09].

The analysis of the quantitative study of the glottal flow consisted of a comparative study of the cross-sectional area of the free jet case with those predicted using three theoretical models proposed in [Bailly 09]: the uniform jet theory, turbulent expansion theory, and the laminar jet theory. The results of this comparison showed that the turbulent expansion theory best matched the data gathered experimentally. Fluid mechanical comparisons of the results from the experimental setups were also undertaken considering: turbulence in the jet core, the Reynolds number in the jet core, normalised jet velocity, and vocal fold flow impedance.

Some of the key results from this analysis indicated that, in the free jet case the level of turbulence in the jet is related to the size of the vocal fold opening and the flow deceleration. In agreement with recent work undertaken in [Neubauer 07], jet flapping was observed indicating that large vortical structures are present at either side of the jet at different points in the phonatory cycle. The stability of the two ventricular band setups, measured using the standard deviation of the jet velocities, was shown to be higher than that for the free jet case. It is then postulated that this result indicates that the jet reattaches at the ventricular bands leading to the structure observed in the free jet case degrading. It was found that the jet in the realistic ventricular band case was slightly more stable than the case with the impeding ventricular bands on account that the standard deviation for the jet core velocity was lower. Limitations of this work

include three aspects: the PIV laser pulse separation window (thereby capping the flow speeds measured), optical access to the first 8 mm within the laryngeal ventricle on the *in vitro* models, and that the PIV images acquired are not exactly phase-locked to a certain point on the phonatory cycle. An idea for any future work might be to also include deformable ventricular bands rather than just static models, which was also a point raised in [Alipour 12].

Finally, the most recent study using self-oscillating *in vitro* models is that by Krebs *et al.* [Krebs 12]. This study uses a simplified *in vitro* model of the human larynx which is very similar to that used in this study (which is unsurprising as they were both modelled on the replica used at GIPSA-lab in Grenoble, France). Two significant differences are to be noted though, the first is that the *in vitro* model used by Krebs *et al.* is presumed to be life-size and includes a 17 cm long vocal tract. This model therefore includes the effects of acoustical coupling both on the dynamics of the jet and of vocal fold oscillation. The second difference is that the Krebs *et al.* model does not include ventricular bands, so therefore cannot measure their effect in any way. The study presents novel results using stereoscopic PIV (SPIV) in order to acquire full flow-field data for the *in vitro* model. The SPIV was repeated at several points down the vocal tract in order to acquire a mean volumetric representation of the velocity flow field. As these results were acquired from a model which is similar to that used in this study, this will be one of the main studies used for comparison of three-dimensional data acquired during this study.

*“Essentially, all models are wrong, but
some are useful.”*

(George E. P. Box)

3

Physics and Fluid Dynamics in Models of the Human Larynx

3.1 Introduction

The human voice is a remarkable instrument capable of producing a myriad of different sounds, of varying timbre and tone. As has already been discussed, one of the overwhelming difficulties with studying the human voice and the elements from which it is constructed within the larynx is the ability to gain access to it. Experimental and computer-based replicas of the voice allow us to have this access, albeit with a limitation to the degree of realism achieved. Nonetheless, there are distinct advantages to using models in studying the dynamics of the human voice, the reasons for which will be explored in more detail later.

In this chapter, the underlying aerodynamic theory and assumptions which are made in the state-of-the-art computational lumped element physical model of the human larynx are considered. The aerodynamic background behind the formation of the glottal jet is also discussed. Before details of the *in vitro* model of the human larynx are discussed, the non-dimensional parameters used in an analysis of the model in comparison to those observed *in vivo* are explained and considered. Next the physiology of phonation is detailed with how the complex vocal fold anatomy, already discussed in Section 2.2, is represented in a simplified model with the reasons for this approach. A detailed description of the *in vitro* model used in this study is then considered. Although this model is based on an earlier model discussed in [Newton 09], significant changes have been made to this model in order to consider

it a model of the vocal folds and on which to undertake PIV. These changes were designed to make it possible to acquire novel PIV results from the point at which the glottal jet leaves the vocal folds up to the ventricular bands, which was previously not possible.

The last three sections of this chapter consider two experimental setups used with the *in vitro* model of the human larynx to provide information needed to undertake a complete PIV study of the human larynx and for parameters required in a computational physical model of the same. The first experiment, the mechanical response, is used to acquire the natural resonance frequencies of the *in vitro* model and the quality factor for these resonances as input parameters to the computational physical model. The second experiment, measuring the model open height and area using a high-speed camera, is undertaken in order to synchronise the acoustic cycle, which is extracted from signals recorded during PIV measurements, with the open area of the *in vitro* model in order to consider the PIV flow-field maps against the model dynamics. This experiment is also used to see the impact of the ventricular bands on the open area and centreline open height of the vocal folds.

The final section details the state-of-the-art computational physical model used in this study. The same model was used in [Bailly 09, Newton 09]; however, as well as being translated from French, modifications have been made to the model in order to undertake this study. In addition, the way in which the model has been interfaced with Condor will be discussed as a further novel contribution of this study to the field.

3.2 Fundamental Aerodynamic Theory

In order to model the airflow through the human larynx, it is necessary to consider the Navier-Stokes equation and to reduce this down to a form which is both as simple as possible and yet provides a sufficiently accurate model of the fluid. The full Navier-Stokes equation governing the basic motion for a fluid arises primarily from Newton's second law of motion and includes terms concerning fluid viscosity and pressure. Tritton [Tritton 88] defines the full Navier-Stokes equation in vectorial form as being given by

$$\underbrace{\rho \frac{D\vec{u}}{Dt}}_{\text{Fluid mass-acceleration}} = \underbrace{-\vec{\nabla} p}_{\text{Pressure gradient}} + \underbrace{\mu \nabla^2 \vec{u}}_{\text{Viscosity}} + \underbrace{\frac{1}{3} \vec{\nabla} (\vec{\nabla} \cdot \vec{u})}_{\text{Compressibility}} + \underbrace{\vec{F}}_{\text{Body forces}}, \quad (3.1)$$

3.2. FUNDAMENTAL AERODYNAMIC THEORY

where ρ is the density of the fluid, μ is the coefficient of viscosity, p is the pressure acting on the fluid, \vec{u} is the fluid velocity, \vec{F} is the body force per unit volume, and $\frac{D}{Dt}$ is the substantive or material derivative which is defined for a vector field \vec{u} as

$$\frac{D\vec{u}}{Dt} = \frac{\partial\vec{u}}{\partial t} + \vec{u} \cdot \vec{\nabla}\vec{u}. \quad (3.2)$$

The Navier-Stokes equation is highly non-linear due to the $[\vec{u} \cdot \vec{\nabla}\vec{u}]$ term from the substantive derivative, often called convective acceleration. To solve this analytically presents one of the most difficult problems known in mathematics and is one of the reasons that a large amount of knowledge regarding fluid behaviour comes from experiments.

Incompressible Fluid

For an incompressible fluid, where the density does not change with respect to time or position, it is possible to state that $\vec{\nabla} \cdot \vec{u} = 0$, which therefore means that it is possible to write

$$\rho \frac{D\vec{u}}{Dt} = -\vec{\nabla}p + \mu \nabla^2 \vec{u} + \cancel{\frac{1}{3} \vec{\nabla} (\vec{\nabla} \cdot \vec{u})}^0 + \vec{F}. \quad (3.3)$$

The external forces acting on the fluid are typically

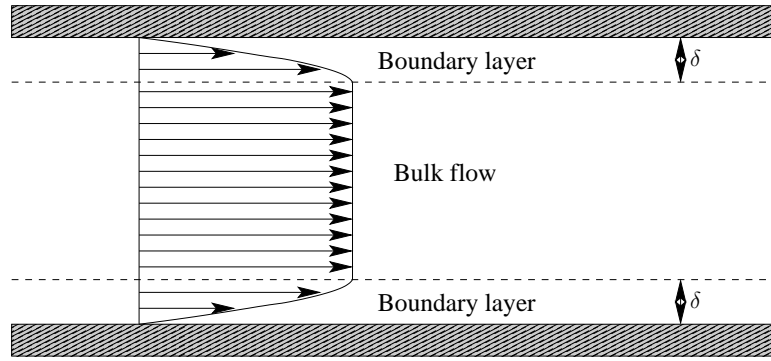
$$\vec{F} = \rho \vec{g}, \quad (3.4)$$

where \vec{g} is the gravitational force vector. As the source of forces acting on the fluid are usually considered to be due to a pressure difference or moving boundaries, it is also then possible to negate this term and write $\vec{F} = 0$. Therefore, the Navier-Stokes equation for an incompressible fluid neglecting external forces due to gravity can be written as

$$\rho \frac{D\vec{u}}{Dt} = -\vec{\nabla}p + \mu \nabla^2 \vec{u}. \quad (3.5)$$

Inviscid Fluid

When the viscous forces within a fluid, defined as the resistive forces of the fluid to either shear or tensile stress, are insignificant in comparison to its inertial forces then the fluid is considered as being inviscid. This condition is not usually true close to a



Source: Redrawn from [Hofmans 98]

Figure 3.1: Schematic diagram showing the *boundary layer* and *bulk flow* regions in pipe flow.

fluid boundary due to the fluid adhering to the wall (termed the ‘no-slip’ condition) forming a velocity gradient, with the region over which this effect takes place known as the *boundary layer*. The remaining part of the flow is known as the *bulk flow*.

If the fluid is described as being inviscid, then the following statement can be made

$$\rho \frac{D\vec{u}}{Dt} = -\vec{\nabla}p + \mu \nabla^2 \vec{u}, \quad (3.6)$$

meaning that the Navier-Stokes equation can be further reduced to Euler’s equation of incompressible fluid motion

$$\boxed{\rho \frac{D\vec{u}}{Dt} + \vec{\nabla}p = 0.} \quad (3.7)$$

Bernoulli Equation

Bernoulli’s equation provides a description of the fluid velocity for a given pressure assuming that the fluid is both incompressible and inviscid. This is a very useful equation for modelling the dynamics of the human larynx and can be derived in a number of different ways. Here we will assume that the flow is both steady and irrotational and shall derive Bernoulli’s equation in this case from Euler’s equation as shown in [Faber 95]. Firstly, expanding out the substantive derivative yields the

3.2. FUNDAMENTAL AERODYNAMIC THEORY

equation

$$\rho \left(\frac{\partial \vec{u}}{\partial t} + \vec{u} \left(\vec{\nabla} \cdot \vec{u} \right) \right) + \vec{\nabla} p = 0. \quad (3.8)$$

Assuming that the fluid is steady (i.e. time-independent) the $\frac{\partial \vec{u}}{\partial t}$ term is removed such that the equation now takes the form

$$\rho \vec{u} \left(\vec{\nabla} \cdot \vec{u} \right) = -\vec{\nabla} p. \quad (3.9)$$

If the fluid is assumed to be irrotational (satisfying Laplace's equation) then it can be presumed that

$$\frac{\partial v}{\partial x} = \frac{\partial u}{\partial y}, \quad \frac{\partial w}{\partial x} = \frac{\partial u}{\partial z},$$

so that

$$\begin{aligned} (\vec{u} \cdot \vec{\nabla}) u &= \frac{\partial \left(\frac{1}{2} u^2 \right)}{\partial x}, \\ \therefore (\vec{u} \cdot \vec{\nabla}) \vec{u} &= \vec{\nabla} \left(\frac{1}{2} u^2 \right). \end{aligned}$$

Returning the newly calculated term for $(\vec{u} \cdot \vec{\nabla}) \vec{u}$ to Euler's equation:

$$\begin{aligned} \rho \vec{\nabla} \left(\frac{1}{2} u^2 \right) &= -\vec{\nabla} p, \\ \therefore \vec{\nabla} \left(p + \rho \frac{1}{2} u^2 \right) &= 0, \end{aligned}$$

and integrating in any direction, it is therefore possible to write Bernoulli's equation as

$$\boxed{p + \frac{\rho u^2}{2} = \text{constant}}, \quad (3.10)$$

where p is the static pressure and ρ is the fluid density.

3.2.1 Dimensionless Fluid Mechanical Measures

Aspect Ratio

The aspect ratio Ar is the ratio of the opening in one plane and the opening in the plane perpendicular to this plane. The aspect ratio in this study is defined as

$$Ar = \frac{h_{vf}}{W_{vf}}, \quad (3.11)$$

where h_{vf} is the centreline open height of the vocal folds and W_{vf} is the glottal open width. The aspect ratio is an important parameter in this study as it permits an assessment of the two-dimensionality of the glottal opening and hence the validity of the assumption that the glottal jet can be modelled as a two-dimensional flow.

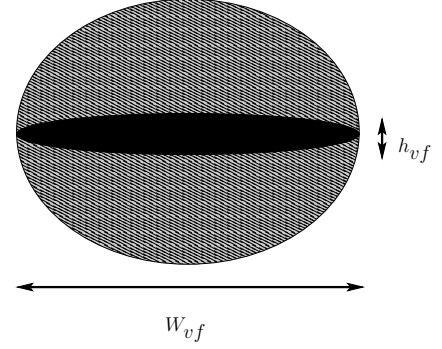


Figure 3.2: Schematic diagram of the vocal folds and glottis showing the glottal centreline open height h_{vf} , and the glottal open width W_{vf} .

Reynolds Number

The Reynolds number is a parameter which expresses the ratio of a fluid's inertial forces against viscous forces. This in turn provides us with a measure of the likelihood of turbulence occurring within the flow. As the Reynolds number increases then the inertial forces within the fluid dominate and the likelihood of encountering turbulence within the flow increases, whereas, as the Reynolds number decreases the viscous forces become more significant and the likelihood of encountering turbulence within the flow decreases. The Reynolds number is calculated using the equation

$$Re = \frac{UL}{\nu}, \quad (3.12)$$

where U is a characteristic velocity, L is a characteristic length of the system, and ν is the kinematic viscosity which is defined as

$$\nu = \frac{\mu}{\rho},$$

where μ is the coefficient of viscosity and ρ is the fluid density.

In pipe flow, it is customary to set the value of L to the minimum pipe diameter. In this case, L would be set to the minimum opening of the vocal folds measured at a certain time. This will mean that the Reynolds number will be different for different glottal open height values, due to the oscillation of the vocal folds. Therefore, the fluid properties of the glottal airflow will not be constant throughout the phonatory cycle. The Reynolds number calculation using the length scale L begins to break down in the boundary layers, due to the flow supposing a much smaller length scale than the bulk flow [Tritton 88]. To this end, the Reynolds number decreasing in the phonatory cycle could be an indication of a decreased ratio between the size of the bulk flow and that of the boundary layers.

Strouhal Number

The Strouhal number provides a measure of the effect of periodic vortices on measured flow velocities [Kundu 02], which can also be considered as a measure of the influence of unsteady effects on the flow [Hofmans 98]. As in [Newton 09], the Strouhal number is defined as

$$Sr = \frac{f_0 d}{U}, \quad (3.13)$$

where f_0 is the oscillation frequency and d is a relevant flow distance. For this study, d could be taken as the length of the vocal folds in the streamwise direction. As a measure of unsteadiness, the Strouhal number is useful in the current study because it can be used to validate whether or not the assumption of a quasi-steady flow within the *in vitro* model is correct.

Mach Number

The Mach number provides an indication of compressibility of the fluid under investigation. In this study the number is defined as

$$M = \frac{U}{c}, \quad (3.14)$$

where c is the speed of sound in air, which is defined in [Kinsler 00] as

$$c = c_0 \sqrt{1 + \frac{T}{273}},$$

where c_0 is the speed of sound in air at 0°C at 1 atm having the value $c_0 = 331.5 \text{ ms}^{-1}$ [Kinsler 00] and T is the temperature of the air in $^\circ\text{C}$.

If the Mach number is below 0.3 [Kundu 02] (or 0.4 in [Massey 98]), then the effects of compressibility on the flow can be neglected. As has been seen already, if the flow is incompressible then the Navier-Stokes equations are greatly simplified. The Mach number is often quoted squared (M^2), with this value being the Cauchy number (C) for an isentropic process which provides the ratio of the fluid's inertial forces against elastic forces [Massey 98].

Helmholtz Number

The Helmholtz number is defined as

$$H_\lambda = \frac{L}{\lambda}, \quad (3.15)$$

where λ is the acoustical wavelength. In this study, the wavelength is that for the fundamental frequency of oscillation for the vocal folds in the *in vitro* model and L is the mean open height of the glottis ($\overline{h_{vf}}$). The Helmholtz number quantifies the contribution of an acoustic field to the compressibility of a fluid; where the value of H_λ is much less than 1, then the wavelength is much larger than the source dimensions [Skulina 05], and therefore any compressibility associated with the acoustic field can be neglected.

Womersley Number

The Womersley number, also known as the oscillatory flow parameter and usually denoted α , is a dimensionless number which is used to characterise the nature of oscillatory flow [Mills 72], and can be written as

$$\alpha = L \cdot \sqrt{\frac{2\pi f_0 \rho}{\mu}}, \quad (3.16)$$

where, as for the Helmholtz and Reynolds numbers, L is an appropriate length scale. It is also possible to write the Womersley number in terms of Re and Sr

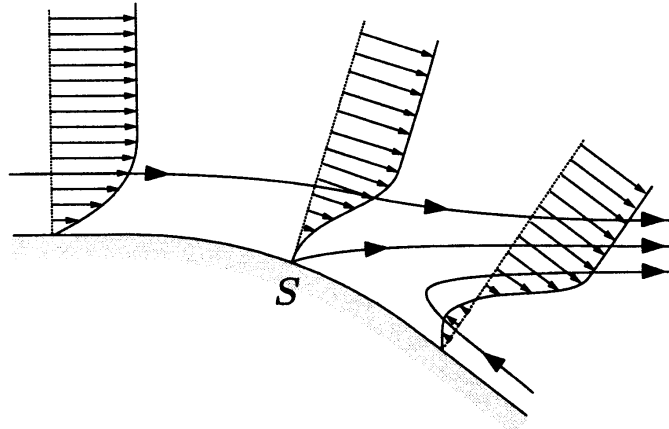
$$\alpha = \sqrt{2\pi \cdot Re \cdot Sr}. \quad (3.17)$$

Being a combination of Re and Sr the Womersley number is a useful representation of the flow which directly expresses the effects of inertia on the flow and thereby consider whether or not the flow is steady, quasi-steady or unsteady in nature. If α is low (of the order of 1), then the flow is said to be quasi-steady as it has sufficient time to adjust fully to pressure gradient changes whereas for flows with intermediate ($\alpha = 5$) or high values ($\alpha = 100$), there is a phase difference between the fluid and pressure gradient as inertial effects become more significant [Greated 90].

3.2.2 Flow Separation and Jet Formation

Flow separation is the mechanism by which the airflow through the glottis detaches from the walls of the vocal folds, thereby forming the glottal jet. In Figure 3.3 flow separation takes place at point S , where the value of $\frac{\partial u}{\partial y} = 0$, due to a reduction in the velocity for the fluid closer to the surface caused by it having less momentum than the surrounding fluid [Massey 98]. This therefore increases the velocity gradient within the boundary layer and causes a adverse pressure gradient to form (shown by the streamline directed against the bulk flow after flow separation) which results in the fluid no longer being able to follow the curvature of the fluid boundary, causing it to separate.

Flow separation has been identified as playing an important role in more realistic voice synthesis through better models of flow behaviour [Pelorson 95, Pelorson 96] with several studies devoted to this cause [Alipour 04, Zhang 08, Van Hirtum 09, Cisonni 10, Šidlof 11]. The impact of two methods for calculating the flow separation condition, the Thwaites' method and Liljencrants' criterion, is discussed in [Bailly 06] where little difference was found between the results from the two methods. However, the computation time required for Liljencrants' criterion is considerably less than that needed for Thwaites' method and so will be used in the computational physical model discussed later.



Source: After [Hofmans 98]

Figure 3.3: A schematic diagram showing the boundary layer separation from a flow boundary, with S marking the point of flow separation. Streamlines are shown as continuous lines with arrows.

3.3 Modelling Complex Laryngeal Anatomy and Physiology

As has been discussed in Section 2.2 from the previous chapter, the composition of the human larynx and of the vocal folds in particular is extremely complicated. Indeed, Titze [Titze 94] notes that as well as the constituent tissues of the vocal folds having non-linear stress-strain curves, they also exhibit a hysteresis behaviour. This presents a significant challenge to the researcher attempting to precisely replicate the dynamics of the vocal folds. In this study as in several others before it [Vilain 02, Vilain 04, Rutty 07a, Cisonni 08a, Bailly 09, Lucero 09, Newton 09], a simplified model of the vocal folds is used in order to study the glottal flow. The argument for the use of simplified models in this case is that although the complex structure and interaction during phonation between the various layers which constitute the vocal folds is crudely approximated, the basic physics underlying the process by which the vocal folds oscillate is still replicated. In addition, using simplified models allows us to observe what behaviour this sort of model can exhibit and what vocal fold behaviour it can not replicate. This is a very important question which then leads to further questions about what physics is actually responsible for the behaviour that is being shown by the simplified model.

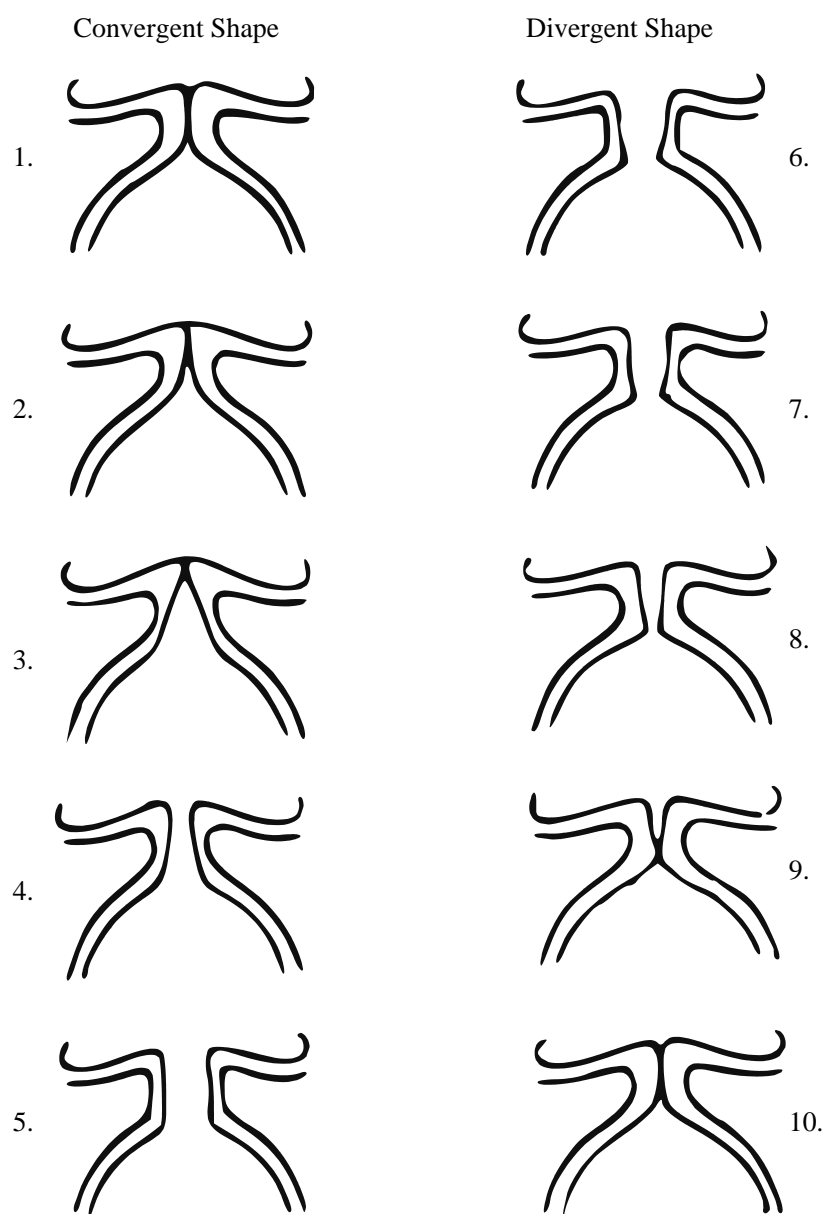
3.3.1 Principles of Vocal Fold Oscillation

During phonation a supply of air at constant pressure is forced from the lungs into the trachea where it then enters the laryngeal structures. With the vocal folds initially adducted prior to phonation, the subglottal pressure then increases to a critical point at which the vocal folds are forced apart [Erath 06]. Once the vocal folds are forced apart they are then drawn back together primarily through a force as a consequence of Bernoulli's principle and the elastic and inertial properties of the vocal fold tissues [Titze 88]. When this behaviour becomes periodic in nature the vocal folds are described as being in *self-sustained oscillation*. The subglottal pressure required to reach this point is described by a variety of authors as the *phonation threshold pressure (PTP)* [Drechsel 07, Titze 92, Tao 09].

For self-sustained oscillation or self-oscillation of the vocal folds to be maintained, the Bernoulli force alone can not be solely responsible for this or be dependent on the vocal fold glottal open width, as this force would act against the opening of the vocal folds with the same force as is applied during closure, thereby imparting no net energy to the vocal folds. This would result in no self-sustained oscillation. In order for this to work the forces acting on the vocal folds need to be 'in phase', so that they reinforce one another and cause a positive net force to act on the vocal folds, required to overcome frictional forces [Titze 88]. This is achieved through either a change in the point of flow separation within the glottis [Hirschberg 92], or through the air above the vocal folds retaining its forward momentum and thereby reducing the supraglottal pressure [Titze 88], which could be responsible for the observed asymmetric opening behaviour.

Due to their elastic nature, determined by their construction, the vocal folds assume very different geometries throughout a period of self-sustained oscillation. Figure 3.4 demonstrates some of the shapes (called glottal geometries) that the vocal folds might assume during one complete cycle. In the figure, glottal geometries numbered 1 - 5 are described as being convergent and 6 - 10 as being divergent in profile. This repeating cycle is termed the *phonatory cycle*. Details of these geometries at varying points during the cycle first appear in [Hirano 87] but are also often cited by other authors [Triep 05, Hofmans 98]. This change in glottal geometry causes the glottis to be asymmetric, thereby creating a disparity in the pressures at the subglottal and supraglottal apertures (described as the intra-glottal pressure).

3.3. MODELLING COMPLEX LARYNGEAL ANATOMY AND PHYSIOLOGY



Source: Redrawn from [pho 01]

Figure 3.4: A diagram showing changes in the shape of the vocal folds and the geometry of glottis through a phonatory cycle.

3.3. MODELLING COMPLEX LARYNGEAL ANATOMY AND PHYSIOLOGY

During the closing phase, where the glottal geometry is described as being divergent, as has been discussed an area of lower pressure is established at the upper part of the glottis. As the airflow from the lungs is forced through the narrow glottis, which acts as an oscillating semi-sharp edge, it is forced into a jet and detaches from the vocal fold and tract walls. This jet then becomes unstable within the laryngeal ventricle introducing turbulence and vortices downstream of the supra-glottal exit. The role of these vortical structures in glottal closure and its effect on sound production is examined from a clinical perspective in [Khosla 08b].

Previously, it was thought that vocal fold oscillation was controlled entirely through the use of laryngeal muscles. According to Sundberg [Sundberg 87], Raoul Husson, using the argument of instantaneous accurate note pitching by singers, believed that aerodynamic forces were not responsible for continued vocal fold oscillation. Although this theory (termed the *Neurochronaxic theory* [Pelorson 08, Berke 87]) was later disproved in [Hast 61], the laryngeal muscles are shown to contribute to phonation by controlling the dimensions of the glottis and hence the extent to which aerodynamic forces act.

Using a high-speed camera, the glottal shapes seen in the same *in vitro* model used in this study from preliminary measurements can be seen in Figure 3.5. Although the extent of the movement is easier to see in the movie from which the images that constitute Figure 3.5 are taken, it can be seen how the glottis changes and that the changes are not large in order to maintain self-sustained oscillation. As can be seen in [Titze 08b] the relatively small amount of vocal fold movement is commensurate with the seen for the *falsestto* register or the M2 laryngeal mechanism as discussed in [Roubeau 09].

3.3.2 The Vocal Tract and Vowel Production

The sound produced by the vocal folds in the form of pressure waves or the dissipation of vortical structures is then modulated into either intelligible speech or song through careful manipulation of the vocal tract and mouth. The configuration of the vocal tract for phonation is called *articulation* [Sundberg 87]. These changes in the profile of the vocal tract and mouth produce areas which are more open and some which are more constricted, which gives rise to resonances called *formants*, which enhance the spectrum of the sound emitted and produce distinguishable and recognisable vowel

3.3. MODELLING COMPLEX LARYNGEAL ANATOMY AND PHYSIOLOGY

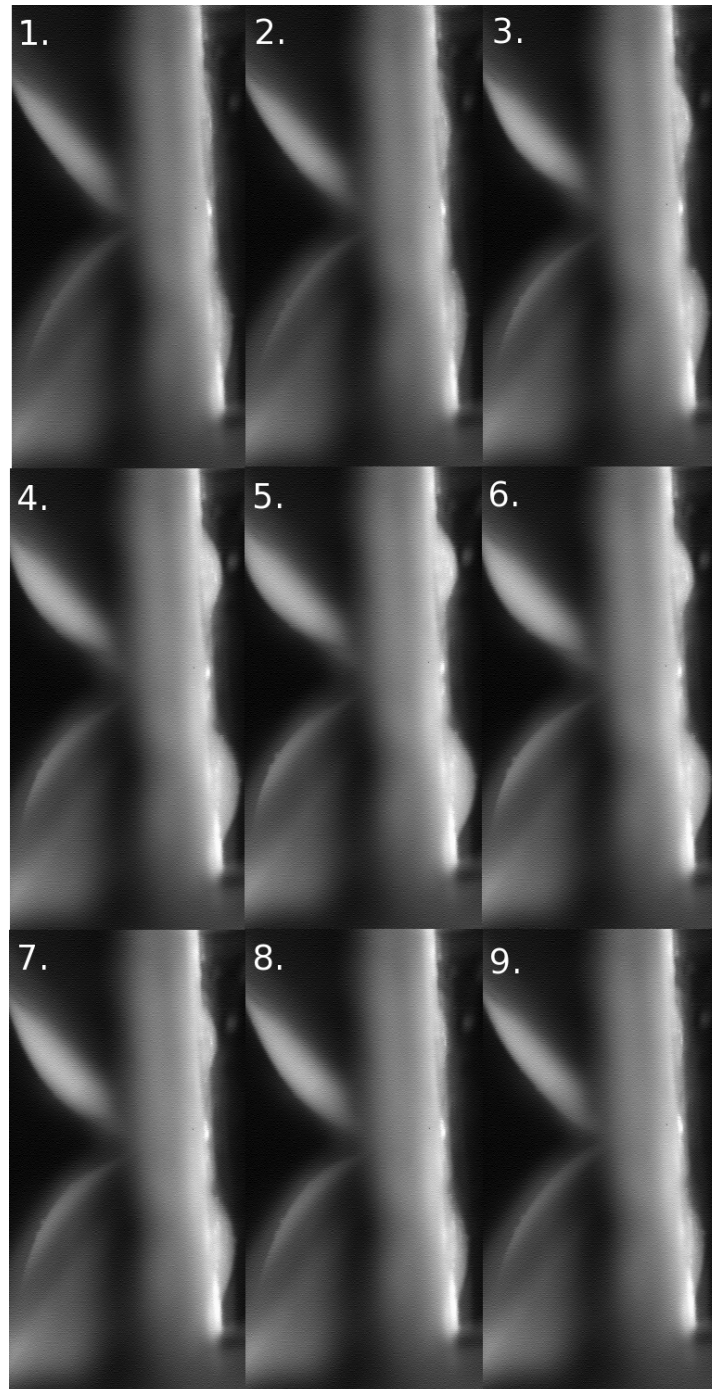
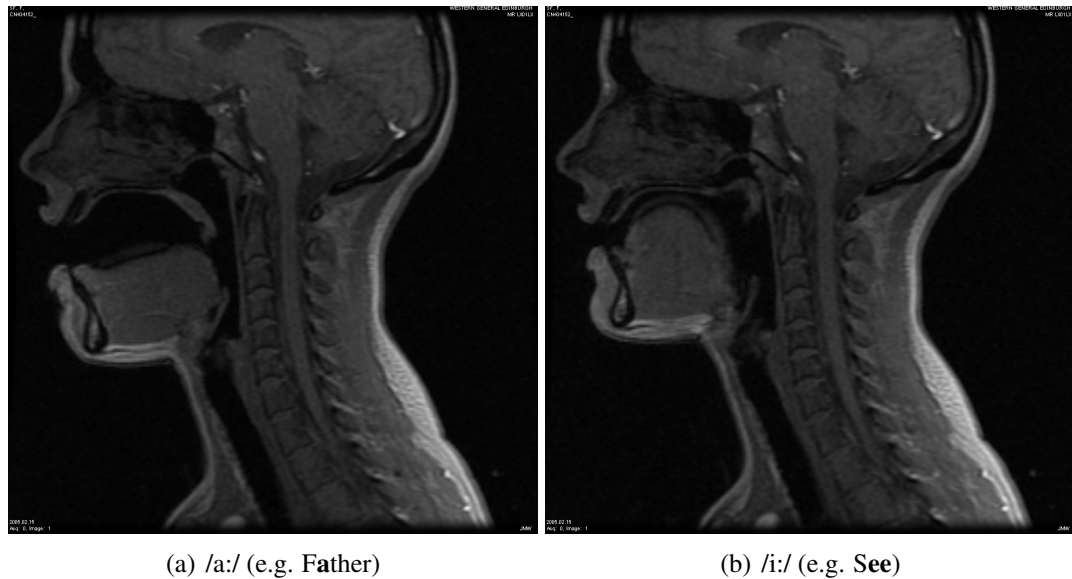


Figure 3.5: Image showing subglottal and supraglottal geometrical changes from high-speed camera filming of the *in vitro* model of the human larynx with a vocal tract but without ventricular bands in self-sustained oscillation through a side window. In each image in this figure the flow moves from left to right.

3.3. MODELLING COMPLEX LARYNGEAL ANATOMY AND PHYSIOLOGY



Source: After [Gray 05]

Figure 3.6: Mid-sagittal plane view of a human head showing the vocal tract shape for two different vowels using Magnetic Resonance Imaging (MRI).

sounds. An additional source of sound is found to come from vortices formed by the glottal jet. Following the complicated interaction of the glottal air jet with the surrounding structures of the larynx, these vortices are found to interact with the acoustic field, characterised in Lighthill's analogy¹ [Lighthill 52, Lighthill 54], to generate wideband noise. This noise is then modulated by the vocal tract to form different voiced sounds (e.g. consonants) used in speech and song.

The dimensions of the vocal tract for specific vowels differ considerably (as illustrated in Figure 3.6). For vowel shapes, the sound tends to be periodic with energy concentrated at low frequencies (typically 50 - 5000 Hz) [Shadle 85]. Unvoiced sounds (e.g. fricatives) are produced by a constriction in the vocal tract, usually at the end towards the mouth. Due to this constriction and because phonation does not occur, this sound manifests itself as noise, typically in the range of 3 - 10 kHz [Shadle 85]. It is noted, however, that there are some fricatives that are voiced, but these are formed simply by adding the voiced vowel and fricative sounds together.

¹Lighthill's analogy describes the way in which sound production information can be obtained from flow-field data [Hofmans 98].

This particular element of voice production is not considered in this study and so will not be covered in any great detail. However, the interaction between the vocal folds and pressure waves within the vocal tract are of interest to researchers in the field and a number of studies have been carried out which take account of their interactivity [Childers 94, Kob 02, Titze 04, Titze 08b, Titze 08a, Titze 09, Kaburagi 11, Zañartu 11].

3.4 *In vitro* Models of the Human Larynx

As has already been established, the vocal folds are built up from an array of different tissue and mucosal layers, and modelling the physics of these layers during oscillation precisely is not something that we are attempting to do in this study. However, in this section the *in vitro* model used in this study and the effects of scale will be discussed.

3.4.1 Using Scaled Models

The issue of scaling is an important one when considering fluid mechanical and acoustical effects, as it is the boundaries surrounding the fluid which are scaled and not the fluid itself. Therefore in the artificial model of the larynx, where fluid-structure interaction is the entire basis by which the system works, the scaling of the whole model is examined and the effects of these deviations from typical dimensions of the human larynx (detailed in Table 2.2) explored in order to relate observed effects in the artificial model to those observed in the natural human larynx.

Through comparing the range of *in vivo* and *in vitro* values quoted in Table 3.1 it is clear that the *in vitro* model used in this study is two times life-size. It is not uncommon for experimental *in vitro* models of the larynx with similar dimensions to be used with a different scaling value quoted in studies. The reason for this is that the larynx is not a fixed structure and can assume many different geometries dependant on the task (i.e. speaking or singing) being performed. In addition, there is a large degree of variability in the geometry of laryngeal structures from person to person. It is due to these differences that such variability and individuality is observed in voices the world over.

In the Table 3.2 can be found the dimensionless parameters, discussed earlier, with values calculated using preliminary measurements from the *in vitro* model. The

3.4. IN VITRO MODELS OF THE HUMAN LARYNX

	<i>in vivo</i> data	<i>in vitro</i> data
Scale	1	2
Glottal depth, d_{vf} (along x -axis)	3 - 9 mm	9 mm
Glottal height, h_{vf}	0 - 1.02 mm	0.20 - 2.34 mm
Glottal width, W_{vf} (along z -axis)	14 - 22 mm	20 mm
Ventricular gap, h_{vent}	0 - 9.0 mm	3.0mm, 8.0 mm
Ventricle length, L_{vent}	3.3 - 7.5 mm	16 mm
Ventricle height, h_{vent}	9.6 - 23.0 mm	20 mm
Subglottal pressure, P_{sub}	300 - 1000 Pa	800 - 820 Pa

Table 3.1: Table comparing physiological characteristics of an adult male voice in speech and singing with geometrical and dynamical measures of the replica larynx model [Bailly 08]. The *in vitro* data is that for the model used in this study.

values associated with the dimensionless parameters are then used to confirm which assumptions are most appropriate with regards to constructing a model of the fluid flow. This table is similar to that used in [Van Hirtum 09] for the same task.

3.4.2 Construction of the *in vitro* Model of the Human Larynx

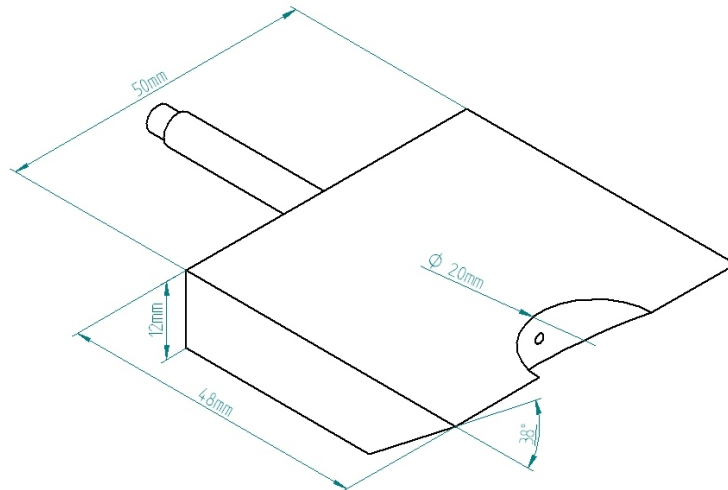


Figure 3.7: A diagram of one of the vocal fold blocks (including stud) with key dimensions labelled.

3.4. IN VITRO MODELS OF THE HUMAN LARYNX

	<i>in vivo</i> data	<i>in vitro</i> data	Assumption
Ar	$0 - 0.14^a$	$0.01 - 0.12$	$Ar \ll 1$ therefore the flow can be considered two-dimensional
Re	$1700 - 3300^b$	$300 - 5050$	$Re \gg 1$ therefore flow can be considered inviscid
M^2	$\approx 10^{-2c}$	$4.00 \times 10^{-4} - 1.44 \times 10^{-2}$	$M^2 \ll 1$ therefore the flow can be considered incompressible
Sr	$0.01 - 0.03^d$	$0.04 - 0.26$	$Sr \ll 1$ therefore the flow can be considered steady
H_λ	$0 - 1.30 \times 10^{-3e}$	$1.19 \times 10^{-4} - 1.24 \times 10^{-3}$	$H_\lambda \ll 1$ therefore flow is not affected by the acoustic field
α	7.86^f	$12.19 - 13.08$	$\alpha \approx 10$ therefore flow is partially affected by inertial forces

^a Ar for *in vivo* data calculated as h_{vf}/W_{vf} .

^b Re for *in vivo* data calculated using average glottal width $h_{vf} = 1$ mm.

^c From [Van Hirtum 09].

^d Sr for *in vivo* data calculated using average glottal width $h_{vf} = 1$ mm and average frequency $f_0 = 150$ Hz.

^e H_λ for *in vivo* data calculated using $h_{vf} = 0 - 3$ mm and $f_0 = 150$ Hz.

^f α for *in vivo* data calculated using $h_{vf} = 1$ mm and $f_0 = 150$ Hz.

Table 3.2: A table showing typical non-dimensional numbers observed *in vivo* and *in vitro* and subsequent flow assumptions.

A self-oscillating *in vitro* model of the vocal folds, including a trachea and vocal tract with and without downstream constrictions was used for this study. Each of the vocal folds was created from an aluminium block, with an edge cut at the top forming a 38° angle with the topside of the block, as shown in Figure 3.7 and seen in a detailed plan for the block in Figure C.4. Out of this edge a half-circle was cut with a diameter of 20 mm over which sheet latex of 0.2 mm thickness is stretched and fixed in place using superglue.

A great deal of care was required in order to fix the latex to the aluminium vocal fold blocks as imperfections in the adhesion would cause water to leak, rendering the model unusable. In addition, it was found that the sheet latex, once stuck, came away from the aluminium block and that imperfections formed in the adhesion after the model had been constructed. A way to counteract this problem was found in fixing double-sided carpet tape (0.5 mm thick) between the sheet latex and the aluminium

block, with the tape fixed both to the sheet latex and the aluminium block with superglue. The carpet tape (with the area covering the cavity cut into the aluminium block) was found to provide a much better surface for adhesive surface for both the latex and the aluminium.

Through holes in the aluminium blocks, the cavities in the vocal fold blocks were then connected to a head of water via Portex flexible tubing and studs attached to the blocks, the plans for which can be found in Figure C.5. After the cavities were filled with water the vocal folds then assumed their initial or resting shape due to the elasticity of the latex. The vocal fold blocks were then mounted into an outer casing, produced from perspex with side viewing windows made from glass, which were then fixed in place with a new purpose-built front plate and sealed using vacuum grease, so as to be air-tight. This new front plate, detailed in Figure C.6 and constructed from polycarbonate, used on the vocal fold model casing was specially designed to support a free-standing vocal tract and to allow as much optical access as possible. Plans for the supports for vocal tract can be found in Figure C.8.

After a period of time it was found that mould developed within the Portex tubing. By replacing the water with Sodium metabisulphite ($\text{Na}_2\text{S}_2\text{O}_5$) diluted using distilled water with a concentration of 0.178 g/l it was found that mould was much less of a problem. Sodium metabisulphite at this concentration posed no risk either to the experimenter or to the equipment or latex (in the form of degradation) as it is commonly used as a preservative and antioxidant in food, known as E223. Careful adjustment of the height of the head of water was used to determine the pressure of water within the vocal folds. The pressure within the vocal folds was determined by

$$P_{in} = \rho gh, \quad (3.18)$$

where $\rho = 1000 \text{ kgm}^{-3}$ is the density of water at 4° , $g = 9.81 \text{ ms}^{-2}$ is the Earth's gravitational constant, and h is the height of the head of water above the centreline of the *in vitro* vocal folds. This was an important control parameter in the experiment, as it allowed for the control of the stiffness of the vocal folds and hence to make adjustments to the frequency at which the vocal folds were oscillating.

The vocal fold model was connected to a 15.3 cm long perspex trachea, which was attached to a large wooden box, modelling the lungs. This box had a volume of approximately 1 m^3 and was lined with acoustically absorbing foam, so as to minimise

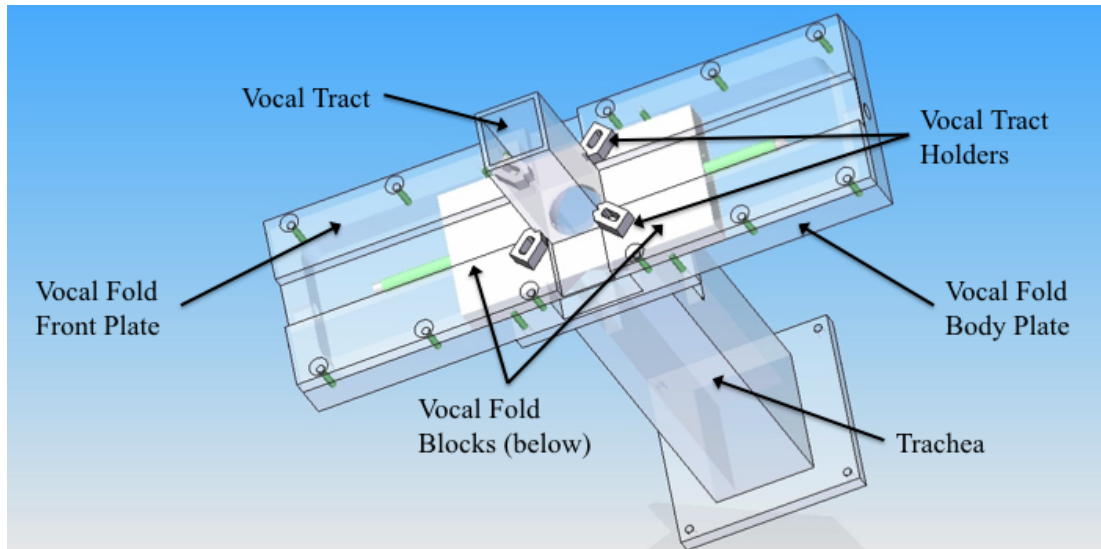


Figure 3.8: A labelled diagram showing the *in vitro* model of the human larynx once constructed.

any possible upstream acoustic resonance and to maintain a constant upstream pressure. A plan of the lung model can be found in Figure C.9. Measurements of the acoustic input impedance for the trachea with and without the artificial lung attached were taken using BIAS equipment and software provided by the Institut für Wiener Klangstil, Austria. From these measurements the impact of the model lung on the upstream resonances are seen in Figure 3.9, where the peaks in the magnitude of the measured input impedance for the trachea with the lung model are about 5 times lower than those without the lung model attached, thereby significantly reducing chance of any upstream acoustic resonance effects seen in [Zhang 06].

Connected to the downstream part of the vocal fold model was one of two glass vocal tracts, one with downstream constrictions and the other without. The glass vocal tracts were hollow cuboidal structures which were 58 mm long and 20 mm wide (internally). This specific geometry was chosen so that optical distortion caused through the use of curved surfaces would be avoided. Figure 3.8 shows the vocal fold model fully constructed and without the lung model attached.

The downstream constrictions, a simplified representation of the ventricular bands, were built from aluminium and had a semi-circular top with a radius of 5 mm and flat sides extending down to the walls of the vocal tract. The separation between the

minimum opening of the two constrictions was 3 mm and the constrictions were placed 16 mm downstream of the entrance to the vocal tract.

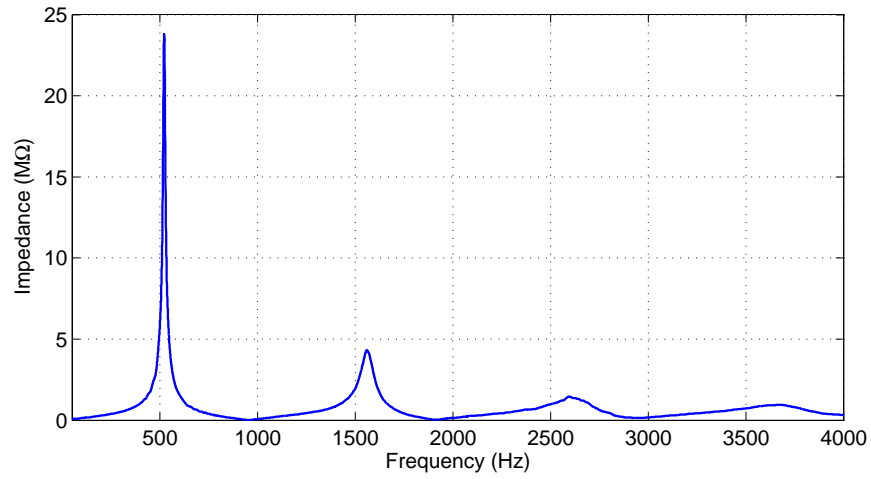
Although the *in vitro* model used in this study is similar to replica B detailed in [Newton 09], it should be noted that Newton's model was that of a brass player's lips and not the vocal folds. Furthermore, in their collaborative work Newton and Bailly used replica C to model the vocal folds which belonged to GIPSA-lab at INPG in Grenoble, and which subsequently went back there once the collaboration was completed. Therefore, replica B was adapted for studying the vocal folds with a new front plate, vocal fold blocks, and vocal tracts with ventricular bands designed and built as detailed above.

3.5 Mechanical Response

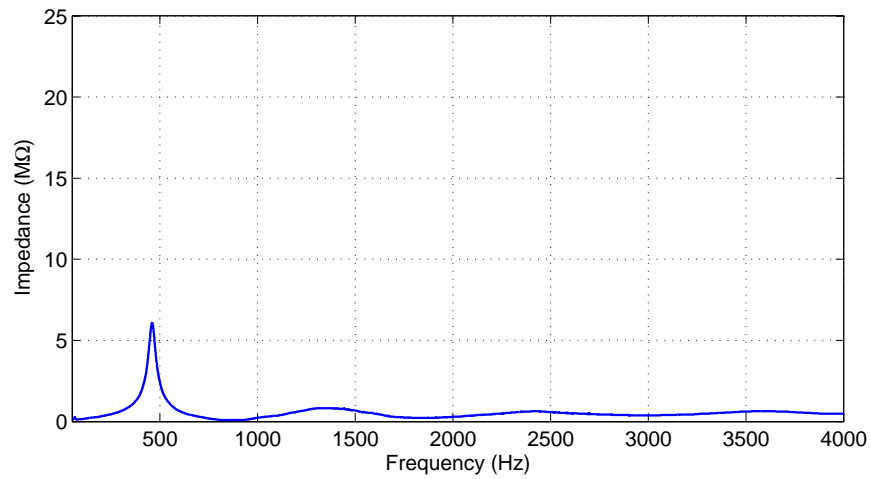
The mechanical response for a structure is the response (often in the form of a displacement) of that structure to a known mechanical driving force. When the driving force is in the form of an oscillation of constant amplitude with the frequency as its variable then the response of the structure becomes known as the frequency response. If the frequency response is conducted over a range of different frequencies it is then possible to construct a frequency response function which then makes it possible to observe natural resonances of the structure under scrutiny.

Mechanical response measurements have been used to characterise simplified models of either the lips of a brass player or the vocal folds in many different studies over a number of years [Gilbert 98, Cullen 00a, Cullen 00b, Neal 02, Richards 03, Ruty 07a, Cisonni 08a, Newton 08, Bailly 09, Newton 09, Cisonni 11, Lucero 12]. Over this time, three different methods have been developed:

1. The mechanical response in one dimension at a fixed point which is measured using a stepped sine wave and a laser vibrometer,
2. The mechanical response of the entire structure across all degrees of freedom which is reduced to single response function, using an expanded laser beam and a laser diode to measure changes in aperture.
3. The mechanical response for the entire structure which is measured using a high speed camera.



(a) without *in vitro* model of the lungs



(b) with *in vitro* model of the lungs

Figure 3.9: Plots of the magnitude of the acoustic input impedance for an *in vitro* model of the human larynx with and without a model of the lungs attached.

In this study, the mechanical response for the whole of the vocal folds will be measured using an expanded laser beam and a laser diode. The method used was exactly the same as the transmission method detailed in [Newton 09] and, as such, the principles behind this measurement technique will be summarised below. The mechanical response function once calculated for the *in vitro* model is used to acquire the correct values for the spring stiffnesses and damping factors for the dashpots in the computational physical model in order to relate the two models.

3.5.1 Principles of Mechanical Response Measurement

The mechanical response of the vocal folds is expressed as the magnitude of their response to an acoustic driving force. As it is assumed that there is a total pressure loss downstream of the vocal folds, the acoustic pressure measured just upstream of the vocal folds therefore represents the total pressure drop across the glottis, therefore meaning that

$$\Delta P_{mr} = p_{mr}, \quad (3.19)$$

where ΔP_{mr} is the total pressure change across the glottis and p_{mr} is the acoustic pressure just upstream of the vocal folds.

As the acoustic driving force used is a sinusoid (a chirp signal for this study), if the vocal folds are driven from downstream rather than upstream then the phase of ΔP will need to be shifted by π radians [Neal 02, Richards 03].

In order to measure the response of the vocal folds to an acoustic driving signal, the change in the glottal opening was measured as a function of time. The mechanical response function can then be expressed as the ratio of the change in the open area of the glottis to the change in the acoustic driving pressure

$$\hat{M}_{mr}(\omega) = \frac{\hat{h}_{mr}(\omega)}{\hat{p}_{mr}(\omega)} \quad (3.20)$$

where $\hat{h}_{mr}(\omega)$ is the Fourier transform of the glottal opening as a function of frequency, and $\hat{p}_{mr}(\omega)$ is the Fourier transform of the acoustic driving pressure as a function of frequency. The $\hat{}$ symbol denotes that the variable is complex.

Both Richards and Newton used the PULSE system [Ban 12] in order to perform data acquisition and signal processing of the acquired pressure and open area data. Due

to the signal processing algorithms afforded by the PULSE system, it was possible to calculate the frequency response function using the averaged power spectrum of the glottal open area evolution and the averaged cross-spectrum of the glottal open area evolution against the acoustic driving pressure. These values are calculated using the following relations:

$$\overline{G_{hh}}(\omega) = \hat{h}_{mr}(\omega) \times \hat{h}_{mr}(\omega), \quad (3.21)$$

$$\overline{G_{hp}}(\omega) = \hat{h}_{mr}(\omega) \times \hat{p}_{mr}(\omega), \quad (3.22)$$

where $\overline{G_{hh}}(\omega)$ is the averaged power spectrum of the glottal open area evolution in the frequency domain and $\overline{G_{hp}}(\omega)$ is the averaged cross-spectrum of the glottal open area evolution against the acoustic driving pressure also in the frequency domain.

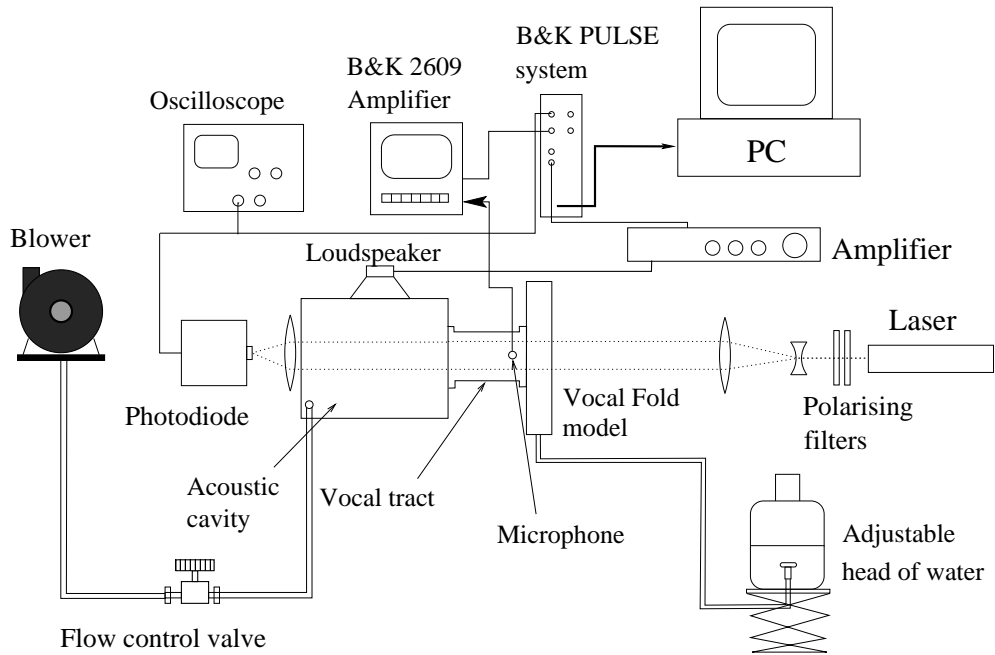
Using the values shown in Equations 3.21 and 3.22, it is possible to then calculate the frequency response function for the vocal folds using the following relation

$$\hat{H}_{mr}(\omega) = \frac{\overline{G_{hp}}(\omega)}{\overline{G_{hh}}(\omega)}, \quad (3.23)$$

where $\hat{H}_{mr}(\omega)$ is the mechanical response function for the vocal folds in the frequency domain, which is a built-in function of the PULSE system and detailed in [Bru 02]. The reason that the mechanical response function was calculated in this way is that it improved the signal-to-noise ratio through the use of averaging over multiple sweeps using the chirp driving signal.

As the outputted mechanical response function for the vocal folds is a complex signal, it is possible to extract the magnitude and phase relationship between the glottal open area and the acoustic driving signal. Peaks in the plotted magnitude can be interpreted as natural resonances of the vocal folds, and where these coincide with a phase difference of either $\pm 90^\circ$ then the vocal fold behaviour can be characterised as being acting as an outward-striking reed (phase difference of -90°) or an inward-striking reed (phase difference of $+90^\circ$). As the characterisation of the vocal folds reed-like behaviour is not one of the aims of this study, it will not be covered any further; however, a detailed consideration of the theory behind the characterisation of a musical reed can be found in [Campbell 99, Campbell 04].

3.5.2 Experimental Apparatus and Procedure

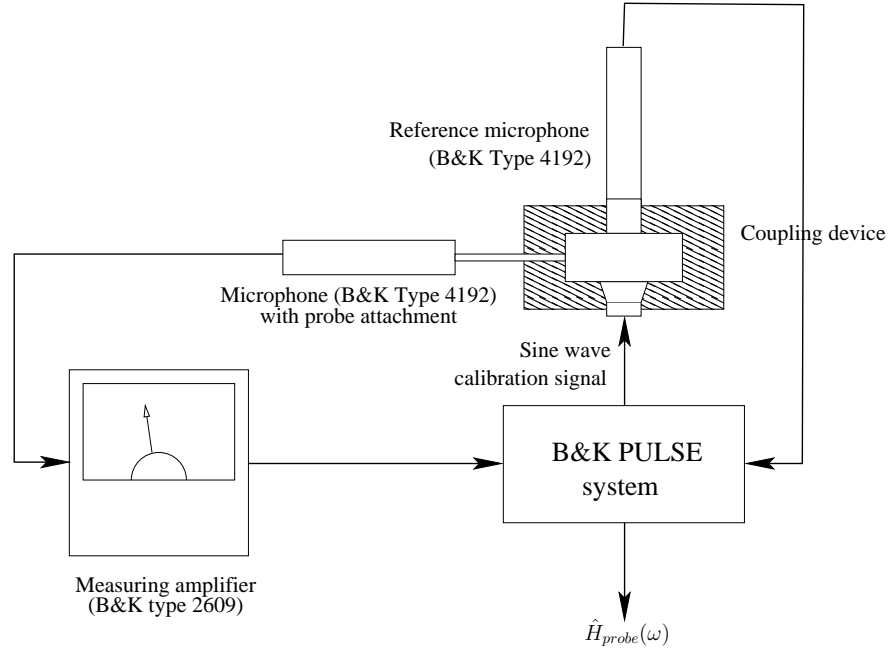


Source: Adapted from [Richards 03]

Figure 3.10: A diagram showing the setup used for undertaking a mechanical response measurement on the *in vitro* model of the vocal folds. Note, the acoustic cavity was only used as part of the mechanical response apparatus and is much smaller than the model lung discussed earlier.

In order to obtain the mechanical response for an *in vitro* model of the vocal folds, a setup separate from that used for PIV measurements was used. A schematic representation of this setup can be seen in Figure 3.10. To record the acoustic driving force on the vocal folds a Bruël and Kjær type 4192 microphone with a short probe attachment was placed 10 mm upstream of the vocal folds and embedded into the wall of the trachea, so that the end of the probe attachment sat flush with the interior wall of the trachea. The response of the vocal folds to the acoustic driving pressure, in the form of a change in the glottal open area was measured using an expanded laser beam from a Melles Griot 5 mW laser shone through the glottal gap which was then focused onto an IPL10530DAL Hybrid Detector photodiode, which Richards notes had a linear response up to 65 kHz [Richards 03]. Therefore, as the open area of the glottis increased, the intensity of the laser light on the photodiode increased resulting

in an increase in the outputted voltage signal. The laser beam was expanded using a concave and convex lens so that the height of the beam extended beyond the full height of the vocal fold glottal open height, and then focused onto the photo diode with a convex lens. The reason for the beam being expanded to such an extent was that if the beam did not cover the full open height of the glottis then the full dynamic range of the evolution of the glottal height would not be captured.



Source: Adapted from [Skulina 05]

Figure 3.11: A diagram showing the setup used for undertaking a mechanical response measurement on the *in vitro* model of the vocal folds.

Before it was possible to obtain a mechanical response measurement, it was important that the microphone with the short probe attachment was calibrated against a standard microphone, so that the effect of the probe attachment could be accounted for. The setup used to do this is detailed in Figure 3.11. A frequency response function $\hat{H}_{probe}(\omega)$ was calculated for the probe microphone for a swept sine wave between 50 and 1600 Hz using the relation

$$\hat{H}_{probe}(\omega) = \frac{\overline{G_{probe\ ref}}(\omega)}{\overline{G_{probe\ probe}}(\omega)}, \quad (3.24)$$

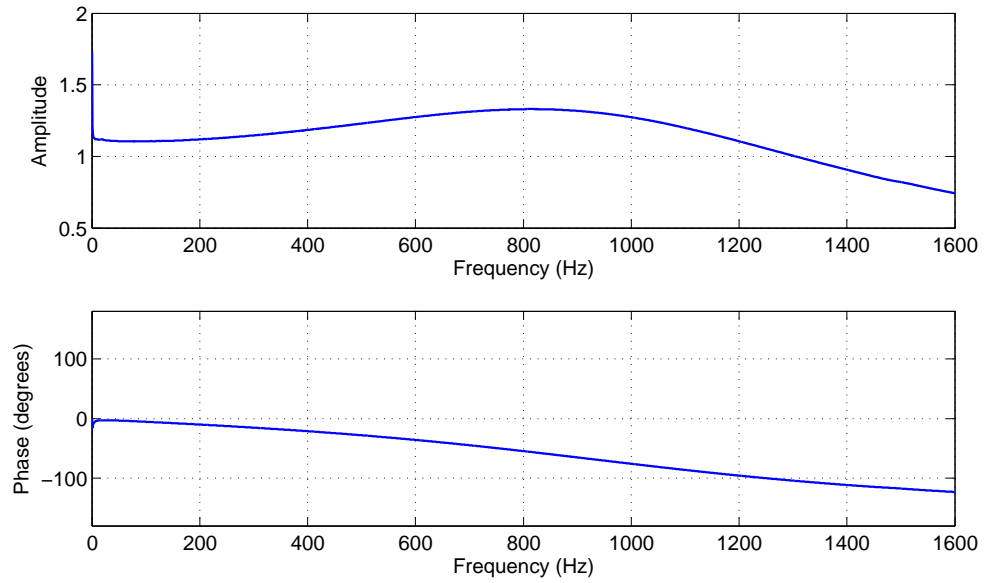


Figure 3.12: The magnitude (*upper*) and phase (*lower*) plots for the frequency response function for the Bruël and Kjær type 4192 microphone with a short probe attachment.

where $\overline{G_{probe\ ref}}(\omega)$ is the averaged cross-spectrum of the probe microphone signal against the reference microphone signal and $\overline{G_{probe\ probe}}(\omega)$ is the averaged power spectrum of the probe microphone signal, both of which are in the frequency domain. The magnitude and phase from the frequency response function for a probe microphone can be seen in Figure 3.12. The probe is seen to have little effect on the magnitude and phase between 50 and 400 Hz, which is the frequency range over which the mechanical response will be taken; however, the probe can be seen to have a more significant impact above this frequency range.

Next, it was important to confirm that the response of the photodiode to the opening and closing of the glottis was linear. In order to do this the vocal fold model was replaced by a rectangular slit which could be open and closed. Measurements were taken at several different slit openings and the results can be seen in Figure 3.13, which show a linear behaviour. Using crossed polarisers to attenuate the power of the laser, a voltage of around 5.5V set for the maximum slit opening of 3 mm in order to achieve the best possible signal-to-noise ratio whilst the photodiode continued to behave linearly. Preliminary measurements were also taken to check that the photodiode did not saturate at any particular frequency during a mechanical response

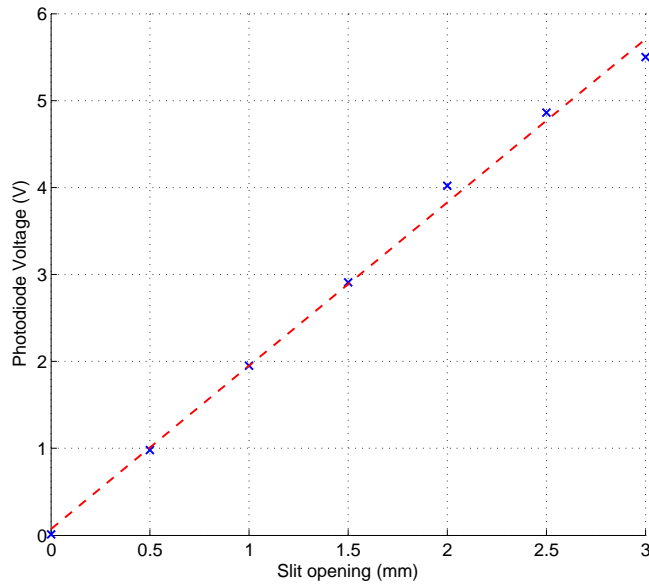


Figure 3.13: A plot showing the photodiode calibration relating the open width of a rectangular opening to the voltage across the photodiode caused by an expanded laser beam shining through the opening. The red dashed line is the straight line fitted to the blue data points.

measurement.

After this had been set up, the sine sweep used to excite the vocal folds was calibrated so that the acoustic driving signal at the opening of the lips was as flat as possible for all frequencies of interest. This was achieved by playing an uncalibrated sine sweep between 50 - 400 Hz over 10 seconds, 3 times, and recording the acoustic pressure at the probe microphone. The auto-spectrum for the probe microphone was then exported from PULSE LabShop into MATLAB [mat 12] and, using programs developed at the University of Edinburgh, a sine sweep was generated which would produce the same acoustic driving frequency across the desired frequency range. This was achieved by inverting the auto-spectrum and using this as an amplitude envelope during re-synthesis of the sine sweep so that it compensated for the natural resonances of the system.

Once this had been completed, the frequency response function between the probe microphone and the open area of the vocal folds, measured using the photodiode, was taken using the calibrated sine sweep. As for the sweep calibration, the sine sweep

ran for 10 seconds and was repeated 3 times with an average then taken. This were recorded using PULSE LabShop at a sampling rate of 65536 Hz and the calculated frequency response function then exported to MATLAB. Measurements were made using the *in vitro* model with and without a glottal flow. For the case involving a flow, a subglottal pressure was chosen below which the vocal folds were observed oscillating.

Finally, it was also found that the Bruël and Kjær 2609 measuring amplifier inverted the phase of the recorded signal, which therefore also had to be corrected by the MATLAB program. In order to take account of the effect of the probe attachment on the recorded pressure signal, the magnitude of the frequency response function for the *in vitro* model was divided in the frequency domain by the magnitude of the frequency response function for the probe microphone and the phase of the frequency response function for the *in vitro* model was taken away in the frequency domain from the phase of the frequency response function for the probe microphone. Mathematically this appears as

$$\left| \hat{H}_{mr-cal}(\omega) \right| = \frac{\left| \hat{H}_{mr}(\omega) \right|}{\left| \hat{H}_{probe}(\omega) \right|}, \quad (3.25)$$

$$\angle \hat{H}_{mr-cal}(\omega) = \angle \hat{H}_{mr}(\omega) - \angle \hat{H}_{probe}, \quad (3.26)$$

where $\left| \hat{H}_{mr-cal}(\omega) \right|$ is the magnitude of the corrected frequency response function for the *in vitro* model of the vocal folds, and $\angle \hat{H}_{mr-cal}(\omega)$ is its respective phase.

3.5.3 Analysis and Application of Results

The measured mechanical response function for the vocal folds in this study is used to provide the natural resonance frequencies and the quality factors of these frequencies to the computational physical model of the vocal folds, so that the two models can be related through the correct values for the springs and dashpots used in the computational being calculated. In order to achieve this, the following equation for an acoustic resonance shown in [Cullen 00b] can be fitted to the mechanical response

$$A(f) = \frac{A_0}{\sqrt{1 + \frac{4Q_0^2(f-f_0)^2}{f_0^2}}}, \quad (3.27)$$

3.6. MODEL OPEN HEIGHT AND AREA USING A HIGH-SPEED CAMERA

where Q_0 is the dimensionless quality factor for the resonance, f is a frequency value within a defined frequency bandwidth, f_0 is the resonance peak frequency, and A_0 is the amplitude of the fitted resonance peak.

After the peaks in the mechanical response had been identified using peak detection software in MATLAB, Equation 3.27 was fitted around the detected peaks using a least-squares fit for $A(f)$ with different values of Q_0 and A_0 trialled for a limited frequency bandwidth until the best fit was found. Cullen's program for this task, originally written in C, was converted to MATLAB and used to provide the fitted values of Q_0 .

3.6 Model Open Height and Area using a High-Speed Camera

Whilst it is possible to study the open area of the vocal folds using the expanded laser beam and laser diode from the mechanical response mechanism, it was not possible to do this whilst the model was attached to the lung or in the confines of the PIV safety enclosure. However, using software developed at the University of Edinburgh and implemented in several studies [Richards 03, Bromage 07, Stevenson 07, Stevenson 09a, Stevenson 09b, Newton 09, Logie 09], it was possible to measure the open area of the vocal folds under the conditions at which they oscillate during PIV image pair acquisitions. This therefore made it possible to synchronise the open area with the upstream pressure signal and therefore consider calculated PIV flow-field measurements against the dynamics of the vocal folds. Another advantage of using the high-speed camera was that it was possible to extract the open width of the glottis at different points along the glottis and consider any phase lag between parts of the vocal folds, as observed in [Roubeau 09] for certain modes of vocal fold oscillation.

3.6.1 Experimental Apparatus and Procedure

Filming of the vocal folds was conducted using a Vision Research Phantom v4.1 high-speed camera which was operated using proprietary software. In order to extract the open area of the glottis using image processing, it was necessary for there to be a high contrast between the vocal folds and the glottis. This was achieved using a Schott

3.6. MODEL OPEN HEIGHT AND AREA USING A HIGH-SPEED CAMERA

KL1500 LCD 150 W swan-neck lamp. The exact positioning of the two available swan necks depended very much on the setup and it took several attempts in order to achieve the best position. High-speed filming was undertaken for each configuration of the *in vitro* vocal fold model (3 in total) at the conditions used to take the image pair acquisitions. A diagram of the experimental setup can be found in Figure 3.14.

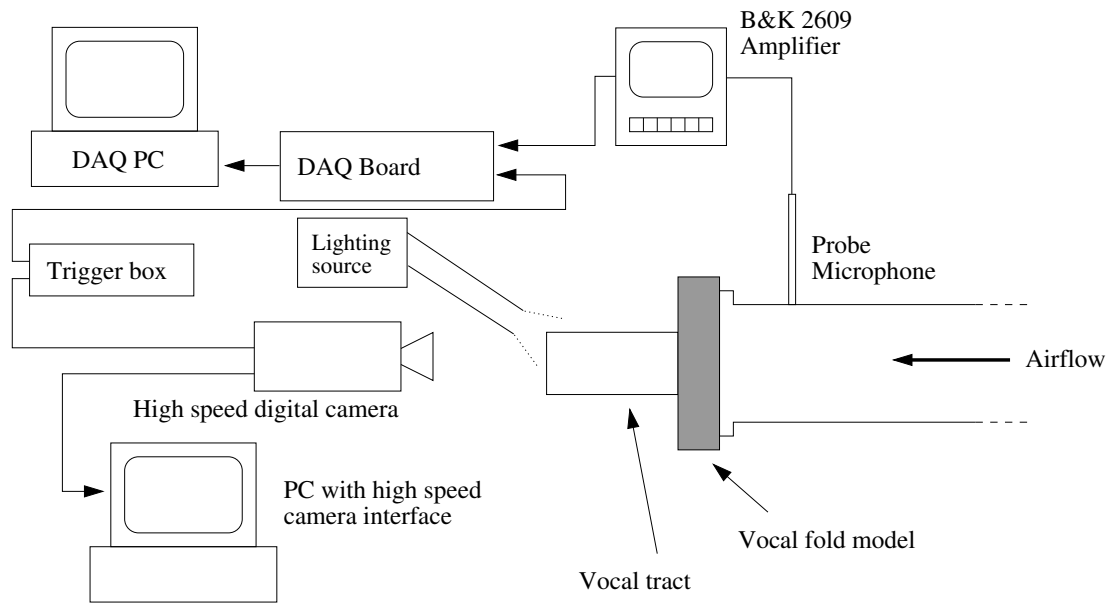


Figure 3.14: A schematic diagram of the experimental setup used for the high-speed camera.

So that the calculated open area of the vocal folds was synchronised with the acoustic pressure signal, the point at which the camera began capturing film and the trigger signal for this was recorded along with the upstream acoustic pressure signal. An advance made during this aspect of the study was the substitution of the previously-used PULSE hardware and LabShop software for data acquisition for the LabVIEW hardware and software used for PIV image pair acquisition. This brought several benefits:

1. The maximum sample rate possible increased from 65534 Hz to 100000 Hz,
2. There was less movement of equipment between laboratories, which meant less disruption to other experiments due to a reduction in the number of pieces of equipment being shared between experiments.

3.6. MODEL OPEN HEIGHT AND AREA USING A HIGH-SPEED CAMERA

However, in order to facilitate this change, new LabVIEW software had to be written to perform the task and the existing MATLAB scripts used to process the data once captured had to be modified to deal with the new data structures. In addition, the software and drivers for the camera were changed in order to address frame corruption which had been a problem in previous studies.

The high-speed camera was set to record with a resolution of 128×256 pixels at a frame rate of 5000 fps. The exposure time for each frame was $180 \mu\text{s}$. The camera was set to record 8144 frames per take, with 1629 frames captured before receiving a trigger signal. A key component in the open area calculation is the calibration measurement, in order to convert an area in pixels into an area in meters. To do this a piece of 5 mm squared paper was placed in front of the vocal folds whilst not oscillating and a video taken of this. The camera was triggered manually by a pulse using a BNC Berkeley Nucleonics 500C delay generator. The pulse and the acoustic pressure signals were recorded by the LabVIEW program for a short period of time preceding the camera's pre-trigger frames until a short time after the last frame had been taken and were then exported to MATLAB for analysis and processing. The the pre-trigger frames and 1000 frames after the trigger pulse (2630 in total) from the videos captured by the high-speed camera were converted, cropped, and exported as BMP files to be processed by MATLAB.

3.6.2 Analysis and Application of Results

The processing of the high-speed camera data for the open area of the glottis required two parts: processing the images from the high-speed footage and extracting the open area, and processing the recorded signals in order to synchronise the open area and centreline width of the glottis with the pressure signal.

The glottal open area and the glottal centreline open width and equidistantly-spaced either side of the centreline were extracted from the exported frames using MATLAB software developed at the University of Edinburgh. This software took each greyscale image and converted all the pixel values below a threshold value to black and all of those above to white, as shown in Figure 3.15.

This process is known as *binarisation*. The value used for the binarisation threshold had to be chosen with care so that the black area of the binarised image represented the open area of the glottis. In order to do this a graphical user interface (GUI) was used

3.6. MODEL OPEN HEIGHT AND AREA USING A HIGH-SPEED CAMERA

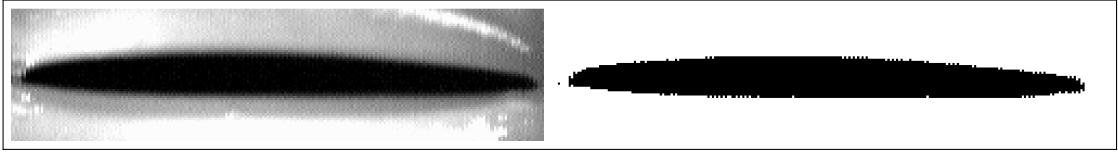


Figure 3.15: A diagram showing the extraction of the glottal open area using a thresholding program in MATLAB. To provide a sense of scale, from one side of the glottis to the other side measures 20 mm.

which made it possible to cycle through the images in order to assess the quality of the value chosen across the entire set. The value chosen depended on the configuration of the *in vitro* model and it is quite common to have to use a different value for each setup, particularly when there is a change in the separation between downstream constrictions. Once the images have been converted, the number of black pixels are counted and then multiplied by the meters-to-pixel ratio extracted from the calibration run.

In order to synchronise the calculated open area and centreline open width of the glottis with the captured acoustic cycle, a further script written in MATLAB was used. This script took the open area data and up-sampled it from 5 kHz to 100 kHz using the resample script from the MATLAB Signal Processing Toolbox. The signal also was zero-padded in order to filter out any spurious end effects. After this, the time at which the trigger was received by the camera is detected and, as the number of images (and hence the period of time) before the trigger was received are known, it is then possible to synchronise the open area signal with the acoustic pressure signal. After this has taken place, a single cycle is then extracted from the acoustic pressure and open area signals using zero-crossings. This single cycle is then used to synchronise the PIV flow-field maps with the open area or centreline open width of the glottis.

It is also possible to extract a single row or column of pixels at a fixed position from each frame and put them next to each other sequentially. The resulting image from this procedure is called a *kymograph* with the line of pixels chosen to create the kymograph called the *kymographic line*. These are useful for making qualitative assessments of vocal fold oscillation and are used in Chapter 5 to discuss the evolution of the open area of the vocal folds in comparison to a kymograph extracted from high-speed footage taken *in vivo*. The kymographs are constructed by the MATLAB scripts,

which are used to calculate the glottal open area.

3.7 Physical Models

In this study, a computational physical model of the human larynx is used in order to test theories and assumptions regarding the dynamics and aerodynamics which take place in the larynx. The model is described as being ‘low-order’ or ‘lumped’ due to the combining the interaction and behaviour of the complex tissue structures within the larynx into simple mass and spring system. The model was originally developed by Bailly and her colleagues at GIPSA-lab in Grenoble [Vilain 02, Ruty 07a, Bailly 09] and the author is very grateful to her for sharing this. The model assumes that the flow is two-dimensional and that the vocal folds oscillate symmetrically.

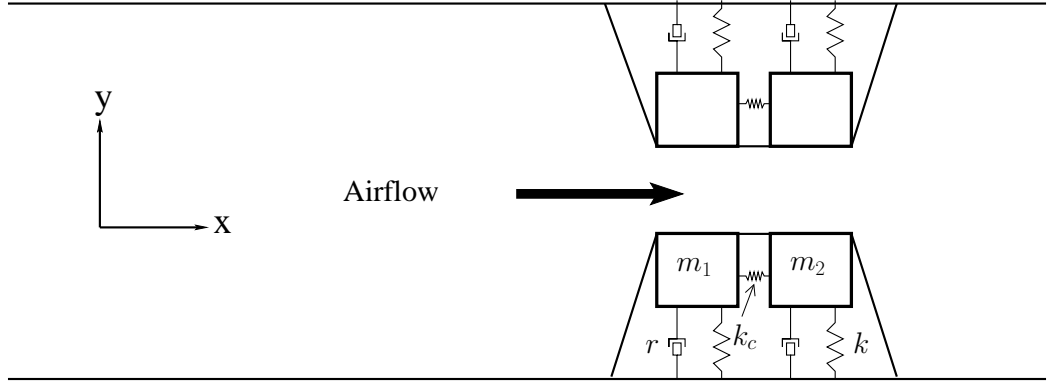
Although more sophisticated models of the vocal folds are used by others, an advantage of using a low-order model is its simplicity [Ruty 07b]. This simplicity affords a reduction in the number of assignable parameters, which allows for a better understanding of what changes are responsible for changes in behaviour through a restriction of the parameter space. One of the challenges presented to those who use models with more springs and masses is that the number of parameters that need to be assigned increases, which therefore makes it more difficult to link theoretical and simulation results with data acquired from *in vitro* models. The reason that a two-mass model was used in preference to a one-mass model was that in order to replicate the motion of the vocal folds, a model with at least 2 degrees of freedom was required [Kob 04].

The simplest model with 2 degrees of freedom is the two-mass model with each mass limited to oscillating in 1 plane. It is possible to use a one-mass model with two degrees of freedom (as in [Adachi 96, Adachi 05]); however, in these models it is not possible to incorporate the change in the shape of the glottis observed earlier in this chapter and hence a moveable point of flow separation already seen to improve the realism of synthesised sound in [Pelorson 96]. A comprehensive survey of different lumped-element models used to study the vocal folds (of which there are many) is provided in [Birkholz 11].

In this section, three different configurations of the computational physical model used are outlined and discussed. As these models were originally developed in other

studies [Vilain 02, Rutu 07a, Bailly 09] their operation will be summarised using these studies. The flow models used in the physical models and hypotheses for the expansion of the glottal jet also are summarised.

3.7.1 Two-Mass Model without Ventricular Bands



Source: Adapted from [Newton 09]

Figure 3.16: A schematic diagram showing the computational model of the human larynx with the vocal folds modelled as a physical two-mass model and without ventricular bands.

A schematic diagram of the computational physical model of the larynx without ventricular bands is presented in Figure 3.16. Each vocal fold in this model is constructed from two point masses coupled by a spring. Each mass is then also connected to the vocal tract wall using a spring and dashpot. In total, there are three springs and two dashpots for each vocal fold. From [Rutu 07b], the equation of motion used to calculate the displacement of the first mass m_1 during oscillation is given by

$$\begin{aligned} \frac{m}{2} \frac{\partial^2 y_1(t)}{\partial t^2} = & -k(y_1(t) - y_1(t_0)) - k_c(y_1(t) - y_1(t_0) - y_2(t) + y_2(t_0)) \\ & - r \frac{\partial y_1(t)}{\partial t} + F_1(P_{sub}, P_{supra}, H_1, H_2), \end{aligned} \quad (3.28)$$

where m is the total oscillating mass of the entire vocal fold (also known as the *effective oscillating mass*), k is the spring constant, r is the damping coefficient, k_c is the coupling spring constant, $y_i(t)$ is the y -axis position of the i th mass at time t ,

$y_i(t_0)$ is the y -axis position of the i th mass at the time $t = 0$, and F_i is the force acting on the i th mass, which depends on the subglottal pressure (P_{sub}), supraglottal pressure (P_{supra}), and the opening along the y -axis of the i th masses measure between the two vocal folds (denoted as H_1 and H_2).

The equation of motion for the displacement of the second mass m_2 in each vocal folds is

$$\begin{aligned} \frac{m}{2} \frac{\partial^2 y_2(t)}{\partial t^2} = & -k(y_2(t) - y_2(t_0)) - k_c(y_2(t) - y_2(t_0) - y_1(t) + y_1(t_0)) \\ & - r \frac{\partial y_2(t)}{\partial t} + F_2(P_{sub}, P_{supra}, H_1, H_2). \end{aligned} \quad (3.29)$$

The non-coupling spring stiffnesses values (k) and dashpot damping coefficients (r) are determined by the angular frequency of the appropriate natural resonance (ω_0) and its quality factor (Q_0) from the mechanical response of the experimental *in vitro* model, as discussed previously. These are calculated using the following relations:

$$k = \frac{m\omega_0^2}{2}, \quad (3.30)$$

$$r = \frac{m\omega_0}{2Q_0}. \quad (3.31)$$

As in [Lous 98, Ruty 07b, Bailly 08], the value of the coupling spring stiffness was set at half of the value for the non-coupling spring stiffnesses:

$$k_c = \frac{1}{2}k. \quad (3.32)$$

A difficult yet important parameter to set is the effective oscillating mass of each vocal fold. As the experimental model used is a constant pressure system, the volume of water (and hence the mass of the vocal folds) can fluctuate during oscillation in order to maintain a constant pressure. The effective oscillating mass was calculated using the relation

$$m = \gamma \cdot \zeta \cdot \rho \frac{\pi \left(\frac{W_{vf}}{2} \right)^2 d_{vf}}{8} \quad (3.33)$$

where γ is the proportion of the total mass oscillating (ranging between 0 and 1), ζ is a multiplication factor used to take account of the latex used to construct the vocal folds stretching, which was set to a value of 1.8. The value of γ had to be estimated based

on an assessment of the proportion of the total mass oscillating. Later in this chapter we will discuss a new method by which it was possible to find an appropriate value for this parameter.

The forces acting on the masses are calculated by resolving the aerodynamic forces applied on the boundaries of the vocal folds (and ventricular bands when included as a second two-mass model), formed by straight lines between the masses and the vocal walls of the trachea or vocal tract, up until the point of flow separation. The flow separation model in these physical models is Liljencrants' criterion, as discussed in Section 3.2.2. Liljencrants' criterion in a two-dimensional physical model is defined as

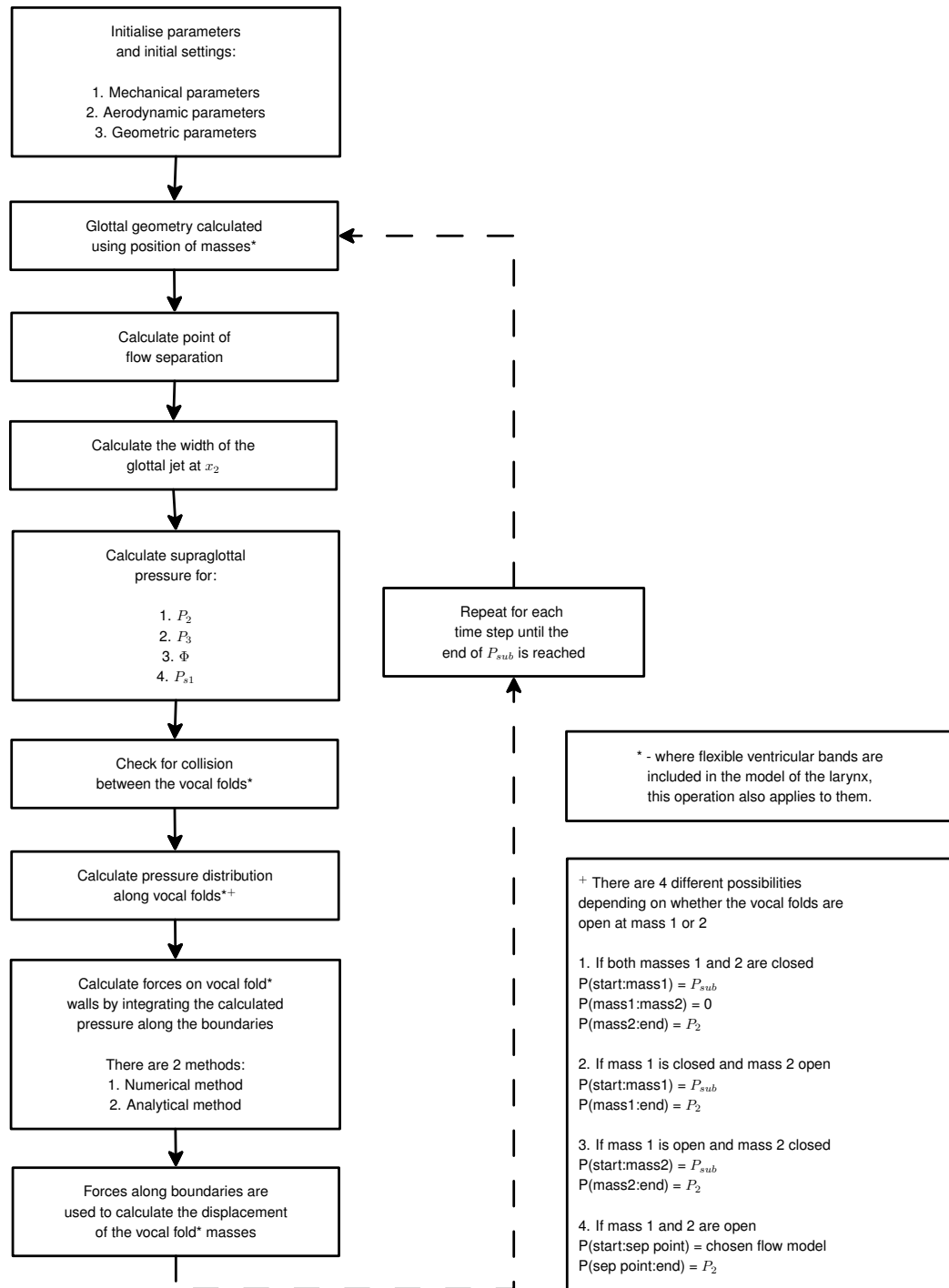
$$h_{sep} = 1.2 \cdot h_{min} \quad (3.34)$$

where h_{sep} is the glottal opening at the point of flow separation and h_{min} is the minimum glottal opening when the glottis exhibits a divergent geometry. For a three-dimensional physical model, this criterion can be defined using glottal open areas rather than open heights, but as this study uses a two-dimensional model, this description would not make sense.

3.7.2 Two-Mass Model with Ventricular Bands

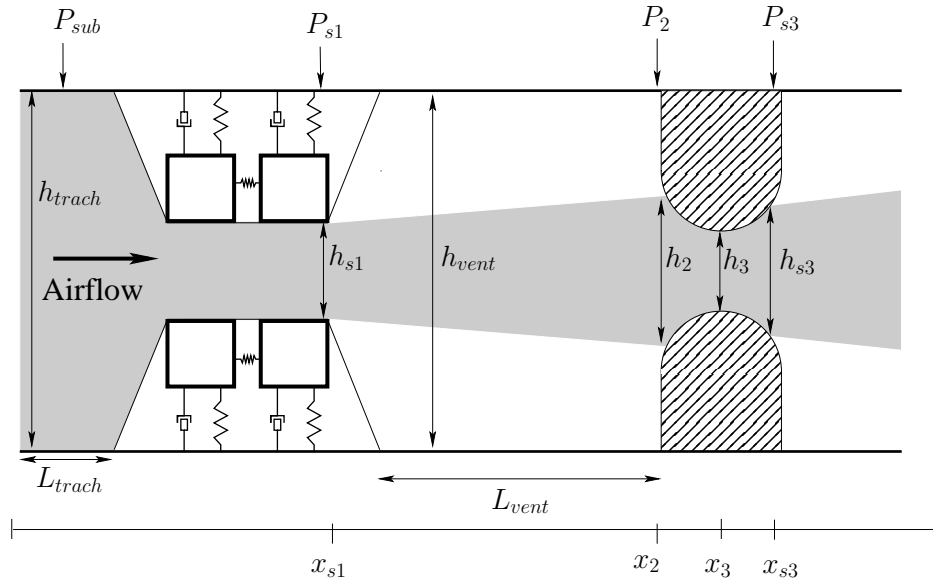
In total, there were 2 two-mass models for the larynx with ventricular bands: one for the case with rigid ventricular bands and another for the case with flexible ventricular bands. The model of the larynx for the case with rigid ventricular bands was a slight modification on the two-mass model developed for the case without ventricular bands. The ventricular bands in this case are modelled as rigid immovable structures with a hemi-circular top (radius 5 mm). For this model, if the width of the glottal jet using one of the hypotheses discussed in Section 3.7.4 was greater than the separation of the rigid ventricular bands then rather than the pressure downstream of the vocal folds being 0, a pressure recovery would occur at the ventricular bands which would then result in a supraglottal force acting on the vocal folds. A schematic diagram of this model can be seen in Figure 3.18 with key parts labelled. The program logic for the model is summarised in a flow chart in Figure 3.17.

Initially, the two-mass model with ventricular bands could not model the case where the ventricular bands were not present and thus was modified to take account



Source: Adapted from [Ruty 07a, Bailly 09]

Figure 3.17: Schematic diagram illustrating the programming logic for computational physical model of the *in vitro* model of the human larynx.



Source: Redrawn and adapted from [Bailly 09]

Figure 3.18: A schematic diagram showing the computational model of the human larynx with the vocal folds modelled as a physical two-mass model and with rigid ventricular bands.

of this case. In addition to this and the translation of the code and comments for this model into English, optimisation was undertaken in order to ensure that the MATLAB code was not running unnecessarily slow and that memory resources were used efficiently.

The two-mass model with flexible ventricular bands described in [Bailly 09] was an extension on the two-mass model with rigid ventricular bands but extended, replacing the static ventricular bands with another two-mass model. Effectively, the behaviour of the model was the same as that for the static ventricular bands, only that additional computing time was needed in order to calculate whether or not the glottal jet makes contact with the ventricular bands at a particular time step, what the forces acting on them are, and their subsequent displacement. Although the same optimisation and translation procedures were applied to the model with flexible ventricular bands as for the model with static ventricular bands, as no equivalent experimental *in vitro* model was used in this study no further development of this model took place.

3.7.3 Fluid Flow Models

Three different simplified models of the flow were used with the physical models described in the previous section. All of these models are one-dimensional, use Bernoulli's theorem, and assume that the fluid is both incompressible and inviscid; however, there are two forms of the model, steady and unsteady. The Bernoulli steady model is used without a loss model applied and with a Poiseuille loss model, added as an additional corrective term. The Bernoulli unsteady flow model is used without an additional loss model applied.

For each of these models, the total pressure loss for the system is expressed using the following relation

$$\begin{aligned}\Delta P_{total} &= \Delta P_{vf} + \Delta P_{jet} + \Delta P_{vb} \\ &= P_{sub}\end{aligned}\tag{3.35}$$

where ΔP_{vf} is the pressure loss within the vocal folds, ΔP_{jet} is the pressure loss within the glottal jet, and ΔP_{vb} is the pressure loss within the ventricular bands (where applicable). Therefore, as a total pressure loss is assumed across the larynx, this pressure loss is equal to the subglottal pressure used to drive the vocal folds into self-sustained oscillation.

Bernoulli Quasi-Steady Assumption without Losses

The Bernoulli quasi-steady assumption without losses is the simplest of the three flow models applied. Using the assumption that there is a total pressure loss across the glottis, and that Bernoulli's principle applies as stated in Equation 3.10 assuming that the constant in this equation is the same for all streamlines [Faber 95] it is possible to calculate the velocity of the bulk flow using

$$u_i = \sqrt{\frac{2}{\rho} P_{sub}}.\tag{3.36}$$

where u_i is the velocity of the fluid at point i along the x -axis.

Having calculated velocity, it is then possible to calculate the volume flow rate

anywhere in the bulk flow using

$$\Phi = A_i \cdot u_i, \quad (3.37)$$

where A_i is the cross-sectional area of the flow at point i along the x -axis.

Now having an expression for the volume velocity, it is possible to calculate the total pressure drop across the vocal folds and ventricular bands (respectively). By applying Bernoulli's principle and the principle of conservation of mass, stating that the volume flow within either the vocal folds or ventricular bands is constant, the following 2 equations are produced:

$$\Delta P_{vf} = \frac{1}{2} \rho \Phi^2 \left(\frac{1}{A_{s1}^2} - \frac{1}{A_0^2} \right), \quad (3.38)$$

$$\Delta P_{vb} = \frac{1}{2} \rho \Phi^2 \left(\frac{1}{A_{s3}^2} - \frac{1}{A_2^2} \right), \quad (3.39)$$

where A_{s1} is the cross-sectional area of the jet formed at the point of flow separation, A_0 is the cross-sectional area of the fluid in the trachea, A_2 is the cross-sectional area of the jet at the point of flow reattachment, and A_{s3} is the cross-sectional area of the jet at the point of flow separation from the ventricular bands.

Where the ventricular bands are either not present or the glottal jet is calculated as not reattaching then no pressure recovery is calculated, therefore $\Delta P_{vb} = 0$. Models for the pressure drop across the glottal jet ΔP_{jet} are considered later in Section 3.7.3.

Bernoulli Quasi-Steady Assumption with Poiseuille Losses

To account for viscous losses encountered by interaction of the fluid with the bounding walls, pressure losses using Poiseuille's description of a parabolic velocity profile is used. In particular, as the glottal open width reduces in the closing phase of the phonatory cycle, the Reynolds number reduces to a point where the flow may no longer be described as being inviscid [Cisonni 08b]. The addition of a Poiseuille loss term will take this change into account thereby providing a more accurate description of the flow at this point. The Bernoulli quasi-steady assumption of the flow with Poiseuille losses uses the same equations as above, only an additional corrective term $\Delta P_{pois.}$ is added to account for these extra losses. The pressure differences across the vocal folds and

ventricular bands can therefore be expressed as

$$\Delta P_{vf} = \Delta P_{vf} + \Delta P_{pois.}, \quad (3.40)$$

$$\Delta P_{vb} = \Delta P_{vb} + \Delta P_{pois.}, \quad (3.41)$$

where $\Delta P_{pois.}$ across the vocal folds is

$$\Delta P_{pois.} = 12\mu \int_{x_{s1}}^{x_0} \frac{\Phi(t)}{A^3(x, t)}, \quad (3.42)$$

and $\Delta P_{pois.}$ across the ventricular bands is

$$\Delta P_{pois.} = 12\mu \int_{x_2}^{x_{s3}} \frac{\Phi(t)}{A^3(x, t)}. \quad (3.43)$$

Once again, where the ventricular bands are either not present or the glottal jet is calculated as not reattaching then no pressure recovery is calculated, therefore $\Delta P_{vb} = 0$.

Pressure Losses over the Glottal Jet

Two models of pressure loss over the glottal jet were used in this study. The first model assumes that no pressure loss takes place, therefore

$$\Delta P_{jet} = 0. \quad (3.44)$$

The second pressure loss model is that proposed in [Ishizaka 72], which is calculated using the equation

$$\Delta P_{jet} = -\frac{\rho\Phi^2}{A_2} \left(\frac{1}{A_{s1}} - \frac{1}{A_2} \right). \quad (3.45)$$

This model results from the combination of the principles of conservation of mass and momentum applied to the fluid and assumes that there is a constant pressure P_{s1} across the jet. A full derivation for which is available in [Bailly 09].

Bernoulli Unsteady Assumption

The final model used with the physical models is the Bernoulli unsteady assumption. As we have already seen, the substantive derivative (Equation 3.2) describing the acceleration of the fluid (not including that due to vorticity) is made up of two parts: the convective acceleration and the acceleration dependent simply on time. Assuming that the flow is irrotational, it is therefore possible to write Euler's equation ignoring gravitational effects (Equation 3.7) in terms of a scalar potential flow ϕ [Faber 95, Kundu 02],

$$\vec{\nabla} \left(\frac{\partial \phi}{\partial t} + \frac{u^2}{2} + \frac{p}{\rho} \right) = 0. \quad (3.46)$$

This can then be integrated and rearranged to give the following equation

$$p_i = -\rho \frac{\partial \phi_i}{\partial t} - \rho \frac{u_i^2}{2} + \text{const.}, \quad (3.47)$$

where p_i is the pressure at the i th position along the x -axis and ϕ_i is the velocity potential at the i th position along the x -axis.

However, this equation only considers the influence of unsteady phenomena using the principle of conservation of momentum. Therefore the equations for the pressure drop including the additional term from the Bernoulli unsteady flow model and incorporating the conservation of mass are

$$\Delta P_{vf} = \Delta P_{vf} + \Delta P_{unsteady} \quad \text{and} \quad (3.48)$$

$$\Delta P_{vb} = \Delta P_{vb} + \Delta P_{unsteady}, \quad (3.49)$$

where $\Delta P_{unsteady}$ across the vocal folds is

$$\Delta P_{unsteady} = \rho \int_{x_{s1}}^{x_0} \frac{\partial \Phi(t)}{\partial A(x, t)}, \quad (3.50)$$

and $\Delta P_{unsteady}$ across the ventricular bands is

$$\Delta P_{unsteady} = \rho \int_{x_2}^{x_{s3}} \frac{\partial \Phi(t)}{\partial A(x, t)}. \quad (3.51)$$

3.7.4 Models of the Glottal Jet

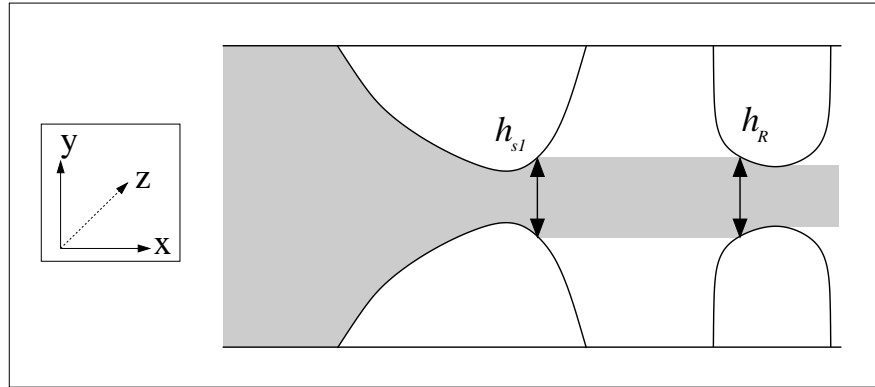
Three hypotheses are proposed for the expansion of the glottal jet over the laryngeal ventricle, which subsequently impacts on the calculated pressure recovery at the ventricular bands (where these are present). These jet expansion theories first appear in [Bailly 08] and are covered in greater detail in [Bailly 09, Newton 09]. A summary of these jet expansion hypotheses is presented here, which was also published in [Apostoli 10b].

Uniform Jet Hypothesis

The simplest of the jet expansion theories, illustrated in Figure 3.19, is the uniform jet hypothesis. This hypothesis assumes that the width of the glottal jet does not increase across the laryngeal ventricle from the point at which it separates until the point where it reattaches to the ventricular bands. This relation is expressed simply as

$$h_R = h_{s1}, \quad (3.52)$$

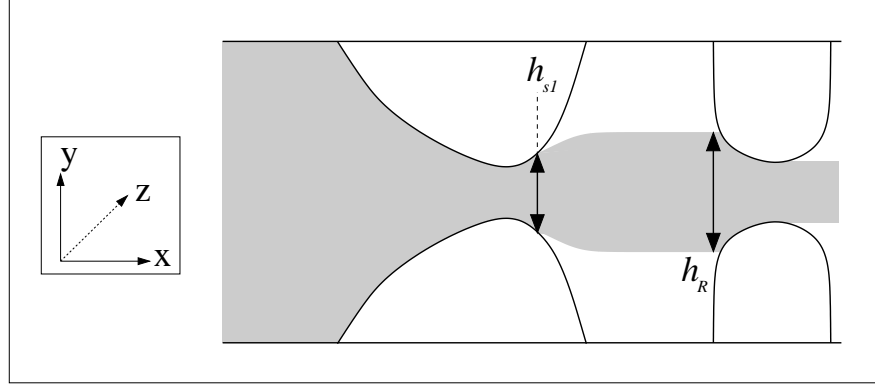
where h_R is the width of the glottal jet at the point of flow reattachment and h_{s1} is the width of the jet at the point of flow separation. In this hypothesis, the jet is assumed not to expand in the z -axis and remains at W_{vf} .



Source: Adapted from [Newton 09]

Figure 3.19: Diagram illustrating the uniform jet expansion hypothesis, where h_0 is the width of the trachea, h_{vf} is the minimum glottal opening, h_{s1} is the point of flow separation, h_R is the point of flow reattachment, and h_{vb} is the minimum ventricular band separation.

Laminar Jet Hypothesis



Source: Adapted from [Newton 09]

Figure 3.20: Diagram illustrating the laminar jet expansion hypothesis, where h_{s1} is the point of flow separation and h_R is the point of flow reattachment.

The second jet expansion hypothesis is that for a laminar jet, shown in Figure 3.20. Modelling the glottal jet as a free shear layer and neglecting edge effects observed in confined jets, it is seen to expand after the point of flow separation up until a point where it then assumes a uniform profile. The point at which this takes place occurs when the pressure gradient across the jet in the x -direction reduces to zero thereby halting the jet expansion. Assuming that the jet grows under the influence of viscous diffusion and that the flow is self-similar, this hypothesis is defined as

$$h_R = h_{s1} + \frac{21.8 \cdot W_{vf} \left(\frac{\Phi^2}{A_{s1}} \right)^{-\frac{1}{3}} \cdot \nu^{\frac{2}{3}} \cdot (x_R - x_{s1})^{\frac{2}{3}}}{W_{vf}}, \quad (3.53)$$

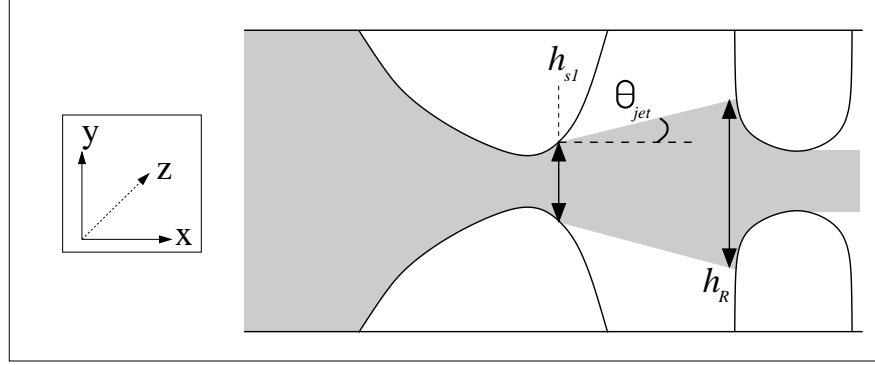
where Φ is the volume flow and ν is the kinematic viscosity. As with the uniform jet, expansion is assumed to be confined to the transverse y dimension, with no out-of-plane z -wise expansion. The jet width at the ventricular bands is thus assumed to be equal to the width at flow separation from the vocal folds, W_{vf} .

$$h_R = h_{s1} + 21.8 \left(\frac{h_{s1} \cdot W_{vf} \cdot \mu^2 (x_R - x_{s1})^2}{\Phi^2 \rho^2} \right)^{\frac{1}{3}}, \quad (3.54)$$

where W_{vf} is the height of the glottis, μ is the dynamic viscosity, x_{s1} is the position

of the point of flow separation along the x -axis, x_R is the position of the point of flow reattachment at the ventricular bands along the x -axis, Φ is the volume flow, and ρ is the density of the fluid.

Turbulent Jet Hypothesis



Source: Adapted from [Newton 09]

Figure 3.21: Diagram illustrating the turbulent jet expansion hypothesis, where h_{s1} is the point of flow separation, h_R is the point of flow reattachment, and θ_{jet} is the half-angle of the jet expansion.

The final jet expansion hypothesis, seen in Figure 3.21, is the turbulent jet hypothesis. This hypothesis is based on the idea that the Navier-Stokes equations can be reduced to the simplified Reynolds equations, which then makes it possible to model the glottal jet as a two-dimensional free turbulent jet. Using this hypothesis, it is shown that the jet grows linearly in the x -direction, which Kundu showed empirically had a half-angle slope (θ_{jet}) of 4° [Kundu 02]. This relation is expressed in the equation

$$h_R = h_{s1} + 2 \cdot \tan 4^\circ \cdot (x_R - x_{s1}) . \quad (3.55)$$

Again, like for the other two hypotheses, the glottal jet was modelled as not expanding in the z -axis and therefore remained at W_{vf} along entire extent of the glottal jet.

3.7.5 Physical Models and High-throughput Distributed Computing

As has already been identified in Section 3.7.1, one of the most difficult input parameters to supply to the physical models is the value for the effective oscillating mass of the vocal folds. In [Cisonni 11], which uses the same type of physical model as that used here, the oscillating mass value is estimated using the equation

$$|C(\omega)| = \frac{\frac{Q_i}{\omega_i^2} \frac{1}{|\mu_i|}}{\sqrt{1 + 4Q_i^2 \left(\frac{\omega - \omega_i}{\omega_i}\right)^2}} \bigg|_{\omega \approx \omega_i} \approx \frac{Q_i}{\omega_i^2 \mu_i} \quad (3.56)$$

$$\therefore m \approx \mu_i \cdot W_{vf} \cdot l \quad (3.57)$$

where $|C(\omega)|$ is the magnitude of the mechanical response, μ_i is the effective mass at the i th peak, m is the vibrating mass portion, and $W_{vf} \cdot l$ represents the effective surface over which the subglottal pressure acts. Even with this definition, the area over which the subglottal pressure acts not only changes considerably during the phonatory cycle, but is very difficult to predict in the first place. In addition, it has been seen throughout studies involving the measurement of the mechanical response of vocal folds or a brass player's lips that the range over which the magnitude of the mechanical response is measured varies quite considerably. Even between results from the same lab, the absolute values for the mechanical response still vary considerably (*viz.* [Ruty 07a, Cisonni 08a]). The magnitude can also be affected by slight variations in the way in which the mechanical response measurement procedure is carried out, as is shown in results in [Newton 09] using an *in vitro* model of a brass player's lips.

A way to avoid the difficulties associated with calculating the effective oscillating mass to perform a parameter sweep using the computational model and to extract parameters like the frequency of oscillation of the vocal folds, the variation of this frequency and whether or not the oscillation is stable. Although the idea of performing parameter sweeps is not a novel one, performing this task using a high-throughput distributed computing application with the physical model used in this study is novel. In order to perform parameter sweeps to extract an appropriate value for the

effective oscillating mass, the computational physical model was modified to work using the pre-existing Condor cluster in the School of Physics at the University of Edinburgh. Condor is a product of the Condor Research Project at the University of Wisconsin-Madison [Con 12] and works on the principle that computing cycles which are unclaimed by either the local user or by remote users can be harnessed to run compute-intensive jobs whilst these resources remain idle. A schematic representation of how Condor works can be seen in Figure 3.22.

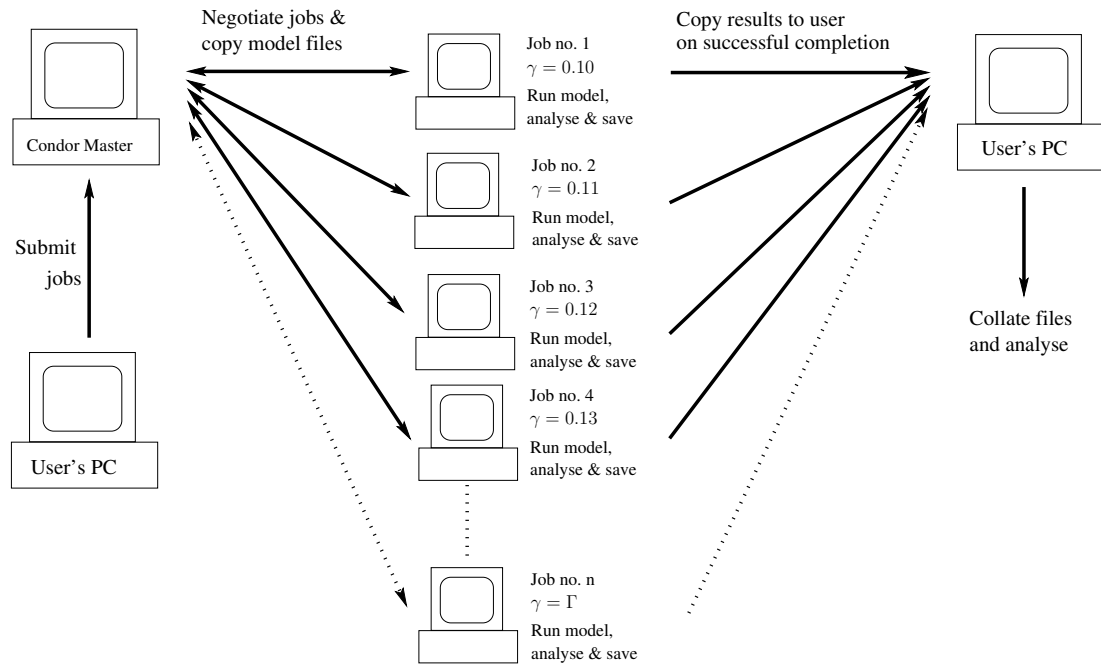


Figure 3.22: Schematic diagram illustrating the Condor system.

For each different configuration of the physical model 331 independent simulations were run, all with different values for the effective oscillating mass. In order to run the same simulations with the ventricular bands set at 3 and 8 mm apart, a total of 993 simulations were run. To get the total number of simulations needed in order to test every different parameter, this number is then multiplied by the number of different flow models and jet expansion hypotheses; all in all a total of 8937 simulations. As each simulation took approximately 10 - 15 minutes to run (depending on the options chosen), running these on a single desktop computer, one after the other, would take approximately 2234 hours or just over 3 months. However, as most desktop computers and some dedicated compute rack-mounted computers in the School of Physics and

Astronomy were members of the Condor cluster, up to 500 processors were available for use rather than just 1. This therefore meant that the time to run a full set of simulations was reduced to a minimum time of approximately 4.5 hours.

One challenge to this approach though was licensing; as there were only 6 licenses available to users within the research group. In order to run the computational physical model, the model had to be made compatible with Octave (an open source resource like MATLAB) which is mostly interoperable with MATLAB. In order to achieve this and to ensure that Octave worked with Condor, a significant amount of time was spent creating shell scripts and trailing the software before any results were acquired, due to there being little documentation available on using Octave with Condor.

A further challenge which presented itself was the amount of data produced by this number of simulations. In total, each simulation produces approximately 15 MB of data. As it was not possible to save all of this data it was necessary to produce automated tests and save the results of these tests in order to find out general trends in the behaviour of the model. These included measuring the mean fundamental frequency of oscillation and the associated standard deviation, whether or not model oscillation was sustained, and jitter and shimmer, which are standard clinical tests used by Otolaryngologists. A further significant portion of time was spent writing MATLAB scripts to collate and analyse the results from these measures once Condor jobs had been successfully completed.

Oscillation Fundamental Frequency and Standard Deviation

In order to calculate the fundamental frequency for each simulation, the positions of the peaks and troughs of the opening between the rear masses (mass 2) of the vocal folds from the model were detected. This was achieved through using the ‘peakdet.m’ script by written by Eli Billauer [Billauer 12]. The mean fundamental frequency and standard deviation were calculated using

$$\bar{f}_0 = \left(\frac{1}{N-1} \sum_{i=2}^N \text{peak}(t)_i - \text{peak}(t)_{i-1} \right)^{-1}, \quad (3.58)$$

$$\sigma_{f_0} = \left(\frac{1}{N-2} \sum_{i=2}^N \left((\text{peak}(t)_i - \text{peak}(t)_{i-1})^{-1} - \bar{f}_0 \right)^2 \right)^{\frac{1}{2}}, \quad (3.59)$$

where \bar{f}_0 is the mean fundamental frequency of oscillation, σ_{f0} is the standard deviation of the frequency, $\text{peak}(t)_i$ is the time position of the i th detected peak, and N is the total number of detected peaks.

Measure of Model Stability

The total length of time simulated by the computational model with each simulation was 0.5 seconds. In many oscillations, it was found that the vocal folds did not oscillate for the total simulated time. To provide an indication of whether or not the vocal folds remain oscillating throughout this period of time, a standard test was performed whereby if a peak was detected in the last 1/4 of the total simulated time then the oscillation is deemed to be stable. However, this did not guarantee that the oscillation was either of constant frequency or of constant amplitude. Where the vocal folds were not found to oscillate throughout the simulated time, the particular simulation in question was no longer considered and the values of \bar{f}_0 , σ_{f0} , κ_{jitt} , and κ_{shim} were set to the computational value *NaN* (not a number).

Jitter and Shimmer

Jitter and shimmer are a measure of the cycle-to-cycle variations in the frequency (jitter) and amplitude (shimmer) of a signal [Aronson 09], which in this case is a signal representing vocal fold oscillation. In this study, jitter and shimmer are expressed as percentages and are calculated using the following formulae detailed in [Lemke 94]

$$\kappa_{jitt} (\%) = 100 \cdot \frac{\sum_{i=2}^N |\text{peak}(t)_i - \text{peak}(t)_{i-1}|}{(N-1) \bar{x}}, \quad (3.60)$$

$$\kappa_{shim} (\%) = 100 \cdot \frac{\sum_{i=2}^N |\text{peak}(y)_i - \text{peak}(y)_{i-1}|}{(N-1) \bar{y}}, \quad (3.61)$$

where κ_{jitt} is the calculated jitter, κ_{shim} is shimmer, $\text{peak}(y)_i$ is the maximum signal amplitude of the i th detected peak, and N is the number of consecutive cycles. When the values of κ_{jitt} and κ_{shim} are low then the vocal fold oscillation shows very little perturbation in frequency and amplitude; however, when values of κ_{jitt} and κ_{shim} are high (typically above 5 - 10%) then a significant amount of perturbation in frequency

and amplitude is exhibited.

*"I hear and I forget.
I see and I remember.
I do and I understand."*
(Confucius)

4

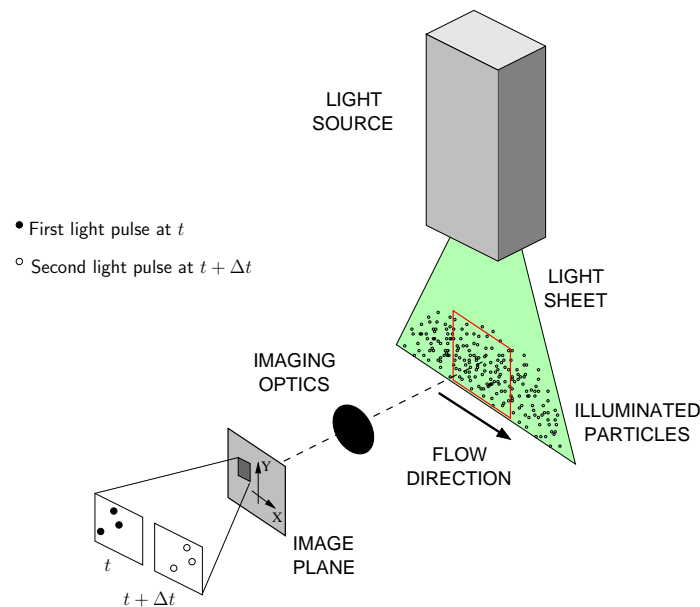
Particle Image Velocimetry Applied to *in vitro* Models of the Larynx

4.1 Introduction

Particle Image Velocimetry (PIV) is a method by which fluid flows can be measured in a way which causes minimum disturbance to the flow under consideration. PIV has developed significantly over the last two decades due to the conversion from film-based to digitally-based techniques, and is now used widely in fluid mechanical studies due to its suitability to the study of complex spatial flows [Skulina 05, Raffel 07]. As it is used extensively in this study and due to the complexities involved in studying a time-varying flow, this chapter is devoted to examining the principles by which PIV is undertaken and the way it is implemented in this study. Full descriptions of the equipment used and how it is used will be detailed. As well as a discussion surrounding the acquisition of the individual flow field maps, the way in which these maps are processed and later analysed will be considered. Finally, the method by which the parameters used in Chapter 5 are extracted is discussed. Other studies have used a very similar PIV configuration and procedure [Skulina 05, MacDonald 09, Newton 09]; however, differences between these studies and this one will be discussed.

4.2 Background Theory to PIV

PIV works on a very simple principle: through the introduction of neutrally buoyant smoke or fog particles evenly distributed into the flow upstream of the area of interest it is possible to take images of these particles which are separated by a short time difference. Once these images have been taken, a cross-correlation calculation is then performed which indicates the mean distance travelled by the particles. Together with the known time separation between the two images, it is possible to calculate the speed of the flow and build up a field of vectors representing flow velocities for the displacement measured between the two images. This process is summarised in Figure 4.1.



Source: After Skulina [Skulina 05]

Figure 4.1: Schematic diagram summarising the basic principles of PIV.

Hot-wire Anemometry and Laser Doppler Anemometry are also other means by which it is possible to measure flow velocity [Alipour 95, Massey 98, Campbell 00, Cullen 00b]. Firstly, Hot-wire Anemometry requires the use of a sizeable probe which is inserted into the flow in order to make a measurement. Within the probe are two heated wires with a temperature difference across the two wires, caused by a flow,

related to the flow velocity. This probe is only able to make a measurement for one point in the flow and which is not directionally resolved. Furthermore, the probe causes an obstruction in the flow, thereby affecting measurements taken downstream by artificially increasing turbulence within the flow. Laser Doppler Anemometry (LDA, also known as Laser Doppler Velocimetry) is an optical technique which, like Hot-wire Anemometry, provides time-varying measurements of the flow velocity for a given fixed point in space [Adrian 93] which is measured using the Doppler shift of light scattered from seeding particles [Cullen 00b].

Unlike Hot-wire Anemometry, Laser Doppler Anemometry does not require the use of a probe to make flow velocity measurements and therefore has the same impact on the flow as PIV. In addition, measurements made using LDA, like PIV, can be directionally resolved. Although it is possible to construct a full map of the flow from successive LDA measurements taken at different spatial coordinates, this is extremely time consuming and would not be appropriate for this investigation. However, it should be noted that measurements made with LDA can be of a higher precision than those made using PIV [Degroot 08]. Due to its limitations, Hot-wire Anemometry was also not deemed appropriate for this investigation.

Images for PIV are taken in pairs with each pair known as an *image pair acquisition*. In order to obtain a full flow field map of the flow velocities from an image pair acquisition, it is necessary to break the image up into sections known as *interrogation areas*. These can vary in size from 128×128 to 16×16 pixels, with the choice of size being dependent on how far the seeding particles move from one image in the pair to the other. A 32×32 interrogation area from two images is shown in Figure 4.2. In order to extract the distance that the particles have moved within the interrogation area, a cross-correlation is performed. A cross-correlation provides a quantitative measure of the similarity between two functions [Riley 98], which in PIV operates over all the individual pixels within the interrogation area. How the cross-correlation works is that it translates the interrogation area from one image over that of the second moving one pixel at a time and quantifies how similar the pixels (represented by an intensity value) in the first interrogation area are to those in the second for that translation. If the positions of the pixels in the first interrogation area (at positions i, j for instance) are found to be at the same values of i and j in the second interrogation area after the translation then the value of the cross-correlation function

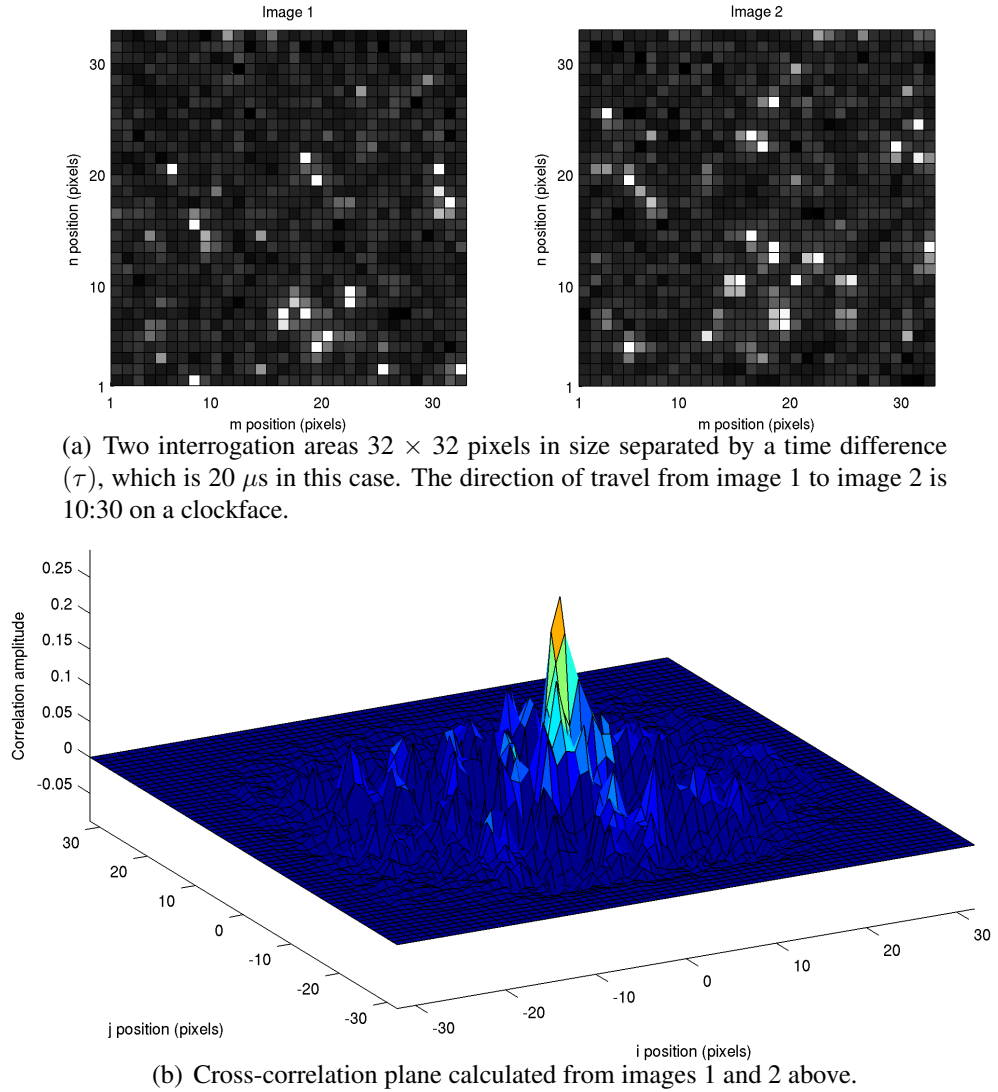


Figure 4.2: Cross-correlation plane and constituent interrogation areas from which the correlation peak can be extracted and a velocity vector calculated.

for that translation will be high. A full and rigorous mathematical treatment of cross-correlation as applied in PIV can be found in [Raffel 07] and will not be repeated here. For an $M \times M$ interrogation area the discrete cross-correlation function applicable to PIV is given by the equation

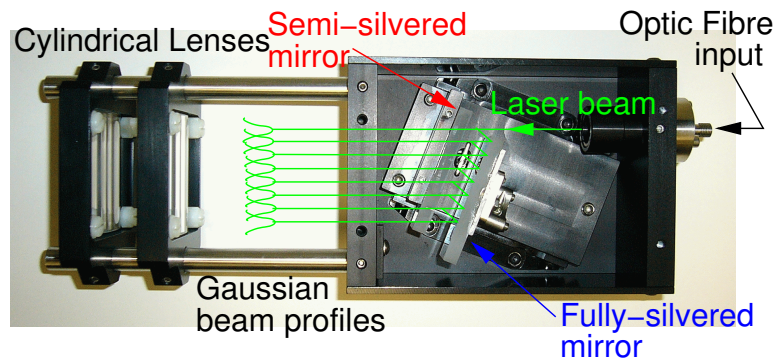
$$R_{I_1 \cdot I_2}(i, j) = \sum_{m=-M}^M \sum_{n=-M}^M I_1(m, n) \cdot I_2(m + i, n + j), \quad (4.1)$$

where $R_{I_1 \cdot I_2}(i, j)$ is the cross-correlation function (note with size $2M \times 2M$), $I_1(m, n)$ is the first image interrogation area, and $I_2(m, n)$ is the second image interrogation area [Keane 92]. Gradually, as the first interrogation area is translated over the second interrogation area and a cross-correlation function calculated for each translation a cross-correlation plane is constructed. A typical resulting cross-correlation plane from a PIV measurement conducted in this study is shown in Figure 4.2(b). The peak in the cross-correlation plane indicates that the translation of the 2 interrogation areas at that point show that the particles in the interrogation area from image 1 which have been translated by (i, j) pixels coincide with those in the interrogation area from image 2 and that the resultant peak shows the flow displacement for that interrogation area between the two images. In order to achieve sub-pixel level accuracy for the displacement peak in the cross-correlation plane, a Gaussian function is fitted to the peak and its nearest neighbours as it displays a shape which is close to that of a typically Gaussian function [Willert 91]. Through using the Gaussian function fit and achieving sub-pixel accuracy, it is then possible to use smaller interrogation areas and therefore attain greater spatial information for the flow [Raffel 07].

The displacement from the cross-correlation plane, expressed in pixels, is converted into metres using a calibration image and then converted to a velocity vector by dividing the displacement by the time separation τ between the two images. By dividing the original PIV image pair acquisitions typically 1280×1024 pixels in size up into interrogation areas and repeating the cross-correlation for each interrogation area, a velocity vector field can be constructed for the flow for that image pair acquisition. Finally, through a series of post-processing procedures it is possible to improve the final maps through the detection and removal of spurious data points. The exact procedure and settings used is highly dependent on the nature of the flow under scrutiny. Those used in this study and the reasons for these choices will be discussed in Section 4.4.1.

4.3 Experimental Apparatus

In order to undertake PIV flow field measurements for glottal flow in the *in vitro* model as detailed in Section 3.4.2, the trachea from the model is mounted to the front plate of the lung model. An Oxford Lasers LS20-50 copper vapour laser [oxf 12], delivering approximately 6 - 10 mJ per pulse, was used as the illuminating source for the seeding particles. The laser beam was delivered via a monofibre fibreoptic cable and then expanded into a thin sheet, approximately 1 - 2 mm thick, using an Oxford Lasers Fibrsheet. Within the fibrsheet the laser light, delivered through fibreoptic cable is bounced back and forth between two angled mirrors, one of which is semi-silvered. This process splits the beam up into a series of beams with a Gaussian profile that, when added together, produces a coherent lightsheet which is then focused using two cylindrical lenses. This process is summarised in a schematic diagram shown in Figure 4.3.



Source: After Skulina [Skulina 05].

Figure 4.3: Oxford Lasers Fibrsheet optical delivery unit.

Due to the LS20-50 rated as having a power of 30 W and therefore being designated as a Class IV laser, the entire model and light sheet arrangement, once set up, was enclosed in a metal housing to protect the user during operation. By default the laser ran in continuous wave mode with a pulsing frequency of 12 kHz; however, it was possible to pulse the laser at a rate of 10 - 50 kHz at a specified time if the laser was put into external trigger mode. This meant that the potential time separation between images in an image pair acquisition was 20 - 100 μ s. Unlike studies using two separate lasers or a dual-headed laser, this time separation range was a limitation on this study

4.3. EXPERIMENTAL APPARATUS

as it placed an upper limit on the velocities which could be measured. This meant that the subglottal pressures used with the *in vitro* model for PIV were limited. As the value of τ is closely linked with the analysis procedure of the image pair acquisitions, this will be discussed in more detail in Section 4.4.1.

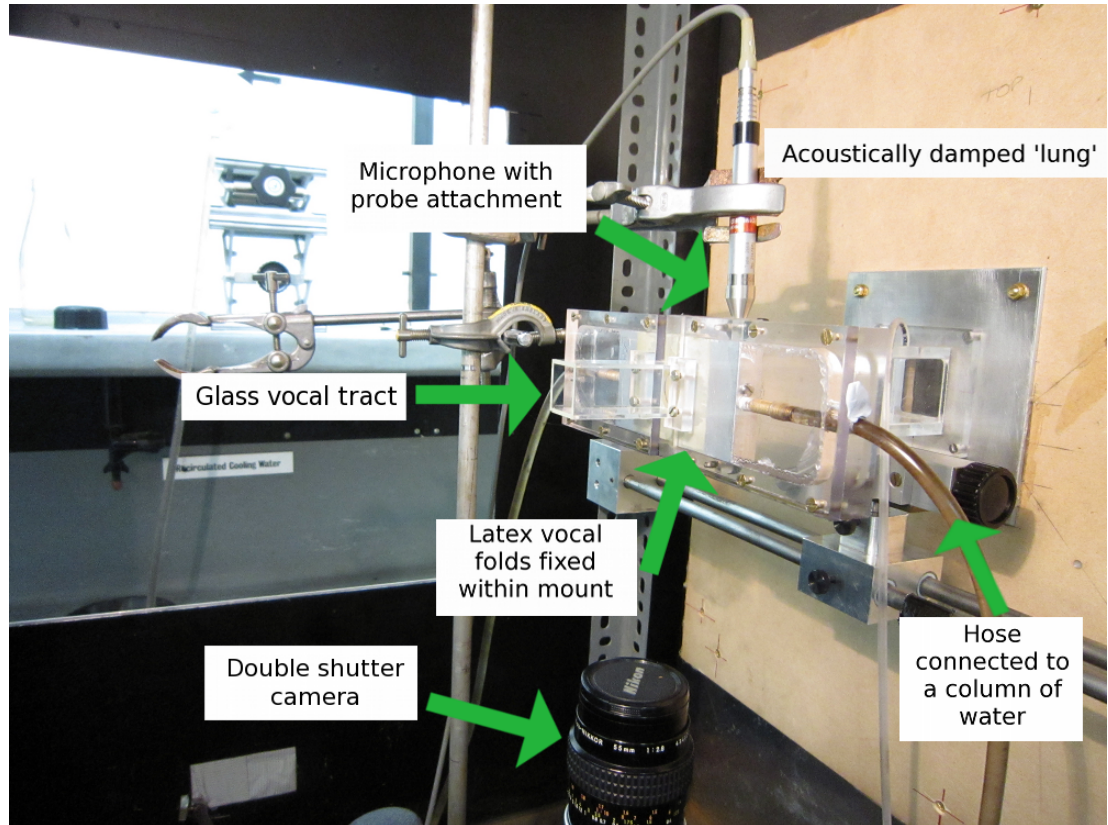


Figure 4.4: Labelled setup of the *in vitro* model in preparation for an image pair acquisition.

A PCO SensiCam Double Shutter digital camera [pco 12], with a resolution of 1280×1024 pixels, was used to capture the PIV image pairs. The camera was connected to a dedicated PC via a 5 m coaxial cable running proprietary software into which the settings were inputted, the image pairs were captured and exported, and the camera was armed. Attached to the camera, via a C-mount to F-mount adaptor, was a Nikon micro-Nikkor 55 mm f/2.8 lens. This lens was chosen due to the exceptional flatness of its field of view, thereby introducing as little distortion to any images taken as possible and thus improving the quality of the image pair acquisitions. The camera

had two exposure time delay settings, short and long, allowing the time delay between the end of the first exposure and the start of the second exposure to be set to either 200 ns or 1 μ s. For this study, the long exposure delay mode was used. The exposure time for the first exposure was set to 25 μ s; however, it was not possible to set the time for the second exposure as this depended on the time taken for the computer to process the first image [Skulina 05]. As the specific times used to control the camera during PIV image pair acquisitions are related to the phase-stepping technique, this will be discussed in detail in Section 4.3.3. The laser and camera were both triggered externally using a Berkeley Nucleonics Model 500A delay generator [bnc 12] which was set and armed using the in-built RS232 protocol.

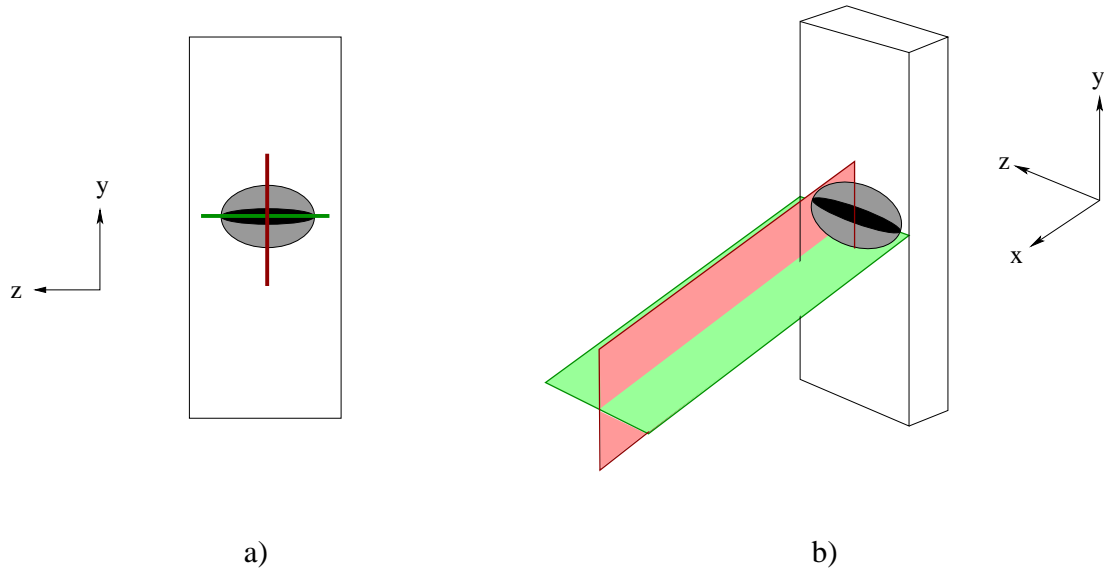


Figure 4.5: Schematic diagram of the laser light sheet planes used during PIV. Light sheet configuration 1 (relating to results discussed in Chapter 5) is the red plane and is perpendicular to the glottal open width. Light sheet configuration 2 (relating to results discussed in Chapter 6) is the green plane and is parallel to the glottal open width.

As seen in Figure 4.4, a Bruël and Kjær type 4192 microphone [Ban 12] with a probe short attachment is found 10 mm upstream of the *in vitro* vocal fold model which is embedded into the upper wall of the trachea. An advantage of placing the microphone upstream of the vocal folds rather than downstream is that our measurements do not suffer from the aeroacoustic noise observed in [Krebs 12], which is audibly more significant when ventricular bands are added to the vocal tract. This

microphone is attached to a Bruël and Kjær type 2609 measuring amplifier which is then connected to an input of a Hewlett Packard 54602A oscilloscope [HP 12], an input of a Kemo type VBF/3 0.1Hz - 10 kHz dual variable filter [kem 12] and to an input of a National Instruments PCI-6024E data acquisition card [NI 12] via a National Instruments SCB-68 connector block. All of this equipment was used to sample and filter the acoustic pressure upstream of the *in vitro* model which is used in the phase stepping mechanism detailed later. Software written in National Instruments' LabVIEW was developed and used to capture simultaneously the pressure signal sampled at probe microphone, the filtered microphone signals, and the triggering signals for later analysis.

To measure the static pressure upstream of the vocal folds a Digitron P200UL digital manometer [dig 12] was connected, via a thin length of Portex flexible tubing, to the upper wall of the vocal tract 10 mm downstream of the entrance to the trachea. A thermometer and barometer were used to record the temperature, atmospheric pressure, and humidity for each experiment. Finally, PIV was undertaken on the *in vitro* model in two planes: perpendicular to the glottal open width (light sheet configuration 1 in Figure 4.5) and parallel to the glottal open width (light sheet configuration 2 in Figure 4.5). This was made possible by rotating the *in vitro* model (only the vocal folds (including enclosure) and vocal tract) by 90°.

4.3.1 Seeding Particle Size

As seeding particles are used to indicate the movement of flow in image pair acquisitions, it is important that their movement imitates that of the flow. In other words, it is important that the particles injected in the flow follow the line of the flow faithfully. An important measure for considering whether or not the seeding particles follow the fluid well, and hence produce accurate flow fields, is the *Stokes number* (Sto) [Raffel 07, Tropea 07, Drechsel 08, Bian 10, Erath 10b]. This is defined as

$$Sto = \frac{\tau_p}{\tau_f}, \quad (4.2)$$

$$\tau_p = \frac{\rho_p D_p^2}{18\mu_0}, \quad \tau_f = \frac{\delta}{u_{cl}}, \quad (4.3)$$

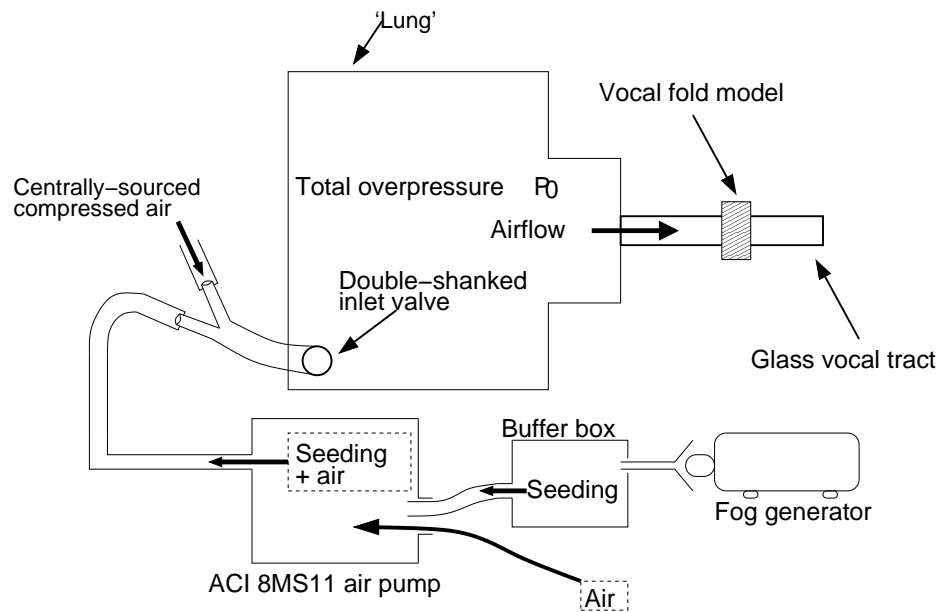
where τ_p is the particle time scale or relaxation time, τ_f is the flow time scale, ρ_p is the particle density, D_p is the particle diameter, μ_0 is the air viscosity, δ is the shear layer thickness, and u_{cl} is the local streamwise centreline velocity. Using the following values acquired from calibration measurements

$$\begin{aligned}\rho_p &= 1.00 \times 10^3 \text{ kgm}^{-3} \\ D_p &= 1.00 \times 10^{-6} \text{ m} \\ \mu_0 &= 18.27 \times 10^{-6} \text{ Pa s} \\ \delta &= 2.00 \times 10^{-3} \text{ m} \\ u_{cl} &= 50.00 \text{ ms}^{-1},\end{aligned}$$

a Stokes number of 0.076 was calculated. This number was sufficiently below 0.2 which is demanded in [Chein 88, Murugappan 08] for a flow visualisation in an incompressible flow, and 0.1 where it is shown in [Tropea 07] that the tracing accuracy errors fall below 1%. It is therefore assumed that the seeding particles will follow the flow faithfully and produce accurate flow fields.

4.3.2 Seeding Particle Delivery System

A schematic diagram for the experimental setup used for providing seeding for PIV and air pressure to the model can be seen in Figure 4.6. The seeding for PIV was provided through the use of a SAFEX-NEBELGERÄT F2004 fog generator [saf 12]. The particles were a mixture of alcohol and water and were approximately $1\mu\text{m}$ in size [Dantec A/S 98]. These particles were collected in a wooden overflow box and then taken up into an Air Control Industries Ltd. 8MS11 0.25kW air pump [ACI 12], which was then fed into the *in vitro* lung model via a double-shanked inlet valve. The seeding particles were delivered into the lung in order to ensure that a consistent density of seeding particles was delivered throughout an image pair acquisition run. An additional source of pressure from a centralised pressurised air supply was fed into the other side of the double-shanked inlet valve. The air pressure (and hence the subglottal pressure) was modified at the source of the centralised compressed air supply within the laboratory as it was not possible to reduce the speed of rotation of the air pump directly, as the flow control valve between the air pump and the lung model was used



Source: Adapted from Newton [Newton 09].

Figure 4.6: Schematic diagram of the seeding particle delivery system.

to control the density of seeding particulate.

4.3.3 Phase Stepping Mechanism and Image-Pair Acquisition

One of the novel contributions of the author to the PIV configuration at the University of Edinburgh is the ability to undertake phase-stepped image pair acquisitions for a self-oscillating *in vitro* model of the human larynx. Although this approach is not novel in itself [Drechsel 07, Drechsel 08] a complete overhaul of the computer software written by previous researchers at the University of Edinburgh to produce image pair acquisitions, the experimental apparatus involved, and the commissioning and development of new hardware was required. In addition, all of the computer software used to produce the results shown in Chapters 5 and 6 had to be re-worked and in some cases completely re-written to facilitate this change. A description of the phase windowing method used previously for making image pair acquisitions can be found in [Newton 09].

The basic principle behind the phase stepping technique is quite simple. The positive-going zero-crossings in the upstream acoustic signal are detected and this

point is then defined as $t = 0$ in that phonatory cycle. The equivalent of the phonatory cycle for the acoustic pressure signal is called the *acoustic pressure cycle*. Assuming that there is only one positive-going zero-crossing per cycle, points in the acoustic pressure cycle can be defined and image pair acquisitions made at these points by simply specifying a time delay from the point $t = 0$. If the model oscillates at the same frequency consistently then the image pair acquisitions will be made at the same point in the acoustic pressure cycle hence establishing a phase step. The reality of this though is not quite as simple.

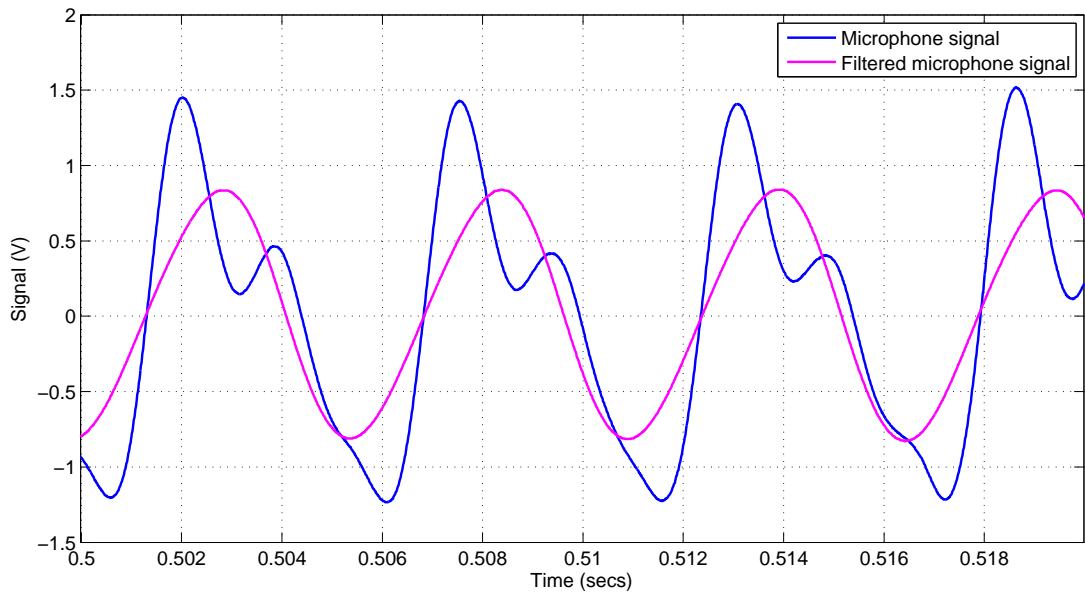


Figure 4.7: Plot showing the upstream acoustic signal and the filtered upstream acoustic signal.

Before any signals were recorded, whilst the vocal folds were oscillating stably, the microphone filtered through the Kemo VBF/3 dual variable filter (acting as a bandpass filter) and connected to the Hewlett Packard oscilloscope along with the unfiltered signal were phase matched so that the filtered and unfiltered microphone signals crossed the zero point at the same point. The reason that it was necessary to filter the acoustic pressure signal was because the signal sometimes had two positive-going zero-crossings per acoustic pressure cycle. This caused problems with the time delay mechanisms and so a filtered acoustic pressure signal, which was phase-matched with the unfiltered acoustic pressure signal was used. This was achieved through

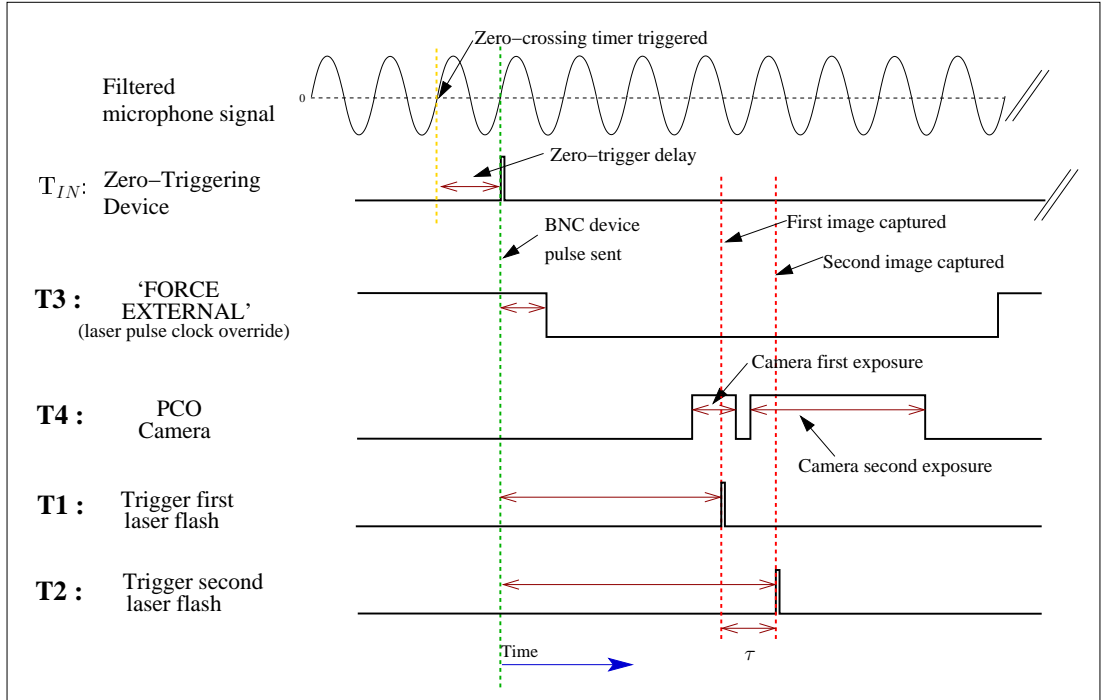
setting the values of the high pass and low pass filters and needed to be completed for each different configuration of the *in vitro* model. An example of the filtered and unfiltered microphone signals which have been phase matched can be seen in Figure 4.7. Although for the majority of the time the two signals crossed the zero point at the same point in time, any instability in the model oscillation would cause the two zero-crossing points to not coincide (as can be seen by a careful look for the last zero-crossing point in Figure 4.7 around 0.518 secs).

A LabVIEW virtual instrument (VI) was used to synchronise the run of image pair acquisitions. The first part of the program recorded a 2 second sample of the acoustic pressure signal using the microphone with the probe attachment. From this signal the fundamental frequency of the vocal fold oscillation (f_0) was extracted. In addition, the rounded frequency (f_{rnd}) is extracted. This frequency is calculated as largest possible even integer below the value of f_0 , e.g. if $f_0 = 178.2$ Hz, $f_{\text{rnd}} = 178$ Hz, equally if $f_0 = 179.9$ Hz then $f_{\text{rnd}} = 178$ Hz. The sampling rate throughout the run was 100 kHz, which was the maximum possible for the data acquisition hardware. The reason that both f_0 and f_{rnd} are extracted is that the process for reconstructing the points at which the image pair acquisitions were taken requires a fixed time delay and with the inherent instabilities in the oscillation of the *in vitro* model having a fixed frequency (f_{rnd}) for all the runs for a particular configuration of the model made the process possible.

Once f_{rnd} was calculated, a time delay was then calculated for the user-specified phase step. Before running the VI, the user is required to specify how many phase steps the acoustic cycle should be split up into (10 were used in this study) and at which phase step image pair acquisitions would be taken for the run. In order to detect the positive-going zero-crossings in the filtered acoustic signal a positive-going zero-crossing trigger was built and developed by Richard Taylor in discussion with the author in the Electronics Workshop in the School of Physics and Astronomy at the University of Edinburgh. A schematic drawing of the device can be found in Figure C.1 in Appendix C. A dedicated zero-crossing trigger was developed so that this element of the apparatus was kept separate from the data acquisition PC and therefore not place any further load on the CPU and avoiding errors associated with lag. The device was USB controlled with dedicated LabVIEW VIs to test and run it, which were also integrated into the main PIV VI.

A further function of the zero-crossing trigger was the ability to hold a time delay

before sending a 3.3V TTL signal. The zero-crossing trigger had a minimum required time delay of 1 ms, therefore a delay of the period of f_{rnd} , T_{rnd} , was added from the point at which a positive-going zero-crossing was detected. As the time delay on the device was quantised in ms, T_{rnd} was split up into a part quantised in ms (Π_{rnd}) which was sent as a delay to the zero-crossing device and the remaining part, π_{rnd} (quantised to 0.1 μ s) was sent as an additional delay to a Berkeley Nucleonics 500A delay generator. The time delay set to channel 1 of the Berkeley Nucleonics delay generator was T_{rnd} plus the time delay required for the desired phase step t_{offset} in addition to π_{rnd} already discussed. All time delays calculated by the PIV VI were sent through to the time delay devices either directly through USB for the zero-crossing detector or via the RS232 protocol. New software was written to make use of the RS232 protocol present on the Berkeley Nucleonics delay generator and incorporate it into the main PIV VI. No image pair acquisitions were made until all the devices had been successfully set and armed.



Source: Adapted from [Skulina 05, Newton 09].

Figure 4.8: Diagram summarising the triggering process used to undertake phase-stepped PIV (not to scale).

4.3. EXPERIMENTAL APPARATUS

	BNC Channel	Delay (ms)	Width (ms)	Polarity
Zero-Trigger	<i>n/a</i>	Π_{rnd}	0.05	+
Laser Pulse 1	T1	$\pi_{rnd} + T_{rnd} + t_{offset}$	0.0004	+
Laser Pulse 2	T2	$T1 + \tau$	0.0004	+
Force External	T3	$T1 - 2$	350	-
PCO Camera	T4	$T1 - 0.09$	0.1	+

Table 4.1: Table summarising the timings for the triggering mechanism used to undertake phase-stepped PIV.

As well as holding the remaining time delay (π_{rnd}) left over from the quantised delay sent to the zero-crossing trigger (Π_{rnd}), as in previous studies [Skulina 05, MacDonald 09, Newton 09] the Berkeley Nucleonics delay generator created the control signals for the pulses and external mode for the copper vapour laser and the camera trigger. The output of the zero-crossing trigger was connected to the input of the Berkeley Nucleonics generator, so that once a trigger had been generated and sent by the zero-trigger the time delays programmed into the Berkeley Nucleonics generator started. A summary of the time delays programmed into the two timing devices can be seen in Table 4.1. The reason that an additional T_{rnd} time delay was added to the time delay for channel 1 or the Berkeley Nucleonics delay generator was that both the PCO camera and laser required a short time to become ready before each image pair acquisition is made. This did add an additional inaccuracy; however, as the *in vitro* model is assumed to oscillate stably the overall impact of this additional delay was not significant. The time between laser pulses (τ) was 20 μ s, the shortest possible for the copper vapour laser. Once the system was armed, image pair acquisitions were taken at a minimum separation of 0.5 secs, due to equipment timing constraints. This minimum separation was set as a ‘blackout time’ on the zero-triggering device which was activated on the rising edge of each successfully sent TTL signal.

The LabVIEW VI recorded the unfiltered and filtered microphone signals and the pulses from the zero-triggering device throughout a complete run, again sampling at 100 kHz. These were used later for synchronising the image pair acquisitions with the acoustic pressure cycle using MATLAB. 40 image pair acquisitions were recorded on each run; however, as noted in [Newton 09] the first image pair acquisition was

discarded due to a distinct difference in the intensity of the lightsheet between the two constituent images. Two runs were completed for each phase step, thereby providing 780 image pair acquisitions for each configuration of the *in vitro* model. This generated a significant amount of data which had to be processed and stored.

Once the image pair acquisitions for a phase step had been made, it was then possible to synchronise the individual image pairs with the acoustic pressure cycle, in a similar way to [Newton 09, Krebs 12]. Firstly, a single complete acoustic cycle was extracted from the recorded unfiltered microphone signal. The values of f_0 and f_{rnd} were calculated from the unfiltered microphone signal and the phase step point then reconstructed by calculating the time delay for the first laser flash using T_{rnd} and π_{rnd} and the calculated phase step offset t_{offset} . The time difference between the closest start of an acoustic cycle (with an absolute time which is less than the absolute time of the phase step position) and the phase step position point was calculated and then recorded; the pressure signal value at this point was also recorded. Once this had been completed for each of the image pair acquisitions in a phase step these were then plotted and the mean and standard deviation of their acquisition in relation to the acoustic cycle recorded. Any variation in their position either in the recorded time or pressure was due to natural inconsistencies of the *in vitro* model's oscillation.

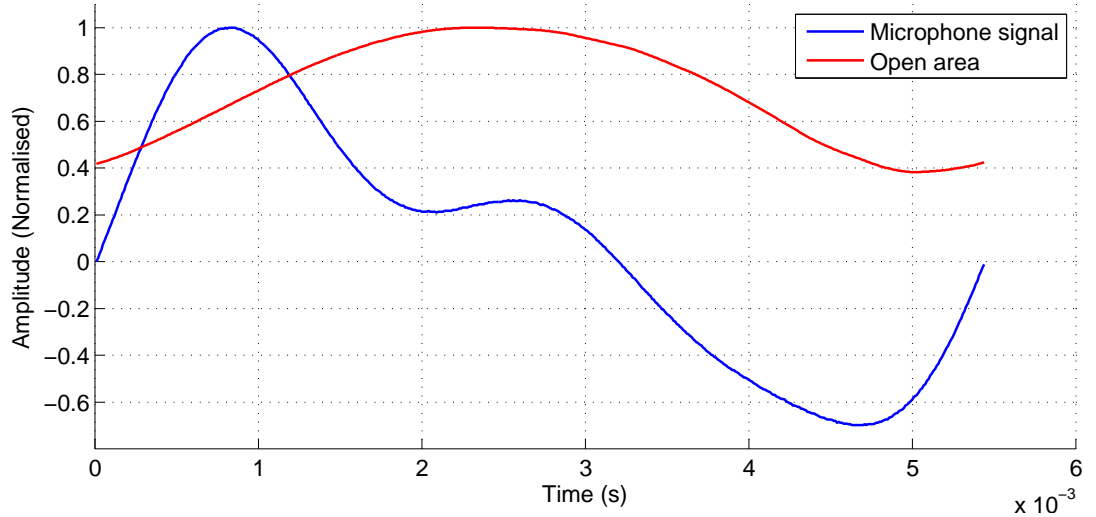


Figure 4.9: Plot showing upstream acoustic signal synchronised with the measured open area of the vocal folds.

Finally, using images from the high-speed camera as discussed in Section 3.6 it was possible to synchronise the acoustic cycle with the open area and centreline open height of the *in vitro* model. Therefore, it was also possible to synchronise the phase stepped image pair acquisitions with the open area and centreline open height of the *in vitro* model and hence analyse the resultant PIV flow field maps in relation to the dynamics of the model. An example of a synchronised acoustic pressure cycle and an open area cycle (normalised) is shown in Figure 4.9. Preliminary results from the PIV system using the phase stepping technique were first presented in [Apostoli 10a], where the advantages over phase windowing system used previously were explored.

4.4 PIV Data Analysis Methods

In this section, the data analysis methods used to produce the PIV flow field data and data extracted from these are detailed. Various tools and scripts written in MATLAB and UNIX bash were used to process the data. In particular, the use of phase-stepped image pair acquisitions in conjunction with using Dantec Dynamics DynamicStudio software [dan 12] to produce the PIV flow field maps meant that many existing analysis scripts had to be re-written and new ones created. The effect of ensemble averaging and the calculation of the vorticity flow field maps is discussed. An algorithm for calculating the jet centreline in order to consider jet flapping and the Coandă effect is introduced. Although this algorithm is not novel, a considerable amount of work was undertaken in order for it to function with pre-existing data structures. Finally, the parameters used in the dimensional analysis performed in Chapter 5 are explained and the way in which they are extracted also is revealed.

4.4.1 PIV Flow Field Data Calculation Routine

The image pair acquisitions were processed using Dantec Dynamics' DynamicStudio v2.30 in order to produce PIV velocity flow field maps. As DynamicStudio is a professional commercial software package, a sincere debt of gratitude is due to Dantec Dynamics for allowing use of this software to complete this study and to Graham Hassell and Robert Jaryczewski for their support. Previous studies [MacDonald 09, Newton 09] at the University of Edinburgh have used the MatPIV package written for MATLAB; however, this package was found to be both extremely

4.4. PIV DATA ANALYSIS METHODS

	Interrogation area size (pixels)			
	128×128	64×64	32×32	16×16
Max. displacement (mm)	1.10	0.55	0.28	0.14
Optimum displacement (mm)	0.74	0.37	0.18	0.09
Max. velocity (ms^{-1})	55.2	27.6	13.8	6.9
Optimum velocity (ms^{-1})	36.8	18.4	9.2	4.6

Table 4.2: Table summarising the optimum and maximum displacements and velocities for four different sizes of interrogation area for this study using PIV.

slow and limited in comparison to Dantec Dynamics' DynamicStudio. DynamicStudio and its predecessor FlowManager have been used in a number of different studies ([Arthur 09, Becker 09, Shinneeb 12] to name only a few of the more recent ones).

One of the significant advantages of using DynamicStudio over MatPIV is the adaptive correlation feature. This feature is based on a cross-correlation technique, and works by iterating over decreasing sizes of interrogation area, using the information from each iteration to improve the dynamic range of the PIV system [Dan 00]. In addition sub-pixel analysis and high accuracy deforming windows add further to the dynamic range required for studying multi-scale flows [Takeuchi 05]. Using a measured calibration showing the number of pixels per metre, in Table 4.2 can be found the maximum displacements and velocities measurable without violating Nyquist's criterion for four different sizes of interrogation area. Included also are the optimum displacements and velocities, which equate to a particle moving one third of the way across an interrogation area.

As the mean maximum velocity value of the glottal flow from preliminary measurements and calculations approached 50 ms^{-1} , the appropriate interrogation area size for this particular velocity, seen in Table 4.2, is 128×128 . Unfortunately, due to experimental constraints it was not possible to either decrease the number of pixels per metre or reduce the amount of time separating the two images in an image pair acquisition thereby increasing the maximum and optimum displacements and velocities. However, due to the large variation in velocity and the complexities of the flow being measured the adaptive correlation function from DynamicStudio proved to be a very suitable tool to undertake this study. A summary of the settings used for the

4.4. PIV DATA ANALYSIS METHODS

Interrogation area:	Initial: 128×128 (2 passes) Intermediate: 64×64 and 32×32 Final: 16×16 (2 passes)
Overlap:	50%
Peak height validation:	1.1
Local neighbourhood validation:	Moving average Neighbourhood size: 3×3 Acceptance factor: 0.15 Iterations: 3 Centre difference scheme used
High accuracy sub-pixel refinement used	

Table 4.3: Table summarising the settings used in the adaptive correlation function in Dantec Dynamics' DynamicStudio v2.30.

adaptive correlation are presented in Table 4.3.

The final choice of parameters was the result of numerous preliminary experiments. A peak height validation (the height between the highest peak on the cross-correlation plane in comparison to the second highest peak) was chosen to be the value 1.1, which is close to the value 1.2 which users are typically advised to select [Keane 92, Jensen 04]. A 50% overlap was chosen, which is in common with other comparable studies [Takeuchi 05, MacDonald 09, Murugappan 08, Erath 10a]. The moving average local neighbouring validation was used with values which were close to those advised in [Dan 09] as they were found to work well, and high accuracy sub-pixel refinement was used to increase the dynamic range of the PIV. The centre difference scheme for the interrogation area offset was chosen as it is shown to be more mathematically accurate than the forward difference scheme [Dan 09].

If no valid peak existed within a correlation plane (i.e. the ratio between the highest and second highest peak is less than the peak height validation value chosen) then no vector was recorded. In addition, the local neighbourhood validation procedure looked at the velocity vectors within a given area (the neighbourhood size) and identifies spurious data points based on the chosen acceptance factor. The acceptance factor is a measure which defines a given degree of freedom on the velocity vector gradient inside the neighbourhood area. If the calculated gradient was larger than the acceptance

factor, the central vector was removed [Dan 09]. Any vectors which were removed by either of the peak height validation or the local neighbourhood validation procedures were substituted for one interpolated locally using either the moving average or local median method (moving average in this case). Finally, a range validation process was used in order to eliminate velocity vectors that violate the Nyquist criterion. This was set at 55 ms^{-1} . A typical PIV flow field map for this study has 127×159 velocity vectors (20,193 in total). Out of these for a typical map 7197 vectors were substituted and 105 were rejected by the range validation.

It has already been mentioned that DynamicStudio was considerably faster than MatPIV. Part of the reason for this is that DynamicStudio supports distributed analysis. What this means is that more than one computer can work on the same problem at a time if an agent with the software is installed. As the computers in the research laboratories are all networked, it was possible to enlist the help of 4 different computers to analyse the image pair acquisitions. Although this feature was available it took quite a long time to implement due to technicalities; however, this facility had a significant impact on the time that it took to process image pair acquisitions. Finally, it should be noted that a series of different UNIX bash scripts and MATLAB scripts had to be written in order to convert the exported data files from DynamicStudio into a data structure which was consistent with pre-existing data structures.

4.4.2 Velocity Magnitude, Standard Deviation, and Ensemble-Averaging

Outputted from DynamicStudio were velocities separated into their x - and y -components. The magnitude of the x - and y -components of the velocity were calculated for each point using

$$|u|(x, y) = \sqrt{(u(x, y))^2 + (v(x, y))^2}, \quad (4.4)$$

where $u(x, y)$ is the component of velocity in the x -direction at the position (x, y) in the flow field map and $v(x, y)$ is the component of velocity in the y -direction at the position (x, y) in the flow field map. It is then common practice in studies of fluid turbulence to consider the ensemble average for a series of measurements for a flow under similar conditions [Tritton 88]. This therefore made it possible to dissect the flow into the parts which remain constant and the parts which fluctuate. In order to

study the elements of the glottal flow which remained steady the mean of the velocity magnitude for each of the points in a flow field map was calculated using

$$\bar{u}(x, y) = \frac{1}{n} \sum_{i=1}^n |u_i|(x, y), \quad (4.5)$$

where n is the total number of constituent flow field maps for that phase step, and i is the individual flow field map number. This then produced a flow field map of the mean velocity magnitude for that phase step with the same dimensions as any of the constituent flow field maps. In order to assess how accurate the mean velocity magnitude map was as a representation of the constituent flow field maps, the standard deviation of the velocity magnitude was calculated

$$u_{std}(x, y) = \sqrt{\frac{1}{n-1} \sum_{i=1}^n (u_i(x, y) - \bar{u}(x, y))^2}. \quad (4.6)$$

The resultant map from this calculation was extremely useful as it provided an indication of the stability of the jet and how much variation took place from cycle to cycle. If the standard deviation of the velocity magnitude was particularly high at one point then this indicated that the constituent velocities for the mean velocity magnitude map differed and that the mean at that particular point was not a reliable representation.

4.4.3 Vorticity

Vorticity is a measure of rotation within a flow and is calculated analytically as $\vec{\omega} = \nabla \times \vec{u}$. A flow without vorticity is known either as an irrotational or a potential flow [Faber 95]. Vorticity and vortical structures within the larynx and vocal tract have been analysed in several different studies [Brücker 04, Krane 05, Khosla 07, Neubauer 07, Khosla 08b, Khosla 09, Erath 10b, Zheng 11]. The mean vorticity map for each phase step can be calculated using the equation

$$\bar{\omega}(x, y) = \left. \frac{\partial \bar{v}(x, y)}{\partial x} \right|_{y=0} - \left. \frac{\partial \bar{u}(x, y)}{\partial y} \right|_{x=0}, \quad (4.7)$$

where $\bar{u}(x, y)$ is the mean component of the velocity in the x -direction at the position (x, y) and $\bar{v}(x, y)$ in the flow field map is the mean component of velocity in the y -

direction at the position (x, y) in the flow field map. This was calculated in the same way as previous studies [MacDonald 09, Newton 09] using the vorticity function in the MatPIV package. The ‘centered’ option was used with this function, which uses a centred differences approach to the calculation [Sveen 04].

One of the main reasons that vortices are studied is that through generating either positive or negative pressures, they can be sources of sound [Khosla 09]. Khosla shows that they may also be responsible for rapid closure of the vocal folds, applying a pressure which is either equal to or greater than the driving pressure. To this end, the vorticity fields calculated from the PIV flow field data are analysed with the possibility of stable recurrent vortical structures appearing in the ensemble-averaged vorticity flow fields.

4.4.4 Jet Centreline

During calibration measurements it was observed that the jet core would occasionally either adhere to one side of the vocal tract or flap from side to side during a image pair acquisition run. Calculating the centreline and subsequent jet deflection is important, as there is evidence to suggest that asymmetric glottal flow can have an impact on pressure losses, vocal fold vibration, and sound production [Zheng 11]. In order to study this phenomenon the centreline of the jets in the calculated flow field data maps are calculated using the algorithm proposed in [Drechsel 08] and first proposed in [Erath 06]. MATLAB code for the algorithm was included in the appendices to [Drechsel 07]; however, this could not be used verbatim and had to be significantly modified in order to work with existing PIV data structures.

Drechsel’s algorithm used to compute the jet centreline, as included in [Drechsel 07], can be summarised in the following steps:

1. Velocity vectors within areas which are masked are set to zero.
2. The following steps are then performed for all velocity vectors in the x -direction (across the glottal jet) for each value of y (displacement from the vocal folds):
 - (a) A minimum velocity threshold in order to detect the jet was established. As in [Drechsel 08] 7 ms^{-1} was used here.

- (b) Smoothing was undertaken on the velocity vectors using a moving average of size $n = 7$.
 - (c) The maximum jet velocity was identified using the smoothed velocity profiles.
 - (d) Velocity vectors within the jet core were identified as those having a value of greater than 80% of the maximum jet velocity.
 - (e) The mean value of the identified jet core was then calculated and the jet centre was defined as the centroid of all the vectors within one standard deviation of this value.
3. Once the above steps have been completed for the all values of y , the jet centreline is constructed from the individually calculated jet centreline points over for all values of y .
 4. The calculated centreline velocity is then smoothed using a moving average of size $n = 5$.
 5. The position and velocity of the both the smoothed and unsmoothed jet centreline are returned to the user.

Considering the results produced using Drechsel's algorithm in preliminary studies it is clear that the jet centreline is well-represented. In order to calculate the jet deflection angle and to account for breakdown of the jet core in the turbulent transition region, a straight line is fitted to the jet centreline points using MATLAB's robust fitting function. This function calculates the weighting of each datapoint in an iterative fashion, which it then uses to fit a straight line to the data, which has the effect of reducing the impact of perceived 'outliers' inherent in experimental data on the final fit. The coefficient of determination for the fitted straight line (R^2) is also calculated and where this falls below a critical value, indicating that the straight line is not a good model for the jet, the associated jet deflection angle is filtered out of the final results. The displacement from the vocal folds over which the jet deflection angle is calculated depends entirely on the nature of the jet for that particular setup.

4.4.5 Dimensional Analysis Parameters

In this section can be found an explanation of the terms used in dimensional analysis of the glottal jet in Chapter 5. The parameters chosen are the same as those used in [Newton 09] as this will permit a comparison to be made between the results from this study and those in [Newton 09], which will be of interest due to the differences between the two studies. A similar nomenclature to that used by Newton also was used to avoid unnecessary confusion.

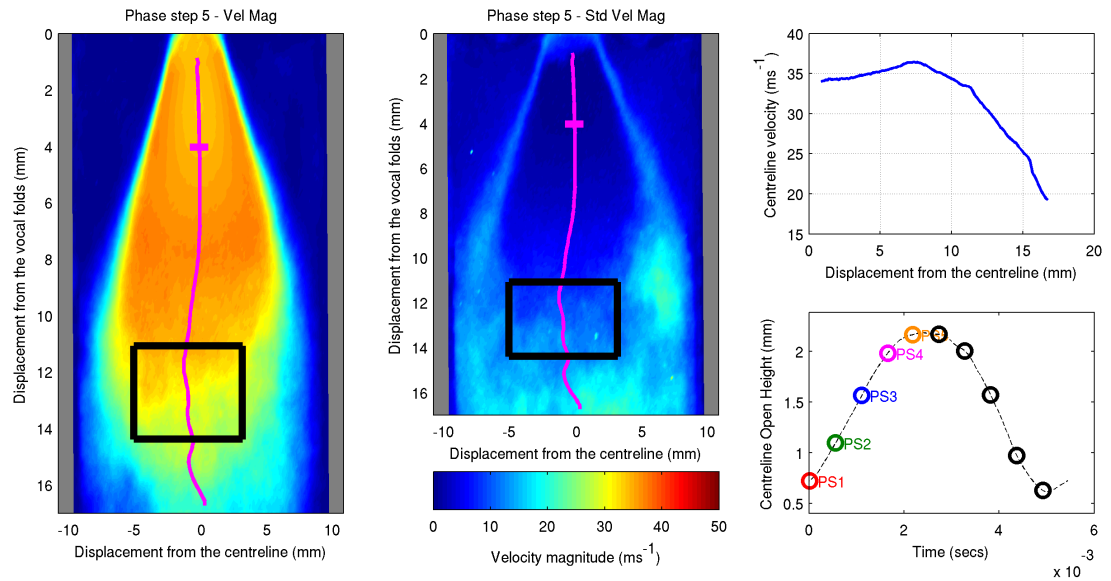


Figure 4.10: Plot showing an example of the areas used for the jet core (shown by a horizontal thick magenta line) and pre-turbulent region (shown by a black square) used in the dimensional analysis marked on an ensemble-averaged velocity magnitude and standard deviation map. The calculated centreline is shown as a vertical magenta line on both maps, and plots showing the jet centreline velocity and phase step position are included on the right hand side.

A considerable number of the parameters used in the dimensional analysis use average velocity magnitude and standard deviation values extracted either from the core the glottal jet or from the pre-turbulent region. Figure 4.10 shows the jet core and pre-turbulent region marked as magenta or black squares (respectively) on the ensemble-averaged velocity magnitude and standard deviations maps. In the interest of clarity, as the jet centreline is also shown in magenta the jet core region can be seen at a 4 mm displacement from the vocal folds. The reason for the disparity in the

size of the two regions is the high degree of change caused by the onset of turbulent dissipation of the jet for the pre-turbulent region whereas a comparatively small degree of change is seen within the jet core.

A novel contribution made in this study is the way in which the positions where the jet core and pre-turbulent regions are extracted are calculated. As seen in Figure 4.10 the centreline velocity within the jet core between 1 and 7 mm downstream of the vocal folds was found to be almost constant. This therefore indicates that the irrotational jet core velocity may be the same as that observed at the point of flow separation and that any points in the jet core chosen between 1 and 7 mm downstream of the vocal folds would be appropriate as a measure of the mean jet core velocity. To this end, an area of size 1×11 pixels was extracted 4 mm downstream of the vocal folds with the central point of the extraction area aligned with the calculated centreline at that point and the mean of the extracted values taken. The mean standard deviation of the jet core region was extracted the same way only from the standard deviation map rather than the velocity magnitude.

The pre-turbulent region mean velocity magnitude was extracted using an area of size 25×61 pixels from the velocity magnitude map and the mean of the extracted values taken. The centre position of this region was calculated as being at a displacement equal to position of the jet centreline where the centreline velocity is 9/12 of the maximum centreline velocity downstream of the point at which the maximum centreline velocity occurs. The reason that 9/12 was chosen was because it was found to place the pre-turbulent region in the correct place. This meant that both the jet core and pre-turbulent region extraction areas moved as the jet dynamics and length of the potential core change, providing a more realistic representation of the velocity magnitudes and standard deviations of the velocity magnitudes in these regions than was possible in [Newton 09].

Jet Core Reynolds Number (Re_{core})

The jet core Reynolds number provides a measure of the properties of the fluid within the jet core and is calculated using the equation

$$Re_{core} = \frac{h_{vf} \cdot \bar{u}_{core}}{\nu}, \quad (4.8)$$

where h_{vf} is the centreline open height of the glottis, \bar{u}_{core} is the mean jet core velocity magnitude, and ν is the kinematic viscosity. This number indicates how the fluid within the jet core will behave and how the properties of this region evolve throughout the phonatory cycle.

Jet Core Turbulence (T_{core})

The jet core turbulence parameter provides a measure of the ratio between the mean velocity magnitude of the jet core and the mean standard deviation of the velocity magnitude. This is calculated using the equation

$$T_{core} = \frac{\bar{\sigma}_{core}}{\bar{u}_{core}}, \quad (4.9)$$

where σ_{core} is the mean standard deviation of the jet core velocity magnitude. This value is important as it provides a direct indication of the degree of measured turbulence within the potential core of the glottal jet, and hence the stability of this jet from cycle to cycle. If this value is near to 0, then the turbulence within the jet core is low in comparison to the measure velocity magnitude; however, if the number is closer to 1 then the measured turbulence within the jet core is of a similar value to that measured for the velocity magnitude. It is possible for this number to increase above 1, which has been seen in results presented in [Newton 09].

Normalised Jet Core Velocity (u_{norm})

The normalised jet core velocity provides an important measure by which it is possible to make a comparison between the velocity magnitude of the flow predicted using a simple flow model and that measured in the jet core. The normalised jet core velocity is calculated using the equation

$$u_{norm} = \frac{\bar{u}_{core}}{u_{VF}}, \quad (4.10)$$

where u_{VF} is the velocity magnitude at the point of flow separation calculated using the quasi-steady Bernoulli flow assumption assuming a total pressure loss of the jet, as discussed in Section 3.7.3, which is calculated using Equation 3.36. With the hypothesis discussed in Section 3.7.3 that the glottal jet reattaches to the walls of the

ventricular bands, Newton notes that it is expected for the value of the average jet core velocity to be less than that calculated for u_{VF} [Newton 09]. As Newton measured the jet core velocity 8 mm downstream of the vocal folds, it was not possible for him to confidently measure the average jet core velocity magnitude (and by extension the normalised jet core velocity) for all phase steps. Whilst the values of u_{norm} are expected to be less than 1, assuming a pressure recovery at the ventricular bands, it is possible for this value to be greater than 1, which may indicate inertial effects above and beyond the simple quasi-steady Bernoulli flow model.

Normalised Glottal Open Height (h_{norm})

The normalised glottal open height is given by the equation

$$h_{norm} = \frac{h_{vf}}{h_{max}}, \quad (4.11)$$

where h_{vf} is the measured centreline glottal open height and h_{max} is the maximum measure centreline glottal open height. This parameter makes it possible to compare the behaviour of vocal folds in different configurations for the *in vitro* model of the human larynx and consider other extracted parameters from the dimensional analysis in comparison to the model phonatory cycle.

Flow Admittance ($1/Z_{core}$) and Resistance (Z_{core})

The flow resistance and flow admittance are useful measures of how efficiently fluid can flow through an orifice and is a normalised measurement of the volume flow against upstream driving pressure [Newton 09]. Newton notes that the flow resistance is expected to be high when the large driving pressure is used and a small volume flow is detected (for instance when the vocal folds are at their minimum opening) and low when a small driving pressure produces a high volume flow. The inverse is true for the flow admittance. The flow resistance is calculated using the equation

$$Z_{core} = \frac{P_{sub}}{\Phi_{core}}, \quad (4.12)$$

where P_{sub} is the subglottal pressure in the *in vitro* model and Φ_{core} is the volume flow within the jet core of the glottal flow. It should be noted that although the flow

resistance has been denoted using Z which is the conventional symbol for complex impedance, the flow resistance is not a complex value.

A novel method for calculating the volume flow is proposed for this study. Due to the glottal jet having an elliptical cross section for the majority of the phonatory cycle as seen in [Krebs 12] and in preliminary measurements in the present study, rather than using the jet expansion hypotheses proposed in [Newton 09] to calculate the jet cross-sectional area, the area of an ellipse was used instead. The minor radius α of the ellipse was calculated as half of the value of the jet width calculated at 1.5 mm downstream of the vocal folds. The major radius β of the ellipse was fixed at 5 mm, as the glottal jet was observed to have twice this width at this point downstream for most of the phonatory cycle in preliminary measurements in the plane perpendicular to the measured jet width.

Through the assumption that the jet shear layers are thin, the volume flow for the jet was therefore calculated by multiplying the mean of the velocity across the measured jet width and multiplying it by the area of an ellipse. This is expressed by the equation

$$\Phi_{core} = \pi \cdot \alpha \cdot \beta \cdot \frac{1}{N} \sum_{x=x_1}^{x_{max}} \bar{u}(x, y_{core}), \quad (4.13)$$

where x is a vector containing the position of the jet core region in the x -direction, y_{core} is the position of the jet core region in the y -direction, and N is the number of elements between x_1 and x_{max} . This difference in the method used to calculate the flow admittance and resistance will inevitably lead to different results from those reported in [Bailly 09, Newton 09].

“Science always doesn’t go forwards. It’s a bit like doing a Rubik’s Cube, you sometimes have to make more of a mess with a Rubik’s Cube before you can get it to go right.”

(Jocelyn Bell Burnell)

5

Vocal Fold and Glottal Jet Dynamics within Models of the Human Larynx

5.1 Introduction

In this chapter, the results from PIV and associated mechanical response experiments conducted on an *in vitro* model of the human larynx will be displayed and analysed. The results from four different configurations of the model will be presented:

1. Model larynx with static vocal folds (with increased stiffness due to the head of water being raised above the range required for self-oscillation to occur) and no vocal tract attached, used as a control.
2. Model larynx with self-oscillating vocal folds and a vocal tract attached but with no ventricular bands.
3. Model larynx with self-oscillating vocal folds and a vocal tract attached with rigid ventricular bands placed 16 mm downstream of the vocal folds, with an 8 mm separation.
4. Model larynx with self-oscillating vocal folds and a vocal tract attached with rigid ventricular bands placed 16 mm downstream of the vocal folds, with a 3 mm separation.

Due to the turbulent nature of the glottal jet, ensemble-averaged PIV flow-field data will be presented for all cases. The number of individual velocity data maps used in each ensemble-averaged plot presented is 78.

Before any presentation or discussion of the results is made, the first part of this chapter (Section 5.2) is concerned with the outlining the basic structure of the glottal jet, how different regions of the jet are identified, and how these regions are used in analysis later in the chapter.

The second part of this chapter (Section 5.3) considers the glottal jet emerging from the *in vitro* model with static vocal folds, acting as a control. This was an important experiment to conduct as when the vocal folds self-oscillate, they impede the airflow through the glottis periodically, which introduces difficulties in testing and analysing the performance of the PIV system used. Recalling that PIV is largely a statistical process it was important to test our system in a standard fluid mechanical scenario, so that appropriate individual settings used for the analysis could be selected and the suitability of this system established for our purpose.

In the third part of this chapter (Section 5.5) PIV velocity field maps showing the ensemble-averaged velocity magnitude and its standard deviation for each phase step will be presented for the *in vitro* model of the larynx with a glass vocal tract but without any ventricular bands. Vorticity maps showing rotation within the flow and shear layer thickness pertaining to this configuration are presented in Appendix B. The velocity magnitude data, showing the glottal jet from the point at which the vocal folds end, makes it possible to consider hypotheses on the expansion of the glottal jet (first proposed in [Bailly 08]) in greater detail and provide further validation as to their suitability. The jet is also represented non-dimensionally and compared to standard fluid mechanical jet models. Within his PhD thesis [Newton 09], Newton identified a series of non-dimensional parameters in order to perform a dimensional analysis of the glottal jet. The same parameters were used in order to perform the dimensional analysis of the glottal jet presented here.

The next part (Section 5.6) considers the case where the same *in vitro* model of the larynx is used with rigid ventricular bands added to the glass vocal tract. The ventricular bands were placed 16 mm downstream of the vocal folds with a separation of either 3 mm or 8 mm. In order to make comparison with the work of Newton and Bailly [Newton 09, Bailly 09], the ventricular bands were placed 24 mm downstream of the vocal folds with a 1 mm separation; however, the vocal folds were not found to self oscillate under these conditions. Velocity magnitudes and standard deviations are once again considered; however, as the vorticity plots were found to be very similar to

those for the model without ventricular bands, showing no new behaviour, these have been included in Appendix B. Non-dimensional measures are once again examined and the effect of the ventricular bands on the glottal jet in comparison to the case without ventricular bands is investigated.

The final part of this chapter (Section 5.7) examines the use of a state-of-the-art computational simplified physical model of the human larynx and comparisons are made between the outputs of this model and the results of experiments undertaken on the *in vitro* model. Novel results acquired from large-scale parameter sweeps using Condor and the implication of these results on current and future work will be discussed.

5.2 Basic Structure of the Glottal Jet

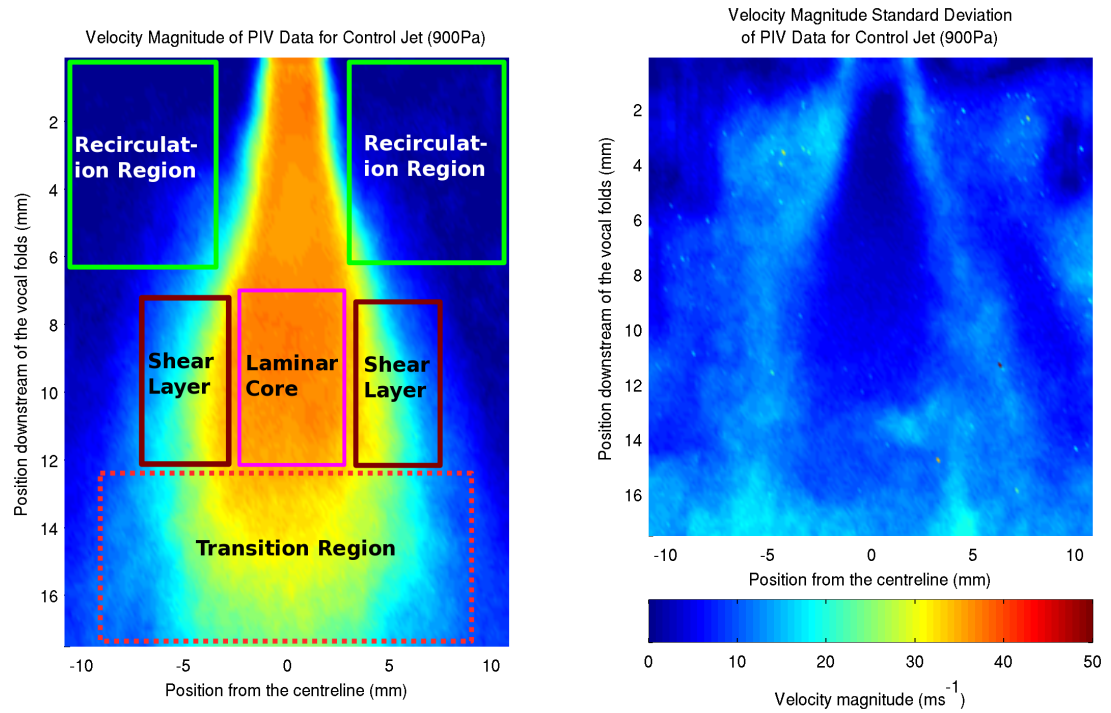


Figure 5.1: Ensemble-averaged velocity magnitude data and standard deviation for a free jet with the key elements of the jet labelled.

Before any consideration of the glottal jet or the impact of the various different

setups used in the *in vitro* model can be made, it is first necessary to define the various components which make up the jet and how they relate to any subsequent analysis. Figure 5.1 shows a jet emerging from a static *in vitro* model of the human larynx. On the left of the figure is the ensemble-averaged velocity magnitude data for the jet and on the right is the standard deviation of the velocity magnitude data. As no vocal tract was attached to the model for this configuration, the jet is defined as being a free jet; when a vocal tract is included it is termed a confined jet.

Identified in the figure are four key regions: the laminar jet core, shear layers, pre-turbulent transition region, and the recirculation regions (known as the regions of entrainment for the free jet control case). The laminar jet core can be found by identifying a central area of the jet where the standard deviation of the velocity magnitude data has a value which is much lower than the surrounding area. The velocity in this area therefore remains mostly constant throughout the individual flow-field data maps acquired with little or no turbulent dissipation. Of course, this procedure does not apply if the captured jet is not stable or flaps from side to side.

On either side of the laminar jet core can be found the shear layers. These can be identified from the standard deviation of the velocity magnitude as areas of increased variation in velocity magnitude over that of the laminar jet core. In these regions the fast-moving jet core comes into contact with the surrounding static fluid and the jet core breaks down, forming the edges of the jet and a velocity gradient. Although marked as discrete areas on the velocity magnitude data, both the laminar jet core and the shear layers extend up to the start of the jet. At the start of the jet the shear layers are very thin with a steep transverse velocity gradient; however, as progress is made away from the point of flow separation the shear layers become thicker and the velocity gradient becomes less steep.

The third component of the jet is the pre-turbulent transition region. In this sizeable region, the streamwise centreline velocity reduces dramatically and the jet begins to break down due to the onset of turbulence. Like the shear layers, this region is easily identified by considering the area downstream of the jet core where the standard deviation of the velocity magnitude increases and the jet core breaks down. The final elements of the jet are the regions of entrainment. Within these regions the static fluid surrounding the jet core and shear layers become drawn in with the flow of the jet due to the momentum of the flow. The fluid which becomes entrained at the start of the

jet decouples from the flow as the core begins to dissipate and then becomes drawn towards the start of the jet, causing this region to also be known as the recirculation region.

5.3 Results for the *in vitro* Model in the Free Jet Control Case

Although the vocal folds are not static during phonation, the study of the glottal jet in the *in vitro* model without oscillating vocal folds using PIV is important. This is because it provides a standard case whereby the flow field for the jet emerging from the vocal folds during oscillation can be compared to that of a steady flow. This then makes it possible to attribute effects observed for the glottal jet in cases where the vocal folds oscillate to the pulsatile nature of the flow during phonation. In addition, obtaining flow fields for the glottal jet in both a static and oscillating setup permits a comparison to be made between the jet dynamics at different points in the phonatory cycle (phase steps) and the glottal jet in the static model at different subglottal pressures (P_{sub}).

The control experiments were conducted on the same *in vitro* model as that used to acquire velocity flow fields for oscillating vocal folds but without a vocal tract attached. For these experiments the head of water, controlling the pressure of the water within the vocal folds and hence their stiffness, was raised such that no oscillation of the model took place at all subglottal pressures used. The head of water remained at a constant height throughout the control experiments, therefore both the geometry and open area of the vocal folds should also remain constant. In addition, the same PIV system analysis settings were used for this control as were used across the entire study. Unlike the case where oscillating vocal folds are considered, the image pair acquisitions for the control experiments were not locked to a particular phase point of any signal. It was considerably easier to achieve high quality images for PIV in the case without oscillating vocal folds due to there being no vocal tract present, thereby eliminating the chance of optical distortion caused by seeding particle deposition and the complication of there being a strong acoustic field downstream of the vocal folds.

5.3. RESULTS FOR THE *IN VITRO* MODEL IN THE FREE JET CONTROL CASE

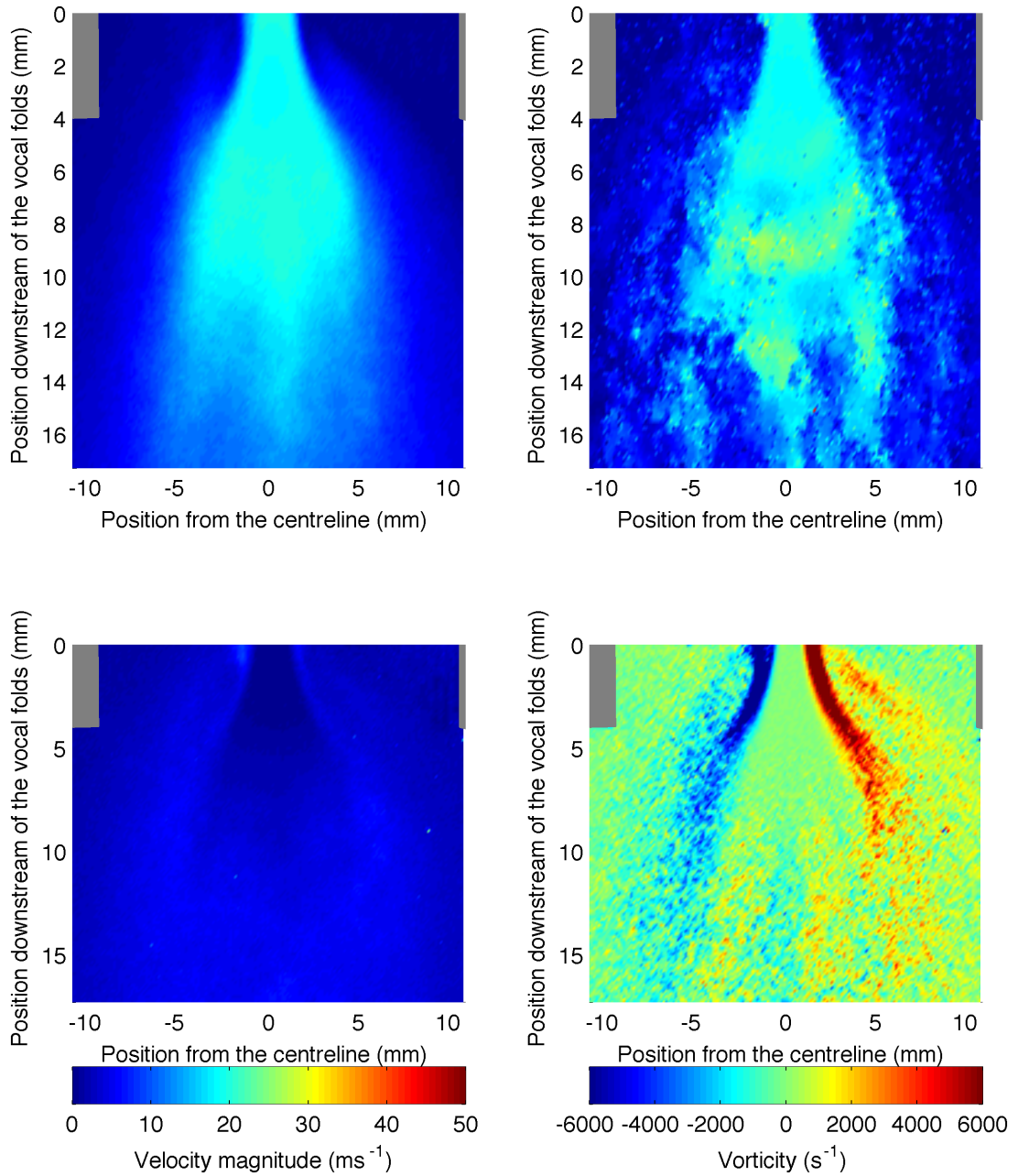


Figure 5.2: Ensemble-averaged velocity magnitude data (*top left*), standard deviation (*bottom left*), and vorticity (*bottom right*), together with an instantaneous velocity flow field (*top right*) from a static *in vitro* model of the human larynx with no vocal tract attached at subglottal pressure ($P_{sub} = 258 \text{ Pa}$).

5.3. RESULTS FOR THE *IN VITRO* MODEL IN THE FREE JET CONTROL CASE

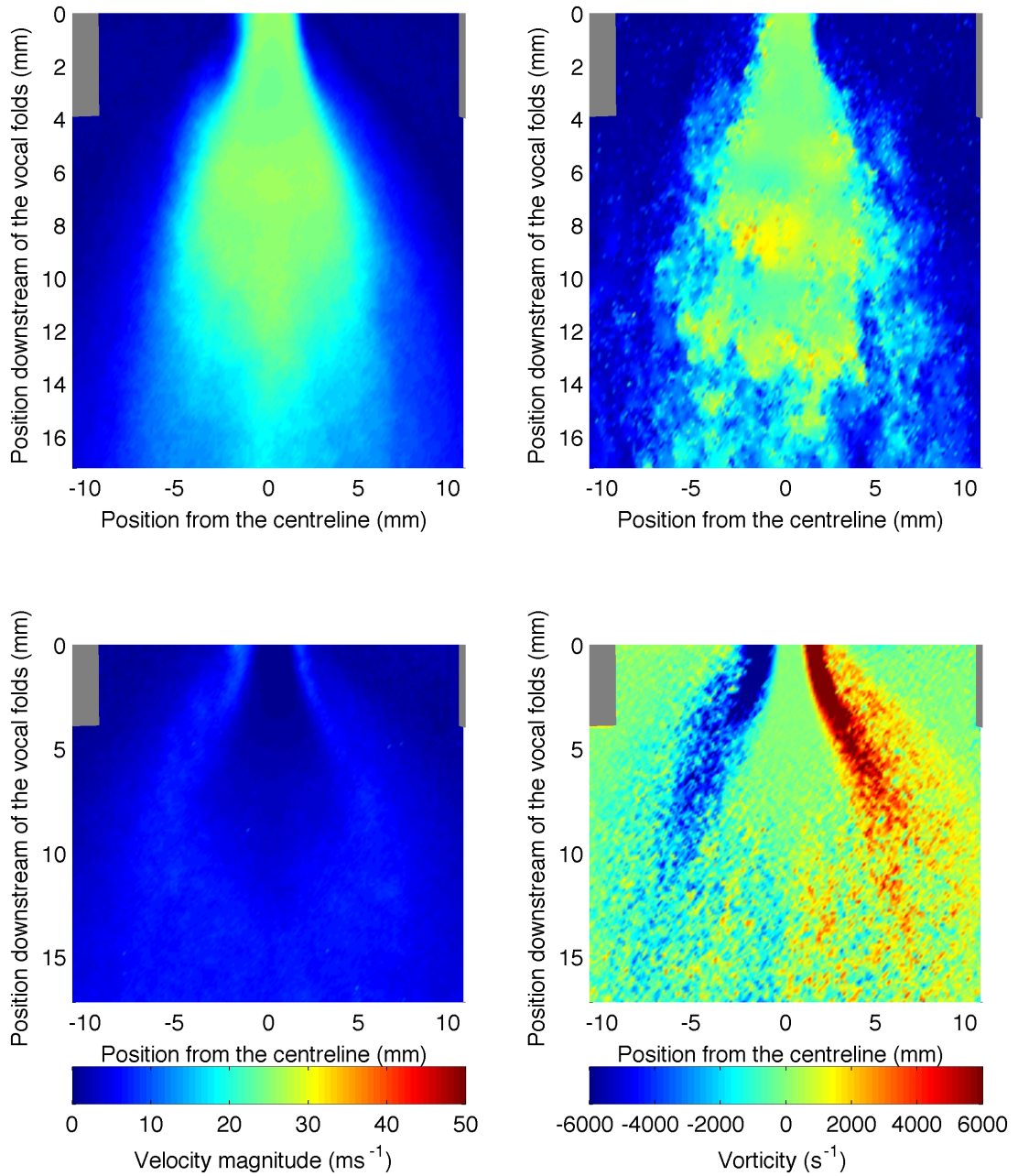


Figure 5.3: Ensemble-averaged velocity magnitude data (*top left*), standard deviation (*bottom left*), and vorticity (*bottom right*), together with an instantaneous velocity flow field (*top right*) from a static *in vitro* model of the human larynx with no vocal tract attached at subglottal pressure (P_{sub}) = 430 Pa.

5.3. RESULTS FOR THE *IN VITRO* MODEL IN THE FREE JET CONTROL CASE

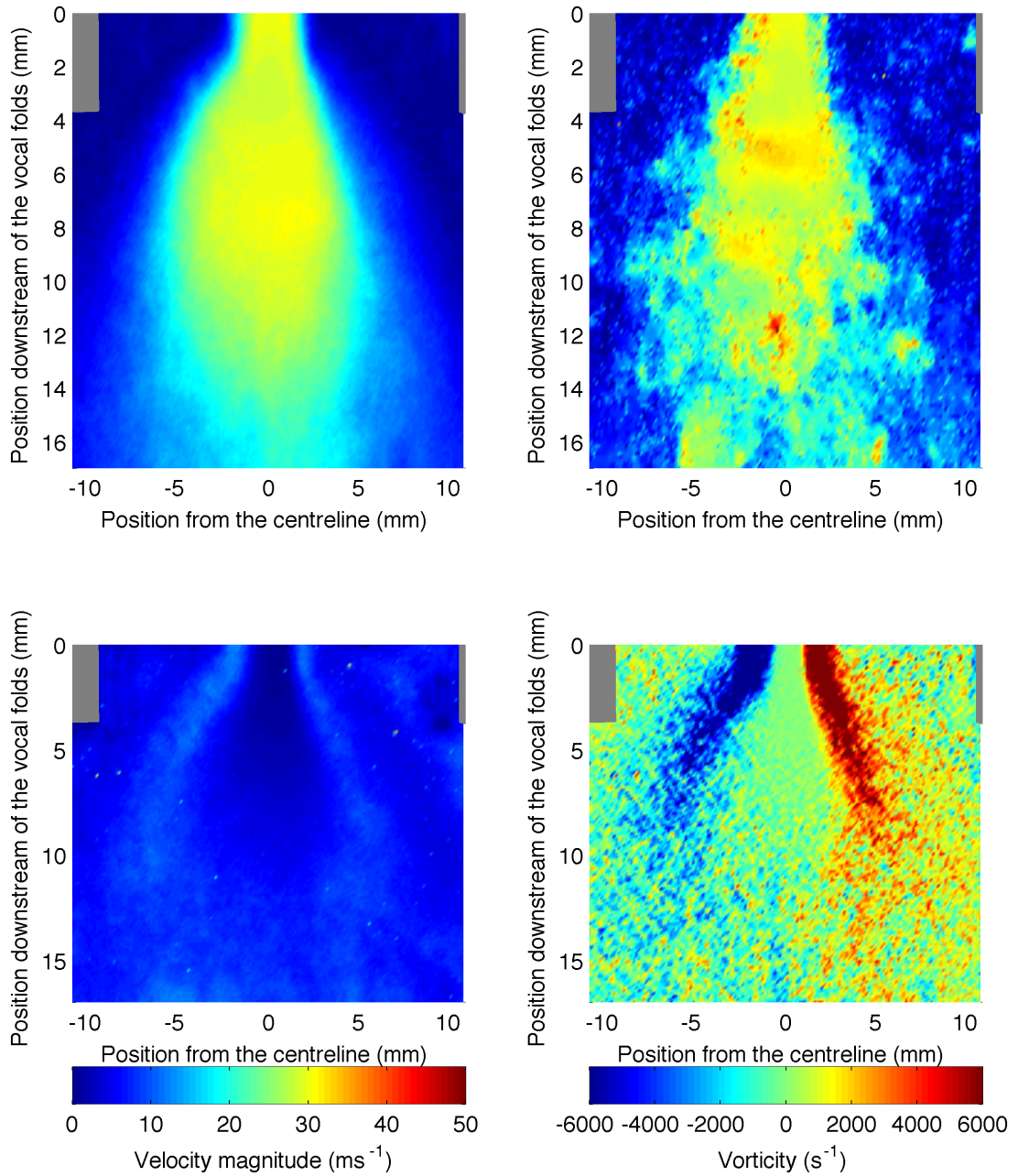


Figure 5.4: Ensemble-averaged velocity magnitude data (*top left*), standard deviation (*bottom left*), and vorticity (*bottom right*), together with an instantaneous velocity flow field (*top right*) from a static *in vitro* model of the human larynx with no vocal tract attached at subglottal pressure (P_{sub}) = 600 Pa.

5.3. RESULTS FOR THE *IN VITRO* MODEL IN THE FREE JET CONTROL CASE

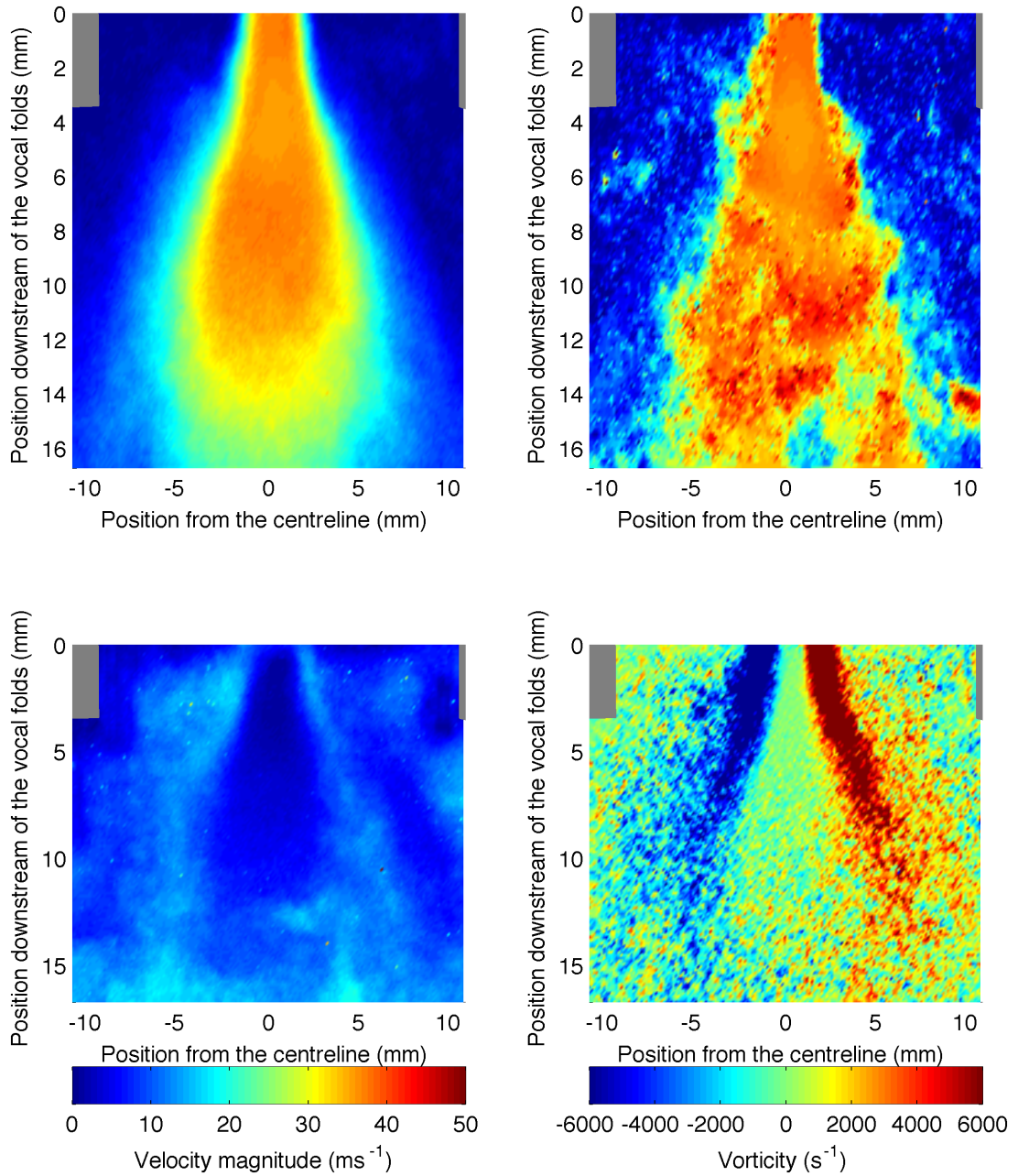


Figure 5.5: Ensemble-averaged velocity magnitude data (*top left*), standard deviation (*bottom left*), and vorticity (*bottom right*), together with an instantaneous velocity flow field (*top right*) from a static *in vitro* model of the human larynx with no vocal tract attached at subglottal pressure ($P_{sub} = 900 \text{ Pa}$).

5.3. RESULTS FOR THE *IN VITRO* MODEL IN THE FREE JET CONTROL CASE

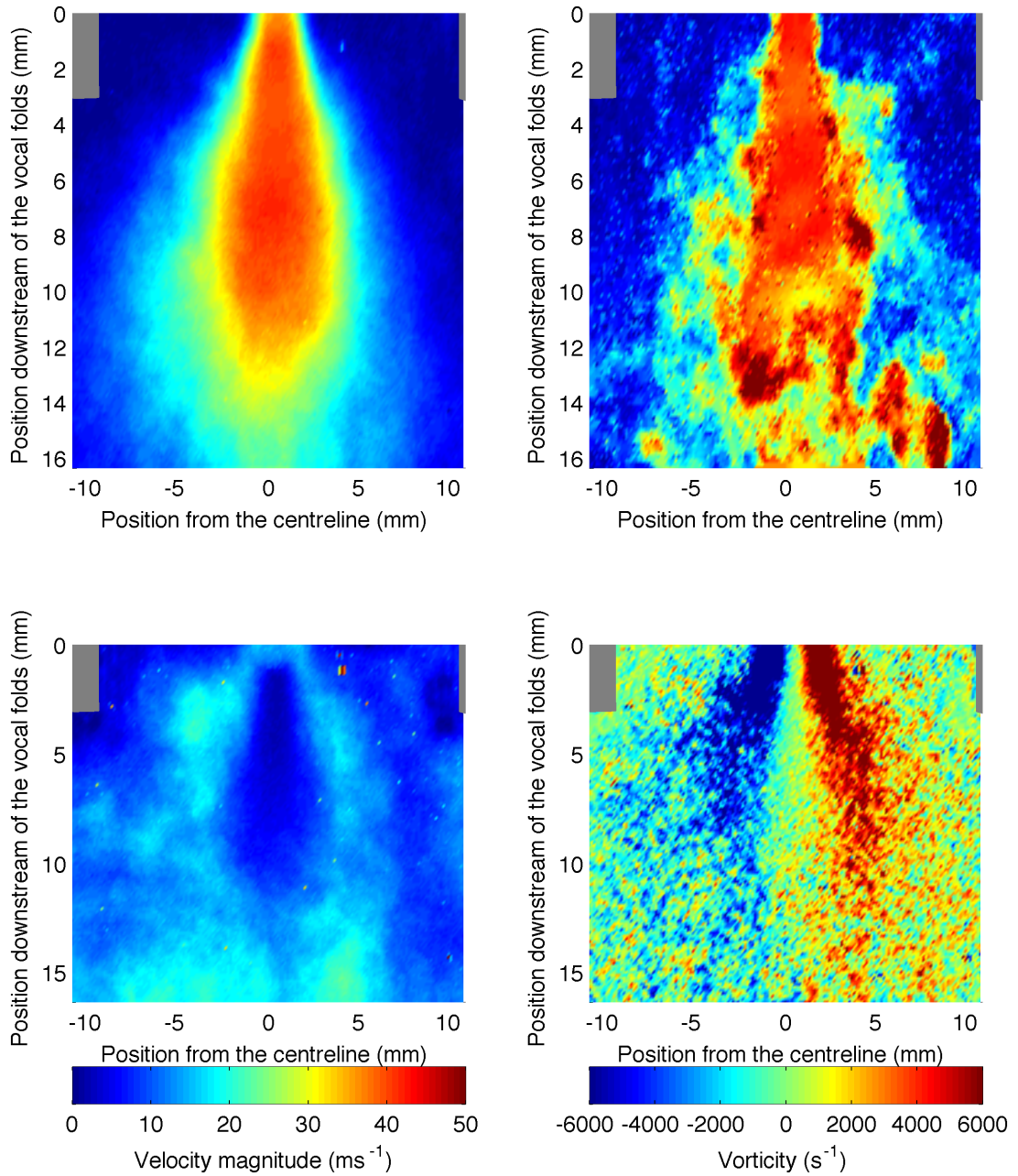


Figure 5.6: Ensemble-averaged velocity magnitude data (*top left*), standard deviation (*bottom left*), and vorticity (*bottom right*), together with an instantaneous velocity flow field (*top right*) from a static *in vitro* model of the human larynx with no vocal tract attached at subglottal pressure (P_{sub}) = 1100 Pa.

5.3. RESULTS FOR THE *IN VITRO* MODEL IN THE FREE JET CONTROL CASE

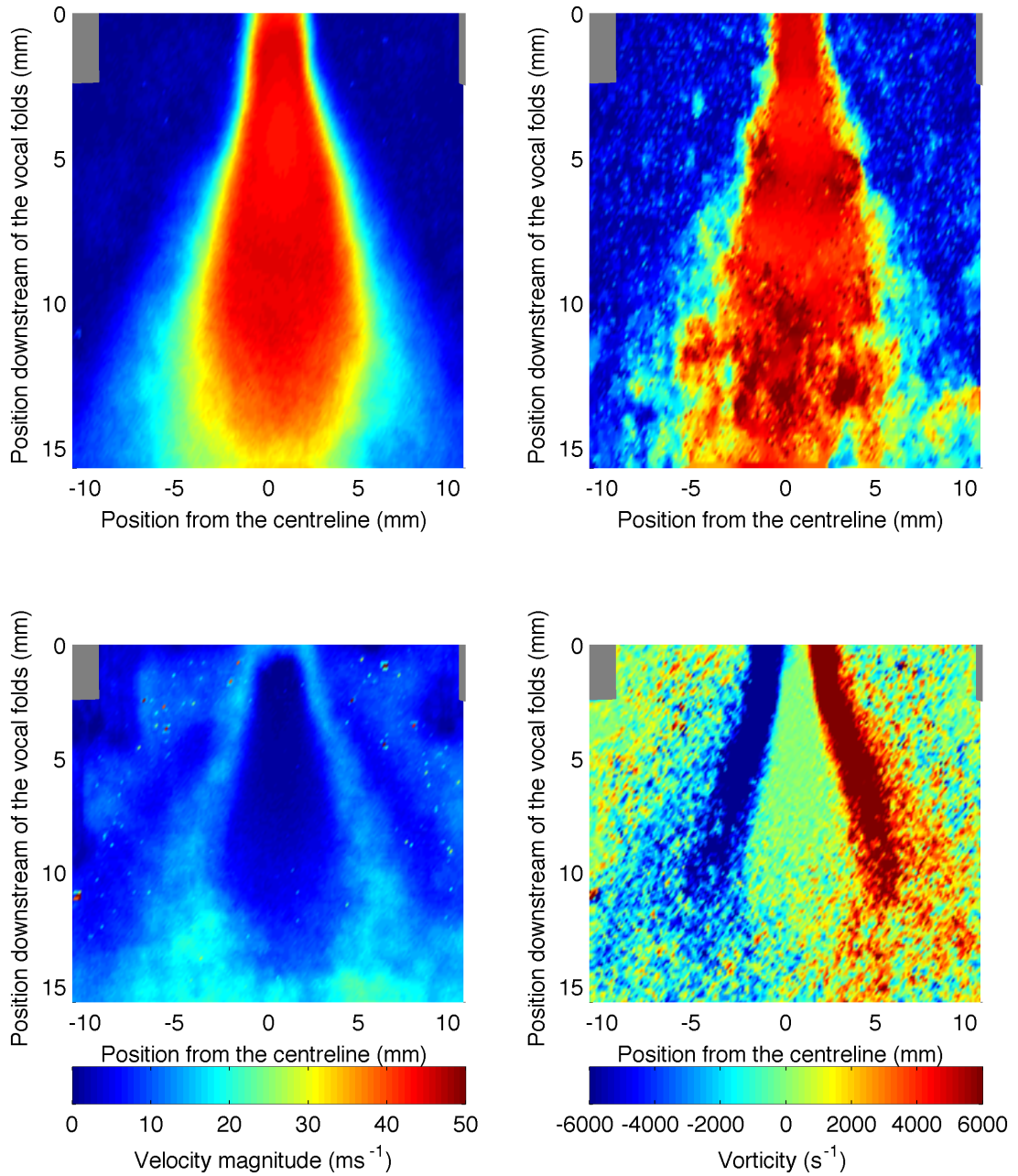


Figure 5.7: Ensemble-averaged velocity magnitude data (*top left*), standard deviation (*bottom left*), and vorticity (*bottom right*), together with an instantaneous velocity flow field (*top right*) from a static *in vitro* model of the human larynx with no vocal tract attached at subglottal pressure ($P_{sub} = 1300$ Pa).

5.3.1 Characterisation of the Jet

In all the velocity magnitude plots of the flow field data shown in Figures 5.2 - 5.7 a clearly distinguishable jet, emerging close to the centreline, is visible. As the velocity magnitudes presented are all ensemble averages, it is important to consider the deviation of the constituent flow fields from the mean presented. The standard deviation of the mean velocity magnitude for each subglottal pressure used in Figures 5.2 - 5.7 is present to the bottom left hand side of each figure. This is a very useful measure as it not only allows the laminar core and pre-turbulent region of the jet to be identified, but it also provides a detailed measure of the stability of the jet and how suitable the mean velocity magnitude is as a representation of the flow field.

The velocity magnitude standard deviation shows clearly that all the jets presented have a stable core with no evidence that either jet flapping or the Coandă effect are taking place. The velocity magnitudes of the jet cores are summarised in Table 5.1. As is to be expected, as the subglottal pressure is increased, the velocity magnitude of the jet core increases along with the values for the standard deviation of the velocity magnitude in the shear layers surrounding the jet core. An interesting observation made in Figure 5.6 is that the velocity magnitude of the jet core approximately between 0 and 1 mm downstream of the vocal folds appears to be lower than the velocity magnitude of the jet core further downstream. On inspection of the standard deviation of the velocity magnitude for this subglottal pressure, it is clear that there is a higher degree of fluctuation in the velocity magnitude in this region than further downstream. A possible explanation for this could be that a proportion of the seeding particles are flowing out of the light sheet plane, making cross-correlation of the image pair acquisitions difficult. It could also be due to the well-known difficulties associated with conducting PIV close to a physical boundary [Raffel 07, Kähler 12, van Hooff 12].

5.3.2 Jet Deflection and Centreline Calculation

An important aspect of glottal jet dynamics is whether or not the jet emerges directly from the vocal folds, whether it skews to one side, or whether it flaps from side to side. This particular aspect of glottal jet behaviour has been investigated in many studies for a considerable length of time ([Triep 05, Erath 06, Neubauer 07, Drechsel 08, Khosla 08b, Erath 10a, Triep 10, Mattheus 11, Zheng 11]), and is important because

5.3. RESULTS FOR THE *IN VITRO* MODEL IN THE FREE JET CONTROL CASE

interaction with the glottal jet provides only means by which the ventricular bands are caused to enter into a state of self-sustained oscillation. In order to consider the deflection of the jet, it is necessary to know the centreline of the jet and how its position changes across all the PIV flow field data maps for a particular model configuration. Drechsel and Thomson [Drechsel 08] present a useful algorithm by which the centreline can be calculated, based on a procedure first conceived by Erath and Plesniak [Erath 06]. A summary of this algorithm was presented in Section 4.4.4 and discussed in the previous chapter. Drechsel published the jet centreline calculation routine he created as a MATLAB script with Scott Thomson in his MSc thesis [Drechsel 07] and it has been used in this study; however, it has been heavily modified in order to function with pre-existing data structures. The method used to calculate the jet deflection angle using the calculated jet centreline is also described in Section 4.4.4. The jet centreline was calculated between between 1 mm and 17 mm downstream of the vocal folds.

Figure 5.8 shows histogram plots for the jet centrelines across all the subglottal pressures used in this configuration of the *in vitro* model. On the histograms, a positive jet centreline deflection angle represents a deflection of the centreline of that angle towards the right hand boundary of the velocity magnitude plot and similarly, a negative jet centreline deflection angle represents a deflection of the centreline of that angle towards the left hand boundary. As can be seen across these plots, all the jets have centrelines which most of the time have only small deflection angles of $\pm 5^\circ$. However, as the pressure is increased the number of jets with larger deflection angles increases indicating that as the pressure through the static *in vitro* model increases then the jet core flaps from side to side more often. This is to be expected as the increase in subglottal pressure for the same glottal aperture increases the jet flow speeds, thereby increasing the Reynolds number of the flow in the jet at the glottal opening indicating an increase in turbulence. This trend applies to all pressure used except 1300 Pa, where the number of jets with deflection angles greater or less than 0° decreases. An important observation from these results is that there is no adherence of the jet to any of the model boundaries (known as the Coandă effect). Furthermore, the jet in this configuration can be considered to be stable and broadly symmetrical about the centreline.

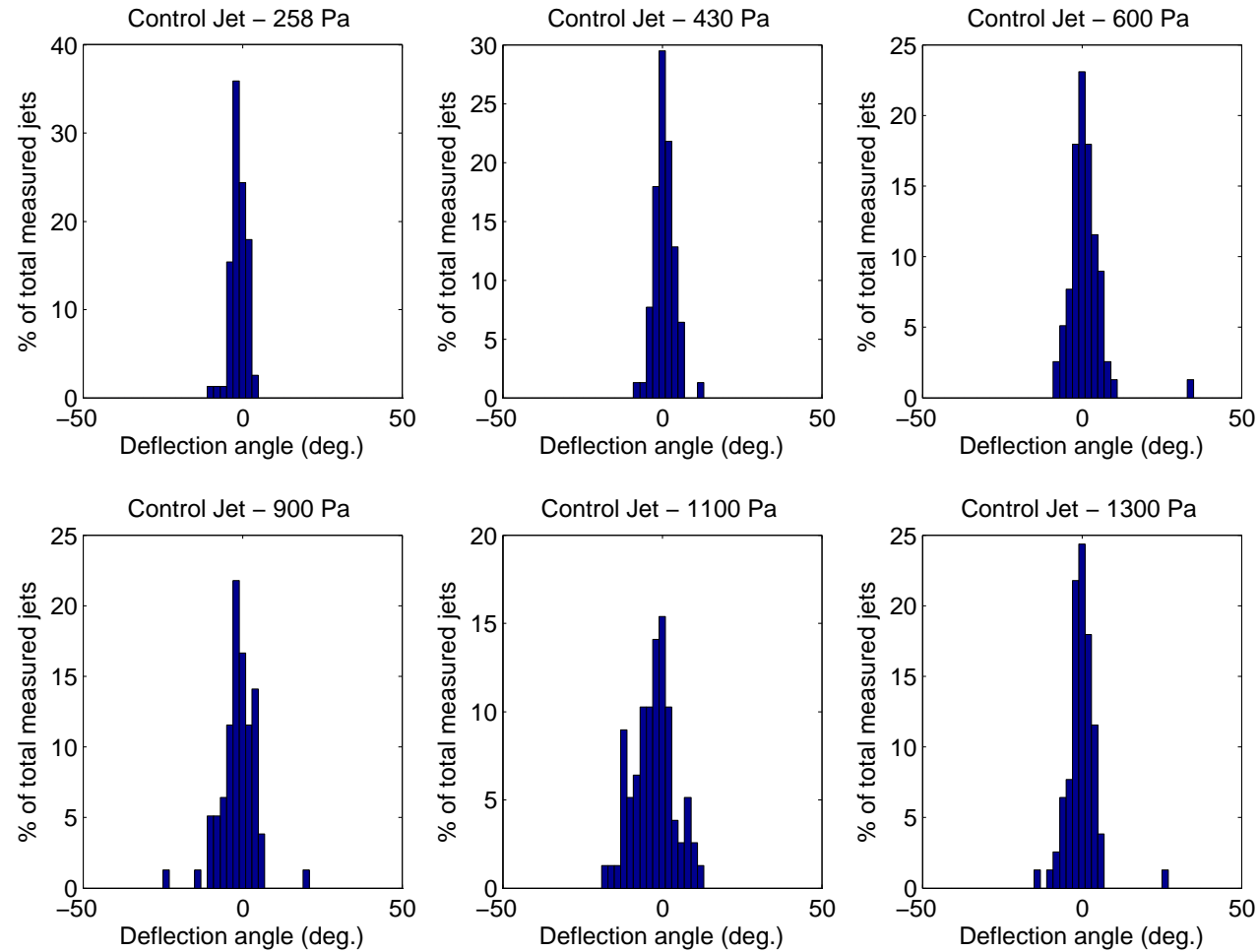


Figure 5.8: Histogram plots of the deflection angle of the centreline of the glottal jet across all subglottal pressures used for a static *in vitro* model of the human larynx with no vocal tract attached.

5.3.3 Expansion of the Jet

P_{sub} (Pa)	u_{core} (ms^{-1})	θ_{jet} ($^{\circ}$)	R^2
258	18 - 24	24.0	0.984
430	24 - 28	23.8	0.993
600	28 - 32	22.7	0.988
900	33 - 38	19.3	0.982
1100	38 - 44	20.0	0.985
1300	44 - 48	17.3	0.965

Table 5.1: Table showing the range of velocity magnitudes of the jet core (u_{core}), half-width expansion angles (θ_{jet}) of the jet, and the coefficient of determination for the line fitted (R^2) at 6 different subglottal pressures (P_{sub}) in PIV runs using a static *in vitro* model of the human larynx with no vocal tract attached.

In order to make comparisons between the static and oscillating configurations of the *in vitro* model, an important value to extract from the flow field data is the expansion angle of the jet. As in other studies of turbulent jets [Bakke 57, Sato 60, Mi 07, Murugappan 08, Krebs 12] the half-width expansion of the glottal jet is extracted and expressed as an angle in order to quantify the rate at which the jet expands as it leaves the glottis. The expansion angle of the glottal jet is calculated using the following procedure:

1. The angle is calculated by first extracting the width of the jet at half of the maximum velocity in the transverse streamwise direction,
2. a straight line is then fitted to this data and the angle of the line then measured relative to the position of the expansion along the jet centreline.
3. The final angle is expressed as half of the measured angle, as (conventionally) the jet is assumed to be axisymmetric.

The angles calculated from the flow field data are shown in Table 5.1 along with the value of the regression coefficient to show the closeness of the fitted straight line to the measured data.

5.3. RESULTS FOR THE *IN VITRO* MODEL IN THE FREE JET CONTROL CASE

The jet expansion angle was measured between 1 mm and 8 mm downstream of the vocal folds as the jet is not found to expand beyond 8 mm and begins to break down as it enters the pre-turbulent region, with the shear layers increasing in size. The jet expansion angle is seen to decrease as the subglottal pressure increases. An important observation in the context of this study is that the values for the angle of the half-width jet expansion are considerably larger than the 4° quoted by Kundu [Kundu 02] and subsequently proposed by Bailly in her turbulent jet expansion hypothesis [Bailly 08]. On examination of other literature, it appears that 4° is considerably lower than that expected. An example is the study by Mongeau *et al.* [Mongeau 97] which showed that the expansion angle was 13° from a small orifice.

Finally, an interesting feature in almost all of the glottal jets is an area of reduced velocity at the centre of the jet, just at the point where the jet begins to expand more rapidly. This is most clearly visible in Figure 5.5 between 4 and 6 mm downstream of the vocal folds. A reason for this might be that there is significant out-of-plane motion due to the nature of the glottal opening indicative of three-dimensional movement which will be considered later (see Chapter 6). Furthermore, asymmetries in the shear layers of the jets could be due to asymmetric flow separation caused by slight imperfections in the *in vitro* model.

5.3.4 Dimensional Analysis

One of the overall aims of this study is to consider the effect of the ventricular bands on the dynamics of the glottal jet in an *in vitro* model of the vocal folds. As seen in Section 2.3, many different models of the human larynx with varying dimensions and properties have been used to study the physical phenomena surrounding its operation. Indeed, even two of the models used in this study, manufactured on two different days, will not be identical, nor will they behave in exactly the same way. In order to make a meaningful comparison between glottal jet behaviour in different *in vitro* models or the same model with different downstream configurations it is necessary to express the measured variables concerned with the jet non-dimensionally. This is accepted standard practice in experimental fluid mechanics studies and allows for comparisons to be made not only between models used in this study but models used in other studies also. Finally, in addition to the variables already considered dimensional analysis provides a set of measures through which it might be possible to identify further

5.3. RESULTS FOR THE *IN VITRO* MODEL IN THE FREE JET CONTROL CASE

relationships between the dynamics of the glottal jet in different configurations.

Dimensional analysis is applied to all PIV velocity flow field data maps in this study, except where three-dimensional effects are considered (*in vitro* model is rotated by 90°). In the current configuration, where the vocal folds are static with no vocal tract attached, performing dimensional analysis on this control case allows for a comparison to be made between the case where the flow through the *in vitro* model is steady and the cases where the flow is pulsatile, or where there are inertial effects due to vocal fold self-oscillation. This is an important step in the analysis, as many studies of the human larynx have used models with static vocal folds (*viz.* Section 2.3.2) and identifying the differences in glottal jet dynamics between the cases with and without vocal fold self-oscillation highlights the importance of using self-oscillating models and the significance of conclusions formed using models with static vocal folds.

In Figure 5.9 are parametric non-dimensionalised flow parameter plots considering changes in turbulence, velocity, Reynolds number, and flow resistance across all subglottal pressures for the current configuration of the *in vitro* model. All of the non-dimensional values shown were calculated using the methods and principles detailed in Section 4.4.5. The results are expressed parametrically so that two parameters can be plotted together and the relationship between them more easily discerned. It can be seen that the jet core turbulence (T_{core}) appears to be consistent across the different subglottal pressures used; however, at 1300 Pa this value decreases significantly, which is also mirrored in the plot where jet core turbulence is plotted against Reynolds number. The Reynolds numbers for this setup varied from 1737 Pa to 3956 Pa, which considering the values for laminar and turbulent flow in [Webber 68, Holman 86] places this flow almost entirely within the transition region.

The normalised jet core velocity (u_{norm}) when plotted against the subglottal pressure produces a reasonably consistent value, rising steadily between 258 and 1100 Pa with u_{norm} at 1300 Pa returning approximately to the value it was when $P_{sub} = 900$ Pa. An explanation for this may be that using this subglottal pressure causes the vocal folds to be forced outwards and hence changes the point at which the flow separates within the glottis. Finally, when the calculated resistance to the flow within the jet core (Z_{core}) is plotted against the subglottal pressure the flow resistance remains around 2.5×10^7 ; however, there is a significant increase at 1300 Pa where a pronounced change is also seen in the other three plots in that figure.

5.3. RESULTS FOR THE *IN VITRO* MODEL IN THE FREE JET CONTROL CASE

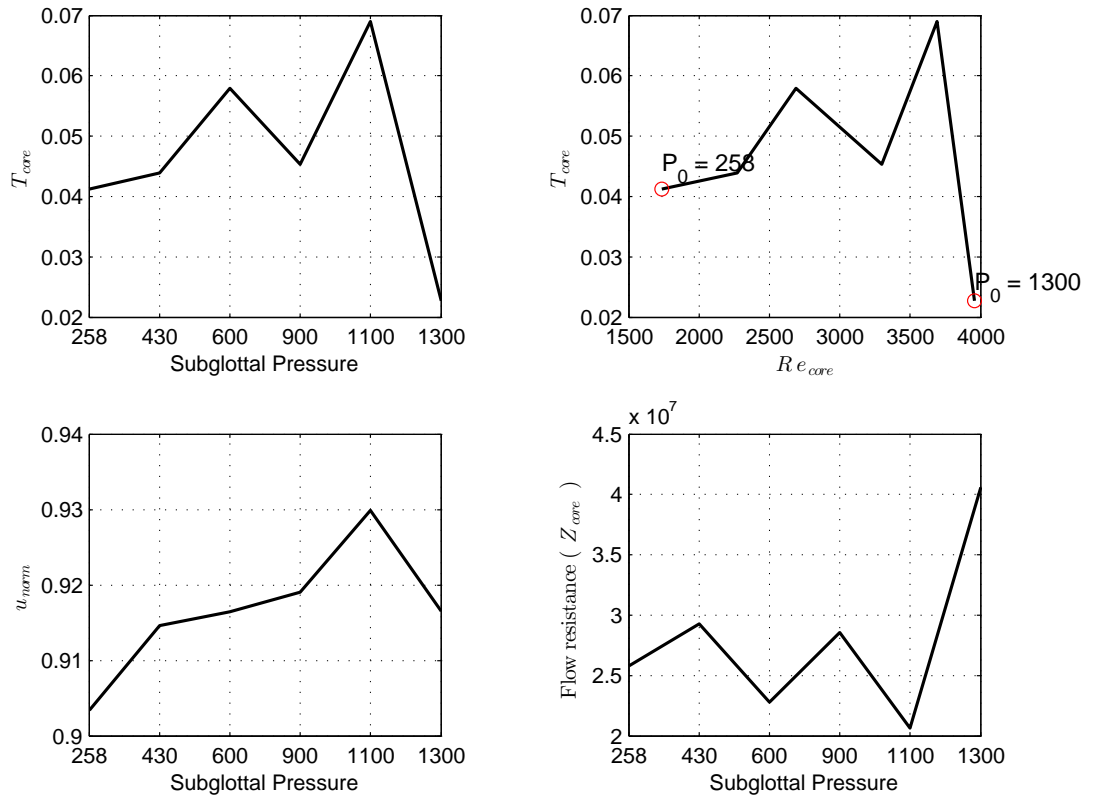


Figure 5.9: Parametric non-dimensionalised flow parameter plots showing the jet core turbulence (T_{core}), normalised jet core velocity (u_{norm}), and jet flow resistance (Z_{core}) against either subglottal pressure or jet core Reynolds number (Re_{core}) across all subglottal pressures used for a static *in vitro* model of the human larynx with no vocal tract attached.

5.4. RESULTS OF EXPERIMENTS UNDERTAKEN PRIOR TO SELF-SUSTAINED OSCILLATION

5.3.5 Summary

In this section the data for the *in vitro* model in the free jet control case has been plotted and analysed. One of the most important points to be highlighted here is that the expansion angle of the glottal jet in this case is significantly larger than that proposed by Kundu [Kundu 02] and subsequently used by Bailly [Bailly 08, Bailly 09]. It was also shown that the expansion angle reduces as the subglottal pressure (and hence the jet core velocity) increased. For all subglottal pressures used with this configuration the glottal jet core, shear layers, and pre-turbulent regions were all clearly visible. However, the results for the subglottal pressure of 1300 Pa are significantly different to the other results and, as such, are not included in any overall trends observed.

5.4 Results of Experiments Undertaken Prior to Self-Sustained Oscillation

As introduced and discussed in Section 2.2, the ventricular bands are complex, soft tissue structures found a short distance above the vocal folds. The close proximity of the ventricular bands to the vocal folds means that it is not possible to consider their presence completely without consequence to the dynamics taking place within the larynx. Indeed, the ventricular bands have been observed playing an important role in specific singing styles [Agarwal 04, Henrich 06b] and in voice pathologies [Nasri 96], so it is fitting that their impact on both the glottal jet and the vocal fold oscillation is investigated. In the remaining sections of this chapter, the effects of ventricular band-like structures in both an experimental self-oscillating *in vitro* model of the human larynx (*viz.* Section 3.4) and a computational simplified physical model are considered and contrasted. In order to make comparisons between the two models, results from mechanical response measurements using the *in vitro* model are presented.

Finally, in order to understand the way in which the vocal folds in the *in vitro* models of the larynx oscillate during self-sustained oscillation and their initial conditions before oscillation an analysis of high-speed camera footage is presented, in particular highlighting ‘bowing’ of the vocal folds in the model. This analysis produces an initial open area of the vocal folds which is used in the computational physical model.

5.4. RESULTS OF EXPERIMENTS UNDERTAKEN PRIOR TO SELF-SUSTAINED OSCILLATION

	Without Flow		With Flow	
	Peak 1	Peak 2	Peak 1	Peak 2
Frequency (Hz)	160.00	181.20	163.10	185.40
Amplitude	0.15	0.09	0.19	0.33
Quality Factor	13.8	12.7	11.2	19.4

Table 5.2: Table containing the amplitude, frequency, and quality factor values extracted from mechanical response plots in Figure 5.10.

5.4.1 Mechanical Response for the *in vitro* Model

As discussed in Section 3.5, the mechanical response of the vocal folds in the *in vitro* model of the human larynx is an important measure from which key parameters used in the computational physical model can be extracted. The mechanical response also provides information on the oscillating characteristics of vocal folds. In Figure 5.10, two different mechanical responses for the same model with and without a glottal flow are presented. As can be seen amongst Cullen’s results [Cullen 00b], the presence of a subcritical (one where self-oscillation of the vocal folds does not occur) subglottal pressure causes the heights of the resonance peaks to significantly increase and the resonance frequencies to shift slightly. The extent to which this takes place is shown in Table 5.2, with the most noticeable change evident in the amplitude of peak 2.

The reason for the difference between the mechanical responses in these 2 cases is that the presence of a subglottal flow causes a change in the point of static equilibrium for vocal folds. Therefore, the presence of the overflow will mean will mean the vocal folds will be more easily driven into forced oscillation. Hence, aerodynamic effects are taken into account by the mechanical response as well as the characterisation of the vocal folds in this case, and so the case without a glottal flow is acknowledge as providing the best characterisation of the vocal folds.

The general shape of the mechanical responses are similar to those published in [Cullen 00a, Lucero 12], however, they are remarkably different to those published in [Ruty 07a, Ruty 07b, Cisonni 08a]. The most likely explanation for this is that the method by which Ruty and Cisonni calculate their mechanical response is different from that described earlier in Section 3.5.

Using the mechanical response without a glottal flow from Figure 5.10 and fitting

5.4. RESULTS OF EXPERIMENTS UNDERTAKEN PRIOR TO SELF-SUSTAINED OSCILLATION

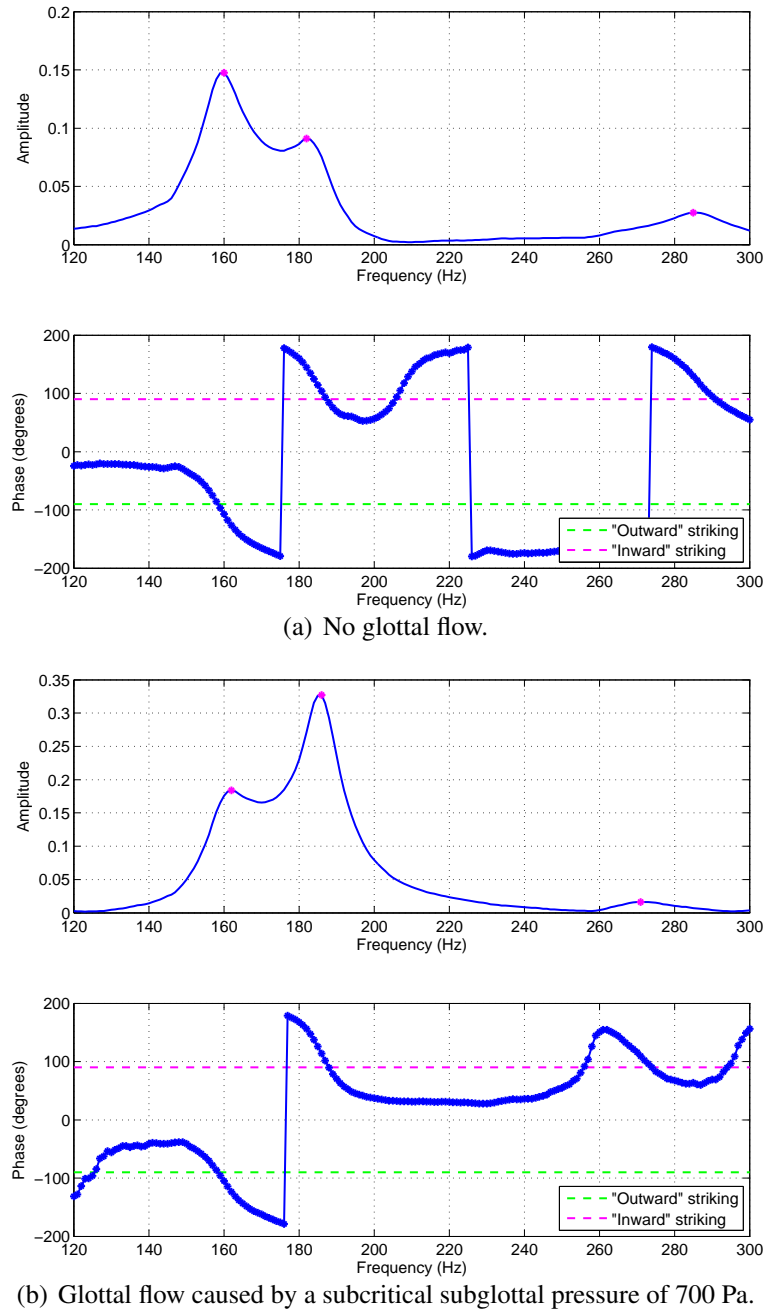


Figure 5.10: Plots showing the mechanical response for a self-oscillating *in vitro* model of the human larynx with no ventricular bands highlighting the change caused by the presence of a flow. The upper plot in each subfigure shows the calibrated amplitude against frequency and the lower plot shows the phase difference between the opening of the vocal folds and the acoustic driving signal. The purple asterisks indicate detected resonance peak frequencies.

5.4. RESULTS OF EXPERIMENTS UNDERTAKEN PRIOR TO SELF-SUSTAINED OSCILLATION

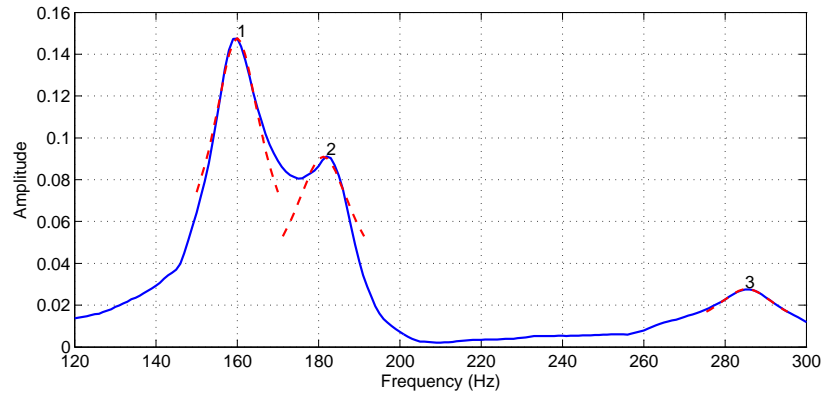


Figure 5.11: Plot showing the mechanical response for a self-oscillating *in vitro* model of the human larynx with no ventricular bands. The red lines indicate the fitted resonance functions from which the quality factors (Q_0) are extracted, and the numbers relate to the detected peak numbers.

Equation 3.27 to resonance peaks in the amplitude, as shown in Figure 5.11 it was possible to extract the quality factor for these resonances. The calculated values for both the case with and without a glottal flow are shown in Table 5.2, however, for reasons discussed earlier only the frequencies and quality factors for the case without a glottal flow are used as input parameters to the computational physical model. The quality factors are used to calculate the damping coefficients and the frequencies to calculate the spring constants as described in Section 3.7.

As the PIV velocity flow field data presented in this thesis were all acquired on the same day, there is no need to present several mechanical response curves for the *in vitro* model. However, a systematic study of the degree to which the mechanical response for this type of model changes on daily basis has been undertaken, the results of which will be presented at a later stage.

5.4.2 ‘Bowing’ and the Impact of Initial Observations

Some important measures afforded through using the high-speed camera setup detailed in Section 3.6, are the open area and open height of the glottis in the *in vitro* model of the larynx. Using the technique detailed in Section 3.6.2 it is possible to process high-speed images of the glottis and quantify the open area and open height at defined points whilst the vocal folds are both stationary and whilst they are in motion. As

5.4. RESULTS OF EXPERIMENTS UNDERTAKEN PRIOR TO SELF-SUSTAINED OSCILLATION

explained previously, recording the upstream acoustic signal and filming in high speed simultaneously makes it possible relate the upstream acoustic signal to the open area of the vocal folds, thereby permitting changes seen in the PIV flow field velocity data to be correlated with changes in the vocal fold open area or open height. Another method of calculating the open area is to use an expanded laser beam and calibrated linear photodiode as used in [Vilain 02, Ruty 07a, Ruty 07b, Cisonni 08a, Cisonni 11] relating the measured voltage to the open area. The problem with this approach is that it only provides the value for the open area; any open height value is calculated as the open area divided by the width of the glottis, assuming that the vocal folds open as a uniform rectangular orifice, which as can be seen in Figure 5.12 is certainly not the case.

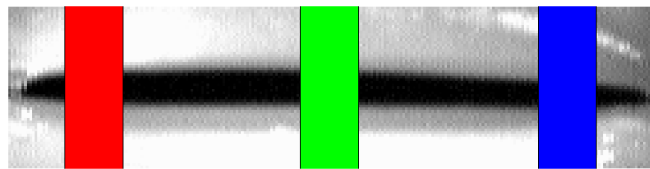


Figure 5.12: Image illustrating the lines of analysis in high-speed camera filming used to calculate the degree to which the *in vitro* model of the human larynx is bowed in its initial state and its initial opening.

By splitting the individual images from the high-speed camera horizontally into 11 equal parts, selecting three parts (as shown by the blue, green, and red coloured segments in Figure 5.12) and binarising these separate parts, it is possible to analyse how separate elements of the vocal folds oscillate in relation to each other. In order to measure the initial open height of the vocal folds before self-oscillation takes place, the centre (green) section was binarised, the open area calculated and then divided by the width of the section in pixels. As this process provided a value for each of the images used, the mean of these values was taken and produced a value of 1.38 mm. This initial opening was directly related to the tension applied and the seating of the superglue between the vocal fold block and the latex cover during the vocal fold manufacturing process. Unfortunately, despite a great number of attempts complete initial closure (or indeed an initial smaller closure) was not achievable.

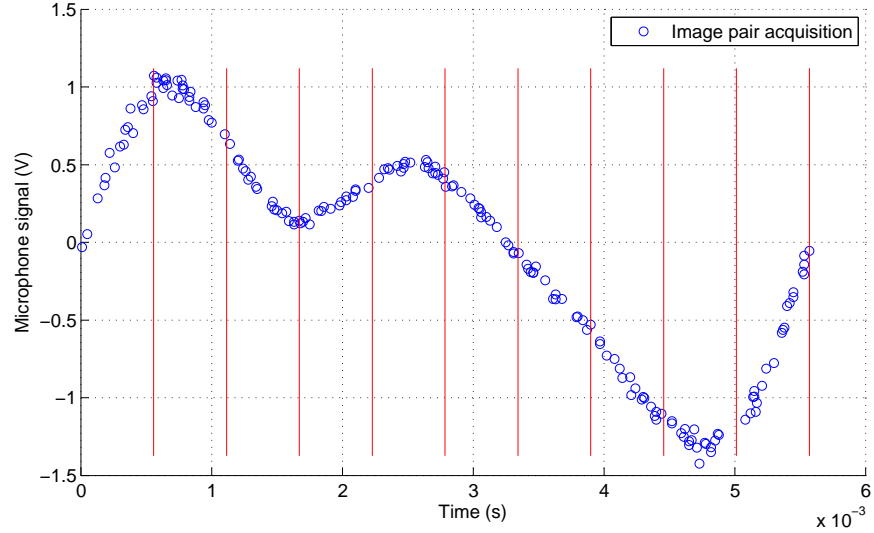
When considering the image of the vocal folds in Figure 5.12 it is clear that their initial state is not closed. Indeed, the vocal folds appear to bow outwards towards

the centre where the open height is greatest. In all the experiments conducted in this study the vocal folds did not close fully during phonation, thereby causing them to bow inwards towards the centre of the glottis when the glottal opening was at its minimum in the phonatory cycle. This behaviour is consistent with that observed in larynges of the elderly, as shown and described by Hagen *et al.* [Hagen 96]. A particular point of interest raised by Hagen *et al.* is that this vocal fold bowing (through the vocalis muscle losing mass and being replaced with fibrous tissue) causes the supraglottic structures in some patients to be engaged during phonation in order to compensate for an incomplete glottal closure. This behaviour is ascribed as an attempt of the patient to “reduce air-wasting associated with such a large glottic opening” [Hagen 96]. Whether or not the ventricular bands are engaged in this process is not clear, but the effect of the ventricular bands on the vocal folds for an incomplete glottal closure in an *in vitro* model is something which will be considered later in Sections 5.5.2 and 5.6.1.

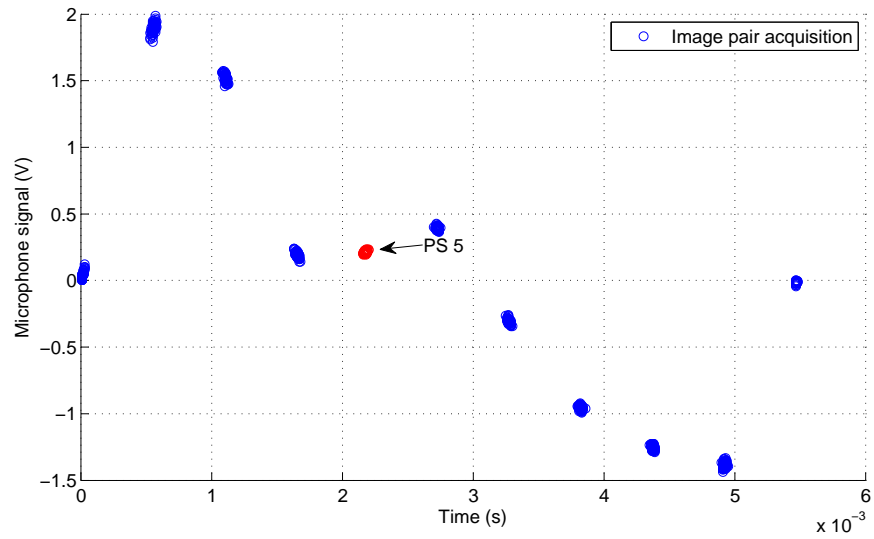
5.5 Results for the *in vitro* Model without Ventricular Bands

This section of the chapter considers results for the *in vitro* model without ventricular bands within the vocal tract and with PIV flow field velocity data extracted for the plane perpendicular to the glottal height abscissa. For results for the same model without ventricular bands in the plane parallel to the glottal height abscissa see Section 6.1. A study using a model which was close to the one used in this investigation is that of Krebs *et al.* [Krebs 12]. However, although some aspects of the models are similar there are distinct differences. One of these differences is that the *in vitro* model used in this study did not achieve full glottal closure. This had the effect of increasing the subglottal pressure required for self-oscillation compared with other studies [Bailly 09, Newton 09] using a model of a comparable size, but was less than the pressures used in [Krebs 12, Drechsel 07, Drechsel 08], where the vocal folds either had more mass or were made from a different material. Due to experimental limitations the subglottal pressure used in this study was chosen as the minimum possible pressure at which stable self-sustained oscillation of the vocal folds occurred across all the different configurations of the *in vitro* model.

5.5.1 Phase Stepping and Ensemble-Averaging



(a) Phase windowing technique.



(b) Phase stepping technique (image pair acquisitions at phase step 5 are highlighted in red)

Figure 5.13: Plots illustrating the image pair acquisition times aligned to the phonatory cycle using the phase windowing and phase stepping techniques for a self-oscillating *in vitro* model of the human larynx.

In order to synchronise the PIV image pair acquisitions with the required points in

5.5. RESULTS FOR THE *IN VITRO* MODEL WITHOUT VENTRICULAR BANDS

the phonatory cycle the phase stepping technique, as described in Section 4.3.3, was used. Image pair acquisitions made using the phase windowing method as detailed in [Newton 09] and those made using the phase stepping method are presented in Figure 5.13. The difference in the data sets between the two techniques shown in this figure is due to the data being taken from the model on different days. A comparison between these methods, first discussed in [Apostoli 10a], shows that the phase stepping technique provides a significant improvement over the phase windowing technique in the ability to achieve image pair acquisitions at a given point in the phonatory cycle of the vocal folds for an *in vitro* model of the human larynx. Data presented in [Apostoli 10a] shows that the phase stepping technique reduces the standard deviation for image pair acquisitions by an order of magnitude.

As the calculated velocity magnitude and standard deviation of ensemble-averaged data are used to establish the behaviour and stability of the glottal jet at defined points in the phonatory cycle, possessing the ability to make ensemble-averages of PIV flow field data at points which are significantly closer together in the phonatory cycle allows for a more definitive view on these aspects. For instance, if image pair acquisitions are taken at a number of points within a phase window the opening between the vocal folds could be a range of different values indicating that the glottal channel might hold a number of different shapes within the same window. Of course, the glottal channel shape has a direct impact on the jet which emerges and hence, should an ensemble average be made of the PIV velocity flow field data for points in this phase window, any increase in the standard deviation of the velocity magnitude could be misattributed to jet instability.

The phase step mean time and standard deviation in relation to the phonatory cycle are shown in Table 5.3. The rounded fundamental frequency (f_{rnd}) for this setup was 182 Hz, mean of f_0 was 182.87 Hz, and standard deviation of f_0 was 0.53 Hz. The pressure of water within the vocal folds P_{in} , which is kept constant (See Section 3.4) and is the same for the *in vitro* model with or without ventricular bands, is 2260 Pa. This value was chosen as it allowed the lowest possible subglottal pressure for self-sustained and stable oscillation and is comparable to the value used in [Bailly 09]. It was important that the subglottal pressure required for self-sustained oscillation was low due to the limitations of experimental equipment used. Comparison between the mean of f_0 for the model with and without ventricular bands at different separations

5.5. RESULTS FOR THE *IN VITRO* MODEL WITHOUT VENTRICULAR BANDS

Phase Step	Mean (secs)	Standard Deviation (secs)
1	1.00×10^{-5}	1.12×10^{-5}
2	5.57×10^{-4}	1.15×10^{-5}
3	1.11×10^{-3}	9.68×10^{-6}
4	1.66×10^{-3}	1.05×10^{-5}
5	2.18×10^{-3}	9.22×10^{-6}
6	2.73×10^{-3}	8.84×10^{-6}
7	3.27×10^{-3}	9.49×10^{-6}
8	3.83×10^{-3}	1.00×10^{-5}
9	4.37×10^{-3}	9.07×10^{-6}
10	4.92×10^{-3}	9.87×10^{-6}

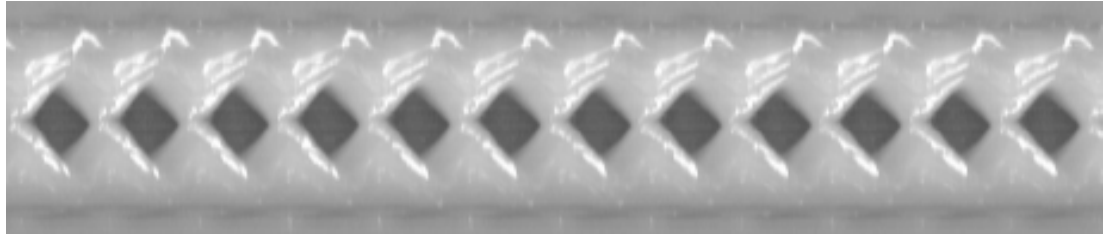
Table 5.3: Table showing the mean and standard deviation of image pair acquisition times for each phase step in PIV runs using an *in vitro* model of the human larynx with no ventricular bands.

will illustrate changes in vocal fold oscillation caused by the presence of the ventricular bands and differences in the standard deviation of f_0 could indicate changes in the stability of the oscillation.

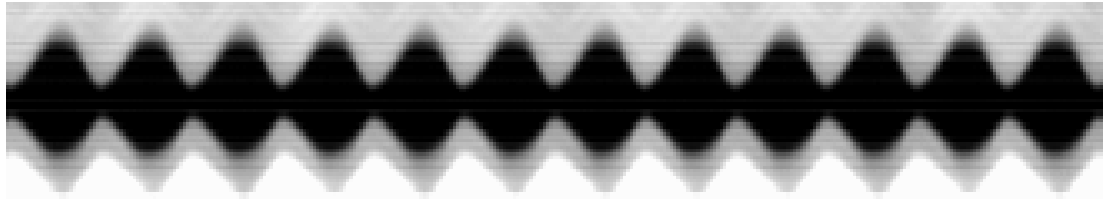
5.5.2 Vocal Fold Open Height through High-Speed Camera Analysis

Using images from the high-speed camera when PIV is not undertaken, it is possible to extract a single line of pixels from each image and create a kymograph. Initially defined and discussed in Section 3.6, kymographs are a standard diagnostic tool in the clinical environment and allow for a direct comparison to be made between vocal fold oscillation *in vivo* and within experimental *in vitro* models. In Figure 5.14 are shown two kymographs, the upper one is taken *in vivo* and has been kindly provided by Nathalie Henrich from her work and the lower one is taken from the *in vitro* model without ventricular bands. Although the *in vivo* kymograph shows full closure of the vocal folds and *in vitro* one does not, there are similarities between the shapes of the opening for both. A noticeable difference is that the opening gradient (from the point of minimum to maximum opening) in the *in vivo* kymograph is steeper than the closing

5.5. RESULTS FOR THE *IN VITRO* MODEL WITHOUT VENTRICULAR BANDS



(a) *in vivo* (from N. Henrich)



(b) *in vitro* model of the human larynx without ventricular bands

Figure 5.14: Several kymographs taken either *in vivo* or from an *in vitro* model of the human larynx without ventricular bands.

gradient, whereas the reverse is true for the *in vitro* model kymograph. A similarity however, is a slight asymmetry in the opening between the two vocal folds which can be seen in the kymographs for both the *in vivo* and *in vitro* models.

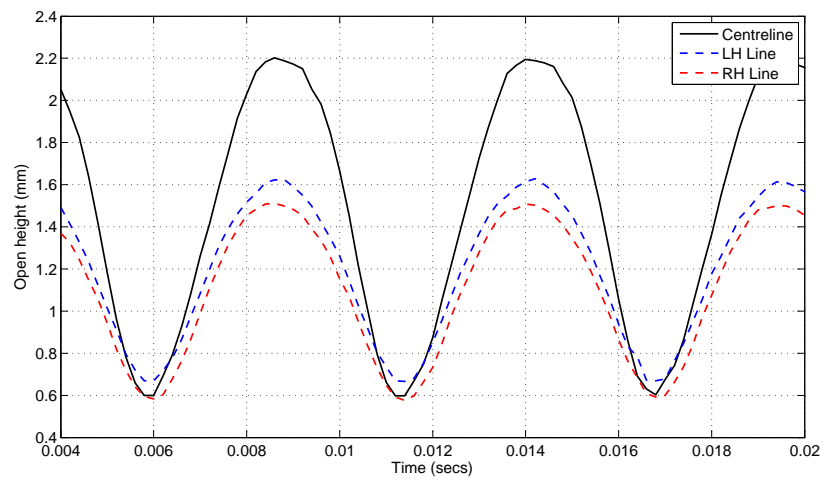


Figure 5.15: Plot showing the measured open height of the vocal folds in the centre and at two lines either side equidistant to the centreline for an *in vitro* model without ventricular bands.

5.5. RESULTS FOR THE *IN VITRO* MODEL WITHOUT VENTRICULAR BANDS

	$\overline{h_{min}}$ (mm)	$\overline{h_{max}}$ (mm)
LH line	0.67	1.61
Centre line	0.60	2.18
RH line	0.59	1.50

Table 5.4: Table containing the mean minimum ($\overline{h_{min}}$) and maximum ($\overline{h_{max}}$) open heights for the left hand, centre, and right hand lines of analysis for an *in vitro* model without ventricular bands.

Through the analysis of 3 separate elements of the vocal folds using the technique outlined in Section 5.4.2, it is possible to see whether a phase difference exists between the oscillation of different elements of the vocal folds. In addition, it is possible to observe whether inward bowing of the vocal folds takes place at the point of minimum opening. Figure 5.15 shows the measured open height for 3 equidistant elements of the vocal folds. As there appears to be no phase difference between the open height of the 3 elements then no ‘zipping’ motion, observed for some laryngeal mechanisms [Roubeau 09], is taking place. Finally, as the minimum centreline opening values do not fall below the minimum opening values for the 2 other elements, no inward bowing of the vocal folds is observed. The measured values for the maximum and minimum openings of the 3 elements analysed are summarised in Table 5.4.

5.5.3 Characterisation of the Jet

Figures 5.16 and 5.17 show the velocity magnitude for ensemble-averaged PIV flow field velocity data for phase steps 1-10 for an *in vitro* model of the larynx without ventricular bands. The corresponding standard deviation of the ensemble-averaged velocity magnitude is shown in Figures 5.18 and 5.19. As can be seen from the vocal fold centreline open height in the bottom right hand corner in all these figures, phase steps 1 - 5 (shown in Figures 5.16 and 5.18) represent the opening phase of the phonatory cycle and phase steps 6 - 10 (shown in Figures 5.17 and 5.19) represent the closing phase. The greyed out area represents the walls of the vocal tract which can be seen. Considering the velocity magnitude data in Figures 5.16 and 5.17, a clear and discernible jet is shown for phase steps 2 - 9 emerging close to the centreline. A possible reason for there being no clear jet in phase steps 1 and 10 could be due to

5.5. RESULTS FOR THE *IN VITRO* MODEL WITHOUT VENTRICULAR BANDS

significant three-dimensional motion of the jet causing significant out-of-plane motion of the seeding particulate. The standard deviation of the velocity magnitude shows that the jet has a stable laminar core with clear shear layers and pre-turbulent region. Confirmation of the irrotational laminar core and the presence and thickness of the jet shear layers can be seen in ensemble-averaged vorticity plots in Figures 5.20 and 5.21.

Considering the jets from phase steps 2 - 9 in Figures 5.16 and 5.17, the glottal jet core appears to extend furthest downstream from the vocal folds at phase step 3 and then recedes slightly during phase steps 4 and 5 as the glottal opening reaches its maximum. A reason for the glottal jet core reaching a maximum downstream displacement at this point could be that the pressure build-up behind the vocal folds whilst the folds are at a minimum open height as well as forcing the vocal folds apart might also be responsible for the long thin jet shown in phase step 3. When comparing the glottal jet between phase steps and assessing the stability of the jet using the standard deviation of the ensemble-averaged velocity magnitude it is important to bear in mind that the glottal jet may change more in one phase step than another. For instance, regardless of any advantage associated with using phase steps over phase windows, the range of values for the glottal opening in phase step 3 is likely to be greater than that in phase step 5, owing to the shallower gradient at this point.

In the closing phase (phase steps 6 and 9) the glottal jet core recedes yet further, with the velocity magnitude within the glottal jet increasing as the phase step number progresses. This results in an asymmetry in the glottal jet during oscillation. This observation is commensurate with observations made in [Newton 09]; however, Newton makes no attribution as to the cause for this observation. A possible reason might be that during the closing phase with the vocal folds are drawn together by Bernoulli's force and inertial forces. As the glottal opening reduces the velocity magnitude of the jet increases thereby reducing the pressure between the vocal folds and further increasing the effect of the Bernoulli force. This results in a maximum velocity magnitude value seen at phase step 9. The velocity magnitude asymmetry may also be due to the opening asymmetry seen in the kymograph for the model discussed earlier.

Phase steps 1 and 10 have been observed as not having clear glottal jets and occurring at the minimum glottal opening. As Newton identifies [Newton 09], with these phase steps having standard deviation values which are comparable to the

5.5. RESULTS FOR THE *IN VITRO* MODEL WITHOUT VENTRICULAR BANDS

velocity magnitude values (if not greater) it is an indicator that the jet in these phase steps is fully turbulent and undergoing rapid disintegration. Considering the glottal jet in phase steps 4 - 8, a noticeable contoured drop is visible in the velocity magnitude centred around 3 mm downstream of the vocal folds. This drop in velocity magnitude can be considered a stable feature of glottal jet as there is no increase in the standard deviation of the velocity magnitude in the area over which the drop takes place. A reason for this drop could be that the jet undergoes a change (either a significant expansion or contraction) in another plane which causes some of the seeding particulate to be affected by this change. As the PIV flow field data presented here is taken for a single plane, if the seeding particulate is influenced by a change in another plane, the nature of this change will only be visible when PIV is undertaken in that plane.

Finally, looking at the graph of the vocal folds open height, it is clear from this plot that the open heights at phase steps 2 and 9 are almost the same. In the same way, phase steps 3 and 8 also appear at very similar vocal fold open heights. However, regardless of these similarities the jets shown in phase steps 2 and 9 and those shown in 3 and 8 are in fact quite different. For instance, jets in phase steps 8 and 9 are significantly wider than and have a different shape to those shown in phase steps 2 and 3. In addition, phase steps 8 and 9 have a more significant pre-turbulent region visible in the standard deviation of the velocity magnitude than the corresponding opening phase phase steps. Once again, Newton [Newton 09] attributes this to the jet's rapid deceleration and thereby reaffirms his general finding that the glottal jet exhibits a strong turbulent asymmetry between the opening and closing phases.

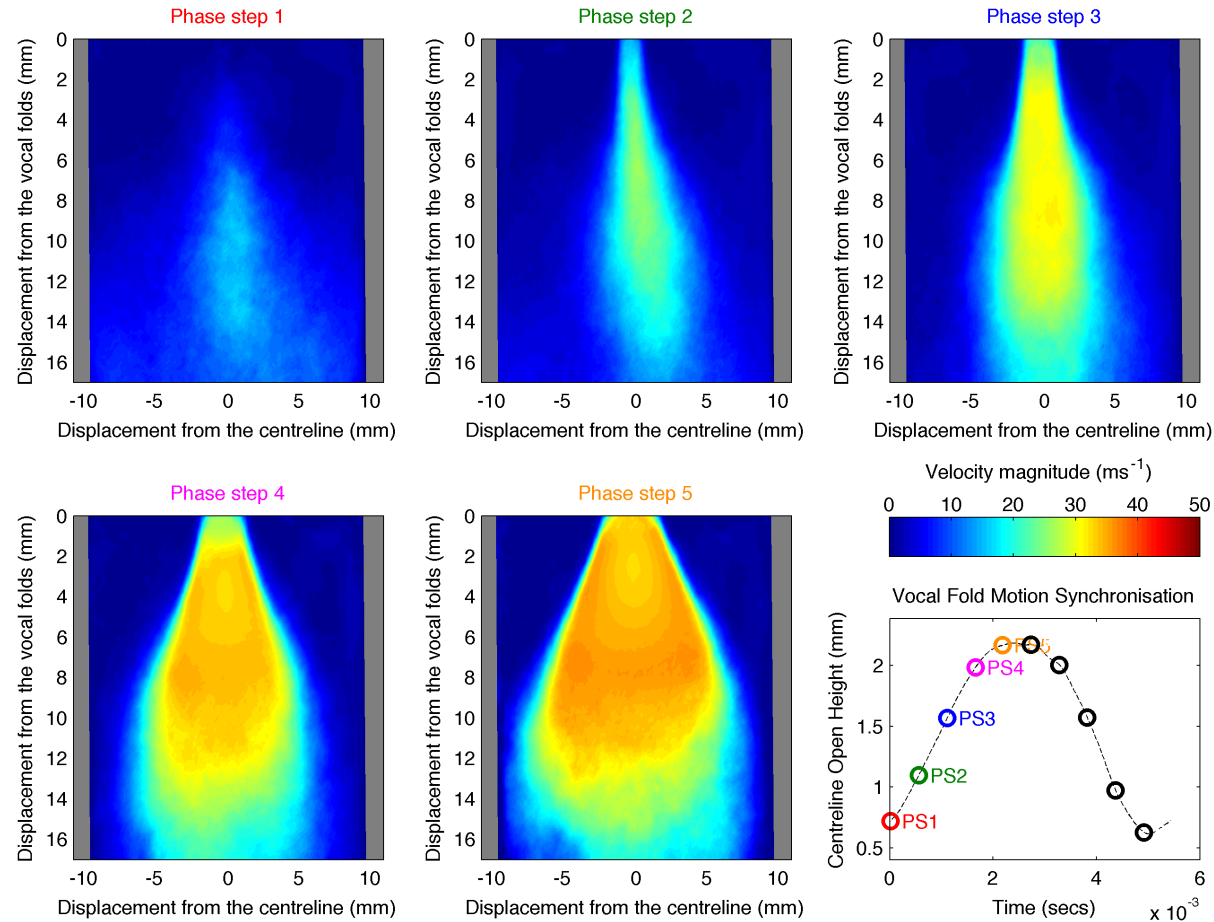


Figure 5.16: Ensemble-averaged velocity magnitude data for phase steps 1 - 5 on an *in vitro* model of the human larynx **with no ventricular bands**. The positions of the phase steps in relation to the centreline open height of the vocal fold model are included. $P_{sub} = 813$ Pa.

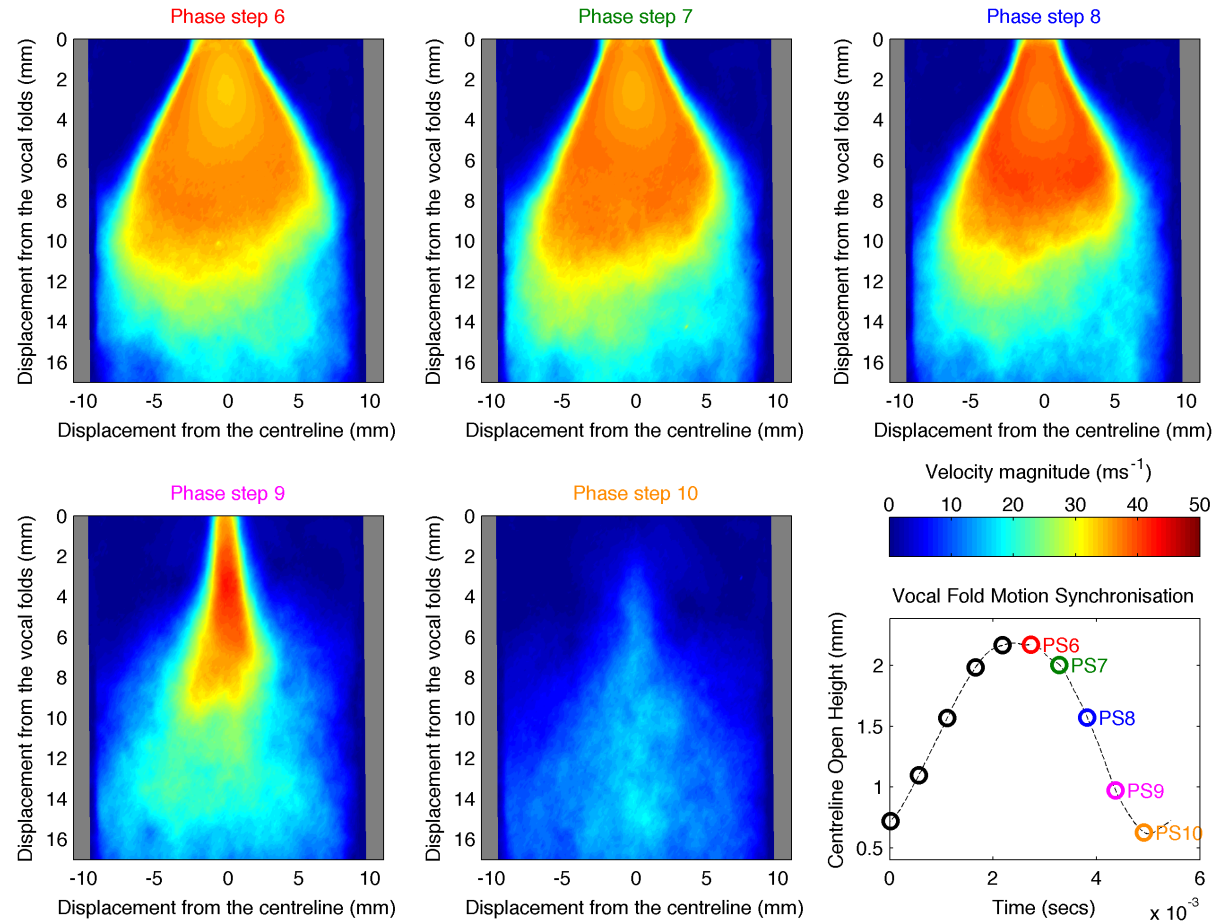


Figure 5.17: Ensemble-averaged velocity magnitude data for phase steps 6 - 10 on an *in vitro* model of the human larynx **with no ventricular bands**. The positions of the phase steps in relation to the centreline open height of the vocal fold model are included. $P_{sub} = 813$ Pa.

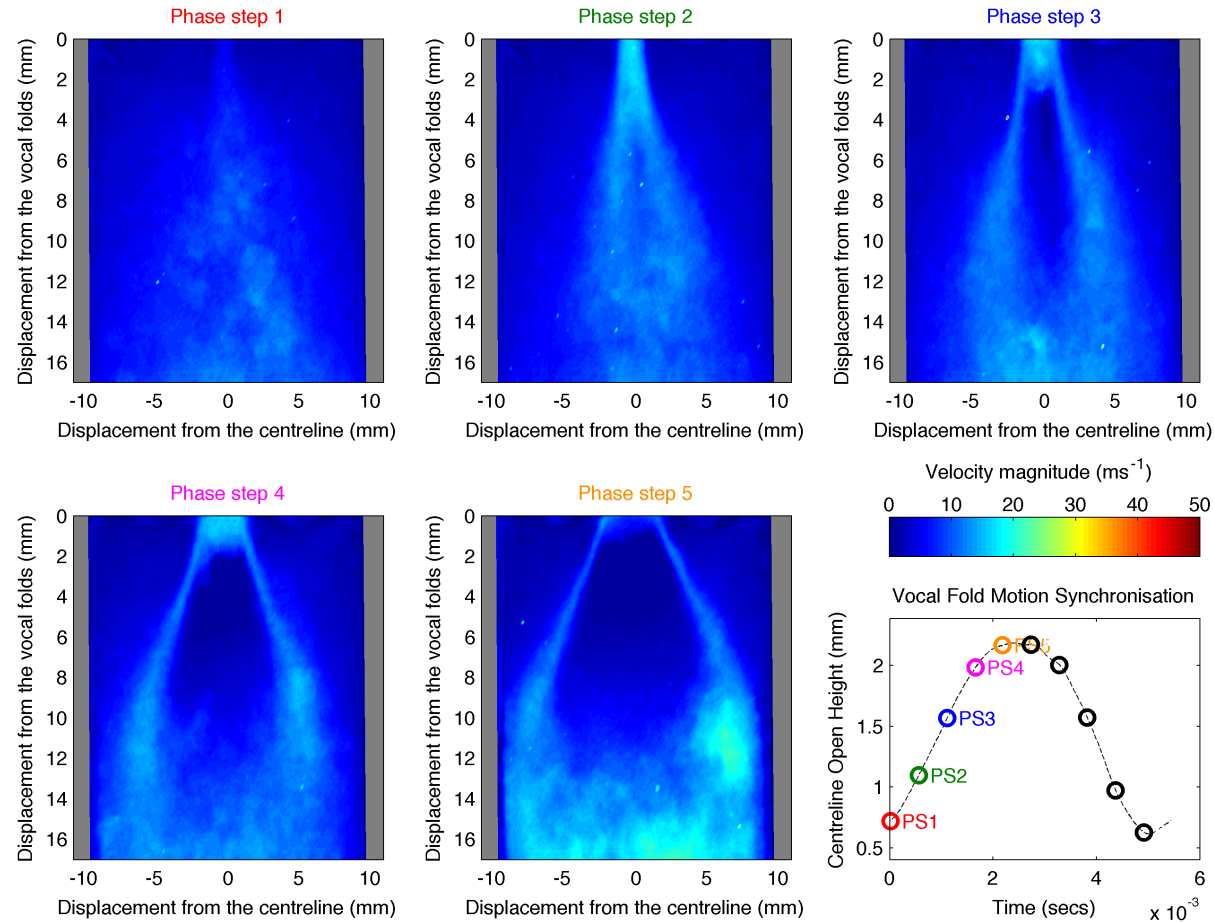


Figure 5.18: Standard deviation of the ensemble-averaged velocity magnitude data for phase steps 1 - 5 on an *in vitro* model of the human larynx **with no ventricular bands**. The positions of the phase steps in relation to the centreline open height of the vocal fold model are included. $P_{sub} = 813$ Pa.

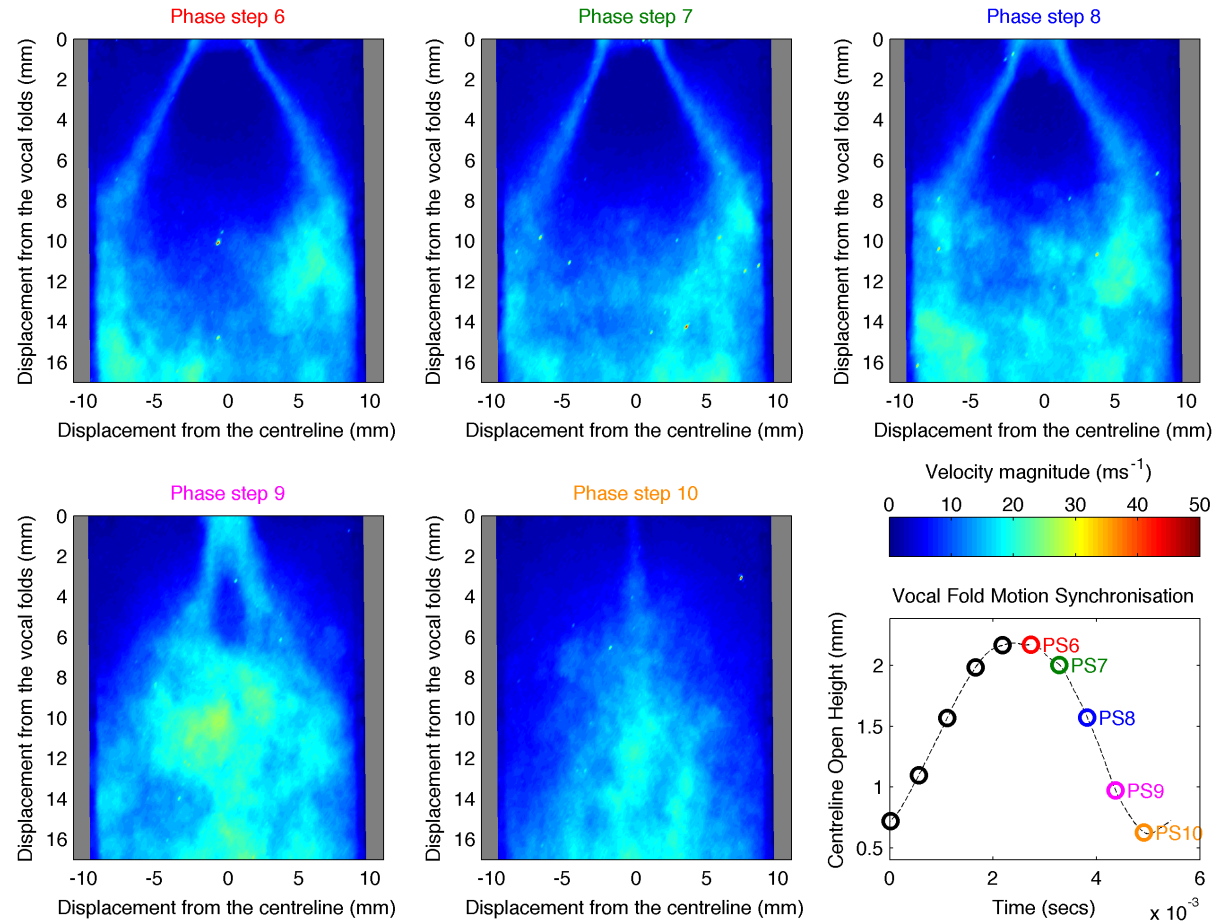


Figure 5.19: Standard deviation of the ensemble-averaged velocity magnitude data for phase steps 6 - 10 on an *in vitro* model of the human larynx **with no ventricular bands**. The positions of the phase steps in relation to the centreline open height of the vocal fold model are included. $P_{sub} = 813$ Pa.

5.5.4 Vorticity Flow Field Data

In Figures 5.20 and 5.21 are the vorticity flow fields, calculated as shown in Section 4.4.3, for phase steps 1 - 5 in one figure and 6 - 10 in the other. The colour in each of the vorticity flow fields represents the amount of rotation within the flow, with a negative vorticity representing rotation of the flow in the clockwise direction and a positive vorticity representing rotation of the flow in the anti-clockwise direction. The intensity and direction of the rotation is shown by the colour scheme in both figures. As in Figures 5.16 and 5.17 a clear jet can be seen for phase steps 2 - 9, with a clear irrotational laminar core and measurable shear layers signified by two distinct regions of high vorticity in opposite directions which bound the irrotational core. There are signs of shear layers in phase steps 1 and 10; however, there is no evidence of an irrotational core seen in the other phase steps.

When comparing the vorticity shown in Figures 5.2 - 5.7 to those in Figures 5.20 and 5.21 the shear layers for the self-oscillating model are narrower and more clearly defined than those for the free jet control case and have less vorticity either side of the shear layers of the jet core. The reason for this is due to the jet in the case with the self-oscillating *in vitro* model being a confined jet (due to the presence of a vocal tract) whereas the jet in the free jet control case is an unconfined jet. In addition, coherent vortical structures can be seen in the recirculation regions in the self-oscillating case, which is to be expected due to entrainment of the jet core. Increased vorticity can also be seen along the walls of the glass vocal tract due to the ‘no-slip’ condition of the flow at the walls discussed in Section 3.2.

Finally, the vorticity flow field plots for the *in vitro* model with ventricular bands in this PIV plane orientation are included in Appendix B due to there being insignificant differences between the vorticity flow fields for the case with and without ventricular bands. However, the vorticity flow fields for the case with and without ventricular bands for the PIV plane orientation perpendicular to that in this chapter are included in Chapter 6.

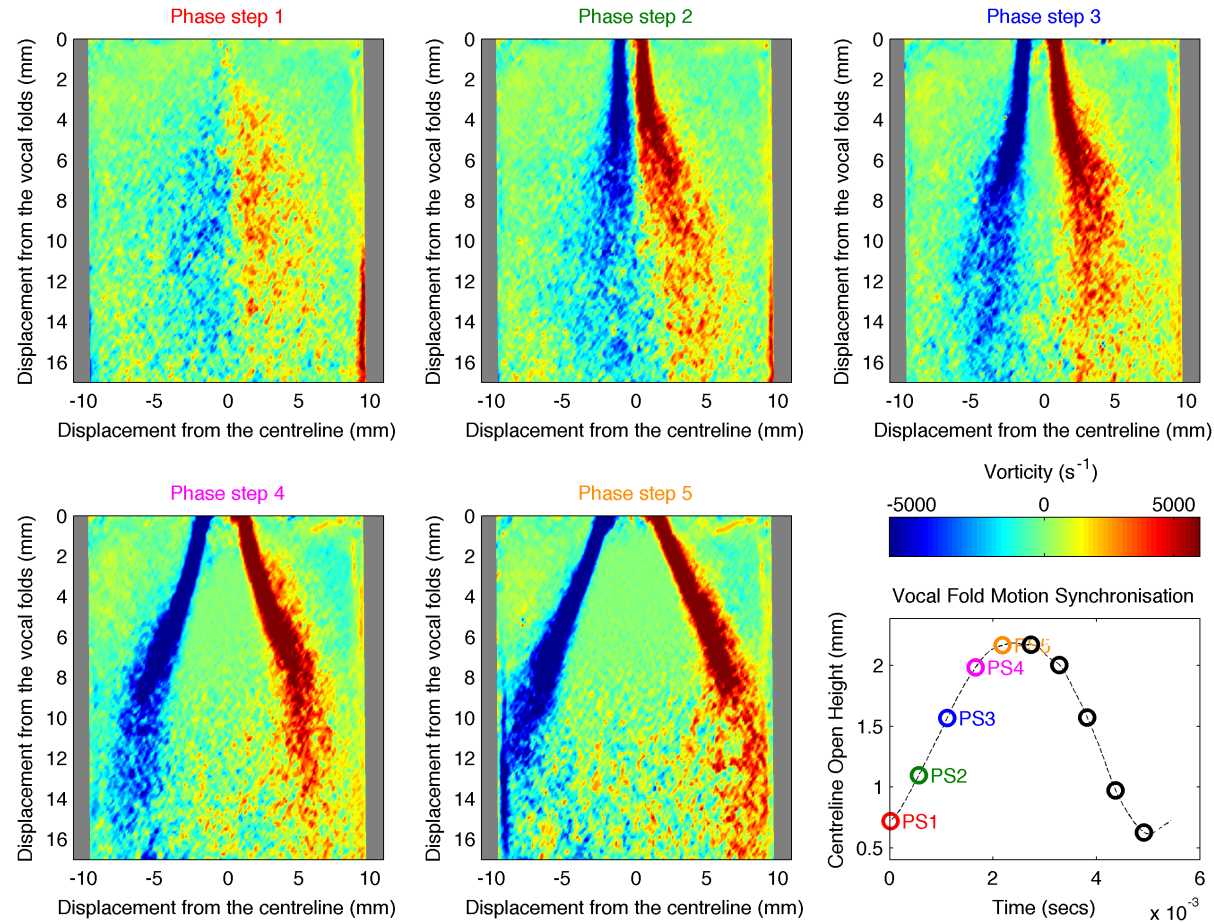


Figure 5.20: Vorticity ensemble-averaged PIV data for phase steps 1 - 5 on an *in vitro* model of the human larynx **with no ventricular bands**. The positions of the phase steps in relation to the normalised open area of the vocal fold model are included. $P_{sub} = 813$ Pa.

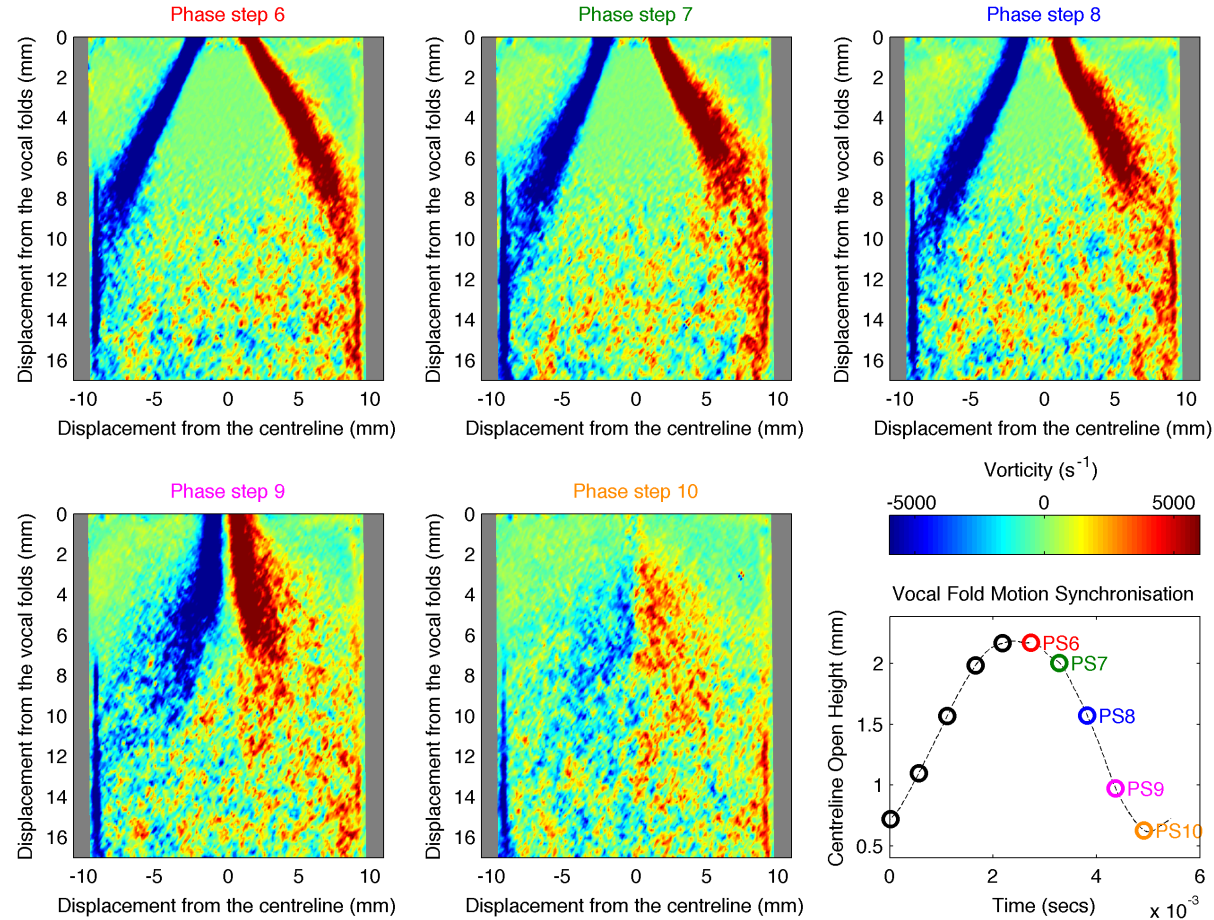


Figure 5.21: Vorticity ensemble-averaged PIV data for phase steps 6 - 10 on an *in vitro* model of the human larynx **with no ventricular bands**. The positions of the phase steps in relation to the normalised open area of the vocal fold model are included. $P_{sub} = 813$ Pa.

5.5.5 Jet Deflection and Centreline Calculation

Using the published algorithm detailed in Section 4.4.4, the centreline for the jet in each individual PIV velocity flow field map within each phase step was calculated. Subsequently the deflection angle of the jet centreline for each individual PIV data map was calculated using the method discussed in Section 5.3.2, organised into phase steps, and represented by histograms. Due to the changing nature of the jet between phase steps, the centreline of the jet for this setup was measured between 0 and 6 mm downstream of the vocal folds. The resulting histograms for the centreline and jet deflection calculations can be seen in Figure 5.22 for phase steps 2 - 9, as no clear and stable jet was visible in phase steps 1 and 10. The total number of velocity flow field maps per phase step was 78, the reason that the number of maps used to create each of the histograms in Figure 5.22 is less than this value is that the deflection angles of some of the jets in the flow field data maps were not well-modelled by a straight line. If either the value of R^2 fell below a threshold or the number of data points constituting the centreline fit of the jet fell below a certain value then the angle made by that jet was not included in the histogram plot for that phase step. The percentage of the measured jets shown on the y -axis of the histograms is the percentage of all the measured flow field data maps in each phase step and not just those which passed the filtering process.

Taking an overall view of the results presented in Figure 5.22, the glottal jet for this setup does not appear to exhibit any clear Coandă, bi-modal, or significant jet flapping behaviour. Throughout glottal cycle a high proportion of the deflection angles are either 0° or are very close to it. However, a overall small deflection is visible in phase steps 7 and 8 where the majority of the jet deflection angles increase. Another observation is that the variation in jet deflection angles appears to reduce between phase steps 2 and 4 until it reaches a minimum at phase step 5, after which it then increases. If there are any minor deviations in the jet deflection angle ($\pm 5^\circ$ for instance) this will probably be due to the turbulent nature of the individual jets to which the centrelines used to calculate the deflection angle have been fitted.

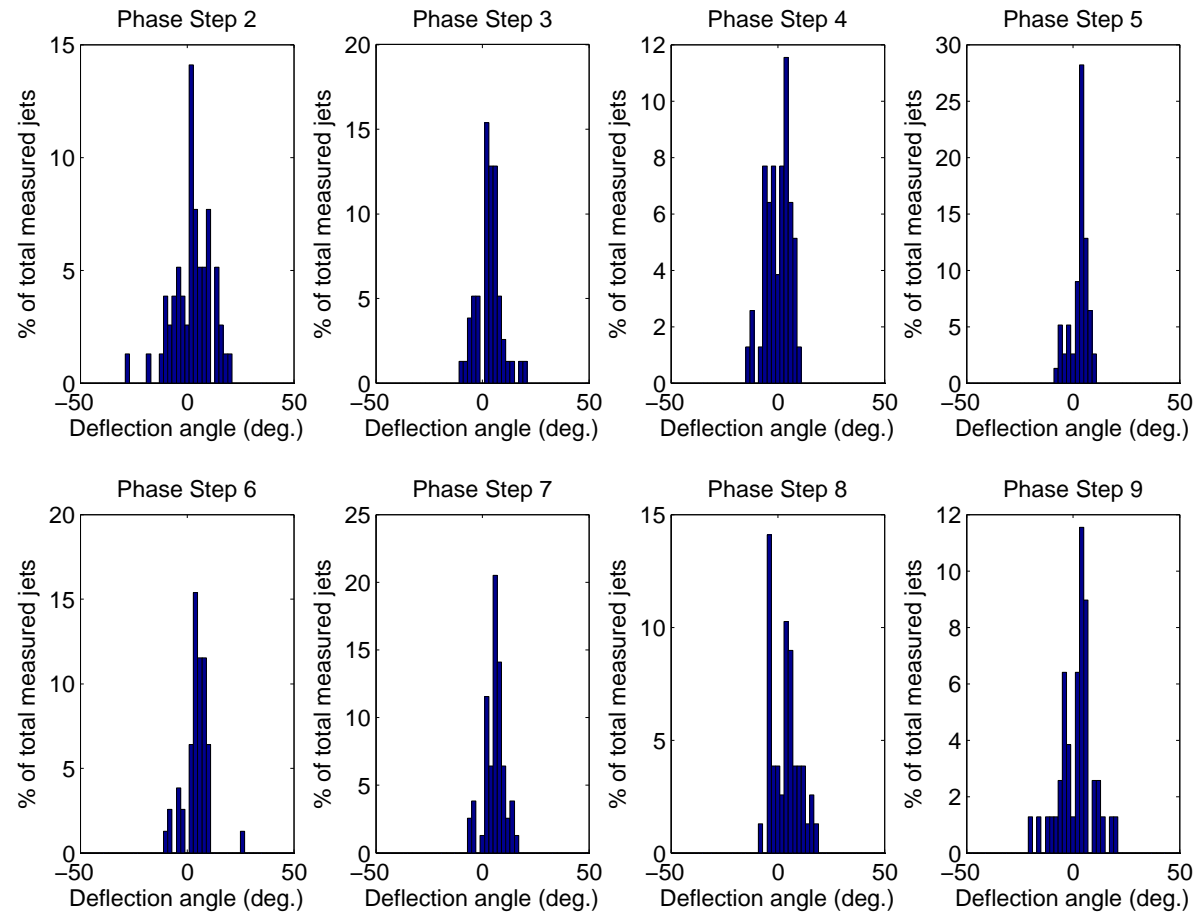


Figure 5.22: A series of histograms showing the jet deflection angle against the total percentage of measured jet centrelines, organised by phase step, for an *in vitro* model of the larynx **without ventricular bands**.

5.5.6 Expansion of the Glottal Jet

In order to consider the expansion hypotheses for the glottal jet proposed by Bailly [Bailly 09, Newton 09] and summarised in Section 3.7.4 the expansion angle of the glottal jet was measured for phase steps containing a clear jet (phase steps 2 - 9) using the method described earlier in Section 5.3.3. Before any results are discussed, what is immediately clear is that the uniform jet hypothesis (assuming no glottal jet expansion) is not suitable in this case. The results of the expansion angle fit are presented in Table 5.5, the coefficient of determination (R^2) is given to show quality of the fit to the measured jet width data.

Phase Step	$\theta_{jet} (^{\circ})$	R^2
2	11.2	0.940
3	14.8	0.956
4	22.0	0.993
5	24.6	0.999
6	26.7	0.994
7	26.0	0.996
8	26.3	0.993
9	18.1	0.959

Table 5.5: Table showing the half-width expansion angles (θ_{jet}) of the jet and the regression coefficient for the line fitted (R^2) across phase steps 2 - 9 in PIV runs using a self-oscillating *in vitro* model of the larynx **without ventricular bands**.

The fitting method applied assumes that the glottal jet expands linearly (as to be expected for the turbulent jet hypothesis), which would broadly agree with the jet shapes seen in the velocity magnitude in Figures 5.16 and 5.17; however, this may not be the case for all the phase steps. Indeed, the values of R^2 for phase steps 2, 3, and 9 are noticeably lower than those corresponding to the other phase steps. This is to be expected as, although the linear fit is still a good assumption, the shapes of the jets as shown in velocity magnitude plots are not quite so linear in their expansion, exhibiting a shape more commensurate with the laminar jet expansion hypothesis.

Considering the values of the half-width expansion angle (θ_{jet}) in Table 5.5 it is clear that the jet expands rapidly from 14.8° in phase step 3 to 22.0° in phase step 4 then

5.5. RESULTS FOR THE *IN VITRO* MODEL WITHOUT VENTRICULAR BANDS

increasing to its maximum at 26.7° in phase step 6. After this point the jet half-width expansion angle remains at about 26° until phase step 9 when it reduces significantly to 18.1° . This is an interesting observation for the reason that if comparison is made between the data for this setup and data for the free jet in Table 5.1; for a static model, as the velocity magnitude of the jet core increases due to an increase in P_{sub} the value of θ_{jet} decreases; whereas for this setup, as the velocity magnitude of the jet core increases then the value of θ_{jet} increases, except in the case of phase step 9 (although this still produces a larger value of θ_{jet} in comparisons to phase steps 2 and 3).

Collecting the phase steps into opening and closing phase groups, what is apparent is that there is once again a strong asymmetry between these two phases of the phonatory cycle. The half-angle jet width is seen to increase during the opening phase whereas it remains constant for most of the closing phase, only reducing in the penultimate phase step. This observation and that of the previous paragraph could be feasibly attributed to inertial effects caused by vocal fold oscillation, as there are distinct differences in the glottal jet in terms of its linear expansion and the velocity magnitude of its jet core for phase steps where the glottal open height is almost the same. Finally, as was observed with the free jet case in Section 5.3.3 all of the values for θ_{jet} are significantly larger than the 4° used in the turbulent expansion hypothesis proposed by Bailly.

5.5.7 Dimensional Analysis

Using the non-dimensional terms as described in Section 4.4.5 and already applied to the control jet case in the non-oscillating *in vitro* model of the larynx in Section 5.3.4, Figures 5.23 and 5.24 show non-dimensional parameters plotted for the self-oscillating *in vitro* model of the larynx without ventricular bands. Considering the plot showing the jet core turbulence (T_{core}) plotted against phase step number in Figure 5.23 (top left-hand corner), it is clear that the jet core turbulence is lowest between phase steps 4 and 8, and highest at phase step 2. In general the jet core turbulence is considerably lower during the closing phase than the opening phase. However, it should be noted that the difference between the values of T_{core} from phase steps 4 and 8 is not significant when compared to the individual values of phase steps 2 and 9. Naturally, a significant number of the phase steps show higher jet core turbulence values than those shown in Figure 5.9, due to the unsteadiness caused by self-oscillation of the vocal folds,

5.5. RESULTS FOR THE *IN VITRO* MODEL WITHOUT VENTRICULAR BANDS

particularly during the opening phase and at the end of the closing phase. However, phase steps 4 - 8 show T_{core} values which are comparable to (if not slightly lower than) those for the free jet control case.

When T_{core} is plotted against the normalised glottal open height (h/h_{max}) a hysteresis behaviour is seen, which is also observed in [Newton 09]. The T_{core} values presented here are significantly lower than those shown for the free jet case with a self-oscillating *in vitro* model in [Newton 09]. The reasons for this could be related either to improvements associated with the phase stepping technique over phase windowing, or in the fact that Newton measured the values for T_{core} 8 mm downstream of the glottal opening (in comparison to 4 mm used in this study), which he identifies in some phase windows may lie in a strongly transitional region of the flow with significant turbulence evident. This may suggest that some of the jet core turbulence observed in that study may be due to the phase windowing technique used and hence may not be a feature of the glottal flow. What this parametric plot communicates is that the turbulence within the jet core is not solely dependent on the open height of the vocal folds but on whether the vocal folds are in their opening or closing phase.

The next plot showing Reynolds number against normalised glottal open height makes it possible to consider whether or not the ratio of the fluid inertial to viscous forces is the same for the different glottal open heights. This plot shows that the Reynolds numbers range from 1687 to 5042 and also shows a hysteresis behaviour, although to a lesser extent than T_{core} against h/h_{max} . With Re_{core} values over 4000, this puts the glottal jet into the turbulent regime [Webber 68, Holman 86] for part of the phonatory cycle. The Re_{core} values are higher than those shown in [Newton 09]; however, a reason for this may be that the increased value of P_{sub} required for self-oscillation and subsequently the higher measured magnitudes shown in Figures 5.16 and 5.17 flowing through a similar-sized orifice will have been responsible for this. The final plot in Figure 5.16 shows jet core Reynolds number against jet core turbulence. This plot makes it possible to see how the fluid properties of the glottal jet are related to turbulence measured in that phase step. Unlike in [Newton 09], a strong hysteresis behaviour is not shown which suggests that the turbulence within the jet core may be directly related to the fluid properties of the glottal jet. The same reasons for the discrepancy in the values of T_{core} may also be responsible for the difference seen here.

The first plot in the top left hand corner of Figure 5.24 shows the normalised jet

5.5. RESULTS FOR THE *IN VITRO* MODEL WITHOUT VENTRICULAR BANDS

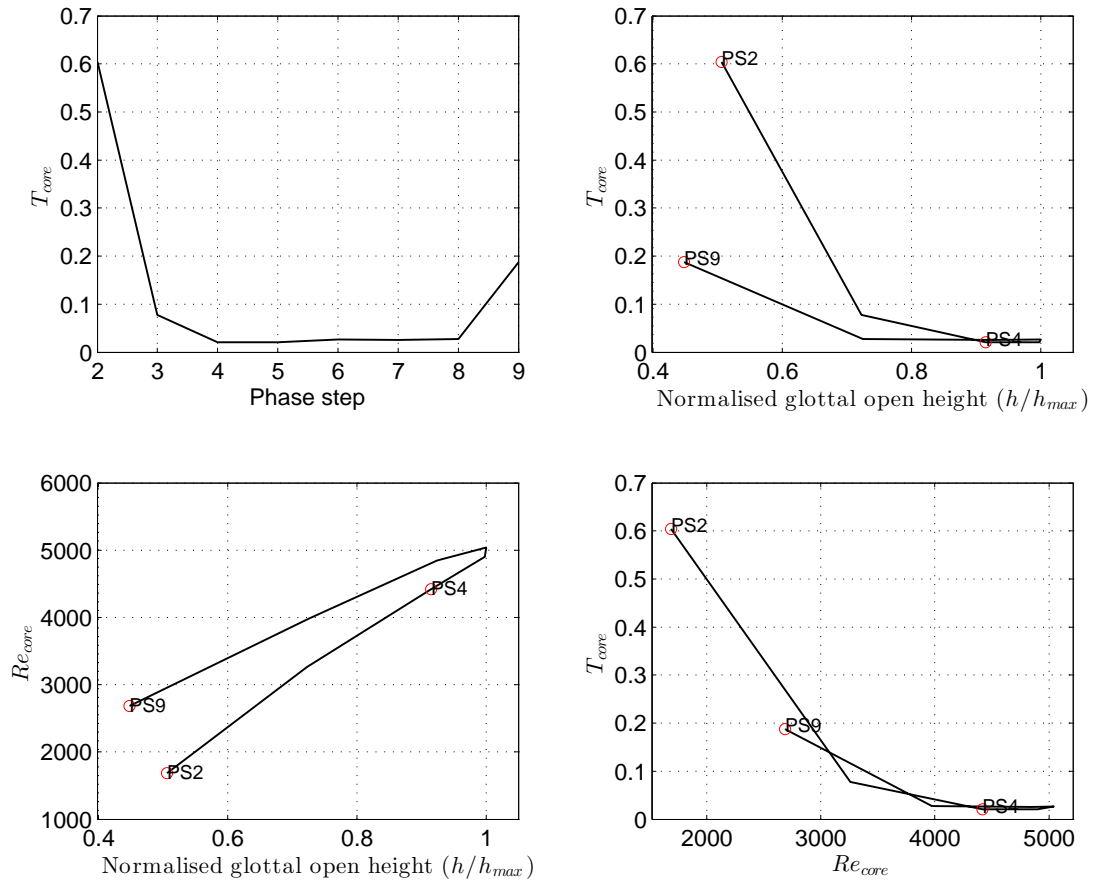


Figure 5.23: Non-dimensional flow parameter parametric plots illustrating changes in turbulence and the Reynolds number across established phase steps for a self-oscillating *in vitro* model of the human larynx **with no ventricular bands**. Phase steps 2, 4, and 9 are highlighted.

5.5. RESULTS FOR THE *IN VITRO* MODEL WITHOUT VENTRICULAR BANDS

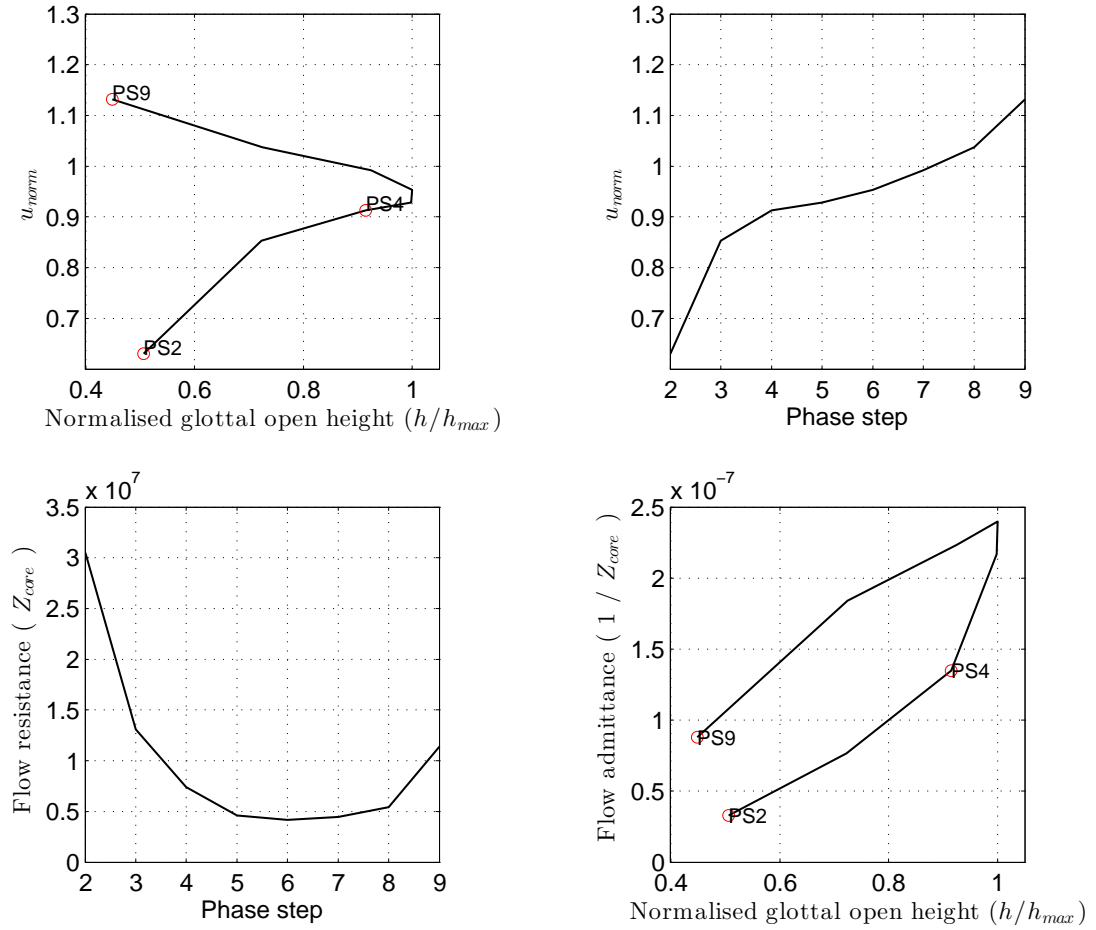


Figure 5.24: Non-dimensional flow parameter parametric plots illustrating changes in jet speed and flow admittance and resistance across established phase steps for a self-oscillating *in vitro* model of the human larynx **with no ventricular bands**. Phase steps 2, 4, and 9 are highlighted.

5.5. RESULTS FOR THE *IN VITRO* MODEL WITHOUT VENTRICULAR BANDS

core velocity plotted against normalised glottal open height. What this plot illustrates is how the velocity of the jet core is affected by the glottal open height, all normalised in order to make comparisons with other model setups. A hysteresis behaviour is seen once again here, thereby showing an indirect relationship between the 2 variables. This behaviour is similar to what is shown in [Newton 09] for the free jet case; however, the values for u_{norm} in this case are significantly higher and the hysteresis much more pronounced. A reason for this could be that the *in vitro* model in this case had a vocal tract attached thereby rendering the jet a confined jet, whereas the model used by Newton in the free jet case did not have a vocal tract attached. The plot in the top right hand corner shows the evolution of the normalised jet velocity over the phonatory cycle. One of the most significant observations from this plot and the parametric plot preceeding this is that the value of u_{norm} during the closing phase of the phonatory cycle exceeds 1. This suggests that inertial effects are taking place during this phase and this has the effect of increasing the jet velocity during closure. It should be noted that although the value of u_{norm} in Figure 5.9 approaches 1, it never exceeds it.

The bottom left hand plot in Figure 5.24 shows how the calculated resistance met by the glottal flow at the point of separation changes by phase step. What can be deduced from this plot is that most of the glottal flow resistance is experienced during the opening phase of the phonatory cycle. The reason for this is that the vocal folds are forced apart by the subglottal pressure, the jet therefore experiences resistance and loses part of its energy forcing the vocal folds apart. This results in a lower velocity magnitude within the glottal jet core which then translates to an increased flow resistance. A possible reason for a high flow resistance for phase step 2 could be due to the combination of a pressure build up behind the vocal folds during the closing phase and a small glottal opening measured at this point. The final plot in this figure shows how the glottal flow admittance, demonstrating transmission efficiency of the vocal folds, relates to the normalised glottal open height. Once again a strong hysteresis can be seen, thereby showing that a direct relation does not exist between the glottal flow admittance and the normalised glottal open height. It will be interesting to see whether this is the case when ventricular bands are present and how much change is observed. Finally, it is interesting to note that for all phase steps, except phase step 2, the flow resistance is lower in the self-oscillating model, than for the control free jets. The reason for this could be due to the jet in this configuration being a confined

jet.

5.5.8 Summary

Over the past two sections various results have been presented and analysed. In Section 5.4 the resonance peak frequencies and quality factors for these resonances were extracted from the mechanical response measurements taken for the *in vitro* model without a vocal tract attached. These results are summarised in Table 5.2 and the values from the setup without a glottal flow are later used in the computational model. The reasons for this choice and for the differences seen between the mechanical response of the model with and without a glottal flow have been discussed. In this section also results have been shown and discussed for experiments undertaken using a high-speed camera. Important observations from this part were that for the *in vitro* model used in this study full closure of the vocal folds was not achieved and that an outward initial bowing of the vocal folds was observed. In addition, inward bowing at the minimum glottal open height in the phonatory cycle was observed which was shown to be a pathology usually presented in the voices of the elderly. The measured initial centreline open height was noted and is later used in the computational physical model.

In Section 5.5 data for the *in vitro* model without ventricular bands has been presented and discussed. Firstly, a clear glottal jet was visible in all phase steps except 1 and 10 and so were not considered further analysis of the glottal jet. Key observations from this data were that, like that free jet control case, the glottal jet expansion angle of 4° proposed by Bailly was far too small. However, for the majority of the phase steps the turbulent jet expansion hypothesis appeared to model the glottal jet expansion well (not taking the value of the expansion into account), with the jet in phase steps 2 and 3 showing an expansion geometry similar to the laminar expansion hypothesis. A clear hysteresis in the glottal jet geometry and flow field velocities were observed, as were identified by Newton in [Newton 09]. This hysteresis was also seen in the dimensional analysis and also in the glottal jet expansion angle, where larger angles were observed during the closing phase than the opening phase suggesting that inertial effects may be responsible. Finally, the vorticity data for the *in vitro* model without ventricular bands have been presented and discussed. Due to the jet in the self-oscillating case being identified as confined, the shear layers were identified as being narrower and there being a lower level of vorticity in general.

5.6 Results for *in vitro* Model with Rigid Ventricular Bands

Using the same model as that used in the previous section, but including ventricular bands within the vocal tract, this section investigates the impact of the ventricular bands on the glottal jet and the oscillation of the vocal folds using high-speed camera data and PIV data in the same plane as Section 5.5. For results for the same model with ventricular bands in the plane parallel to the glottal height abscissa see Section 6.2. A significant advantage over the study undertaken by Krebs *et al.* [Krebs 12] is that ventricular bands are included in the vocal tract used here and that it was possible to undertake PIV with them installed. It should be noted that unlike the results in [Newton 09], the value of P_{sub} used for the *in vitro* model both with and without ventricular bands was kept constant (± 10 Pa due to experimental constraints). The value of P_{in} also was kept constant.

The phase step mean time and standard deviation in relation to the phonatory cycle for the *in vitro* model with ventricular bands placed 16 mm downstream of the exit to the vocal folds and with an 8 mm separation are shown in Table 5.6 and a 3 mm separation are shown in Table 5.7. For the model with ventricular bands separated by 8 mm the value of f_{rnd} was 180 Hz, the mean of f_0 was 181.33 Hz, and the standard deviation of f_0 was 0.75 Hz. For the model with ventricular bands separated by 3 mm f_{rnd} was 178 Hz, the mean of f_0 was 178.71 Hz, and the standard deviation f_0 was 0.68 Hz. What is immediately apparent is that the value of f_0 drops when rigid ventricular bands are added to the vocal tract, which is also observed in computational simulations using linear stability analysis as well as experimental data shown in [Bailly 06]. The largest drop in f_0 was for the ventricular bands with a 3 mm separation, suggesting that the narrower the constriction the lower f_0 will be, which also aligns well with observations in [Bailly 06]. In addition, the value for the standard deviation of f_0 increased with the presence of ventricular bands. This also had effect of just over doubling the standard deviation values associated with the phase step mean times for these two setups as shown in Tables 5.6 and 5.7. This would suggest that the *in vitro* model with ventricular bands oscillates more unstably (with a greater degree of inter-glottal phonatory cycle variation) than that without ventricular bands present.

5.6. RESULTS FOR *IN VITRO* MODEL WITH RIGID VENTRICULAR BANDS

Phase Step	Mean (secs)	Standard Deviation (secs)
1	6.77×10^{-5}	2.88×10^{-5}
2	6.11×10^{-4}	2.20×10^{-5}
3	1.15×10^{-3}	2.85×10^{-5}
4	1.69×10^{-3}	2.46×10^{-5}
5	2.24×10^{-3}	2.67×10^{-5}
6	2.79×10^{-3}	2.74×10^{-5}
7	3.35×10^{-3}	2.27×10^{-5}
8	3.91×10^{-3}	2.17×10^{-5}
9	4.45×10^{-3}	2.36×10^{-5}
10	5.01×10^{-3}	2.13×10^{-5}

Table 5.6: Table showing the mean and standard deviation of image pair acquisition times for each phase step in PIV runs using an *in vitro* model of the human larynx **with rigid ventricular bands placed 16 mm downstream of the vocal folds with an 8 mm separation.**

Phase Step	Mean (secs)	Standard Deviation (secs)
1	5.61×10^{-3}	3.35×10^{-5}
2	5.52×10^{-4}	2.48×10^{-5}
3	1.11×10^{-3}	2.72×10^{-5}
4	1.67×10^{-3}	2.61×10^{-5}
5	2.23×10^{-3}	2.54×10^{-5}
6	2.79×10^{-3}	2.60×10^{-5}
7	3.34×10^{-3}	2.65×10^{-5}
8	3.90×10^{-3}	2.84×10^{-5}
9	4.46×10^{-3}	2.60×10^{-5}
10	5.02×10^{-3}	2.65×10^{-5}

Table 5.7: Table showing the mean and standard deviation of image pair acquisition times for each phase step in PIV runs using an *in vitro* model of the human larynx **with rigid ventricular bands placed 16 mm downstream of the vocal folds with a 3 mm separation.**

5.6. RESULTS FOR *IN VITRO* MODEL WITH RIGID VENTRICULAR BANDS

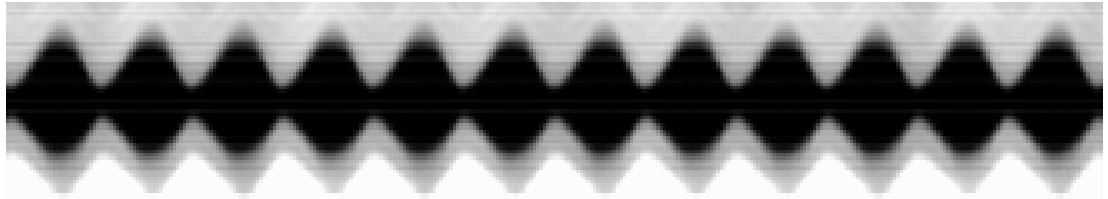
5.6.1 Vocal Fold Open Height through High-Speed Camera Analysis

Figure 5.25 shows three kymographs taken from an *in vitro* model without ventricular bands and with ventricular bands placed 16 mm downstream which are separated either by 8 mm or 3 mm. What is immediately apparent whilst comparing the three kymographs is that the vocal folds appear to close more fully when ventricular bands are present than when they are absent. This is a very significant observation and offers an alternative explanation as to why elderly patients with vocal fold bowing may try to engage supraglottic structures during phonation. On further analysis of the kymographs it is clear that an asymmetry in the between opening and closing phases of the phonatory cycle exists in all three cases, but appears to be stronger in the cases with ventricular bands than without.

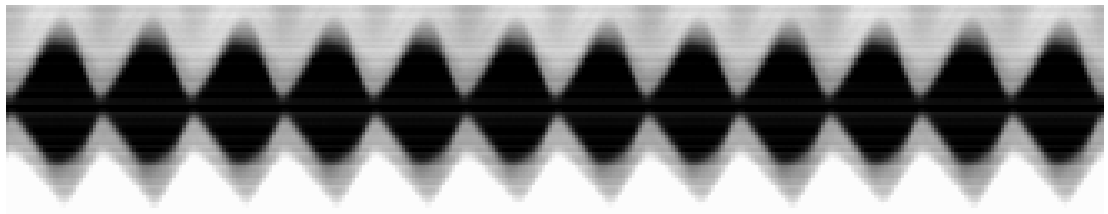
Looking more closely at the differences between the vocal fold opening during oscillation, Figure 5.26 shows the measured open height of the vocal folds in the centre and at two lines either side for the model with ventricular bands at either 8 mm or 3 mm apart. When making a comparison between these two plots and that in Figure 5.15 without ventricular bands it is clear that the addition of ventricular bands to the vocal tract in these 2 cases does not introduce a phase difference in the phonatory cycle between different parts of the vocal folds. The open height across the phonatory cycle also appears to change when ventricular bands are present. The case without ventricular bands produces a centreline open height which is almost sinusoidal. The model with ventricular bands set at 8 mm apart produces a slight aberration of this; however, the model with the ventricular bands separated by 3 mm produces a centreline open height which deviates significantly from a sinusoid. A possible reason for this may be interference caused by the ventricular band separation being very close to the vocal folds opening measured, which was unfortunately unavoidable.

Considering the minimum open heights of the 3 elements of the vocal folds in the plots shown in Figure 5.26 a greater degree of ‘bowing’ takes place with the ventricular bands having a 3 mm separation than having an 8 mm separation. This can be more clearly seen in the results summarised in Table 5.8. What is clear from these results is that a reduction in the separation of the ventricular bands aids vocal fold closure with a separation of 3 mm having a greater effect than a separation 8 mm. Furthermore,

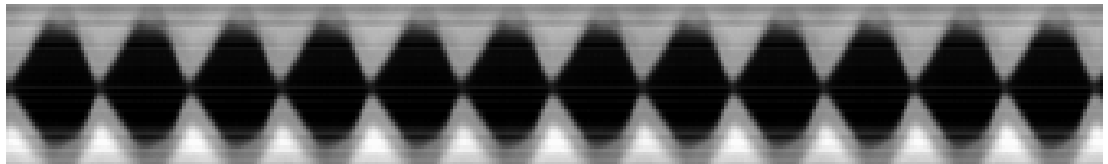
5.6. RESULTS FOR *IN VITRO* MODEL WITH RIGID VENTRICULAR BANDS



(a) *in vitro* model of the human larynx without ventricular bands



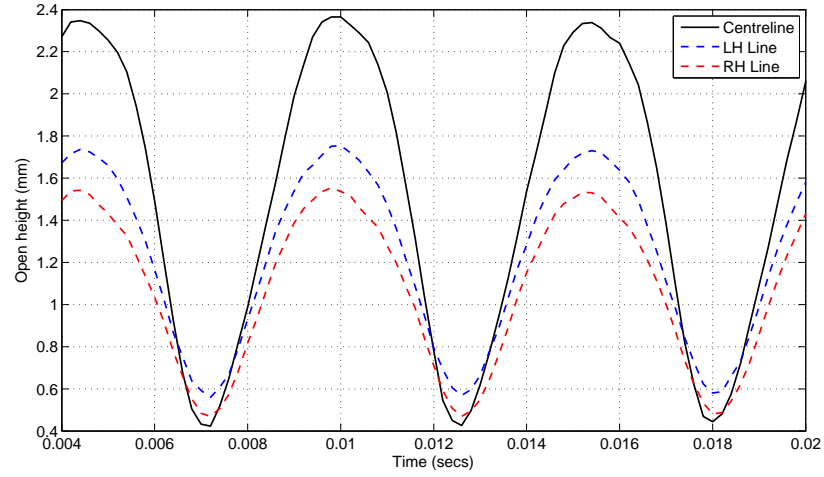
(b) *in vitro* model of the human larynx with ventricular bands 16 mm downstream with an 8 mm separation



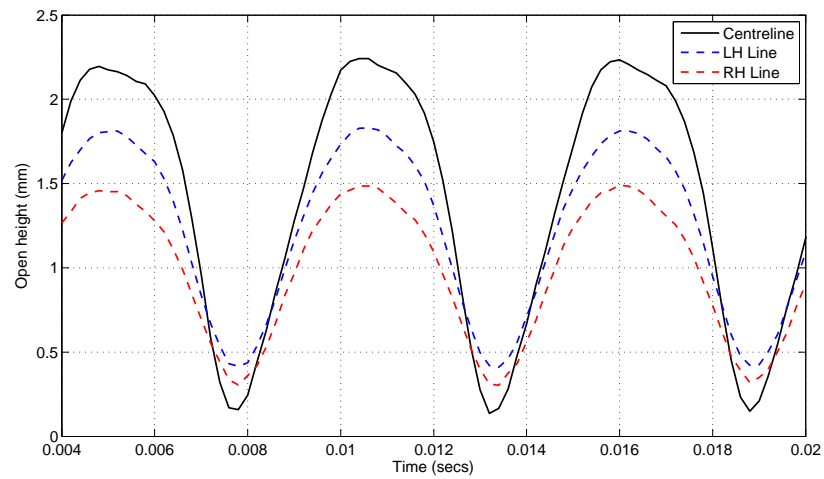
(c) *in vitro* model of the human larynx with ventricular bands 16 mm downstream with a 3 mm separation

Figure 5.25: Kymograph lines taken from an *in vitro* model of the human larynx with and without ventricular bands.

5.6. RESULTS FOR *IN VITRO* MODEL WITH RIGID VENTRICULAR BANDS



(a) *in vitro* model of the human larynx with ventricular bands 16 mm downstream with an 8 mm separation



(b) *in vitro* model of the human larynx with ventricular bands 16 mm downstream with a 3 mm separation

Figure 5.26: Plots showing the measured open height of the vocal folds in the centre and at two lines either side equidistant to the centreline for an *in vitro* model with ventricular bands 16 mm downstream and either 8 mm or 3 mm apart.

5.6. RESULTS FOR *IN VITRO* MODEL WITH RIGID VENTRICULAR BANDS

	8 mm Separation		3 mm Separation	
	$\overline{h_{min}}$ (mm)	$\overline{h_{max}}$ (mm)	$\overline{h_{min}}$ (mm)	$\overline{h_{max}}$ (mm)
LH line	0.56	1.75	0.44	1.81
Centre line	0.41	2.36	0.20	2.20
RH line	0.47	1.55	0.34	1.46

Table 5.8: Table containing the mean minimum ($\overline{h_{min}}$) and maximum ($\overline{h_{max}}$) open heights for the left hand, centre, and right hand lines of analysis for an *in vitro* model with ventricular bands 16 mm downstream and either 8 mm or 3 mm apart.

considering only the case without ventricular bands and the case with ventricular bands separated by 8 mm for the reason mentioned earlier, the presence of the ventricular bands are seen to increase the maximum centreline opening of the vocal folds, thereby facilitating a stronger oscillation. As the upstream glottal pressure for all 3 cases was practically the same, this change appears to suggest that the nature of the aerodynamic interaction between the vocal folds and the glottal jet changes when the ventricular bands are present.

5.6.2 Characterisation of the Glottal Jet

Figures 5.27 and 5.28 show the velocity magnitude for ensemble-averaged PIV flow field velocity data for phase steps 1-10 for the model with ventricular bands with an 8 mm separation. The same information for the model with ventricular bands with a 3 mm separation is shown by Figures 5.31 and 5.32. The corresponding standard deviation of the ensemble-averaged velocity magnitude is shown in Figures 5.29 and 5.30 and Figures 5.33 and 5.34 for the model with ventricular bands separated by 8 mm and 3 mm respectively. The greyed out area represents the walls of the vocal tract and the part of the ventricular bands which can be seen. A clear and distinctive jet can be seen in phase steps 2 - 9 for both model setups in the velocity magnitude plots; however, the jet is less clear in phase steps 2 and 3 for the setup with ventricular bands 3 mm apart than that with ventricular bands with an 8 mm separation. This can be investigated further by considering the plots showing the standard deviation of the ensemble-averaged velocity magnitude. For phase step 2 for the setup with ventricular bands 3 mm apart the velocity magnitude for the jet is approximately the same as the

5.6. RESULTS FOR *IN VITRO* MODEL WITH RIGID VENTRICULAR BANDS

standard deviation in that same area. In addition, the surrounding area both in the velocity magnitude and standard deviation plots are higher than in other phase steps, causing the glottal jet to appear ‘smeared’, which is probably due to the averaged effect of the jet flapping from side to side or to strong turbulent dissipation.

When considering Figure 5.27 what is immediately obvious is the skewing of the glottal jet in phase steps 2, 3, 4, and 9 with the skewing gradually reducing from phase step 2 to 4. On looking at the corresponding standard deviation plot it is clear that this skewing is a clear and stable feature of the flow, as a clear laminar core with a lower standard deviation magnitude than the surrounding shear layers is visible (unlike for phase step 2 in Figure 5.33). This indicates that the glottal jet appears to be adhering to the right hand wall of the vocal tract for this phase step thereby exhibiting behaviour commensurate with the Coandă effect. Phase step 3 also exhibits this behaviour but not for the complete length of the glottal jet and not to the same extent. This effect is also seen to a lesser degree and with jet flapping in phase step 3 of the model with ventricular bands separated by 3 mm but is not seen in the case without ventricular bands at all.

A similarity between the velocity magnitude plots for the model with and without the ventricular bands is the asymmetry in this aspect of the glottal jet between the opening and closing phases. Also, on the whole the velocity magnitudes for the glottal jet in the model with ventricular bands separated by 3 mm appear to be lower than those for the case with ventricular bands separated by 8 mm. For phase steps 5 - 9 in the case with ventricular bands separated by 3 mm the glottal jet appears to extend more symmetrically downstream than in the case with ventricular bands with an 8 mm separation. A possible cause for this could be the same as for the skewing seen in the velocity magnitude plots for other phase steps.

Finally, it has been possible to extract the width of the glottal jet at the exit of the vocal folds from the ensemble-averaged velocity magnitude plots for each of the 3 cases and plot them against the measured vocal fold centreline opening at that phase step. The results of this are shown in Figure 5.35. What this figure allows us to consider is how the ventricular bands affect the glottal jet width at the vocal folds and whether their presence may have an impact on the point at which the glottal jet separates from the walls of the vocal folds. This has been possible due to redesigns of the vocal fold model discussed in Section 3.4 and although PIV velocity flow field

5.6. RESULTS FOR *IN VITRO* MODEL WITH RIGID VENTRICULAR BANDS

data are shown for the glottal jet in [Krebs 12], their first measured point appears 6 mm downstream of the vocal fold exit, as their model is more closely related to that used in [Ruty 07a, Bailly 09, Newton 09]. In addition, Krebs *et al.* acknowledge that the laminar core region of the glottal jet in their experiments is out of the field of view. The first point to draw from this plot is that the glottal jet width changes with vocal fold open height, with the minimum open height corresponding to the minimum jet width; however, the point of maximum vocal fold open height does not correspond to the maximum glottal jet width, this appears 1 or 2 phase steps afterwards. What this may indicate is that the point of flow separation changes as the glottal shape changes during the closing phase.

The ventricular bands can be clearly seen having an effect on the width of the glottal jet as its width at the maximum point in all three cases increases as the separation between the ventricular bands reduces. Another effect is that the minimum glottal jet widths for the case with ventricular bands separated by 3 mm are significantly higher than the equivalent minima for the other case with ventricular bands, which is closer to the case with no ventricular bands. The reason for this may be that the increased constriction posed by the ventricular bands may reduce the volume flow through the larynx and thereby change the pressure distribution in laryngeal ventricle thus causing the glottal jet to separate at a point further down the vocal folds. This also raises the question of whether the flow actually separates outside the glottis, as the measured jet width at some points in the phonatory cycle is just under double the measured vocal fold centreline open height. However, without actually seeing the point of flow separation, this is a difficult question to answer directly and not one which will be possible with the current *in vitro* model.

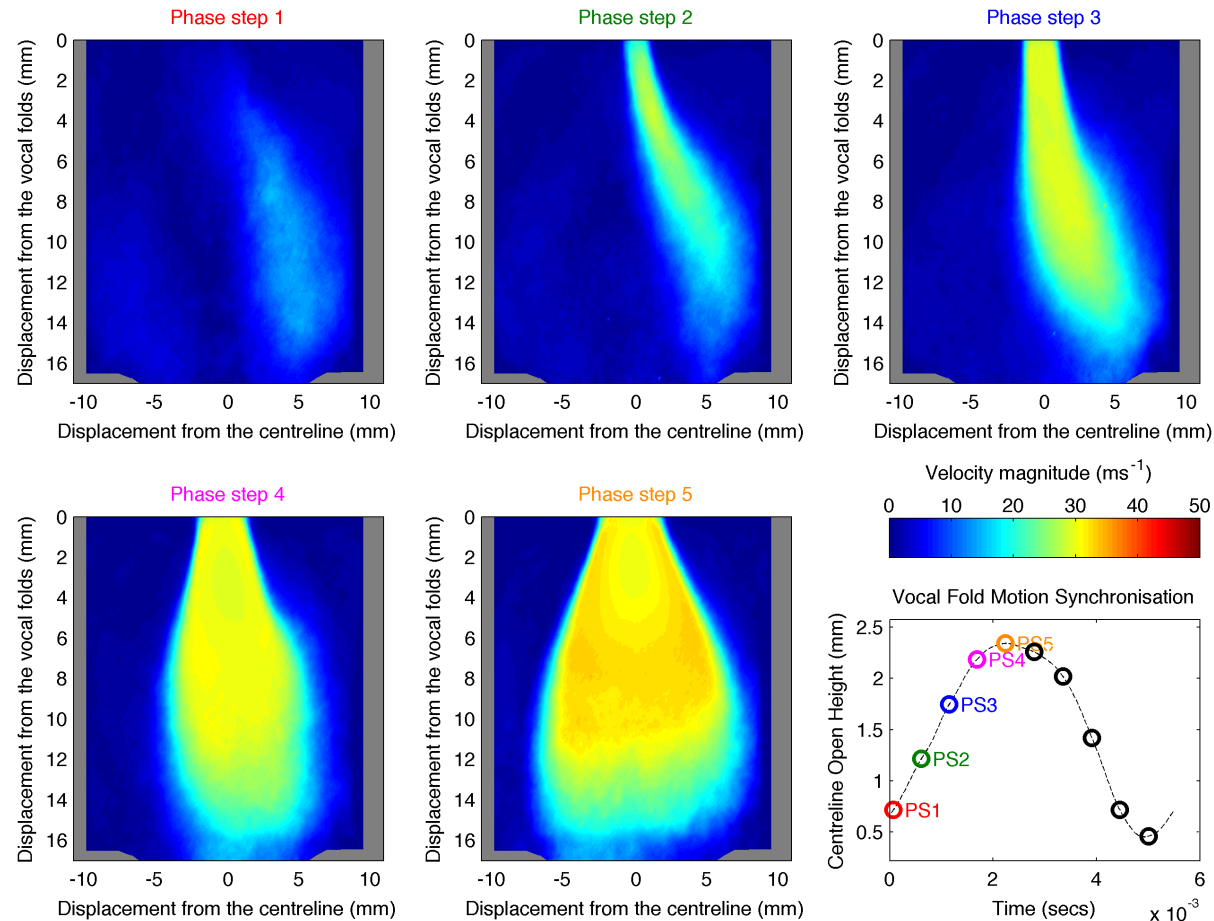


Figure 5.27: Ensemble-averaged velocity magnitude data for phase steps 1 - 5 on an *in vitro* model of the human larynx **with rigid ventricular bands placed 16 mm downstream of the vocal folds with an 8 mm separation**. The positions of the phase steps in relation to the centreline open height of the vocal fold model are included. $P_{sub} = 802$ Pa. Only the top of the ventricular bands are shown in these plots, the reported separation is the minimum constriction formed by the bands further downstream.

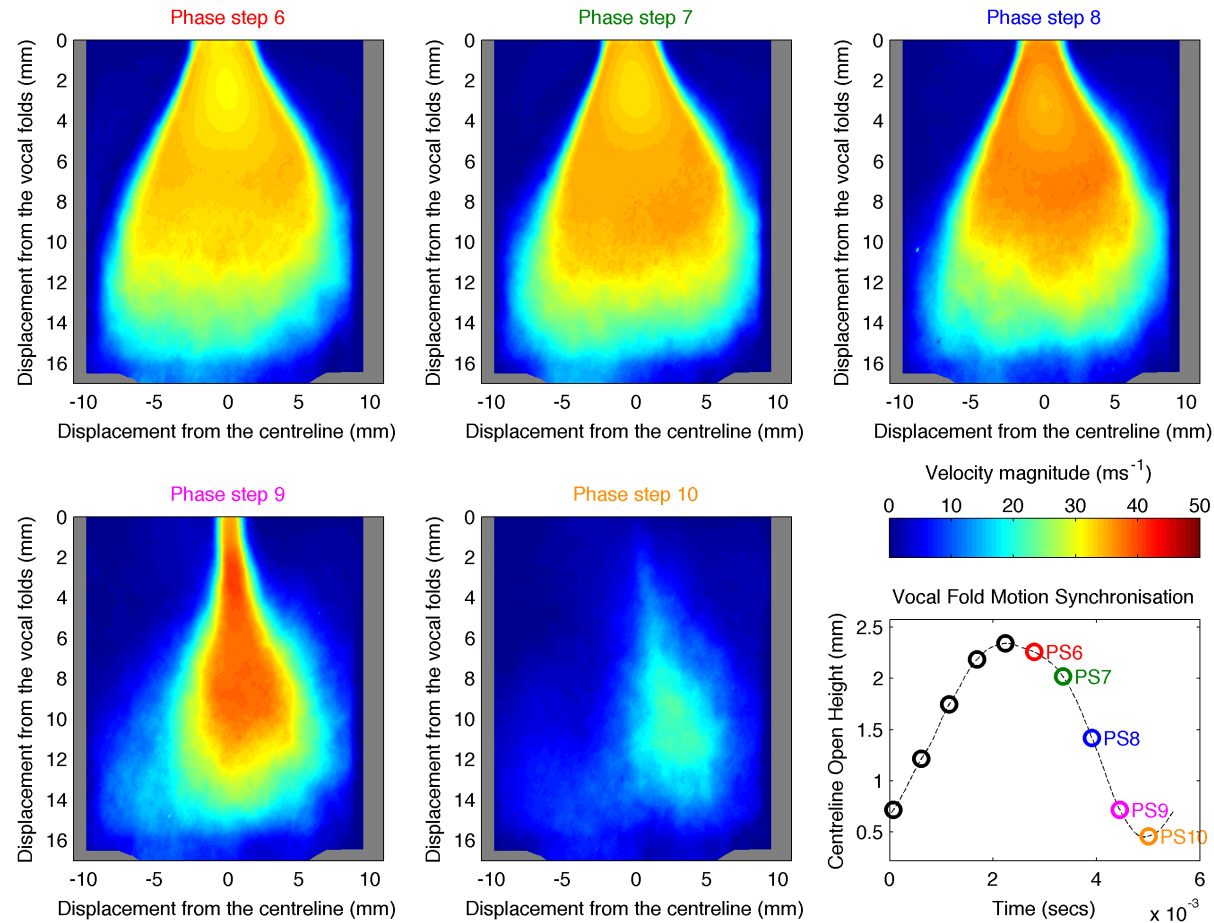


Figure 5.28: Ensemble-averaged velocity magnitude data for phase steps 6 - 10 on an *in vitro* model of the human larynx **with rigid ventricular bands placed 16 mm downstream of the vocal folds with an 8 mm separation**. The positions of the phase steps in relation to the centreline open height of the vocal fold model are included. $P_{sub} = 802 \text{ Pa}$. Only the top of the ventricular bands are shown in these plots, the reported separation is the minimum constriction formed by the bands further downstream.

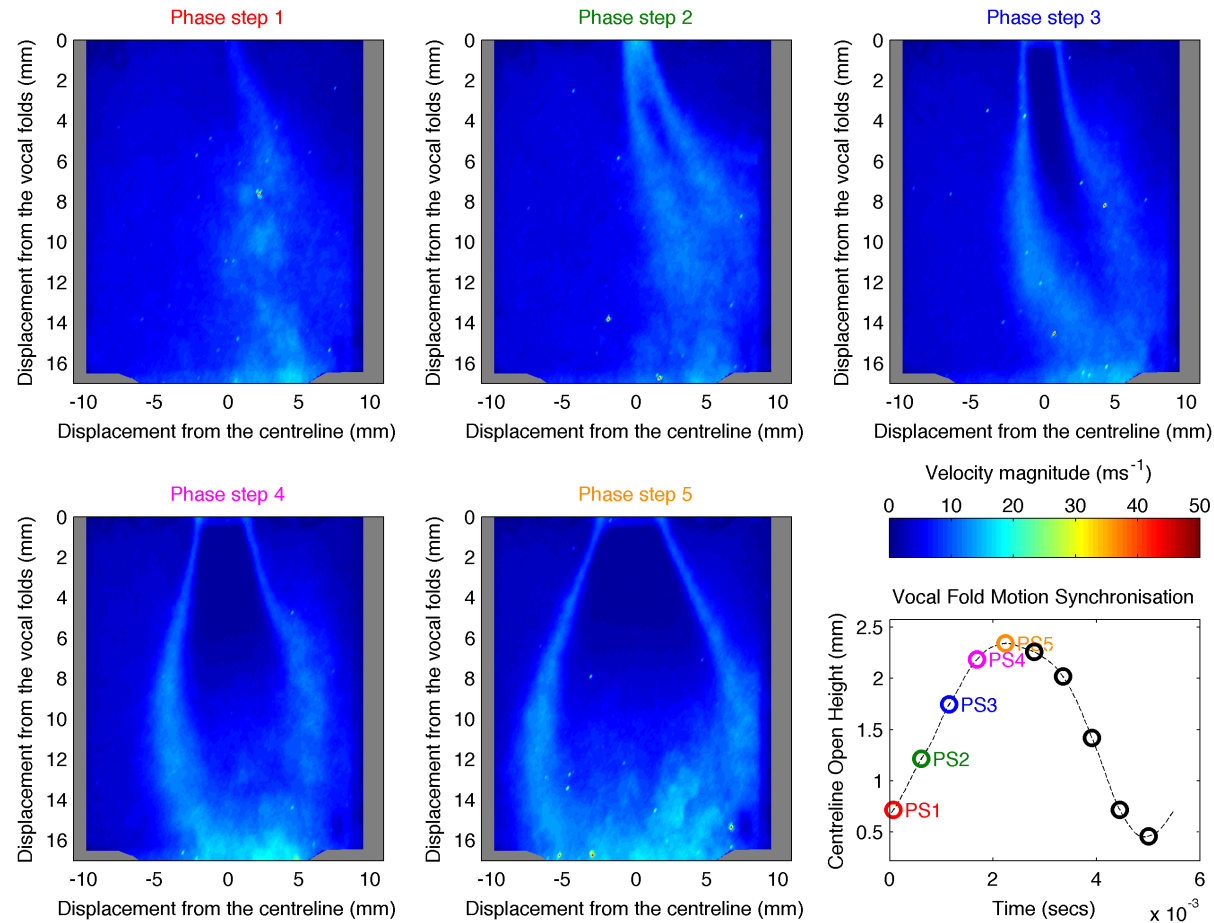


Figure 5.29: Standard deviation of the ensemble-averaged velocity magnitude data for phase steps 1 - 5 on an *in vitro* model of the human larynx **with rigid ventricular bands placed 16 mm downstream of the vocal folds with an 8 mm separation**. The positions of the phase steps in relation to the centreline open height of the vocal fold model are included. $P_{sub} = 802$ Pa. Only the top of the ventricular bands are shown in these plots, the reported separation is the minimum constriction formed by the bands further downstream.

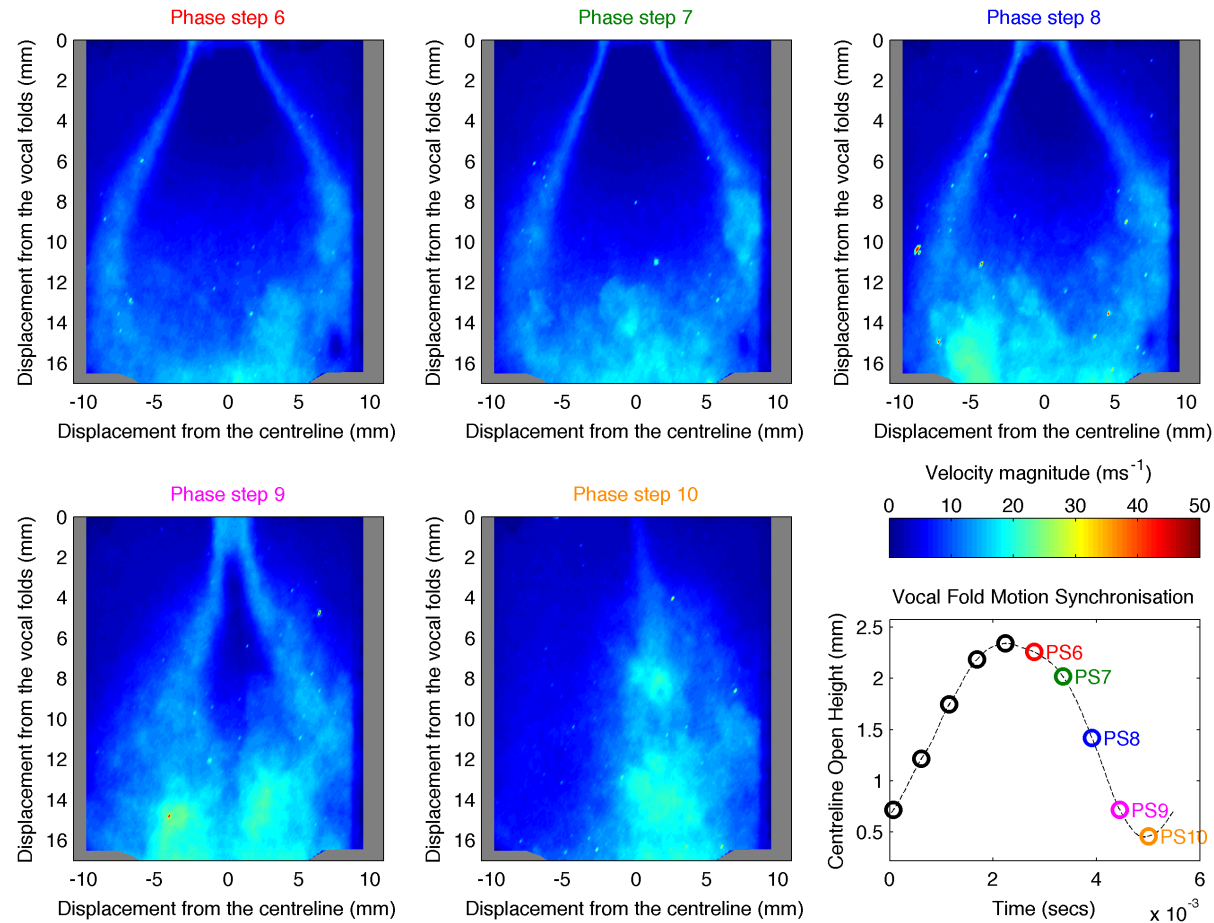


Figure 5.30: Standard deviation of the ensemble-averaged velocity magnitude data for phase steps 6 - 10 on an *in vitro* model of the human larynx **with rigid ventricular bands placed 16 mm downstream of the vocal folds with an 8 mm separation**. The positions of the phase steps in relation to the centreline open height of the vocal fold model are included. $P_{sub} = 802$ Pa. Only the top of the ventricular bands are shown in these plots, the reported separation is the minimum constriction formed by the bands further downstream.

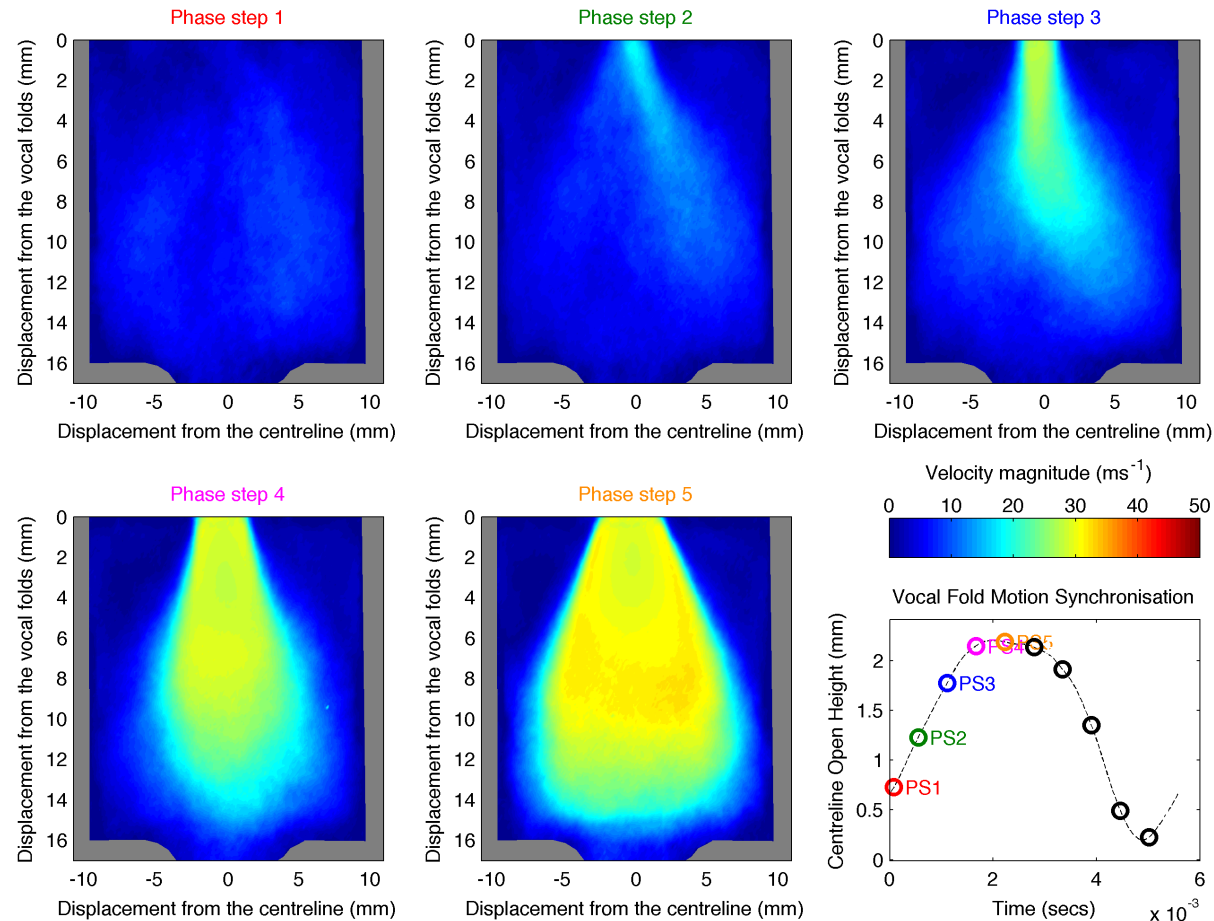


Figure 5.31: Ensemble-averaged velocity magnitude data for phase steps 1 - 5 on an *in vitro* model of the human larynx **with rigid ventricular bands placed 16 mm downstream of the vocal folds with a 3 mm separation**. The positions of the phase steps in relation to the centreline open height of the vocal fold model are included. $P_{sub} = 805$ Pa. Only the top of the ventricular bands are shown in these plots, the reported separation is the minimum constriction formed by the bands further downstream.

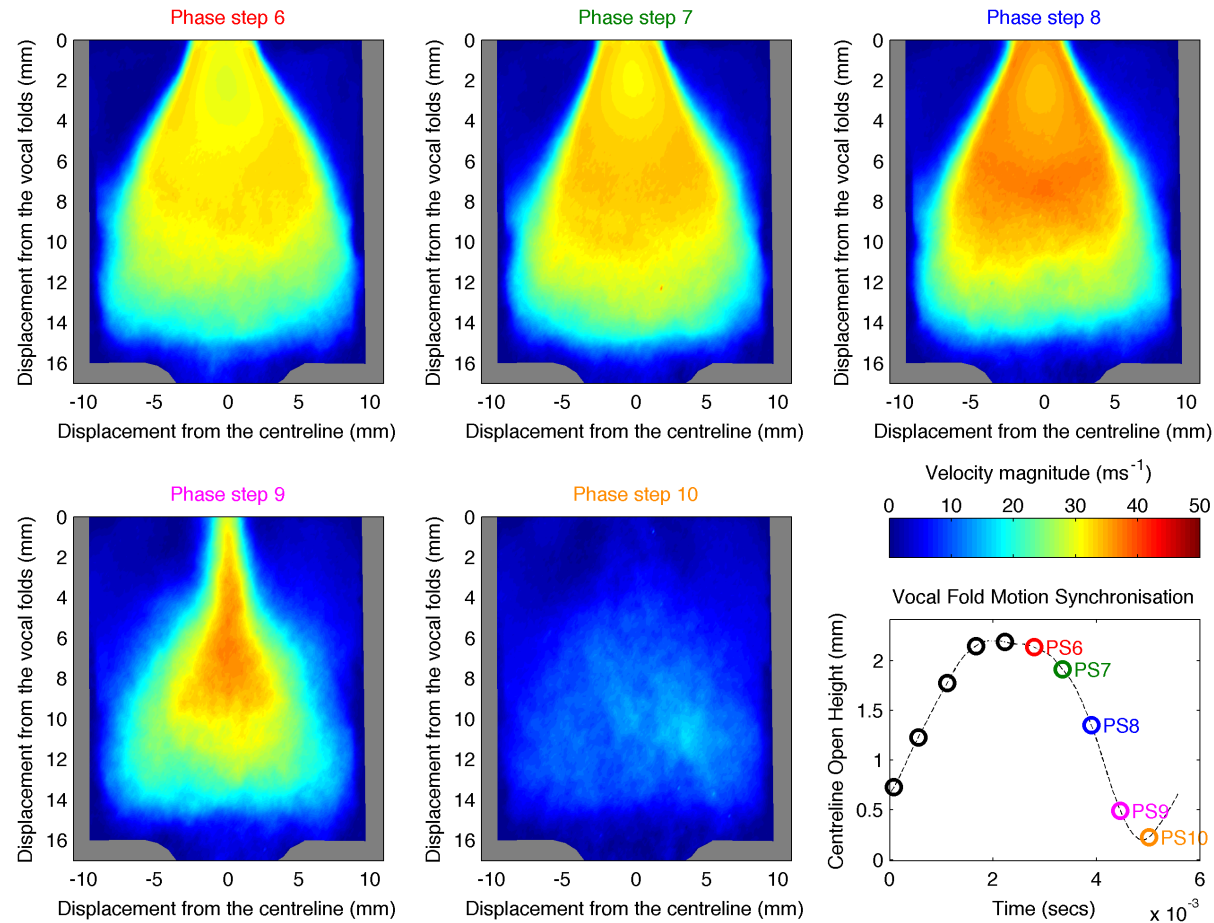


Figure 5.32: Ensemble-averaged velocity magnitude data for phase steps 6 - 10 on an *in vitro* model of the human larynx **with rigid ventricular bands placed 16 mm downstream of the vocal folds with a 3 mm separation**. The positions of the phase steps in relation to the centreline open height of the vocal fold model are included. $P_{sub} = 805$ Pa. Only the top of the ventricular bands are shown in these plots, the reported separation is the minimum constriction formed by the bands further downstream.

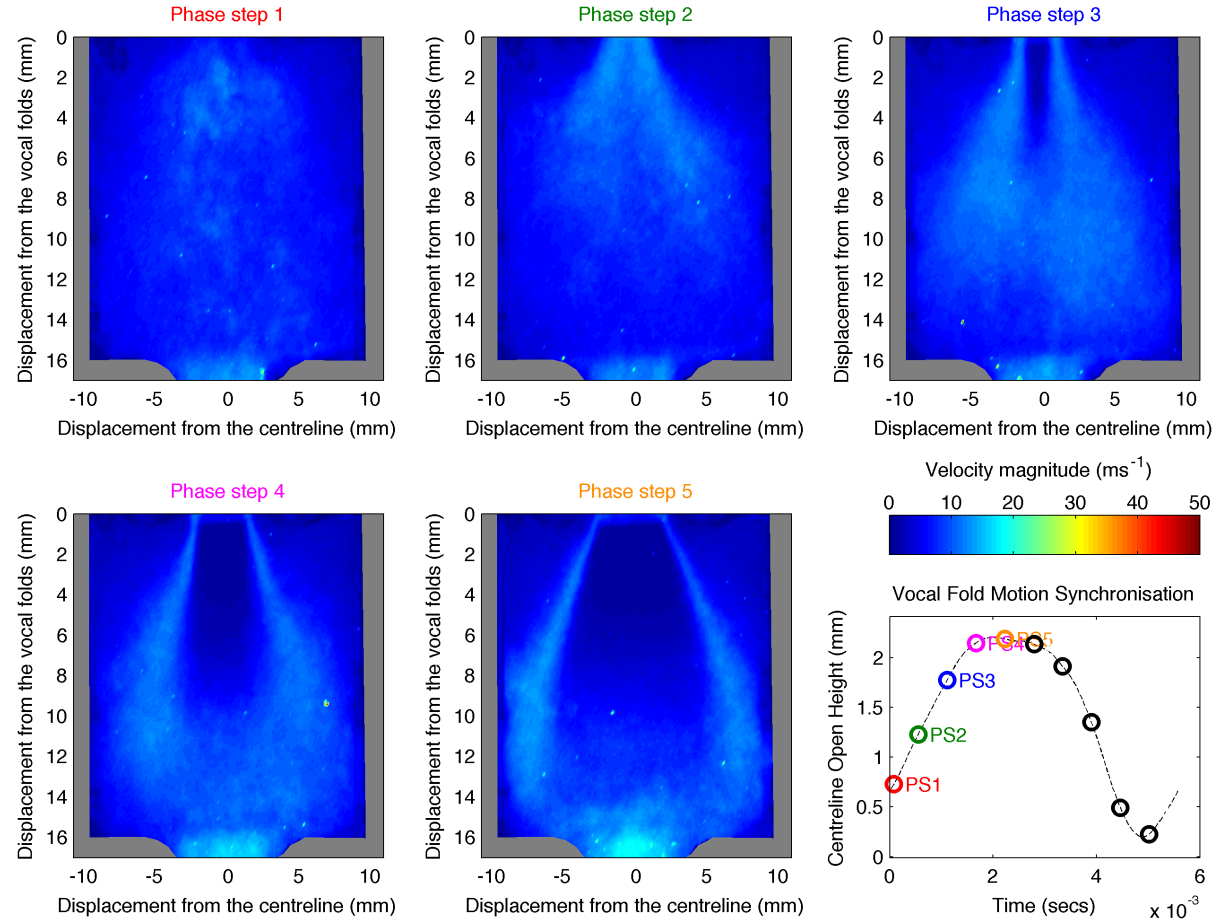


Figure 5.33: Standard deviation of the ensemble-averaged velocity magnitude data for phase steps 1 - 5 on an *in vitro* model of the human larynx **with rigid ventricular bands placed 16 mm downstream of the vocal folds with a 3 mm separation**. The positions of the phase steps in relation to the centreline open height of the vocal fold model are included. $P_{sub} = 805$ Pa. Only the top of the ventricular bands are shown in these plots, the reported separation is the minimum constriction formed by the bands further downstream.

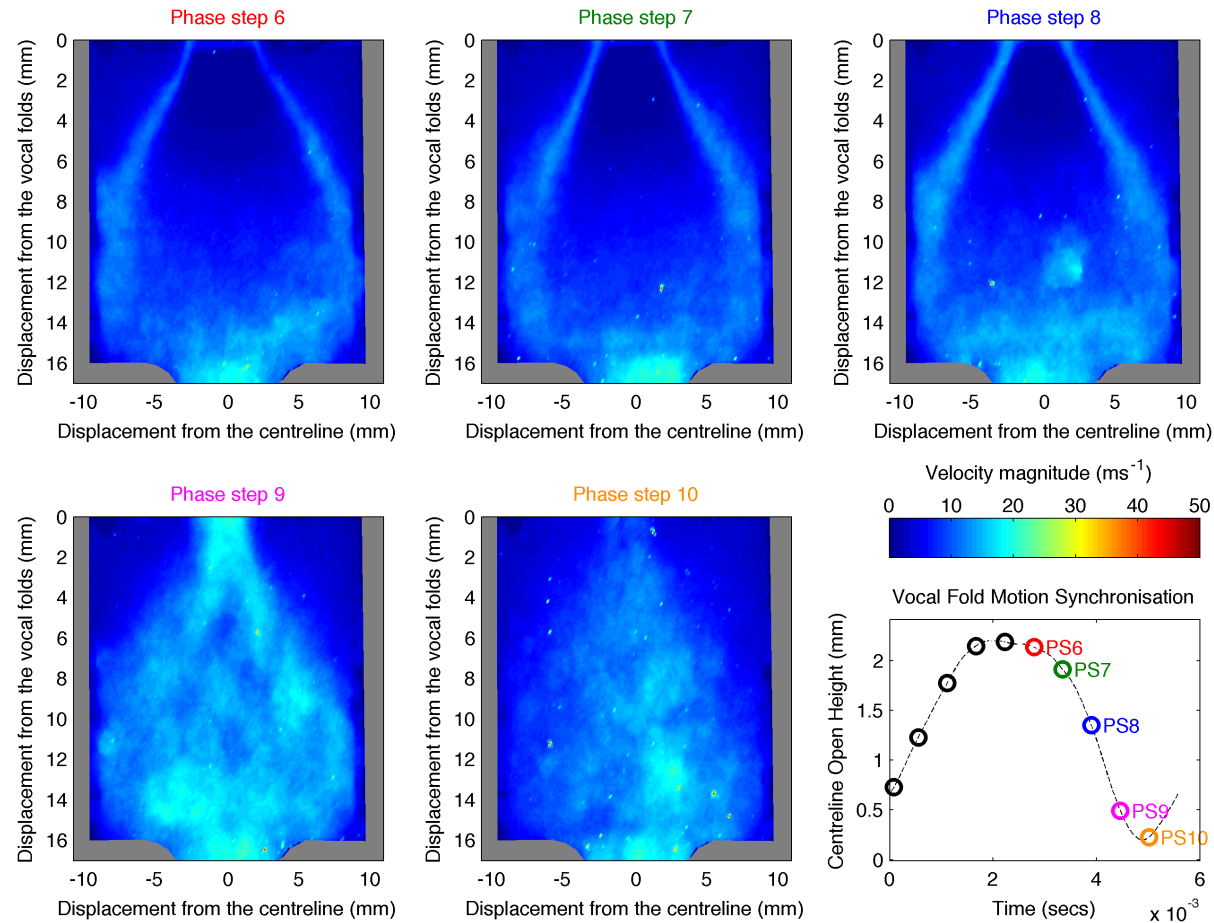


Figure 5.34: Standard deviation of the ensemble-averaged velocity magnitude data for phase steps 6 - 10 on an *in vitro* model of the human larynx **with rigid ventricular bands placed 16 mm downstream of the vocal folds with a 3 mm separation**. The positions of the phase steps in relation to the centreline open height of the vocal fold model are included. $P_{sub} = 805$ Pa. Only the top of the ventricular bands are shown in these plots, the reported separation is the minimum constriction formed by the bands further downstream.

5.6. RESULTS FOR *IN VITRO* MODEL WITH RIGID VENTRICULAR BANDS

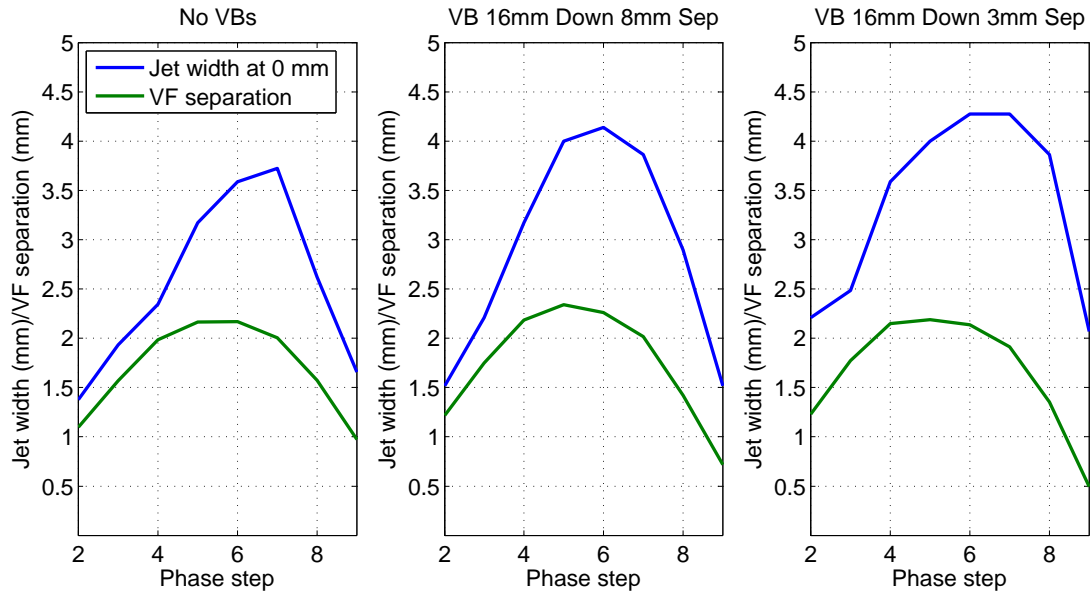


Figure 5.35: A plot showing the measured width of the glottal jet and the opening of the vocal folds for a self-oscillating *in vitro* model of the human larynx with no ventricular bands (*left*), a model with ventricular bands 16 mm downstream of the vocal folds with an 8 mm separation (*centre*), and a model with ventricular bands 16 mm downstream of the vocal folds with a 3 mm separation (*right*).

5.6.3 Jet Deflection and Centreline Calculation

Shown in Figures 5.36 and 5.37 are histograms displaying the calculated deflection angles of the glottal jets across phase steps 2 - 9 for the *in vitro* model with ventricular bands with an 8 mm separation and a 3 mm separation. Comparing Figure 5.36 with Figure 5.22, it is very clear that there is a definite skew to the right (indicated by a positive deflection angle) of the glottal jet centreline. This is most clearly shown in phase step 2 where a significant proportion of the measured glottal jet centreline deflection angles have values over 10° . This correlates closely with what is observed in the ensemble-averaged velocity magnitude for this phase step and setup. What is also intriguing is that the range of jet centrelines in phase steps 3 - 9 for the case with ventricular bands at 8 mm separation when compared to the case without ventricular bands is much less, indicating that although the Coandă effect is observed taking place the jet centreline angle appears to be more consistent. A similarity between the two

5.6. RESULTS FOR *IN VITRO* MODEL WITH RIGID VENTRICULAR BANDS

cases is that a wider range of jet deflection angle values exists for phase steps 2 and 9 than for other phase steps.

When comparing Figures 5.36 and 5.37, several key differences are apparent. One of the most discernible is the jet flapping observed in phase steps 2, 3, and 9, indicated by the large range of jet centreline deflection angles shown indiscriminantly either side of 0° . This confirms the hypothesis for observation of the unclear glottal jet in phase step 2 from Figure 5.31 with a high standard deviation shown in Figure 5.34 surrounding the jet which indicated that this was due to jet flapping. It also transpires that the thicker shear layers seen in phase step 3, and increased standard deviation in phase step 9 is due to jet flapping seen in Figure 5.37. As the phonatory cycle progresses from phase step 2 - 5 in Figure 5.37, the range of jet deflection angles per phase step reduces indicating that the jet no longer flaps from side to side and stabilises. From phase steps 6 - 8 the glottal jet appears to remain stable; however, with the range of jet deflection angles being greater than those seen for the corresponding phase steps in Figure 5.36, jet is interpreted as not being as stable. This flapping may be due to the change in the volume flow through the larynx caused by the constriction posed by the ventricular bands. This may then have an impact on pressure gradient across laryngeal ventricle which could then affect the point of flow separation of glottal jet and hence the oscillation of the vocal folds.

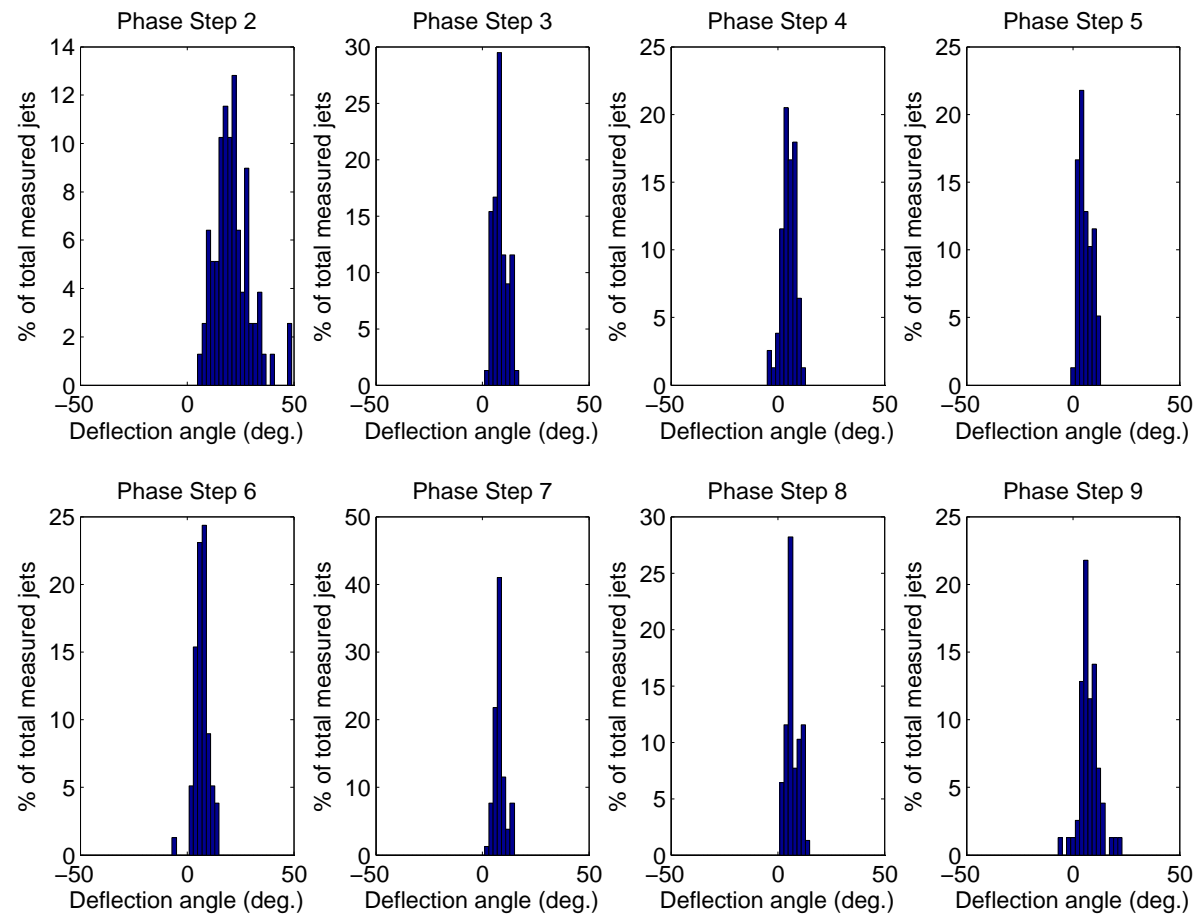


Figure 5.36: A series of histograms showing the jet deflection angle against the total percentage of measured jet centrelines, organised by phase step, for an *in vitro* model of the larynx **with ventricular bands placed 16 mm downstream of the vocal folds with an 8 mm separation.**

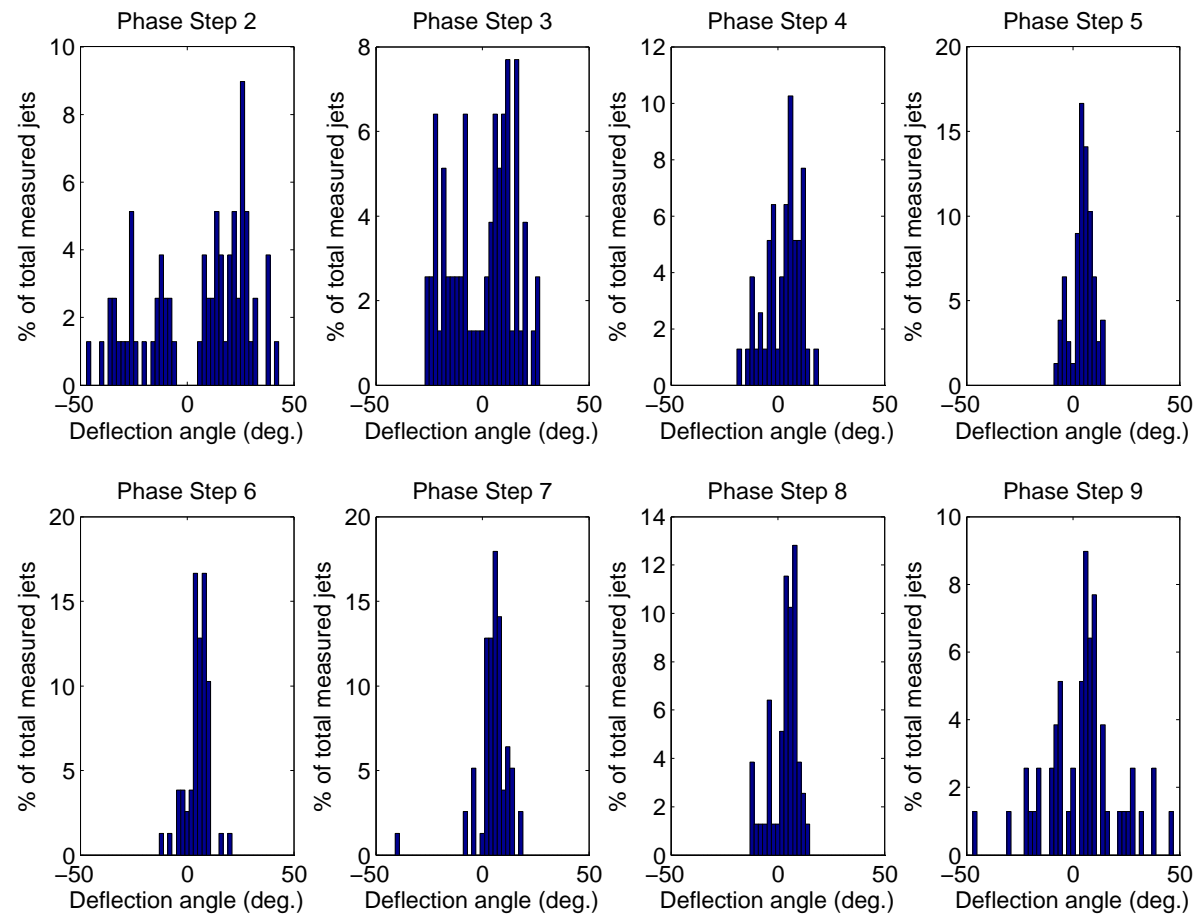


Figure 5.37: A series of histograms showing the jet deflection angle against the total percentage of measured jet centrelines, organised by phase step, for an *in vitro* model of the larynx **with ventricular bands placed 16 mm downstream of the vocal folds with a 3 mm separation.**

5.6. RESULTS FOR *IN VITRO* MODEL WITH RIGID VENTRICULAR BANDS

5.6.4 Expansion of the Glottal Jet

The results of the half-width glottal jet expansion angle measurements are summarised in Table 5.9. Having seen marked differences between jet core velocity and glottal open height measurements made from the two *in vitro* model setups, no major difference in the expansion angle was observed. An explicit difference is noted between the two values of θ_{jet} for the two setups and a difference between phase steps 3 and 9, but these are probably due to the jet flapping identified earlier. The values of θ_{jet} for the setup with ventricular bands separated by 8 mm and those for the model without ventricular bands are very close. These are also similar to the values shown for the setup with ventricular bands separated by 3 mm if the phase steps previously mentioned are ignored. Therefore, the ventricular bands are not shown as having an impact on the expansion angle of the glottal jet in this *in vitro* model.

	8 mm Separation		3 mm Separation	
Phase Step	θ_{jet} (°)	R^2	θ_{jet} (°)	R^2
2	12.5	0.949	27.7	0.974
3	13.1	0.960	19.8	0.960
4	20.0	0.993	19.3	0.997
5	24.0	0.999	23.6	0.998
6	26.6	0.996	27.1	0.995
7	26.3	0.997	26.2	0.997
8	26.6	0.996	27.2	0.998
9	20.7	0.941	22.5	0.942

Table 5.9: Table showing the half-width expansion angles (θ_{jet}) of the jet and the regression coefficient for the line fitted (R^2) across phase steps 2 - 9 in PIV runs using a self-oscillating *in vitro* model of the larynx with rigid ventricular bands placed 16 mm downstream of the vocal folds with an 8 mm and 3 mm separation respectively.

5.6.5 Dimensional Analysis

Using the well-established non-dimensional parameters discussed previously, the results for the dimensional analysis of the 3 model setups (no ventricular bands,

5.6. RESULTS FOR *IN VITRO* MODEL WITH RIGID VENTRICULAR BANDS

ventricular bands with an 8 mm separation, and ventricular bands with a 3 mm separation) are shown in Figures 5.38 and 5.39. The results from the 3 setups are included on the same plots so that similarities and differences between them are more easily discernible. Considering the top left hand plot in Figure 5.38 illustrating the variation of T_{core} against phase step shows that the presence of the ventricular bands with an 8 mm separation produces lower values for T_{core} than for the case without ventricular bands. Conversely, the presence of the ventricular bands with a 3 mm separation produces higher values for T_{core} than for the case without ventricular bands. This result does not agree with those shown in [Newton 09] in which Newton identifies that the ventricular bands with a 3 mm separation placed 16 mm downstream of the vocal folds reduces the jet core turbulence. A possible reason for the departure in these results could be the jet flapping already identified in phase steps 2, 3, and 9. As has already been seen, this has impact of increasing the thickness of the shear layers shown in the standard deviation of the ensemble-averaged velocity magnitude data for these phase steps and, by extension, increases the measured value of T_{core} . In addition, the values of T_{core} for the model with ventricular bands at both 3 mm and 8 mm separations are substantially lower than those quoted in [Newton 09]. Possible reasons for this have already been attributed to the phase windowing technique and to the position at which Newton measured the jet core due to experimental constraints.

The next plot in the top right hand corner shows the variation of T_{core} against h/h_{max} . What is shown is a strong hysteresis behaviour, as seen for the case without ventricular bands. However, the hysteresis is only apparent in phase steps 2, 3, and 9, as the values of T_{core} for the other phase steps are very similar. The bottom left hand plot shows the variation of Re_{core} against h/h_{max} . The values of Re_{core} for the model with ventricular bands with an 8 mm separation range from 1929 to 4786, and for the model with ventricular bands with a 3 mm separation from 1253 to 4316. The cases with ventricular bands show the same hysteresis shape seen and display similar values for Re_{core} , although lower values are displayed for phase steps 2 and 9 in the case with ventricular bands separated by 3 mm. The reason for this may be due to the jet flapping observed previously which will reduce the ensemble-averaged velocity magnitude of the jet core and, by definition, thereby reducing Re_{core} . The final plot of this figure in the bottom right hand corner shows T_{core} against Re_{core} . Once again, hysteresis behaviour is observed just as for the case without ventricular bands; however, between

5.6. RESULTS FOR *IN VITRO* MODEL WITH RIGID VENTRICULAR BANDS

Re_{core} values between 4000 and 5000 the values of T_{core} appears to be almost the same for all cases. This would indicate that observed hysteresis behaviour in the jet core turbulence may be due to effects observed when the fluid properties of the jet core are in the transitional and laminar regions.

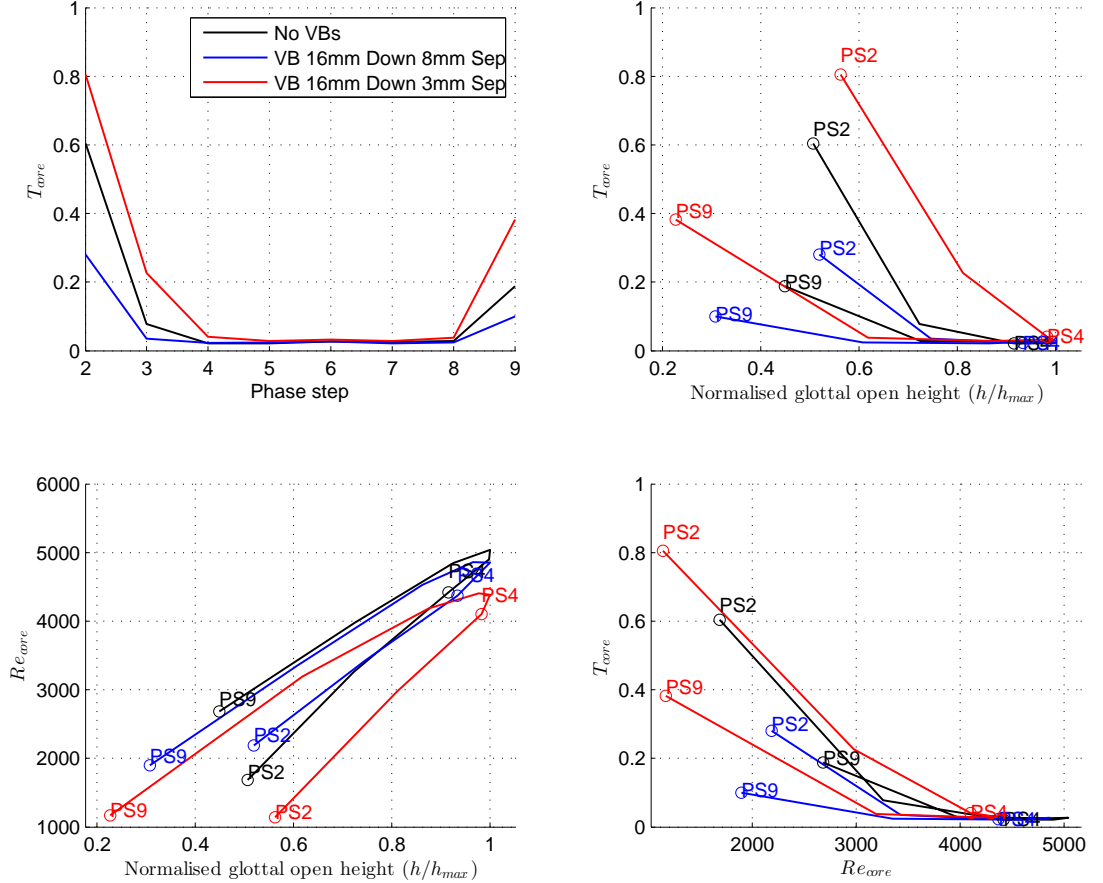


Figure 5.38: Non-dimensional flow parameter parametric plots illustrating changes in turbulence and the Reynolds number across established phase steps for a self-oscillating *in vitro* model of the human larynx with no ventricular bands and with rigid ventricular bands placed 16 mm downstream of the vocal folds with 8 mm and 3 mm separations. Phase steps 2, 4, and 9 are highlighted.

The evolution of u_{norm} against h/h_{max} is shown in the top left hand plot of Figure 5.39. The behaviour of both cases with ventricular bands is hysteresis-like, showing a strong similarity to the case without ventricular bands. However, the general values of u_{norm} are less than those for the case without ventricular bands. This is further

5.6. RESULTS FOR *IN VITRO* MODEL WITH RIGID VENTRICULAR BANDS

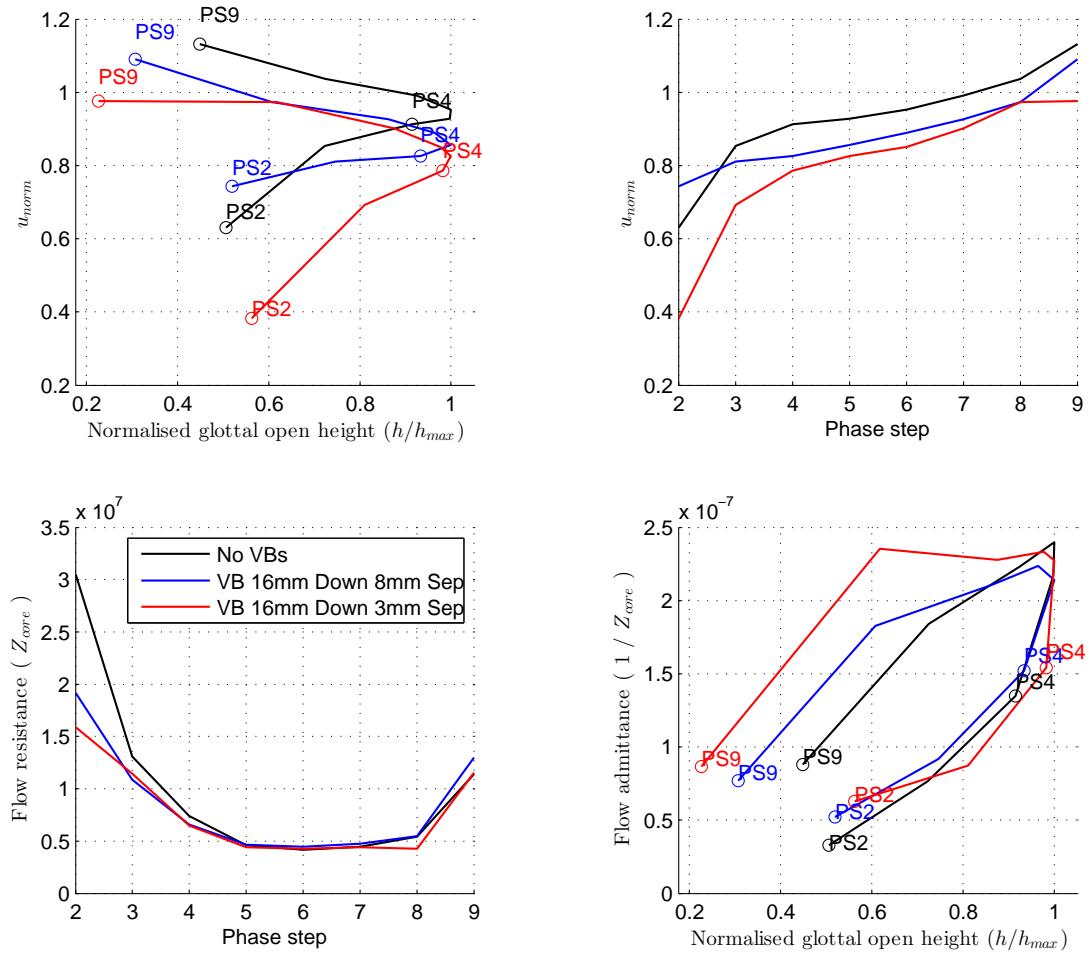


Figure 5.39: Non-dimensional flow parameter parametric plots illustrating changes in jet speed and flow admittance and resistance across established phase steps for a self-oscillating *in vitro* model of the human larynx with no ventricular bands and with rigid ventricular bands phased 16 mm downstream of the vocal folds with 8 mm and 3 mm separations. Phase steps 2, 4, and 9 are highlighted.

5.6. RESULTS FOR *IN VITRO* MODEL WITH RIGID VENTRICULAR BANDS

clarified in the plot displaying u_{norm} against phase step. A possible reason for this is that discussed earlier in Section 5.6.2 where a general reduction in the ensemble-averaged velocity magnitude for the glottal jet was identified. The values of u_{norm} for the model with ventricular bands separated by 3 mm are all lower than those for the model with ventricular bands separated by 8 mm, indicating that the narrowing of the ventricular bands reduces the jet core velocity. This could also be an indication of a pressure recovery taking place at the ventricular bands for the model configurations containing these. This hypothesis is further corroborated by the bottom left hand plot of flow resistance against phase step and by flow admittance against normalised glottal open height, where the flow admittance for a given glottal is found to be higher for the case with ventricular bands than that without, particularly in for the model with ventricular bands separated by 3 mm.

5.6.6 Summary

In this section, the impact of the ventricular bands on the glottal jet in comparison to all the measurements made in Section 5.5 for the *in vitro* model without ventricular bands is considered. Firstly, through the use of the high-speed camera the ventricular bands were shown to decrease the minimum opening height of the vocal folds and increase inward ‘bowing’ in the model where full closure of the vocal folds during phonation was not observed. This is a significant finding as it provides an alternative explanation as to why elderly patients suffering from vocal fold ‘bowing’ and associated dysphonia might engage supraglottic structures during phonation, as identified in [Hagen 96]. The ventricular bands are seen to assist in vocal fold closure which would be expected to improve voice quality. The presence of the ventricular bands were also observed to lower the fundamental frequency of oscillation for the vocal folds and increased the standard deviation of the mean of f_0 , thereby affecting the stability of the model’s oscillation. The drop in f_0 is also observed both experimentally and computationally (using linear stability analysis) by other authors when the separation between the ventricular bands is reduced.

The expansion geometry of the glottal jet for the model with ventricular bands appeared very similar to that for the model without ventricular bands; showing a linear jet expansion commensurate with the turbulent jet expansion hypothesis (notably more so for some phase steps than for others). Beyond one or two values which

5.7. RESULTS FROM COMPUTATIONAL PHYSICAL MODEL SIMULATIONS

were larger than expected, caused by suspected jet flapping, for the model with ventricular bands separated by 3 mm, the expansion angles of the glottal jet were very similar to those measured for model without ventricular bands. The Coandă effect and jet flapping were observed taking place with models containing ventricular bands. However, no such effects were observed for measurements made in the case without ventricular bands. Whether or not this is a crucial part of vocal fold self-sustained oscillation is not clear, but these certainly are features of the glottal jets seen in this section. Finally, comparisons were made between the *in vitro* model with and without ventricular bands for a raft of non-dimensional parameters. These comparisons highlighted that a pressure recovery may be taking place at the ventricular bands, with a smaller separation between them causing a higher pressure recovery and that the same hysteresis behaviour identified for the model without ventricular bands was also present in the model with these included.

5.7 Results from Computational Physical Model Simulations

The computational physical models used to test hypotheses regarding the expansion of the glottal jet and dynamics of the vocal folds have been described previously in Section 3.7 along with the implementation of this model in Condor in Section 3.7.5. This novel approach using Condor to run large-scale parameter sweeps in order to find the oscillating mass value also produces other useful measures which indicate how the physical model behaves. However, it should be clear that not all the results from the model which are calculated as exhibiting a stable oscillation show behaviour which is that expected of vocal fold oscillation. For instance, considering the results in Figure 5.40 if the effective oscillating mass increases then the oscillation frequency of the vocal folds will be expected to drop. Also, for a stable oscillation the jitter and shimmer values associated with that value for the effective oscillating mass will be expected to be very low. In this figure, the areas of the graphs which are greyed out are those where the physical model is considered as exhibiting unphysical behaviour. By matching the frequency of oscillation of the physical model with that measured in the *in vitro* model, it is then possible to extract the value for the effective oscillating mass.

In this section, results showing the effect of the sampling rate at which the model

5.7. RESULTS FROM COMPUTATIONAL PHYSICAL MODEL SIMULATIONS

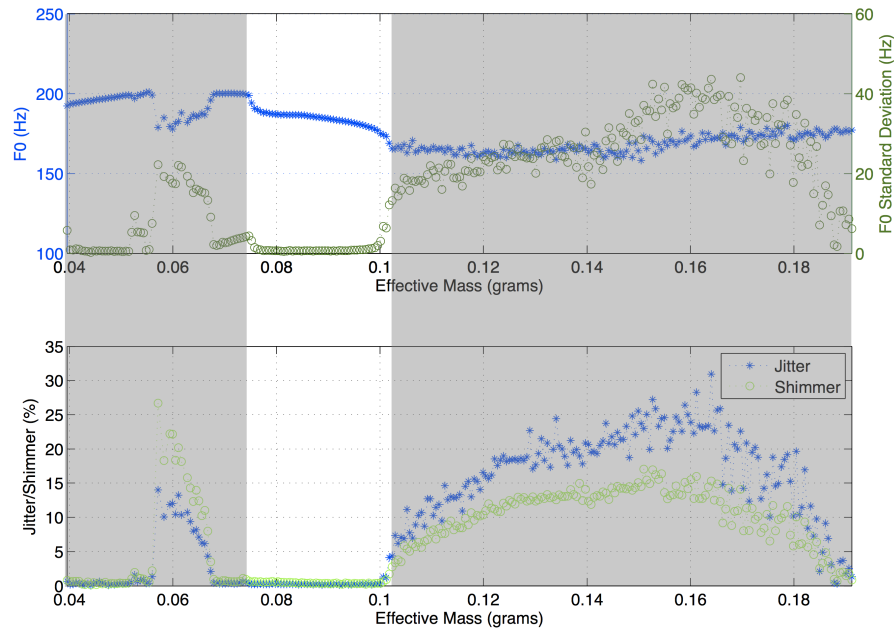


Figure 5.40: Results from a set of physical model simulations using Condor with the values which are considered to exhibit unphysical behaviour shaded in grey. Jitter and shimmer are defined within Section 3.7.5

is run will be discussed. In addition, results showing the effect of the ventricular bands on the behaviour of the model will be discussed along with the effect of aerodynamic changes also. Unfortunately, as no unsteady simulations produced results which exhibited stable and sustained oscillations for the simulation time then data using this flow model will not be present.

5.7.1 Impact of Sampling Rate in Simulations

The effect of the temporal sampling rate (defining the time-step size) on the results of simulations was considered after it was found that the results changed when the sampling rate was increased. Seen in Figures 5.41 - 5.43 are the results of sets of Condor simulations for the exact same physical model run at 5 different sampling rates. The sample rate of a simulation is an important parameter to consider, as if the exact same results are achievable with a lower sample rate, then running the simulation at this lower rate will require less computing time and therefore less power.

Firstly, Figure 5.41(a) shows the results using a sampling rate of 20 kHz. Using

5.7. RESULTS FROM COMPUTATIONAL PHYSICAL MODEL SIMULATIONS

this sampling rate, it is not possible to find a region where steady and stable oscillation takes place, as is identified in Figure 5.40. Figure 5.41(b) shows a similar behaviour to the previous figure, however, a small region of stability showing the correct physical behaviour can be seen between 0.090 g and 0.093 g. Figure 5.42(a) shows a fair degree of similarity to the last figure, but in this plot the area of stability is larger and extends over a different range: from 0.093 g to 0.097 g. Figures 5.42(b) and 5.43 produced very similar results, but again there are small differences between the two figures. The range of stability in these plots is 0.093 g - 0.120 g.

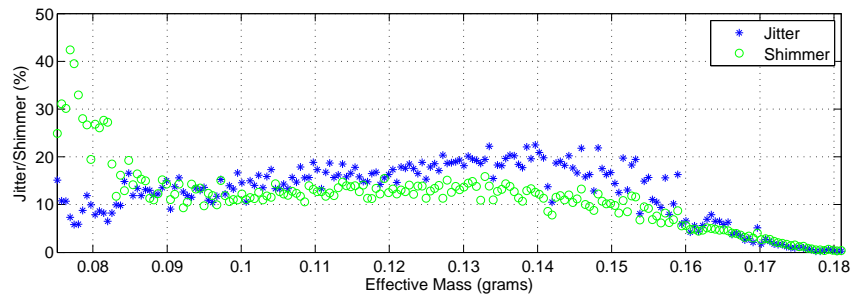
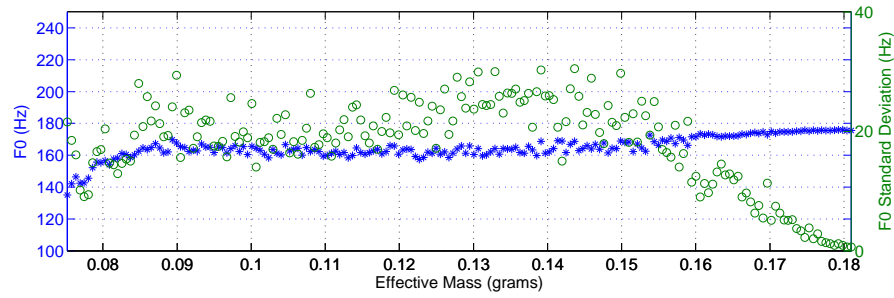
Finally, in Figure 5.44 is shown the results using a sampling rate of 20 kHz only with the output signal sample rate increased to 100 kHz using MATLAB's spline interpolation tools. The reason that this set of simulations was undertaken was to remove the difference between 100 kHz and 20 kHz data in the number of data points used to calculate the output parameters, therefore only considering the effect of the sampling rate on the physical model. The results are seen to be exactly the same as those shown in Figure 5.41(a), which indicates the sampling rate does affect the physical model. In order to account for this, the sampling rate for all other simulations was set at 100 kHz, so that this aspect does not affect future work.

5.7.2 Impact of Ventricular Bands in Simulations

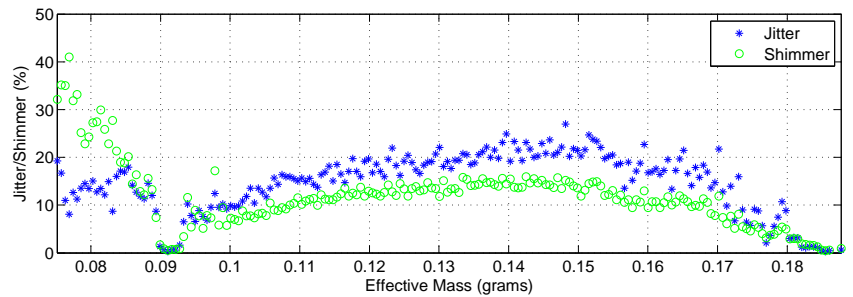
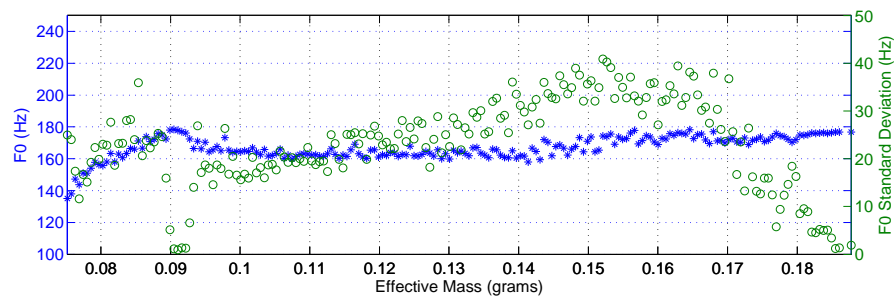
In order to consider the effect of the ventricular bands on the vocal folds, the simulations were run with all three setups of the physical model using the same flow model (Bernoulli quasi-steady with Poiseuille losses) and the same glottal jet expansion model. Having analysed the PIV results earlier in this chapter, the most appropriate model for the jet expansion is the turbulent model with a jet expansion angle of 21° . Figures 5.45 and 5.46 show the results of simulations using Condor for the three different setups of the physical model as discussed.

Analysing these plots, it is clear that there is no significant difference between the results for the setup with ventricular bands separated by 8 mm and the case without ventricular bands. However, there is a marked difference between the results for these two setups and the result for the setup with the ventricular bands separated by 3 mm. The most noticeable difference is that the region of stable and physical oscillation occurs over a substantially more limited range for the effective oscillating mass than is true for the other two setups. However, the frequency of oscillation for the

5.7. RESULTS FROM COMPUTATIONAL PHYSICAL MODEL SIMULATIONS



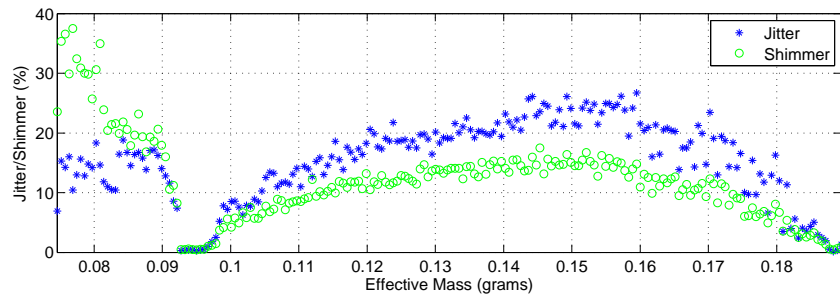
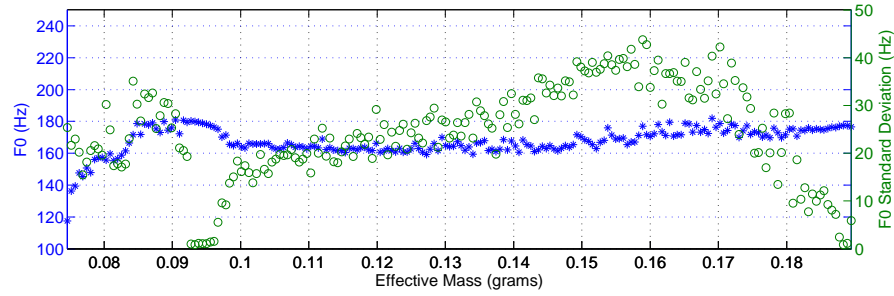
(a) physical model of the human larynx with ventricular bands placed 16 mm downstream with a 3 mm separation. Sampling rate = 20 kHz.



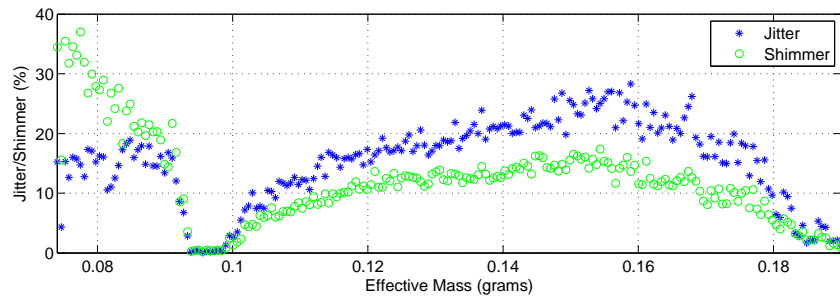
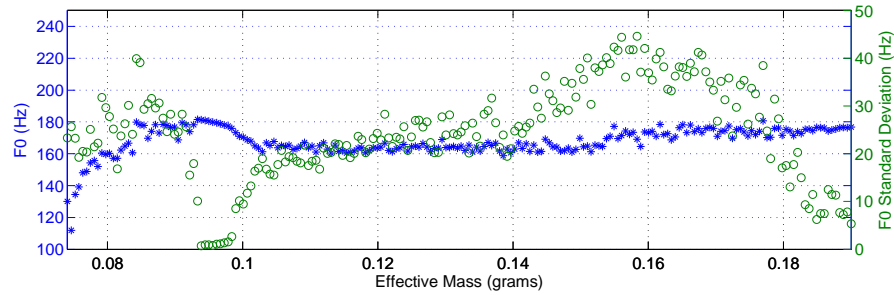
(b) physical model of the human larynx with ventricular bands placed 16 mm downstream with a 3 mm separation. Sampling rate = 40 kHz.

Figure 5.41: Results from a set of Condor simulations for the physical model using a Bernoulli steady flow model with Poiseuille losses, no jet pressure losses, and either a sampling rate of 20 kHz or 40 kHz.

5.7. RESULTS FROM COMPUTATIONAL PHYSICAL MODEL SIMULATIONS



(a) physical model of the human larynx with ventricular bands placed 16 mm downstream with a 3 mm separation. Sampling rate = 60 kHz.



(b) physical model of the human larynx with ventricular bands placed 16 mm downstream with a 3 mm separation. Sampling rate = 80 kHz.

Figure 5.42: Results from a set of Condor simulations for the physical model using a Bernoulli steady flow model with Poiseuille losses, no jet pressure losses, and either a sampling rate of 60 kHz or 80 kHz.

5.7. RESULTS FROM COMPUTATIONAL PHYSICAL MODEL SIMULATIONS

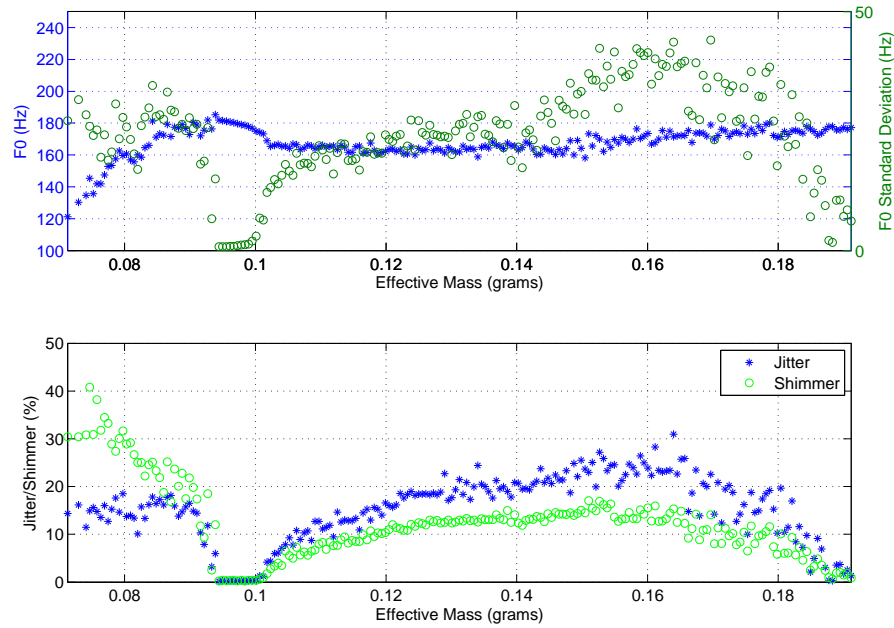


Figure 5.43: Results from a set of Condor simulations for the physical model with ventricular bands separated by 3 mm, placed 16 mm downstream using a Bernoulli steady flow model with Poiseuille losses, no jet pressure losses, and with a sampling rate of 100 kHz.

vocal folds within the regions of stability are the same for the values of the effective oscillating mass where these regions coincide. Therefore, the ventricular bands within the physical model are shown to have an impact on the oscillation of the vocal folds.

5.7.3 Impact of Empirical Aerodynamic Observations in Simulations

Having observed in the PIV results that the glottal jet geometry is most like that seen for the turbulent jet hypothesis, the other hypotheses were no longer considered. However, as has already been discussed, the expansion angle of the jet quoted ([Kundu 02, Bailly 08, Bailly 09, Newton 09]) at being 4° was not seen in the PIV results. Although the expansion angle was not constant throughout the phonatory cycle, the extent to which a change in the expansion angle of glottal jet affects the oscillation of the vocal folds in the computational physical model is of interest. In Figures 5.47 and 5.48, the same physical model configuration and flow model are

5.7. RESULTS FROM COMPUTATIONAL PHYSICAL MODEL SIMULATIONS

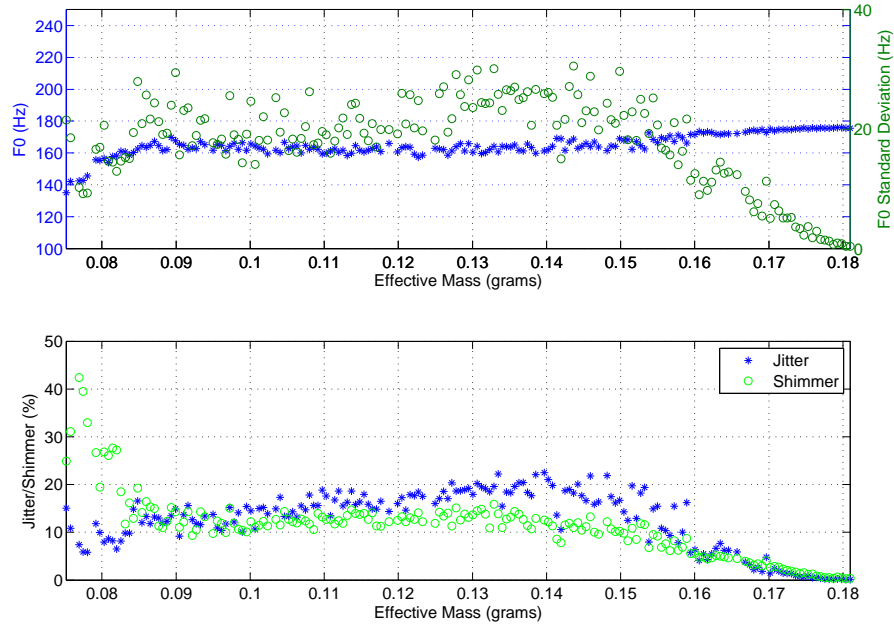
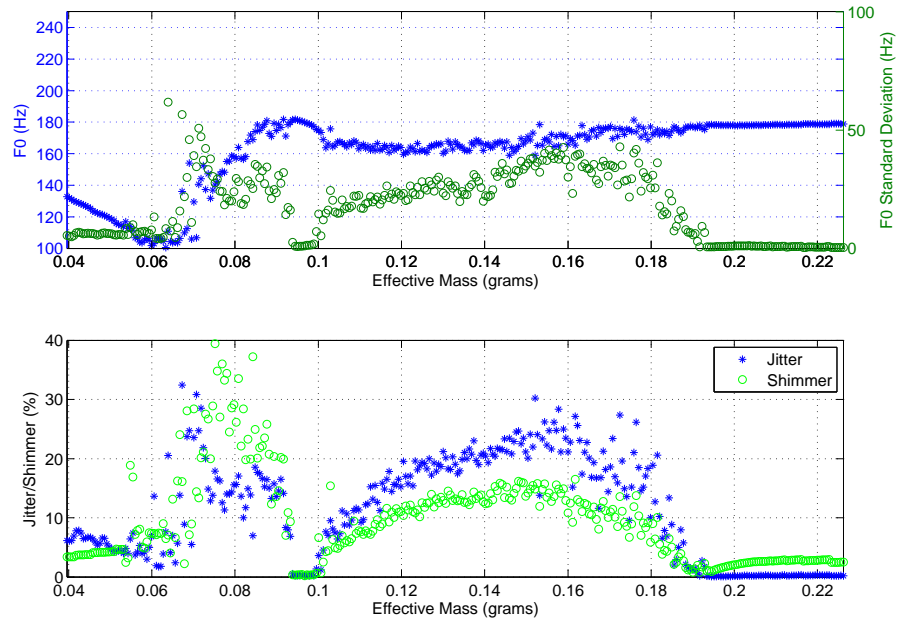


Figure 5.44: Results from a set of Condor simulations for the physical model with ventricular bands separated by 3 mm, placed 16 mm downstream using a Bernoulli steady flow model with Poiseuille losses, no jet pressure losses, and with a sampling rate of 20 kHz but with the number data points increased by a factor of 5 using spline interpolation.

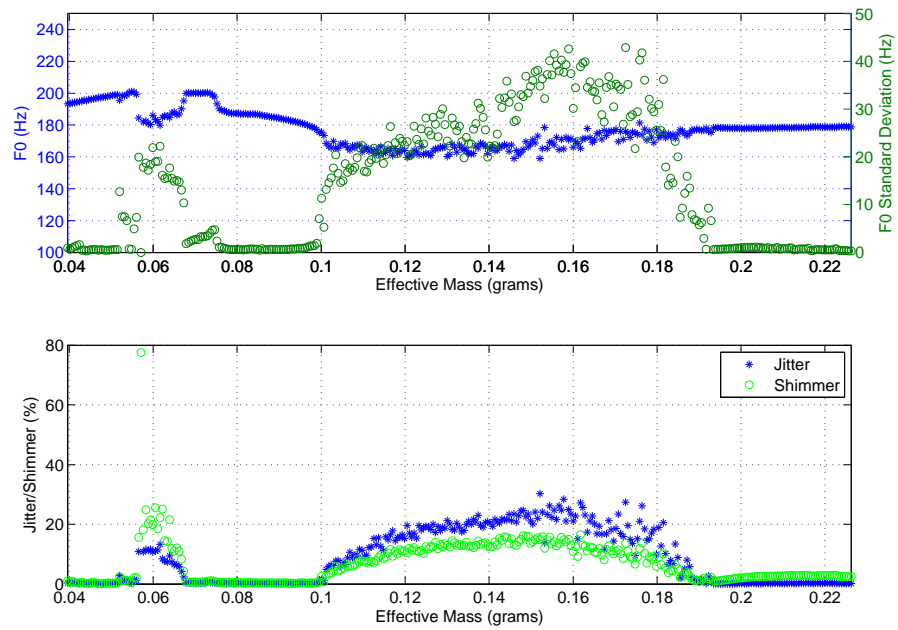
simulated with the only difference between the 3 sets of results being the value of θ_{jet} chosen. The values, 4° , 21° , and 26° were used. These values were chosen because they were either near the measured maximum jet expansion angle or they were lower, which provided an interesting comparison.

When comparing Figures 5.47 and 5.48 it is clear that changing the angle of expansion of the glottal jet using the turbulent jet hypothesis does have an impact on the oscillation of the vocal folds. However, the regions of stable and physical oscillation coincide at the same effective oscillating mass values and produce very similar frequencies of oscillation. It is therefore possible to conclude that although the vocal folds are affected by the change in the value of θ_{jet} the region of stability is unaffected by this change.

5.7. RESULTS FROM COMPUTATIONAL PHYSICAL MODEL SIMULATIONS



(a) physical model of the human larynx with ventricular bands placed 16 mm downstream with a 3 mm separation



(b) physical model of the human larynx with ventricular bands placed 16 mm downstream with an 8 mm separation

Figure 5.45: Results from two sets of Condor simulations for the physical model using a Bernoulli steady flow model with Poiseuille losses, and no jet pressure losses.

5.7. RESULTS FROM COMPUTATIONAL PHYSICAL MODEL SIMULATIONS

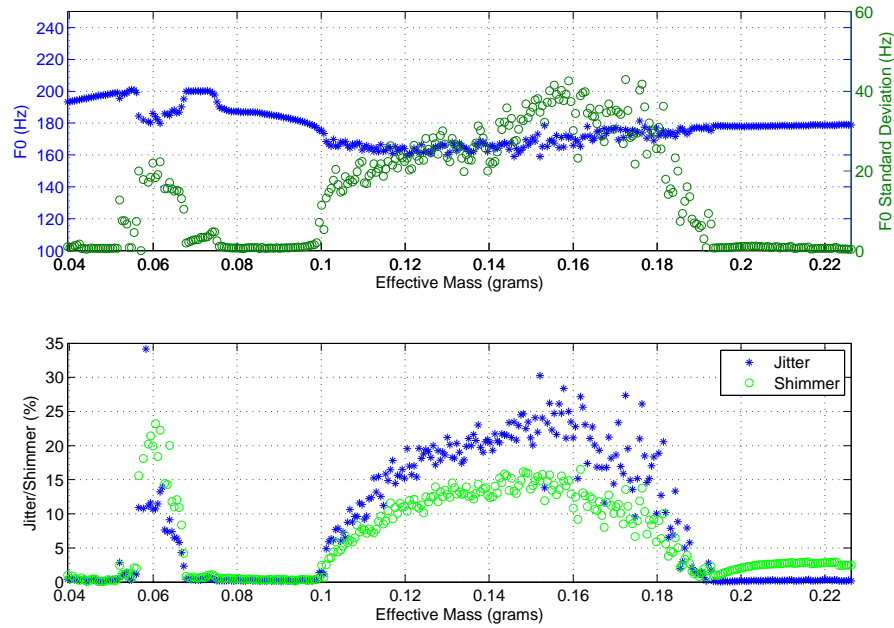


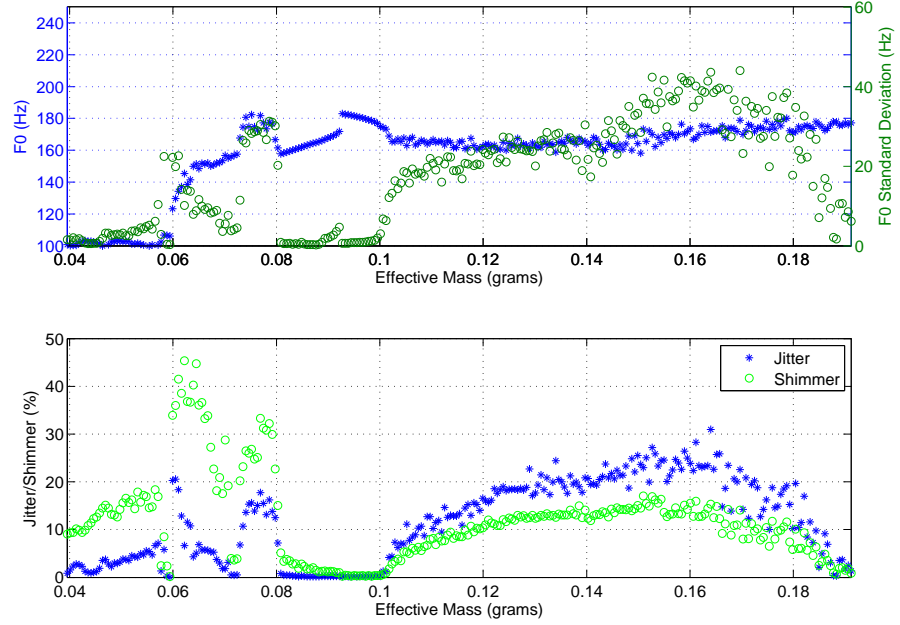
Figure 5.46: Results from a set of Condor simulations for the physical model with no ventricular bands using a Bernoulli steady flow model with Poiseuille losses, and no jet pressure losses.

5.7.4 Comparison Between Simulation and Experiment

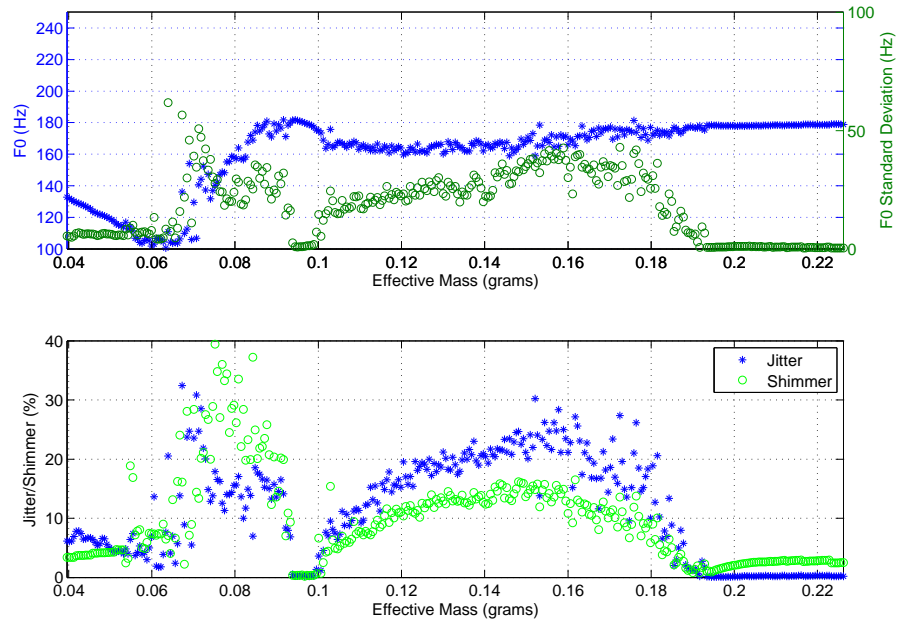
Finally, it is interesting to compare the widths of the glottal jet as measured from the PIV data shown earlier and that modelled using the turbulent glottal jet expansion hypothesis. This comparison provides a measure of how accurately modelled the glottal jet is by the expansion hypothesis and, if the values do not align completely, whether there are any patterns or trends in the data which can be further explored. The measured glottal jet will be compared to the jet hypothesis at 3 points: 0 mm, 4 mm, and 8 mm downstream of the vocal folds. Included in the upper part of each figure is a comparison between the measured centreline glottal open height (h_{vf}) and that produced by the physical model. The comparisons are made across all 10 phase steps.

In Figure 5.49 it is clear that the simulated glottal open height is consistently greater than that measured using the high-speed camera and *in vitro* model. This is particularly pronounced in phase steps 4 - 7 where the simulated glottal open height is just less than 1 mm greater. However, the general shape of the measured glottal open height is sufficiently represented by the simulated glottal open height. In the lower figure, a

5.7. RESULTS FROM COMPUTATIONAL PHYSICAL MODEL SIMULATIONS



(a) physical model of the human larynx with ventricular bands placed 16 mm downstream with a 3 mm separation with $\theta_{jet} = 4^\circ$.



(b) physical model of the human larynx with ventricular bands placed 16 mm downstream with a 3 mm separation with $\theta_{jet} = 21^\circ$.

Figure 5.47: Results from two sets of Condor simulations for the physical model using a Bernoulli steady flow model with Poiseuille losses, no jet pressure losses, and the turbulent jet expansion hypothesis.

5.7. RESULTS FROM COMPUTATIONAL PHYSICAL MODEL SIMULATIONS

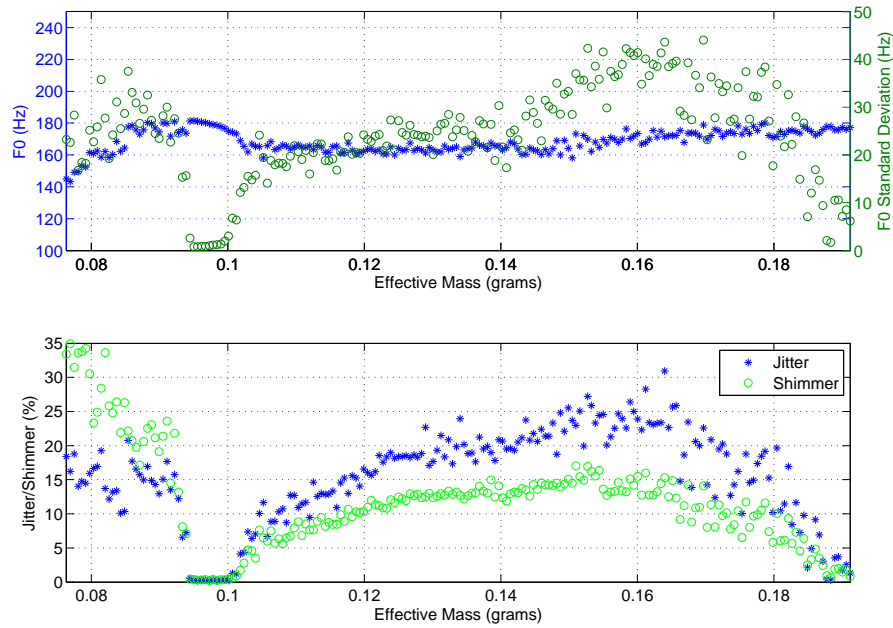


Figure 5.48: Results from a set of Condor simulations for the physical model with ventricular bands placed 16 mm downstream with a 3 mm separation using a Bernoulli steady flow model with Poiseuille losses, no jet pressure losses, and the turbulent jet expansion hypothesis with $\theta_{jet} = 26^\circ$.

comparison between hypothesised and measured glottal jet widths can be seen. Using the value $\theta_{jet} = 21^\circ$ a good representation of the jet measured at 0 mm downstream of the vocal folds is shown by the hypothesised glottal jet, with phase steps 2 - 5 being overestimated. As seen in the PIV results earlier, results for phase steps 1 and 10 in this comparison are not considered, as they exhibited no clear jet in the ensemble-averaged velocity magnitude flow field maps. However, beyond the phase steps 6 - 8 for the line measured 4 mm downstream of the vocal folds, the hypothesised glottal jet widths are not good representations of their measured counterparts. They grossly overestimate the width of the jet, thereby indicating that the turbulent jet expansion model used as proposed is not suitable.

Figure 5.50 shows the same information as the previous figure, only for a configuration with ventricular bands placed 16 mm downstream with an 8 mm separation. In the upper plot, the measured glottal open height is well-represented by that from the computational physical model. There is however a constant offset of approximately 0.3 mm but this could be due to the thresholding value chosen in

5.7. RESULTS FROM COMPUTATIONAL PHYSICAL MODEL SIMULATIONS

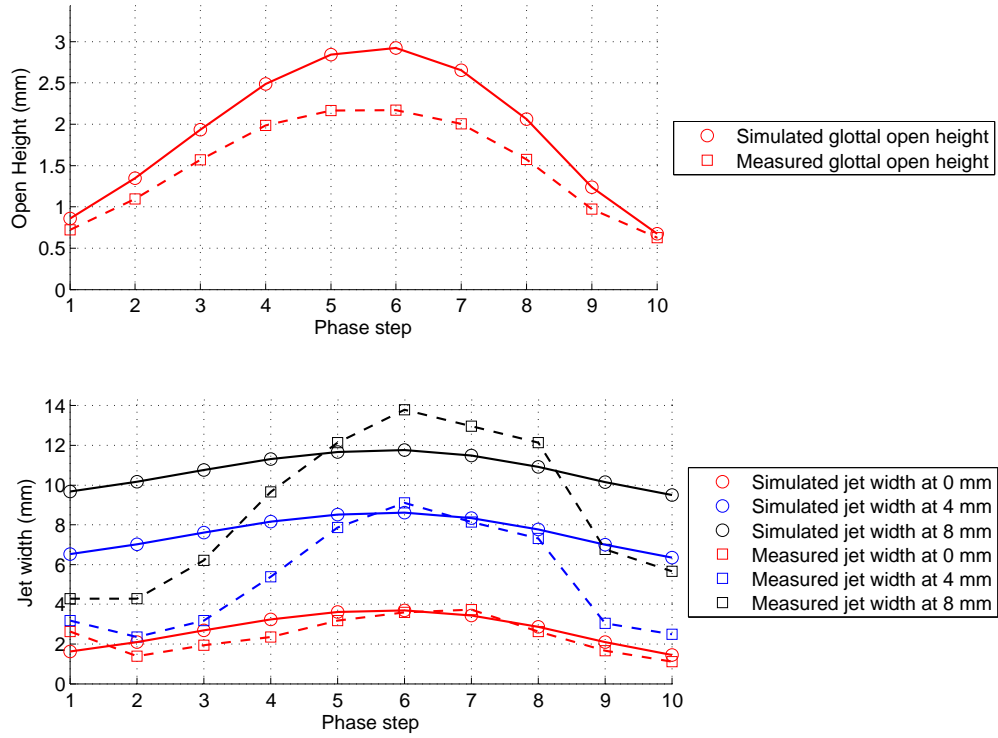


Figure 5.49: Comparison between the measured jet width from PIV data and that from a physical model without ventricular bands using a Bernoulli steady flow model with Poiseuille losses, no jet pressure losses, and the turbulent jet expansion hypothesis with $\theta_{jet} = 21^\circ$.

order to extract the glottal open height and area earlier. Geometrically, the shape of the simulated open height for this set up is closer to its measured counterpart than to that seen in Figure 5.49. Unfortunately, the width of the glottal jet from the *in vitro* model is not as well represented geometrically by the hypothesised value, with the jet width measured at 4 mm and 8 mm downstream poorly represented (except for phase steps 5 - 8 for the jet measured at 4 mm). This thereby further confirms that the turbulent jet expansion model in its current form is not suitable to replicate the expansion of the glottal jet.

Finally, in Figure 5.51 the same data can be found only for a configuration with ventricular bands placed 16 mm downstream with a 3 mm separation, and a turbulent jet expansion angle of 26° . The reason that this was chosen was because the values from the hypothesised jet widths using this value for θ_{jet} were closer to their measured

5.7. RESULTS FROM COMPUTATIONAL PHYSICAL MODEL SIMULATIONS

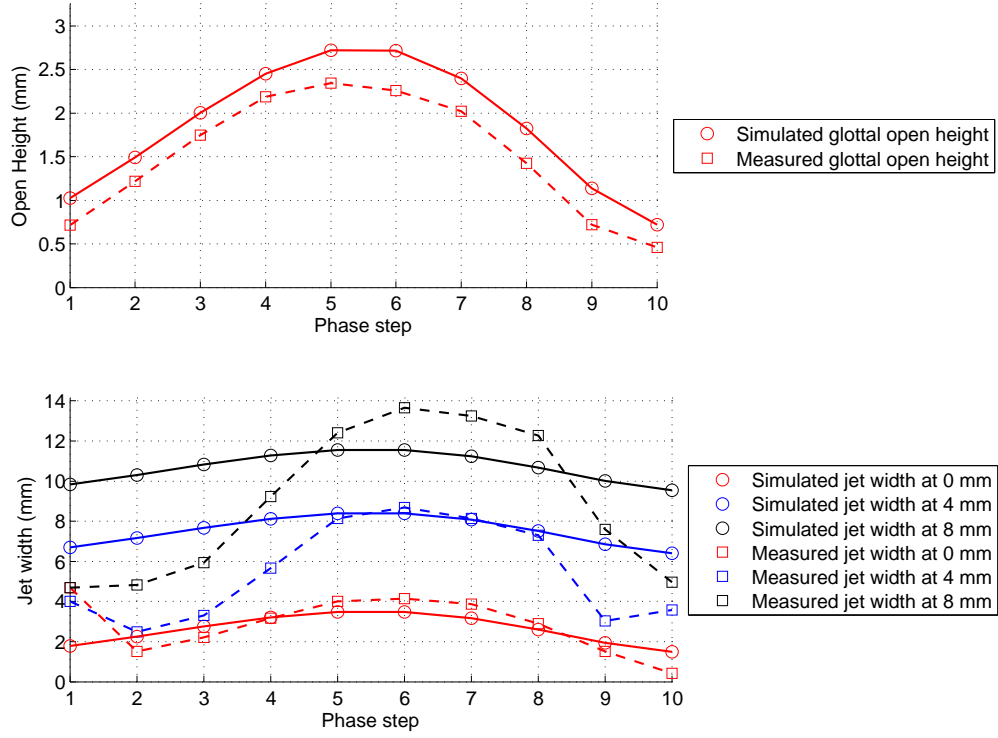


Figure 5.50: Comparison between the measured jet width from PIV data and that from a physical model with ventricular bands placed 16 mm downstream with a 8 mm separation using a Bernoulli steady flow model with Poiseuille losses, no jet pressure losses and the turbulent jet expansion hypothesis with $\theta_{jet} = 21^\circ$.

counterparts than those using $\theta_{jet} = 26^\circ$. As for the results seen in Figure 5.50, the measured glottal open height is well-represented by that from the computational physical model, only with a constant offset of approximately 0.4 mm. This again could be due to the thresholding value chosen when measuring the open area and open height of the *in vitro* model. In the lower plot, the measured glottal jet widths for phase steps 1, 2, and 10 will not be considered due to jet flapping observed in results discussed earlier in this chapter. The general geometry for the glottal jet width for this particular configuration is different to that seen in earlier figures with a pronounced dip at phase step 7 (in Figure 5.51) for the measured jet width using the *in vitro* model. As for the other two figures in this section, the model is a reasonable representation for the jet measured at the point of the glottal exit; however, for the jet width measured further downstream the model is not suitable.

5.7. RESULTS FROM COMPUTATIONAL PHYSICAL MODEL SIMULATIONS

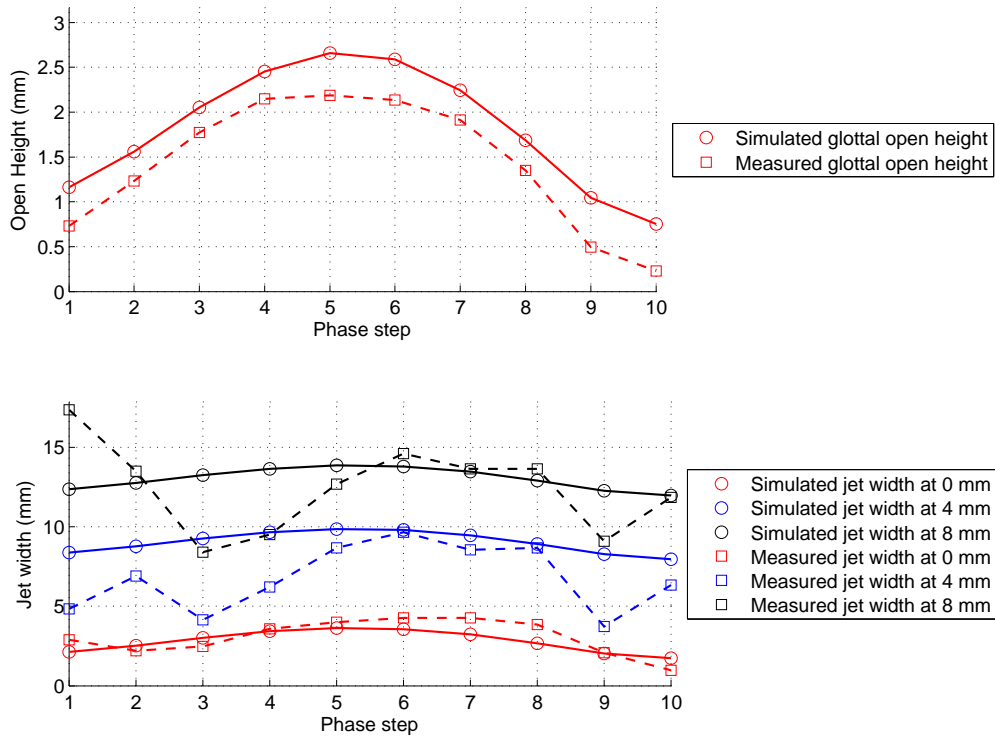


Figure 5.51: Comparison between the measured jet width from PIV data and that from a physical model with ventricular bands placed 16 mm downstream with a 3 mm separation using a Bernoulli steady flow model with Poiseuille losses, no jet pressure losses, and the turbulent jet expansion hypothesis with $\theta_{jet} = 26^\circ$.

5.7.5 Summary

In this section covering results acquired from simulations using distributed computing through Condor, some interesting and useful conclusions can be reached. Firstly, it has been established that the state-of-the-art computational physical model used in [Bailly 08, Bailly 09] is affected by the sample rate at which the simulation is run. This was confirmed by examining the behaviour of the model over five different sample rates. As a result, the high sample rate of 100 kHz was used, as simulations at sample rates above 80 kHz seemed not to display the differences observed at lower sample rates. In addition, the ventricular bands were shown to have a demonstrable effect on the oscillation of the vocal folds. In particular, when the ventricular bands were separated by 3 mm the region of stability, from where a value for the effective oscillating mass of a vocal fold can be extracted, was shown to be reduced in

5.7. RESULTS FROM COMPUTATIONAL PHYSICAL MODEL SIMULATIONS

comparison to the case where the ventricular bands were separated by 8 mm or were not present.

Other findings were that vocal fold oscillation could also be affected by altering the value of θ_{jet} in the turbulent jet expansion hypothesis, which was from earlier results considered the most appropriate of the 3 hypotheses in order to model the glottal jet expansion. This illustrated that even with simple descriptions of the flow, like that used with the simplified computational model used in this study it was possible to capture these small effects and see how they change the behaviour of the model. In the last part of this section, the hypothesised glottal jet widths at 0 mm, 4 mm, and 8 mm downstream of the vocal folds were compared with those measured from PIV undertaken in the *in vitro* experimental model.

In addition, measurements and simulations of the glottal open height were also compared. It was found that the glottal open height was well-represented by that simulated using the physical model. The measured jet widths, however, were not represented quite so well, with the turbulent jet hypothesis for the jet widths at 4 and 8 mm downstream from the vocal folds shown as unsuitable to accurately predict the width of the jet. This is hardly surprising as the jet width was not found to be constant throughout the phonatory cycle in earlier results. Finally, it is worth noting that using the input parameters calculated from the mechanical response measurements made on the *in vitro* model it was possible to extract a value for the effective oscillating mass of the vocal folds for the appropriate frequency of oscillation within a defined region of stability.

"The most exciting phrase to hear in science, the one that heralds new discoveries, is not 'Eureka!' ('I found it!') but rather 'hmm...that's funny...' "

(Isaac Asimov)



Three-dimensional Glottal Flow within Models of the Human Larynx

Following on from Chapter 5, in this chapter novel data are presented for the same three setups of the *in vitro* model only with the model rotated by 90°. This rotation permits investigation of the three-dimensional dynamical nature of the glottal jet in the plane parallel to the glottal height abscissa, thereby making possible a reconsideration of the two-dimensional assumption of the jet's behaviour. As well as ensemble-averaged velocity magnitude plots and the standard deviation for these plots, the calculated vorticity field for the ensemble-averaged velocity data is included as, unlike in the other PIV plane, significant vortical activity is shown. As the state-of-the-art computational physical model assumes a two-dimensional flow, a replication of the results shown in this chapter cannot be achieved through simulation.

6.1 Results for the *in vitro* Model without Ventricular Bands

Presented in Figures 6.1 and 6.2 are the ensemble-averaged velocity magnitude plots for phase steps 1 - 5 and 6 - 10 (respectively) In Figures 6.3 and 6.4 can be found the corresponding standard deviation of the velocity magnitude for each phase step. The greyed out area represents the walls of the vocal tract and the part of the ventricular bands which can be seen (when these are present). As in the velocity magnitude data shown in Chapter 5, a clear and distinguishable jet is visible in phase steps 1 - 9.

6.1. RESULTS FOR THE *IN VITRO* MODEL WITHOUT VENTRICULAR BANDS

Unlike in the results seen previously the jet in phase step 1 is visible; however, the standard deviation of the velocity magnitude for this jet is at a similar value to the velocity magnitude indicating that the jet shown in phase step 1 is not stable and may be subject to a high degree of turbulence. Due to this, the results from this phase step will not be used in further analysis. A possible reason for the glottal jet not being visible in phase step 10 could be that the jet may be strongly unstable here caused by the small vocal fold closure height (smaller than phase steps 1 and 9 for instance) and previously identified inward bowing of the vocal folds. The shear layers and laminar jet core are also visible in phase steps 2 - 9, although more jet core turbulence is evident in phase steps 2 and 9 indicated by raised values in the standard deviation of the velocity magnitude field data.

An interesting observation here is that more jet core turbulence is seen for phase step 2 than phase step 8 even when the glottal centreline open height is at a similar value for both. This indicates that there is an asymmetry in the flow behaviour, like that seen in the results in Chapter 5, and that this may be due to inertial effects caused by the oscillation of the vocal folds. Furthermore, the distance downstream over which this laminar core extends, shown in the standard deviation of the ensemble-averaged velocity magnitude flow data, appears to reduce as the phase step number increases from 2 - 9. This appears to be in line with the increase in the average velocity magnitude from phase step 2 - 9, which was also identified as a feature in Figures 5.16 and 5.17. Also, a noticeable reduction in the ensemble-averaged velocity magnitude can be found with an epicentre at approximately 3 mm downstream of the vocal folds. This localised reduction in the ensemble-averaged velocity magnitude was also observed at the same point in the glottal jets shown in Figures 5.16 and 5.17, and was attributed to strong three-dimensional motion. As the width of the glottal jet is reducing at its highest rate here and expanding continuously in the plane perpendicular to that shown here, this explanation seems plausible.

An important and discernible observation is that the geometry of the glottal jet shown in Figures 6.1 and 6.2 is remarkably different to that shown in Figures 5.16 and 5.17. The jet leaves the glottis at its maximum width in this plane and then reduces in width until a point downstream where it stops decreasing. The geometry of the glottal jet in phase steps 2 - 9 is very similar to geometry shown in [Krebs 12], demonstrating that the glottal jet has a highly three-dimensional geometry; however, it

6.1. RESULTS FOR THE *IN VITRO* MODEL WITHOUT VENTRICULAR BANDS

is not entirely similar to the geometry shown in [Triep 10]. Possible reasons for this could be due to the differences encountered through conducting the experiments in water instead of air, through using a driven rather than a self-oscillating vocal fold system, and because the results presented here are calculated ensemble averages whereas Triep *et al.* present instantaneous flow field data. It is also worth commenting that the average velocity magnitude of the jet core in this PIV plane for each phase step are generally lower than those in the PIV plane considered in Chapter 5. Finally, it should be remarked that the geometry of the glottal jet shown by the ensemble-averaged velocity magnitude data from Figures 6.1 and 6.2 differs significantly from that assumed by the computational physical two-mass model. However, to incorporate the geometry shown here into the computational model will present severe difficulties both computationally and ideologically.

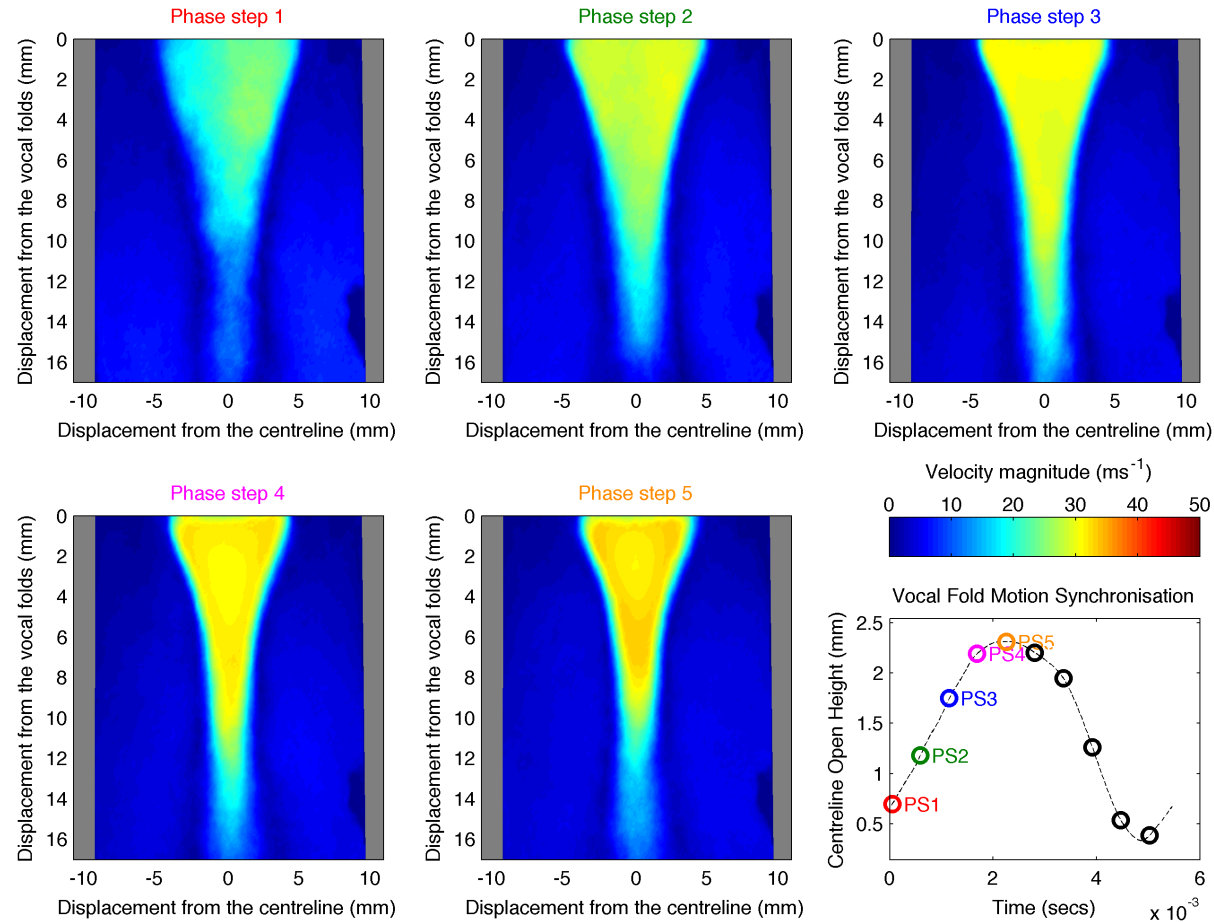


Figure 6.1: Ensemble-averaged velocity magnitude data for phase steps 1 - 5 on an *in vitro* model of the human larynx **with no ventricular bands**. The positions of the phase steps in relation to the centreline open height of the vocal fold model are included. $P_{sub} = 800$ Pa.

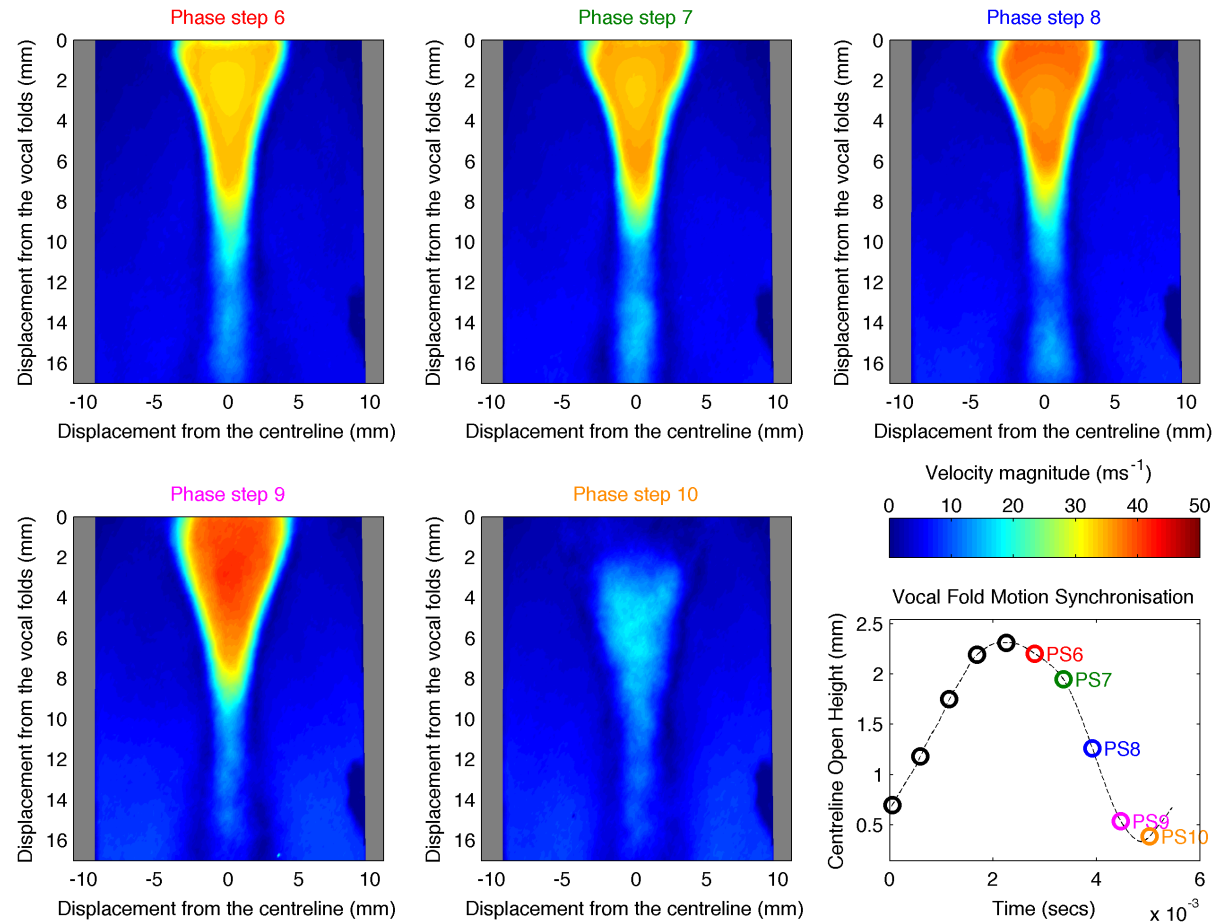


Figure 6.2: Ensemble-averaged velocity magnitude data for phase steps 6 - 10 on an *in vitro* model of the human larynx **with no ventricular bands**. The positions of the phase steps in relation to the centreline open height of the vocal fold model are included. $P_{sub} = 800$ Pa.

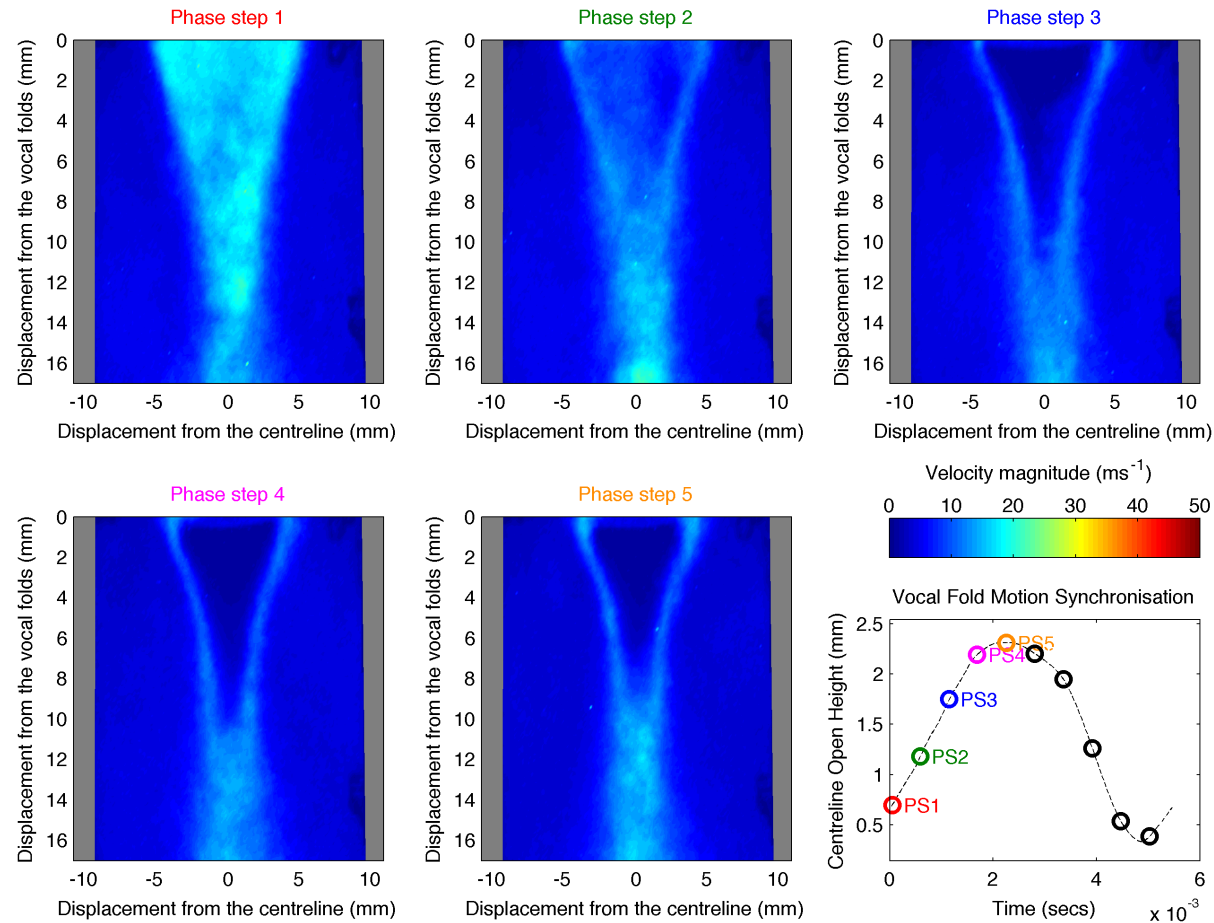


Figure 6.3: Standard deviation of the ensemble-averaged velocity magnitude data for phase steps 1 - 5 on an *in vitro* model of the human larynx **with no ventricular bands**. The positions of the phase steps in relation to the centreline open height of the vocal fold model are included. $P_{sub} = 800$ Pa.

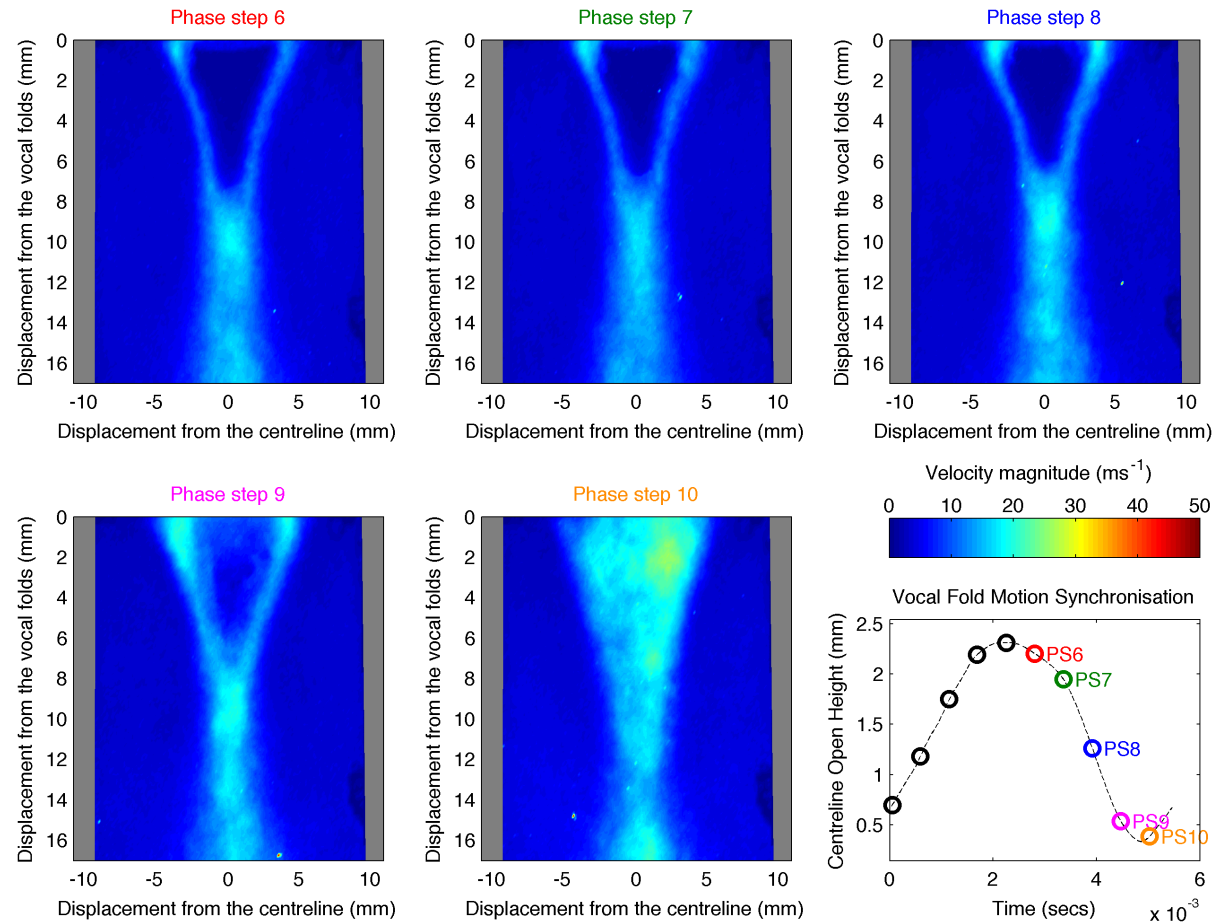


Figure 6.4: Standard deviation of the ensemble-averaged velocity magnitude data for phase steps 6 - 10 on an *in vitro* model of the human larynx **with no ventricular bands**. The positions of the phase steps in relation to the centreline open height of the vocal fold model are included. $P_{sub} = 800$ Pa.

6.1.1 Calculated Vorticity Flow Field Data

In Figures 6.5 and 6.6 can be found the ensemble-averaged data for the calculated vorticity field for phase steps 1 - 5 and 6 - 10 respectively. In phase steps 1 - 9 the irrotational jet core and shear layers can be clearly seen. The thickness of the shear layers is the same as that observed in Figures 5.20 and 5.21. The area of high negative vorticity extending from 16 mm to 12 mm downstream of the vocal folds emerging from the right hand wall of the vocal tract in each of the phase step is due to unavoidable flaring in this configuration and is to be disregarded. A similar level of vorticity between the shear layers and the walls of the vocal tract can be seen in the vorticity data for the PIV plane perpendicular to that shown here, with no increase in vorticity observed throughout the phonatory cycle. An interesting comparison between the glottal jets shown in Figures 5.20 and 5.21 and those in Figures 6.5 and 6.6 is that where the glottal jet dissipates into turbulence at between 8 and 12 mm downstream of the vocal folds in the results from the previous chapter, in the results shown here the glottal jet does not appear to dissipate into turbulence as early with the shear layers growing but there still being a distinguishable irrotational core.

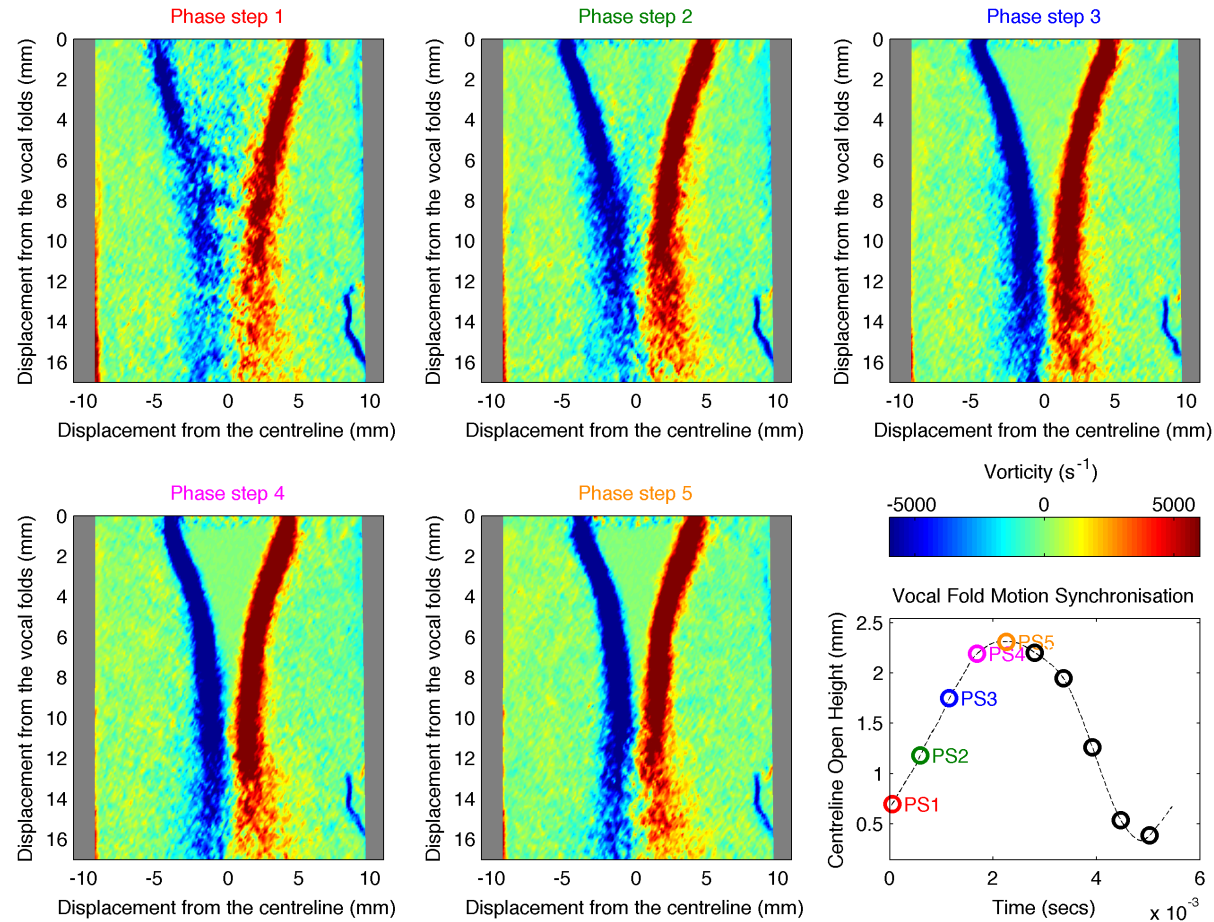


Figure 6.5: Vorticity ensemble-averaged PIV data for phase steps 1 - 5 on an *in vitro* model of the human larynx **with no ventricular bands**. The positions of the phase steps in relation to the normalised open area of the vocal fold model are included. $P_{sub} = 800$ Pa.

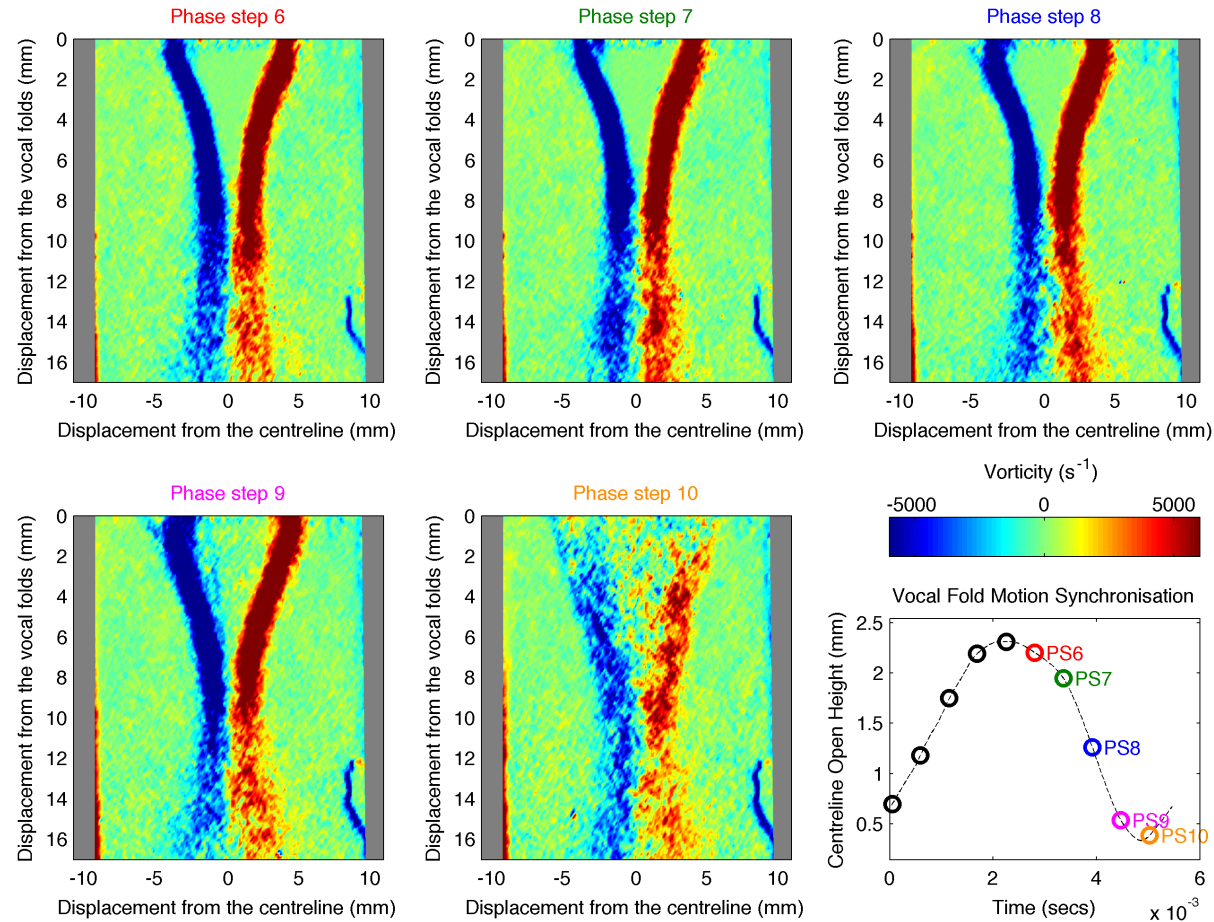


Figure 6.6: Vorticity ensemble-averaged PIV data for phase steps 6 - 10 on an *in vitro* model of the human larynx **with no ventricular bands**. The positions of the phase steps in relation to the normalised open area of the vocal fold model are included. $P_{sub} = 800$ Pa.

6.1.2 Jet Major Axis-Switching

When considering the glottal jet in two perpendicular PIV planes, it is of interest to look at the evolution of the point of jet major axis-switching. Zaman defines jet major axis-switching as “a phenomenon in which the cross-section of an asymmetric jet evolves in such a manner that, after a certain distance from the nozzle, the major and the minor axes are interchanged” [Zaman 96]. In this case, the nozzle is the glottal exit. In Figure 6.7 can be found the two plots: the plot on the left shows the measured point of jet major axis-switching in mm against phase step number, and the plot in the right shows the measured jet major axis-switching point normalised against the glottal centreline open height plotted against phase step.

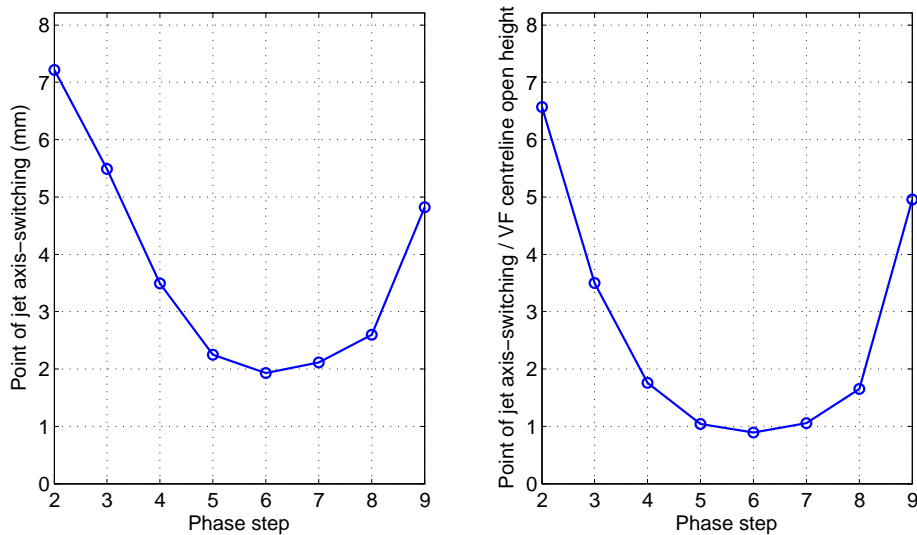


Figure 6.7: Two plots showing the distance downstream of the vocal folds whereby jet major axis-switching take place across phase steps 2 - 9 for a self-oscillating *in vitro* model of the human larynx with no ventricular bands.

One of the most important reasons that the jet major axis-switching point is investigated is because it may be correlated with the point of flow separation in the glottis [Krebs 12]. Therefore, as flow separation has been identified as having a significant effect on glottal jet formation and subsequent vocal fold motion [Pelorson 94], the point of jet major axis-switching could be a useful parameter for comparison between experiments and computational models using more complex flow

6.1. RESULTS FOR THE *IN VITRO* MODEL WITHOUT VENTRICULAR BANDS

descriptions (i.e. full Navier-Stokes simulations rather than simplified Bernoulli flow models). The results from which the jet major axis switching points are extracted are shown in Appendix B in Figures B.5 and B.6. For the *in vitro* model without ventricular bands, the point of jet major axis-switching reduces from 7.2 mm downstream of the vocal folds at phase step 2 until phase step 6 where it reaches 2.9 mm. After this point the jet major axis-switching point increases to 4.8 mm, with the general shape of the axis-switching curve being parabolic in nature. The same shape is exhibited in the plot normalised to the glottal centreline open height on the right hand side. The values, however, change from 6.5 at phase step 2 to 0.9 at phase step 6 and then back to 4.9 at phase step 9, indicating that the jet major axis-switching point moves from 6.5 times the width of the glottal centreline height at phase step 2 to 0.9 times the glottal centreline height at phase step 6.

Firstly, this indicates an asymmetry in the jet major axis-switch point between the opening phase, where this found to be generally further downstream, and the closing phase, where the jet major axis-switch point is observed as being further upstream. This is most likely due to the asymmetry seen in the geometry of the jet in Figures 5.16 and 5.17, where the jet more rapidly expands in phase steps 8 and 9 than in phase steps 2 and 3. The results from this investigation differ from those shown in [Krebs 12], which is to be expected given the differences in the models used in each case. It should also be noted that the jet major axis-switch points measured in this investigation for all points except phase step 2 would be unmeasurable in the setup used by Krebs *et al.*, since as has already been mentioned it is only possible to measure from 6 mm downstream in their model. Possible reasons for the observed differences between the two studies could be that a strong acoustic field, caused by the presence of a 17 cm long vocal tract might cause there to be an interaction without the ventricular bands. Finally, it should be noted that the maximum velocities and the Reynolds number recorded for the two studies differ, with a maximum velocity in [Krebs 12] of 30 ms^{-1} and a max $Re_D = 2600$, which is much lower than those seen in the previous chapter. As jet major axis-switching is known to be dependent on a number of different parameters including Reynolds number [Gutmark 99], it is unsurprising that these differences are manifested.

6.2. RESULTS FOR *IN VITRO* MODEL WITH RIGID VENTRICULAR BANDS

6.1.3 Summary

In this section, the ensemble-averaged velocity magnitude and the standard deviation of the velocity magnitude are presented and discussed for the *in vitro* model without ventricular bands in the PIV plane which is parallel to the glottal centreline open height. As in Section 5.5 a clear and distinguishable jet can be seen in phase steps 1 - 9; however, high values in the standard deviation flow field for phase step 1 indicates that this is an unstable jet. The geometry of the glottal jet for the *in vitro* model in this configuration is similar to that shown in [Krebs 12], although differences between the two studies were highlighted. The calculated vorticity flow field and measured jet major axis-switching point are presented and discussed. No increased vorticity was found in the recirculation regions of the vorticity flow fields in the PIV plane used in this chapter than in the one used in the previous chapter. The turbulent dissipation of the glottal jet seen in the vorticity flow fields for the *in vitro* model in the PIV plane perpendicular to the line of the glottal opening occurring 12 mm downstream of the vocal folds was not seen to take place in the vorticity flow fields for the *in vitro* model in the PIV plane parallel to the line of the glottal opening. Finally, differences between the jet major axis-switching results for the study undertaken by [Krebs 12] and the results presented here were highlighted with possible reasons for these differences explored.

6.2 Results for *in vitro* Model with Rigid Ventricular Bands

This section investigates the impact of the ventricular bands on the glottal jet for the same *in vitro* model and in the same plane as that in Section 6.1. Other studies have considered the three-dimensional nature of the glottal jet experimentally [Mongeau 97, Zhang 02b, Brücker 04, Triep 05, Alipour 06, Neubauer 07, Drechsel 08, Khosla 08a, Triep 10, Krebs 12]. However, this is the first time that PIV results for a simplified *in vitro* model of the human larynx, like that used in [Ruty 07a, Bailly 09, Newton 09], are presented for the plane parallel to the glottal open width, including the ventricular bands and taking their effect on the glottal jet in this plane into account.

In Figures 6.8 and 6.9 are shown the velocity magnitude for ensemble-averaged

6.2. RESULTS FOR *IN VITRO* MODEL WITH RIGID VENTRICULAR BANDS

PIV flow field velocity data for phase steps 1 - 5 and 6 - 10 (respectively) for the *in vitro* model with ventricular bands with an 8 mm separation, in the PIV plane parallel to the glottal open width. The same information for the model with ventricular bands with a 3 mm separation is shown in Figures 6.12 and 6.13. The corresponding standard deviation of the ensemble-averaged velocity magnitude is shown in Figures 6.10 and 6.11 and Figures 6.14 and 6.15 for the model with ventricular bands separated by 8 mm and 3 mm respectively. A clear and distinguishable jet core can be seen for phase steps 3 - 9 in the model with an 8 mm ventricular band separation and phase steps 3 - 8 in the model with a 3 mm ventricular band separation.

Considering the *in vitro* model with ventricular bands separated by 8 mm, the reason that the complete glottal jet cannot be seen in phase step 2 could be due to significant out of plane motion caused by the Coandă effect acting on the glottal jet seen in Figure 5.31. This explanation seems plausible as the standard deviation of the ensemble-averaged velocity magnitude field shown in Figure 6.8 from 5 mm downstream of the vocal folds is very low. This is also a plausible explanation as to why the length of the glottal jet in phase step 3 for the *in vitro* model with an 8 mm ventricular band separation appears to extend less further downstream than that shown in phase step 4. A possible reason for a clear glottal jet not being visible in phase step 10 could be that the jet is unstable and highly turbulent at this point in the phonatory cycle due to the small glottal opening. This seems to be the case here as values for the standard deviation of the velocity magnitude within the area of the glottal jet are significantly higher than those in the velocity magnitude plot. A laminar jet core with a lower standard deviation than the surrounding shear layers can be seen clearly for phase steps 3 - 9. As was observed for the *in vitro* model without ventricular bands earlier in this chapter, the average velocity magnitude of the glottal jet core is found to increase as the phonatory cycle progresses, which is also observed in all of the *in vitro* model setups in Chapter 5 and may indicate the role of fluid inertia in vocal fold oscillation. Finally, it is also noted that the average velocity magnitude of the jet core for each phase step in this PIV plane is similar to the value in the same phase step for the PIV plane considered in Chapter 5, which is different from the observation made for the model without ventricular bands.

Turning our attention to the model with a 3 mm ventricular band separation, a reason that the glottal jets in phase steps 2 and 9 do not appear clearly in Figures 6.12

6.2. RESULTS FOR *IN VITRO* MODEL WITH RIGID VENTRICULAR BANDS

and 6.13 (respectively) may be due to jet flapping identified in Section 5.6.3 causing a significant degree of out of plane motion of the seeding particulate as the jet adheres to either wall of the vocal tract. The geometric shape of the glottal jet is very similar to that of the model with 8 mm separated ventricular bands with a stable laminar jet core for phase steps 3 - 8. However, a noticeable difference is that the average jet core velocity magnitude for each phase step with a clear jet is lower than the equivalent phase step for model with ventricular bands separated by 8 mm. This is consistent with the observation made in Section 5.6.2 where the same behaviour was observed. It is very interesting to note that the glottal jet geometry in this PIV plane appears to be unaffected by the presence of the ventricular bands. Finally, an interesting observation is that for the model with ventricular bands separated by 3 mm the average jet velocity magnitudes in the PIV plane considered in this section are very slightly higher than those for the same phase step for the PIV plane considered in Chapter 5. This is in contrast to the observation made for the model with ventricular bands separated by 8 mm, and the reason for this slight difference is most likely due to the position of the PIV plane in relation to the jet axisymmetric centreline at each phase step and not due to the presence of the ventricular bands.

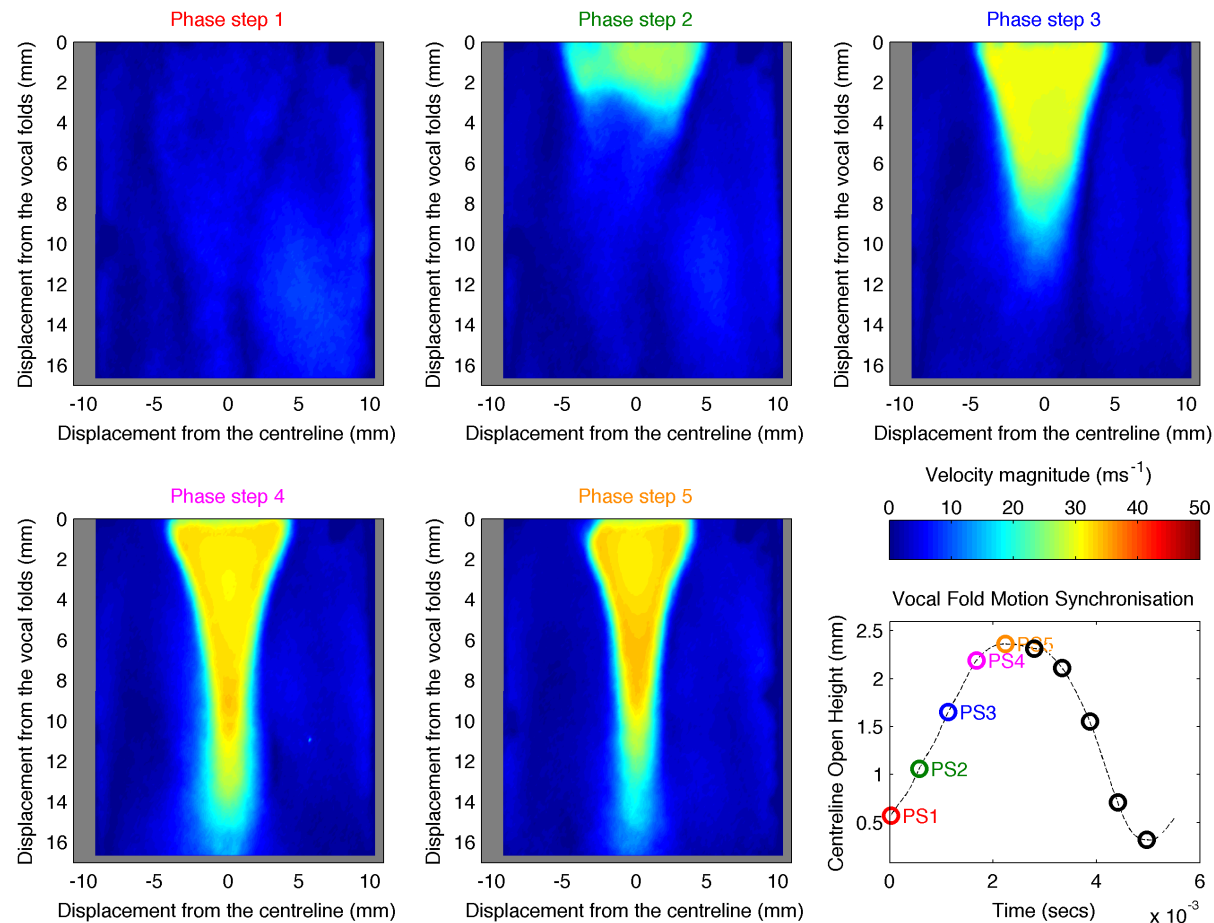


Figure 6.8: Ensemble-averaged velocity magnitude data for phase steps 1 - 5 on an *in vitro* model of the human larynx **with rigid ventricular bands placed 16 mm downstream of the vocal folds with an 8 mm separation**. The positions of the phase steps in relation to the centreline open height of the vocal fold model are included. $P_{sub} = 800$ Pa.

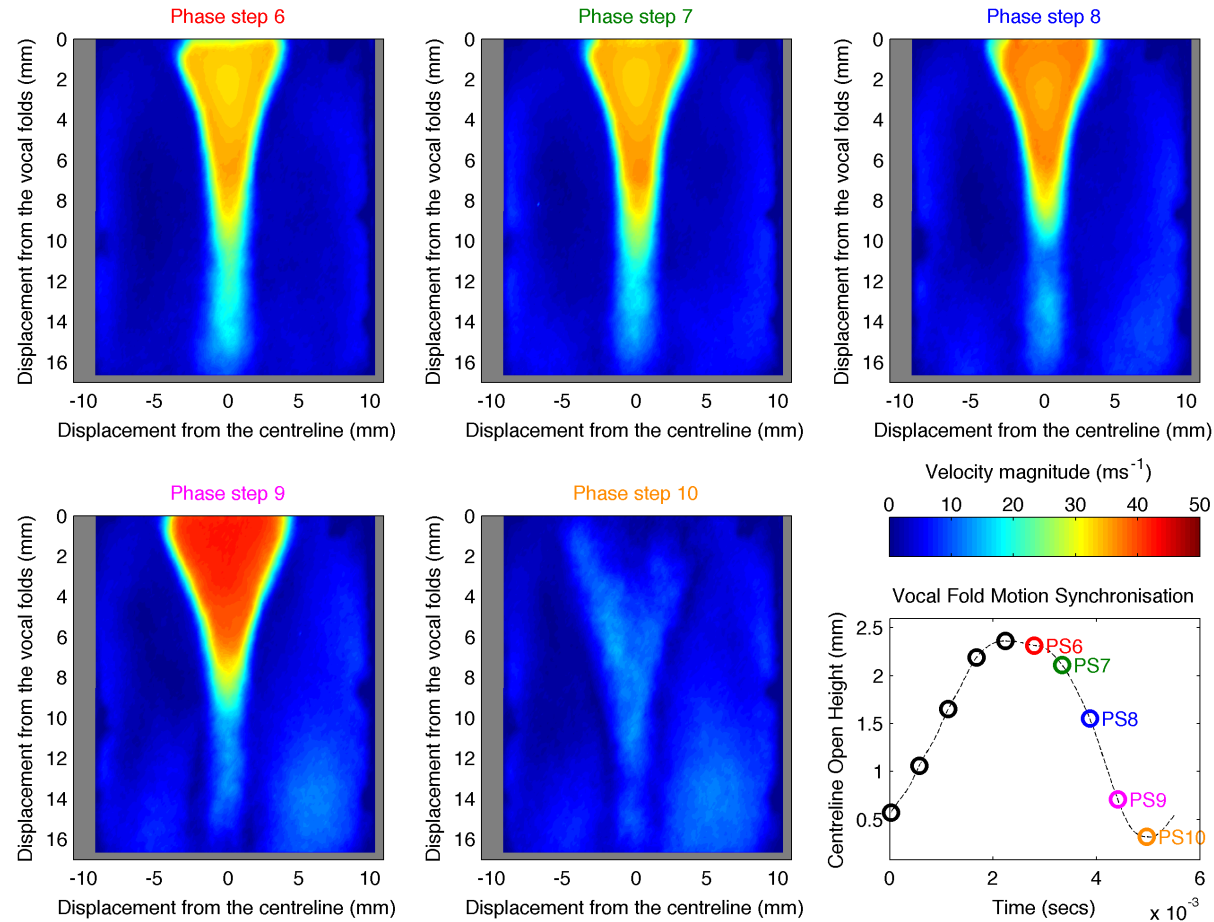


Figure 6.9: Ensemble-averaged velocity magnitude data for phase steps 6 - 10 on an *in vitro* model of the human larynx **with rigid ventricular bands placed 16 mm downstream of the vocal folds with an 8 mm separation**. The positions of the phase steps in relation to the centreline open height of the vocal fold model are included. $P_{sub} = 800$ Pa.

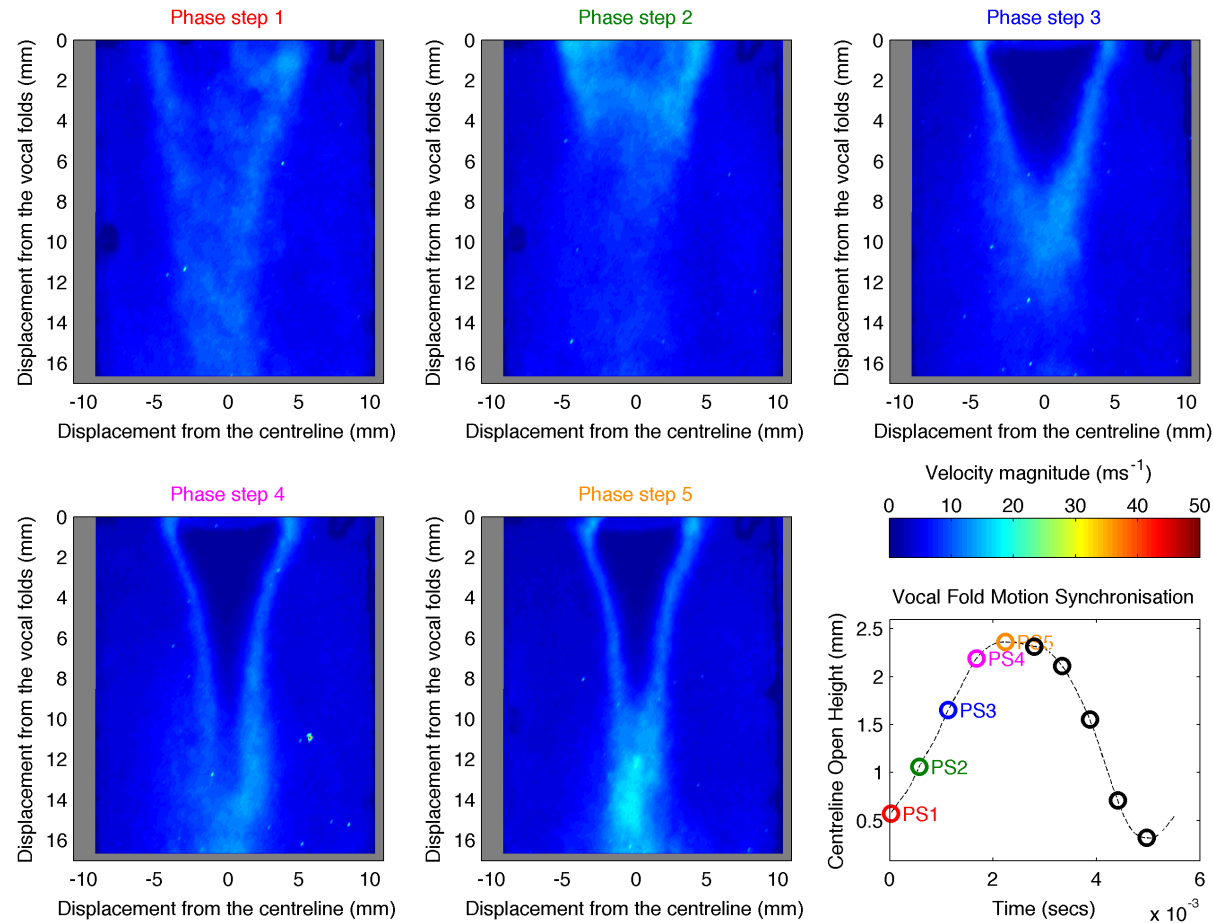


Figure 6.10: Standard deviation of the ensemble-averaged velocity magnitude data for phase steps 1 - 5 on an *in vitro* model of the human larynx **with rigid ventricular bands placed 16 mm downstream of the vocal folds with an 8 mm separation.** The positions of the phase steps in relation to the centreline open height of the vocal fold model are included. $P_{sub} = 800$ Pa.

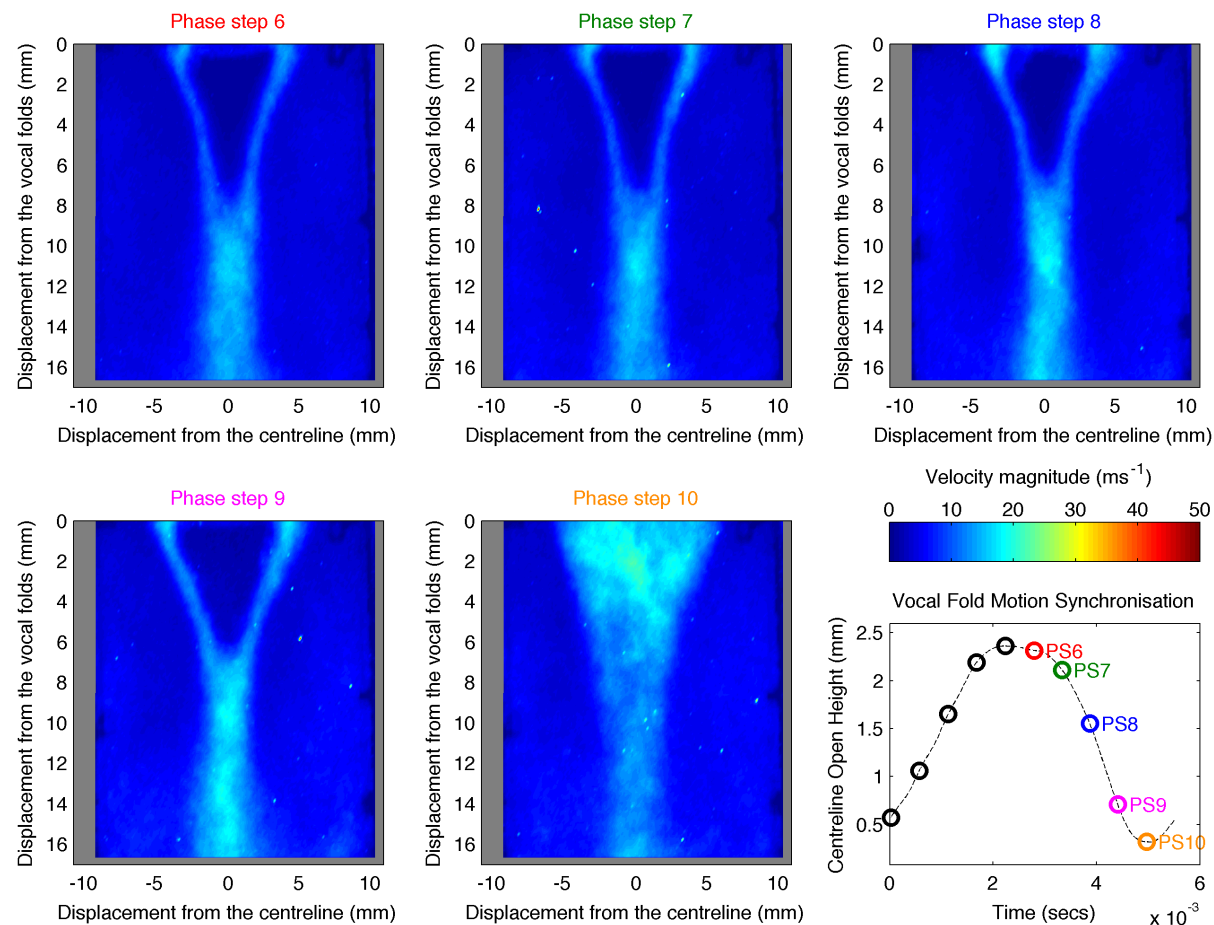


Figure 6.11: Standard deviation of the ensemble-averaged velocity magnitude data for phase steps 6 - 10 on an *in vitro* model of the human larynx **with rigid ventricular bands placed 16 mm downstream of the vocal folds with an 8 mm separation**. The positions of the phase steps in relation to the centreline open height of the vocal fold model are included. $P_{sub} = 800$ Pa.

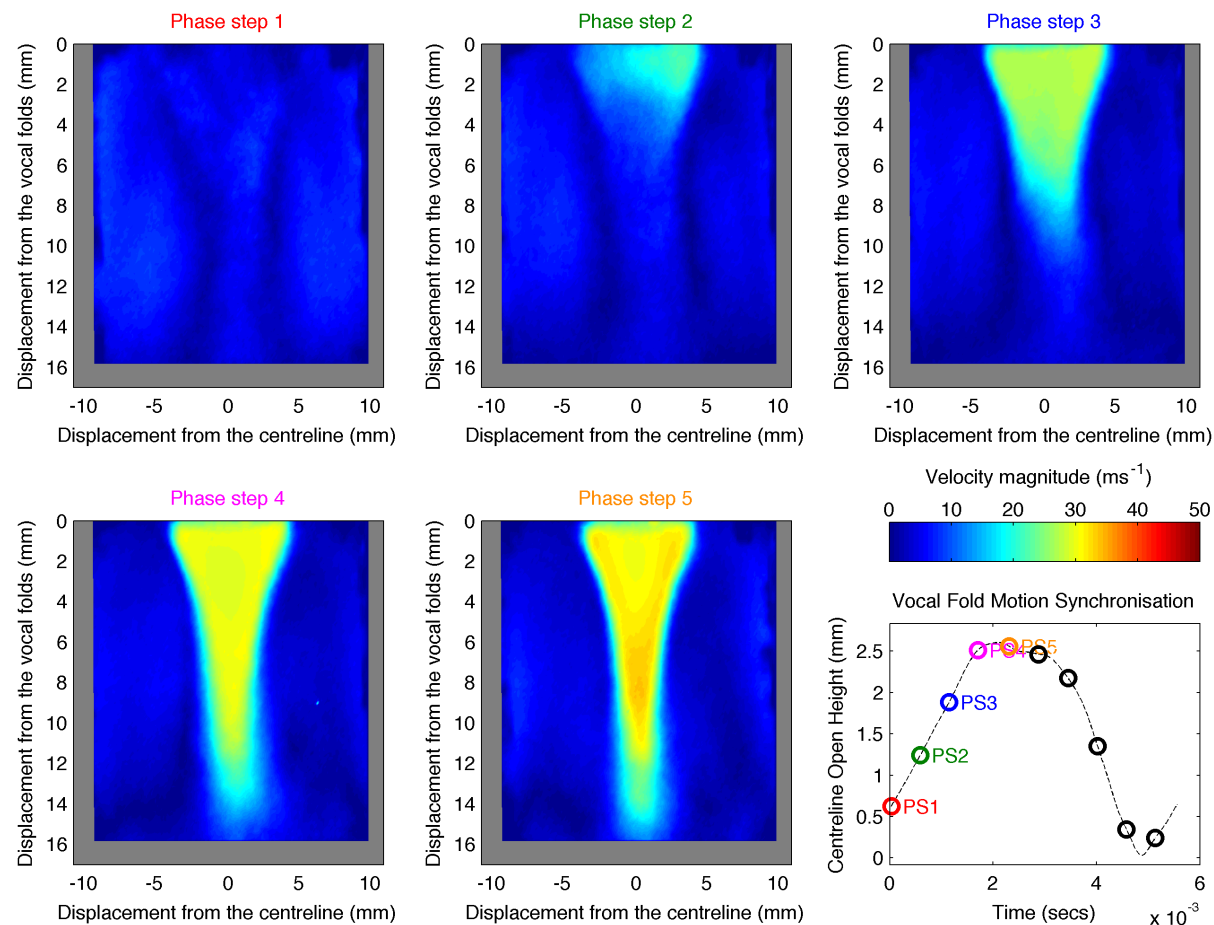


Figure 6.12: Ensemble-averaged velocity magnitude data for phase steps 1 - 5 on an *in vitro* model of the human larynx **with rigid ventricular bands placed 16 mm downstream of the vocal folds with a 3 mm separation**. The positions of the phase steps in relation to the centreline open height of the vocal fold model are included. $P_{sub} = 804$ Pa.

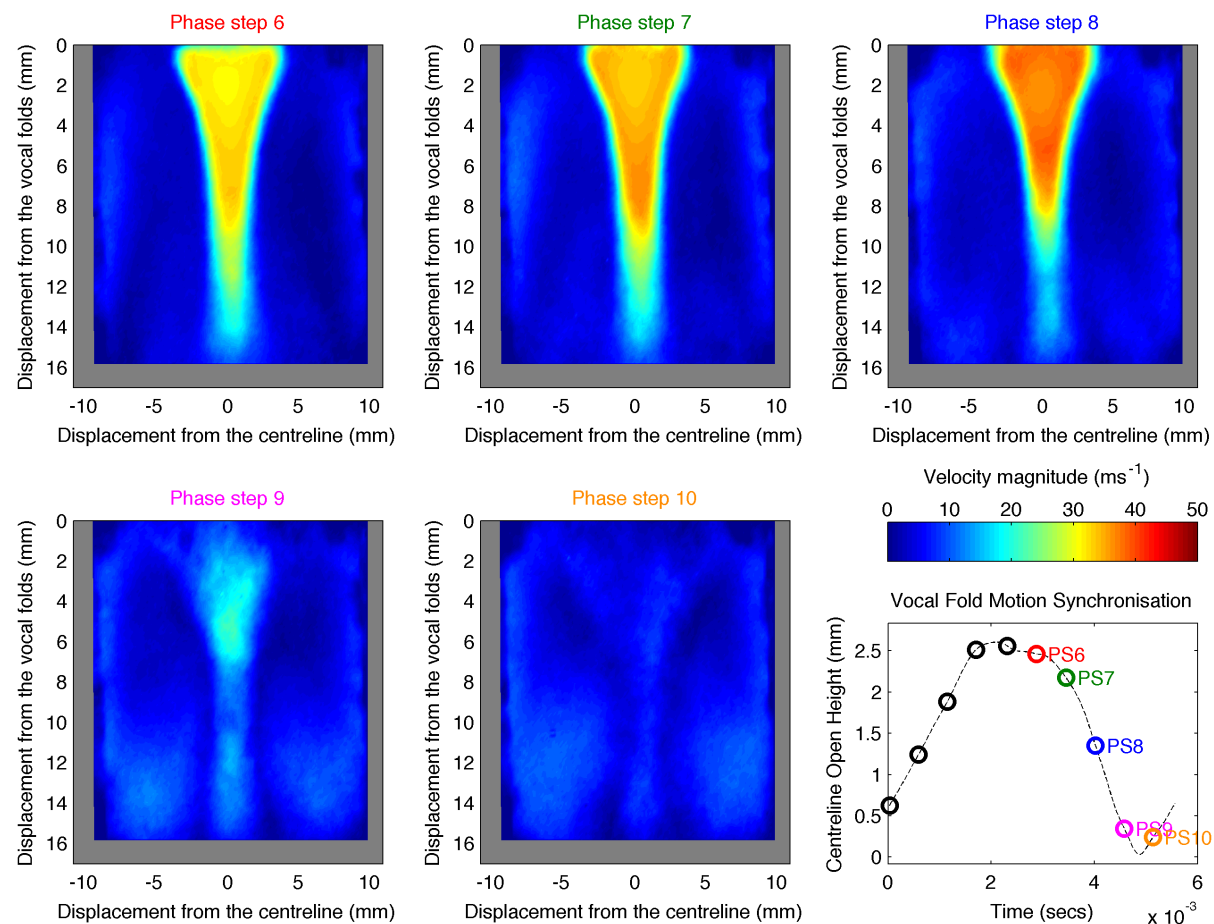


Figure 6.13: Ensemble-averaged velocity magnitude data for phase steps 6 - 10 on an *in vitro* model of the human larynx **with rigid ventricular bands placed 16 mm downstream of the vocal folds with a 3 mm separation**. The positions of the phase steps in relation to the centreline open height of the vocal fold model are included. $P_{sub} = 804$ Pa.

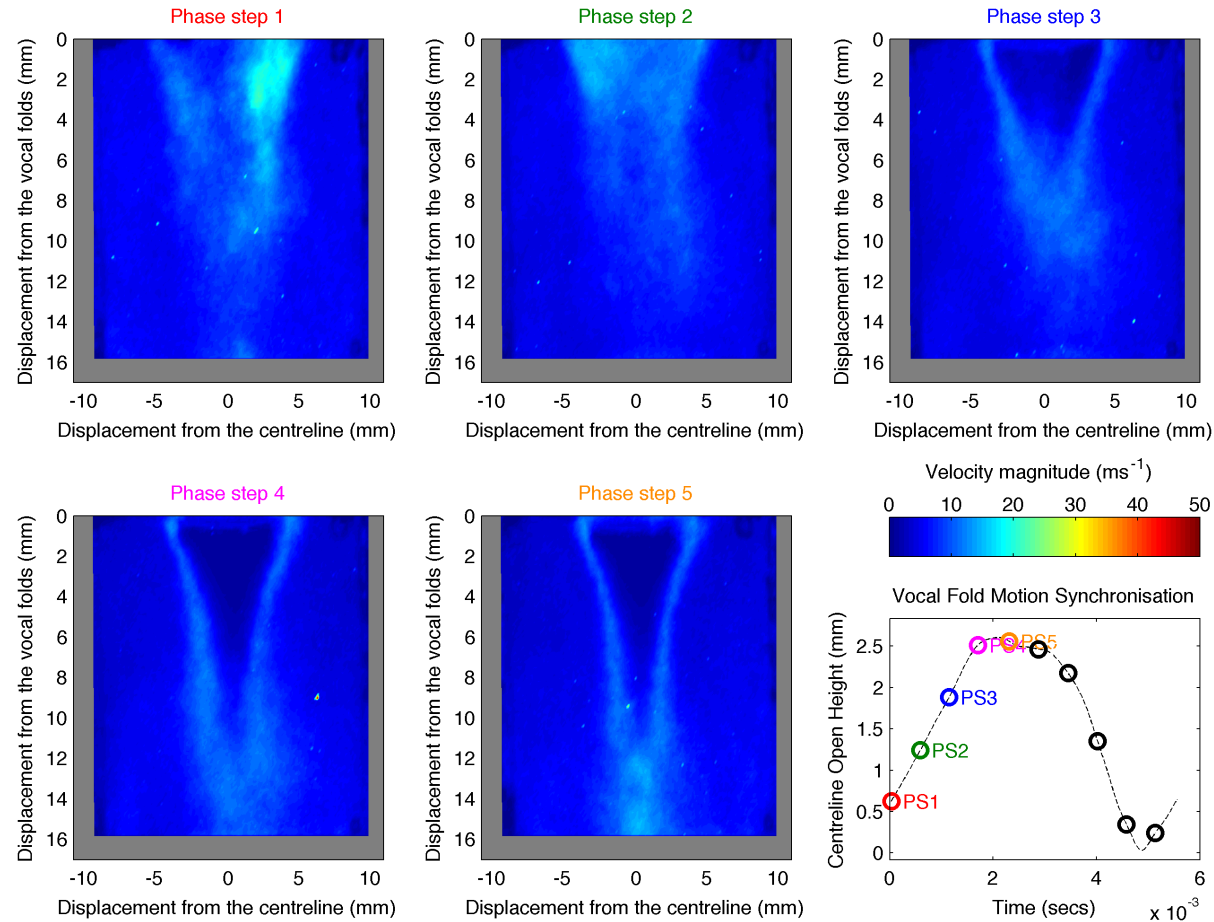


Figure 6.14: Standard deviation of the ensemble-averaged velocity magnitude data for phase steps 1 - 5 on an *in vitro* model of the human larynx **with rigid ventricular bands placed 16 mm downstream of the vocal folds with a 3 mm separation**. The positions of the phase steps in relation to the centreline open height of the vocal fold model are included. $P_{sub} = 804$ Pa.

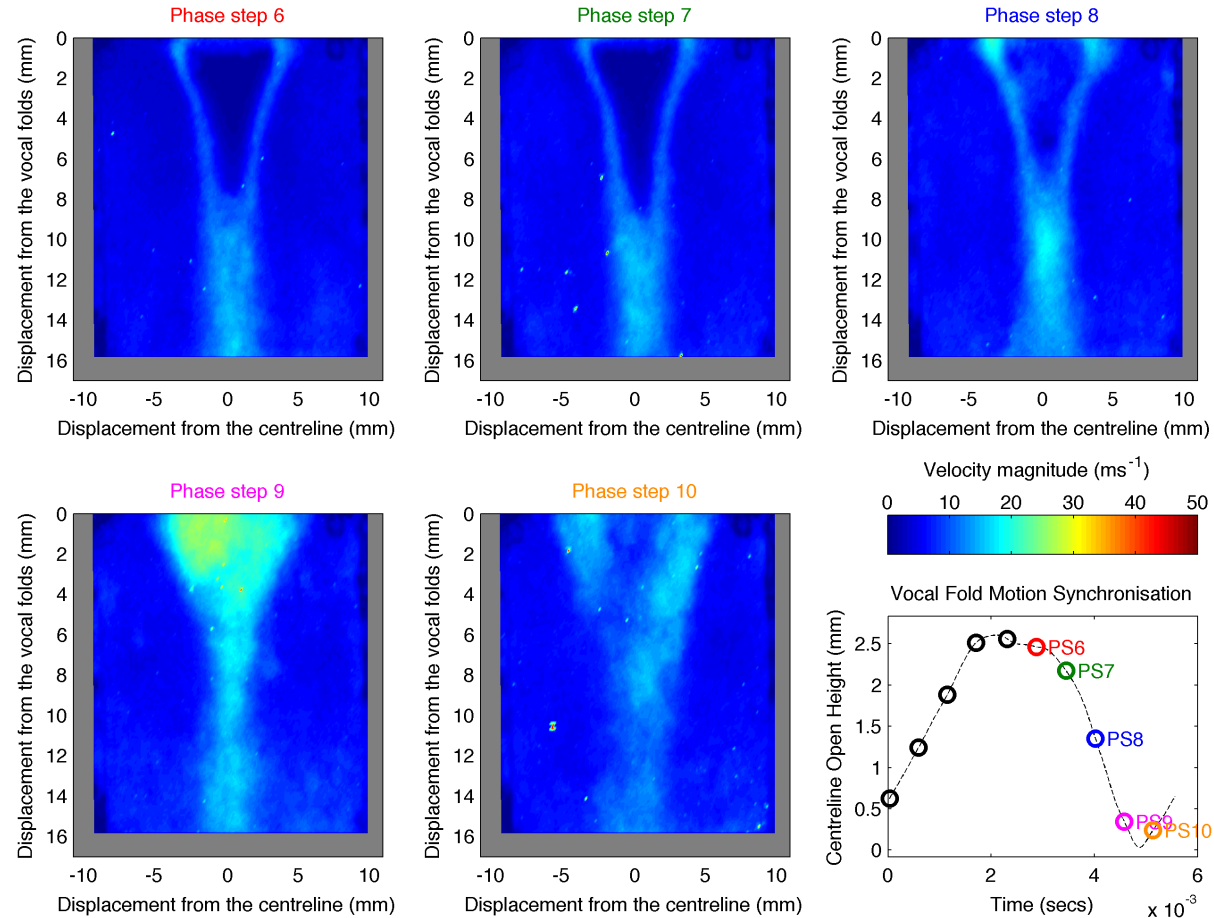


Figure 6.15: Standard deviation of the ensemble-averaged velocity magnitude data for phase steps 6 - 10 on an *in vitro* model of the human larynx **with rigid ventricular bands placed 16 mm downstream of the vocal folds with a 3 mm separation**. The positions of the phase steps in relation to the centreline open height of the vocal fold model are included. $P_{sub} = 804$ Pa.

6.2. RESULTS FOR *IN VITRO* MODEL WITH RIGID VENTRICULAR BANDS

6.2.1 Calculated Vorticity Flow Field Data

Shown in Figures 6.16 and 6.17 are the calculated vorticity flow fields for phase steps 1 - 5 and 6 - 10 (respectively) for the *in vitro* model with ventricular bands separated by 8 mm in the PIV plane parallel to the glottal open width. In Figures 6.18 and 6.19 is the same data only for the model with ventricular bands separated by 3 mm. The geometry of the glottal jet in this vorticity data is very similar to that shown for the model in the same PIV plane only without ventricular bands. An interesting difference is that there is an increased level of vorticity in a region between the shear layers of the glottal jet and the walls of the vocal tract for the cases with ventricular bands when compared to that without ventricular bands.

Although it is difficult to identify large-scale vortical structures explicitly in these plots, in the regions already identified there appears to be a mean vorticity which rotates in opposite directions either side of the glottal jet. Furthermore, in these regions there is greater vorticity in the model with 3 mm separated ventricular bands than for the model with ventricular bands with an 8 mm separation. This is to be expected as the ventricular bands effectively inhibit the transport of the vortical structures downstream of the vocal folds and constrain the vortices. Therefore, the increased vorticity observed for the case with 3 mm separated ventricular bands over that in the case with 8 mm separated ventricular bands can be explained by this as the narrower the ventricular band separation becomes the higher the vorticity observed. Finally, an asymmetry between vorticity in the opening and closing phases of the phonatory cycle is observed; a higher level of vorticity is found in phase steps 6 - 10 than in phase steps 1 - 5. This is consistent with observations made in [Khosla 08b] where vortices are found during the closing phase and it is suggested that these vortices during the closing phase contribute to asymmetry in the phonatory cycle. These vortices may contribute to the differences seen in the phonatory cycle for the *in vitro* model with and without ventricular bands.

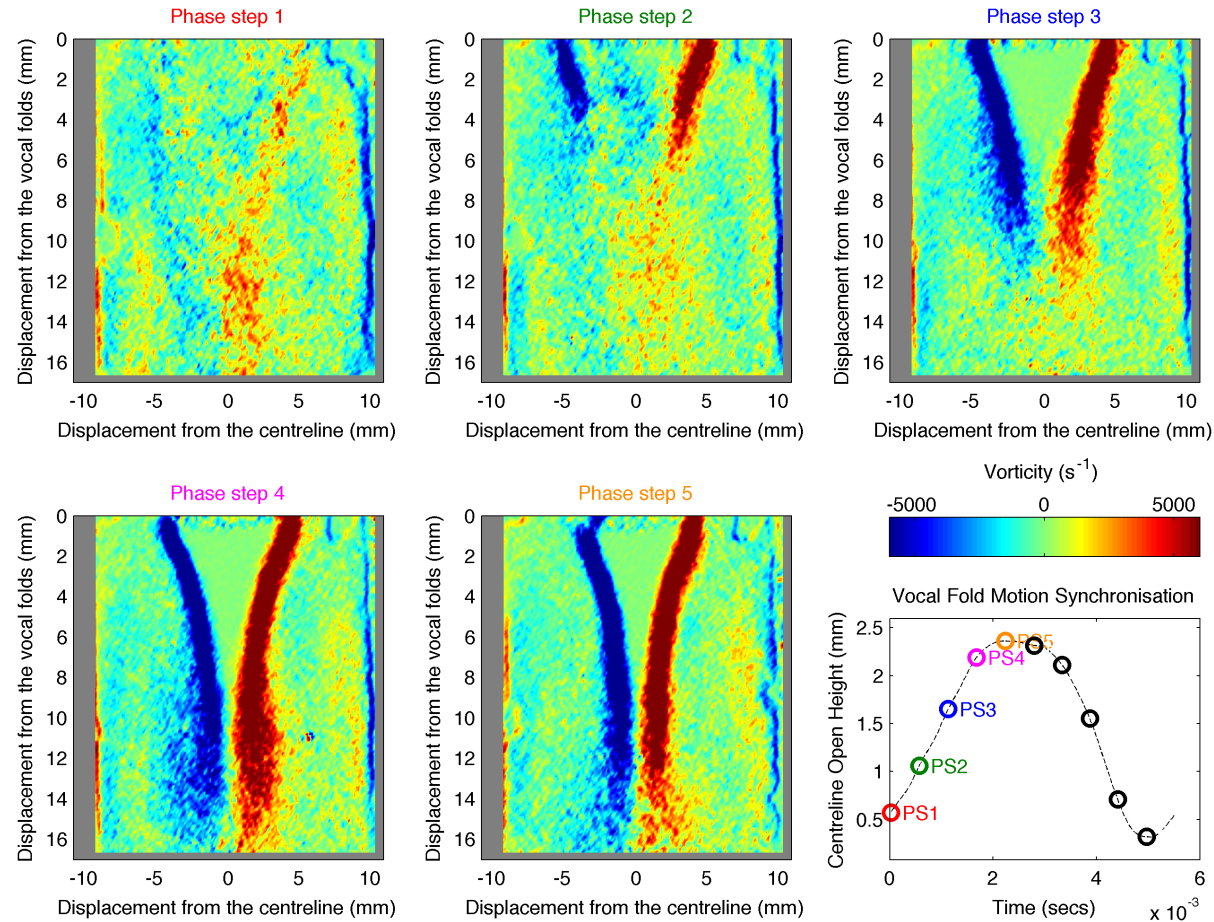


Figure 6.16: Vorticity data ensemble-averaged PIV data for phase steps 1 - 5 on an *in vitro* model of the human larynx rotated by 90° **with rigid ventricular bands placed 16 mm downstream of the vocal folds with an 8 mm separation**. The positions of the phase steps in relation to the normalised open area of the vocal fold model are included. $P_{sub} = 800$ Pa.

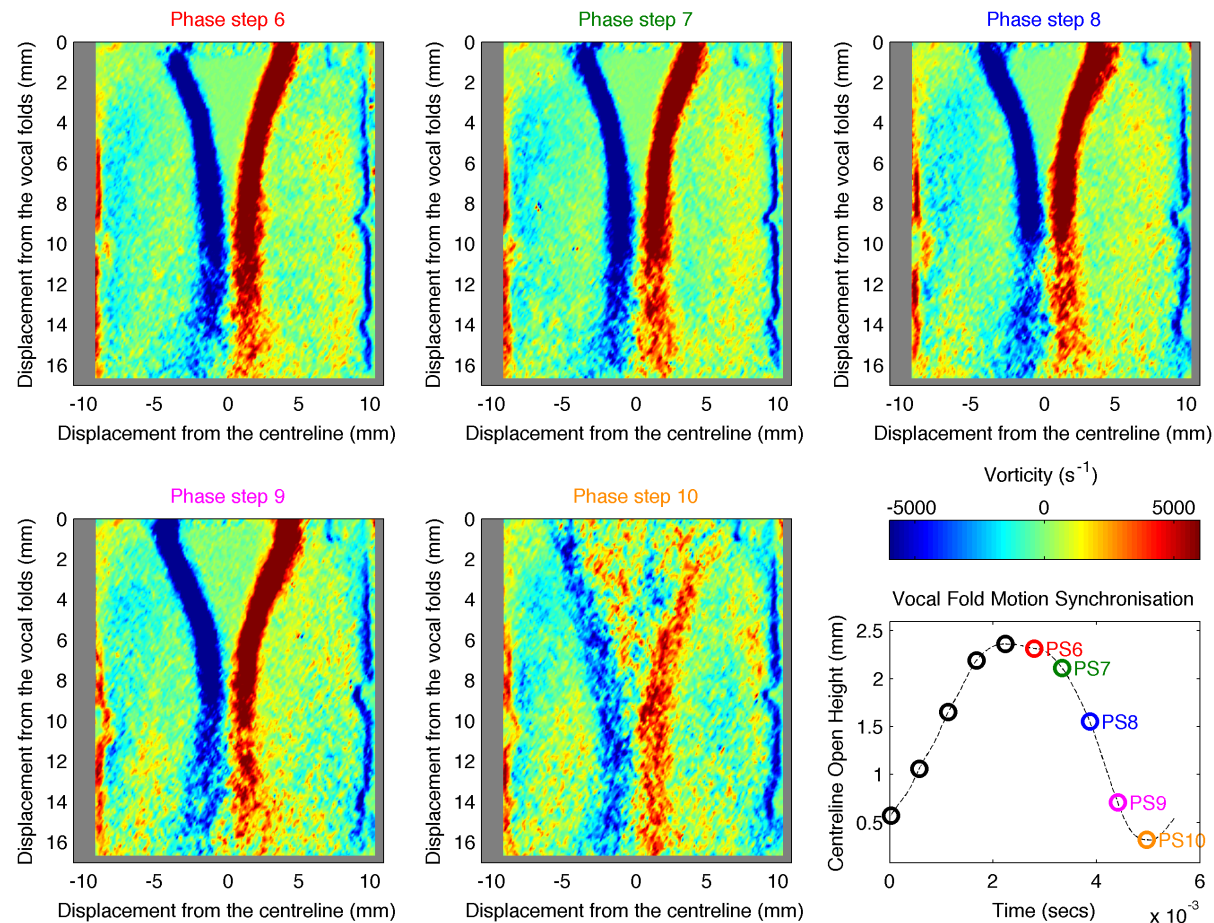


Figure 6.17: Vorticity data ensemble-averaged PIV data for phase steps 6 - 10 on an *in vitro* model of the human larynx rotated by 90° **with rigid ventricular bands placed 16 mm downstream of the vocal folds with an 8 mm separation**. The positions of the phase steps in relation to the normalised open area of the vocal fold model are included. $P_{sub} = 800$ Pa.

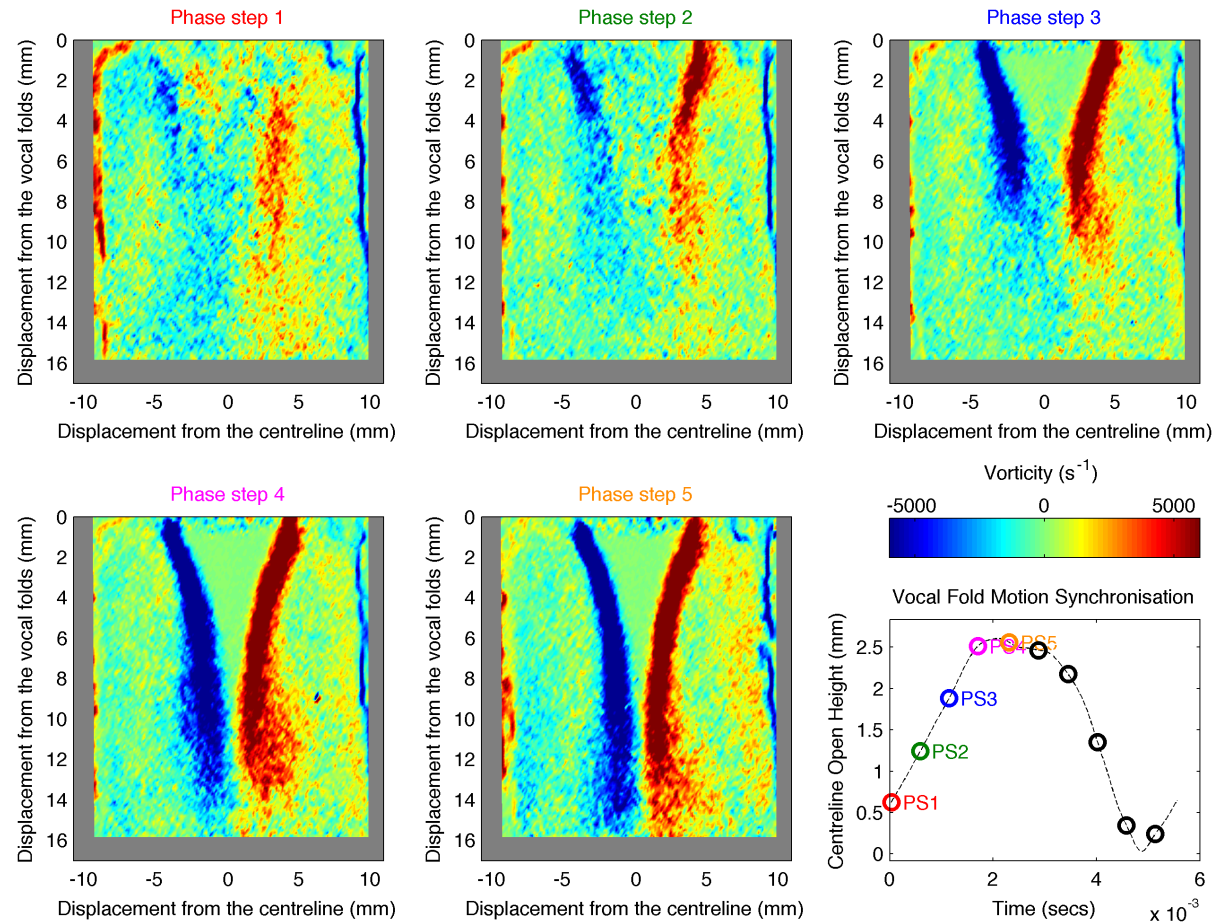


Figure 6.18: Vorticity data ensemble-averaged PIV data for phase steps 1 - 5 on an *in vitro* model of the human larynx rotated by 90° with rigid ventricular bands placed 16 mm downstream of the vocal folds with a 3 mm separation. The positions of the phase steps in relation to the normalised open area of the vocal fold model are included. $P_{sub} = 804$ Pa.

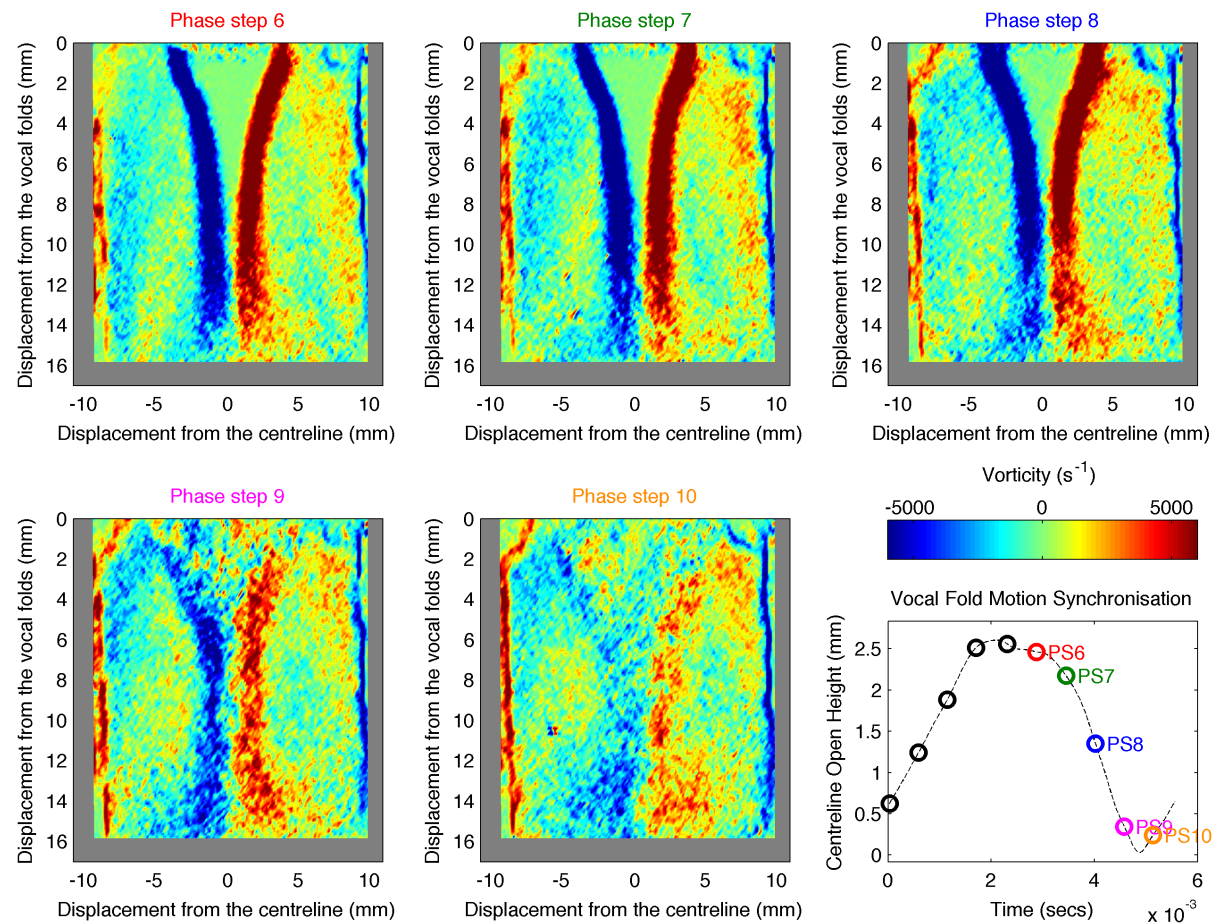


Figure 6.19: Vorticity data ensemble-averaged PIV data for phase steps 6 - 10 on an *in vitro* model of the human larynx rotated by 90° with rigid ventricular bands placed 16 mm downstream of the vocal folds with a 3 mm separation. The positions of the phase steps in relation to the normalised open area of the vocal fold model are included. $P_{sub} = 804$ Pa.

6.2. RESULTS FOR *IN VITRO* MODEL WITH RIGID VENTRICULAR BANDS

6.2.2 Jet Major Axis-Switching

Found in Figures 6.20 and 6.21 are the measured jet major axis-switching points for the *in vitro* model with ventricular bands separated by 8 mm and 3 mm respectively. In the same manner as described in Section 6.1.2, the left hand plot shows the measured jet major axis-switching point against phase step and in the right hand plot the same can be found only with the jet major axis-switching point normalised to the glottal centreline open height. Although jet major axis-switching results are presented in [Krebs 12] for their *in vitro* model without ventricular bands, their study did not consider the case with ventricular bands and the data presented in this section are novel. The measured jet major axis-switching point for the model with ventricular bands separated by 8 mm looks remarkably similar to that presented for the case without ventricular bands; however, phase steps 2 and 3 present jet axis-switching points which are notably further downstream than those for the case without ventricular bands but this difference becomes insignificant when the point of jet axis-switching is normalised. A notable difference found in the normalised plots for the case with ventricular bands set at 8 mm apart and with ventricular bands is for the jet axis-switching point at phase step 9.

Comparing the jet axis-switching points for the model with ventricular bands separated by 3 mm to those of the model with ventricular bands separated by 8 mm, there are clear and distinct differences between the two. One of the most explicit is the difference observed between the jet axis-switching point for phase step 2, which is significantly further upstream in the case with ventricular bands separated by 3 mm. The reason for this is most likely due to the glottal jet at this phase step not being clearly visible in the PIV plane parallel to the glottal centreline, caused by jet flapping already identified in Section 6.2. A significant difference is also evident between the jet axis-switching point for the two ventricular band configurations at phase step 9, most likely due to the same cause as that identified for phase step 2. A lesser difference is also observed at phase step 3, thought to be subject to the same cause. Other than these differences, the values of the major axis-switching points for the glottal jets in both cases with ventricular bands are closely comparable, indicating that the presence of the ventricular bands in these cases has no effect on the point of jet major axis-switching.

6.2. RESULTS FOR *IN VITRO* MODEL WITH RIGID VENTRICULAR BANDS

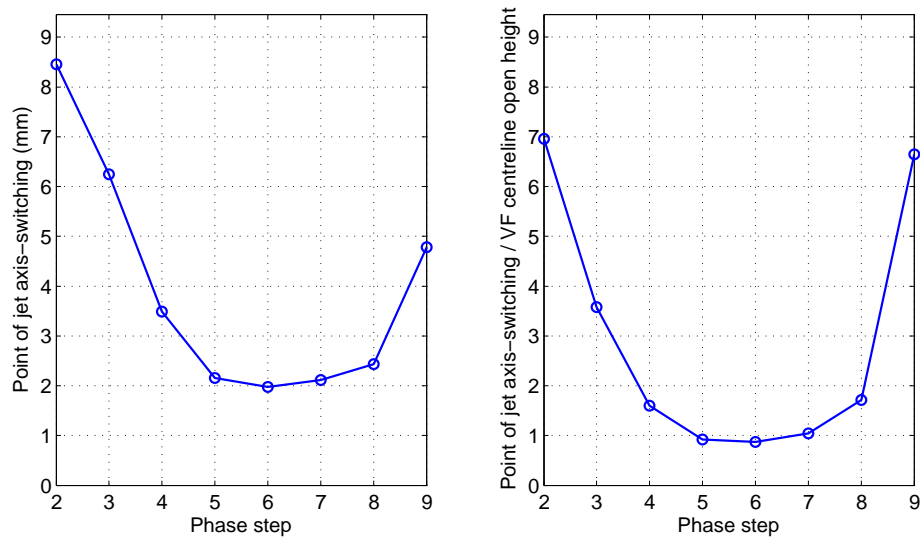


Figure 6.20: Two plots showing the distance downstream of the vocal folds whereby jet major axis-switching take place across phase steps 2 - 9 for a self-oscillating *in vitro* model of the human larynx **with rigid ventricular bands 16 mm downstream with an 8 mm separation.**

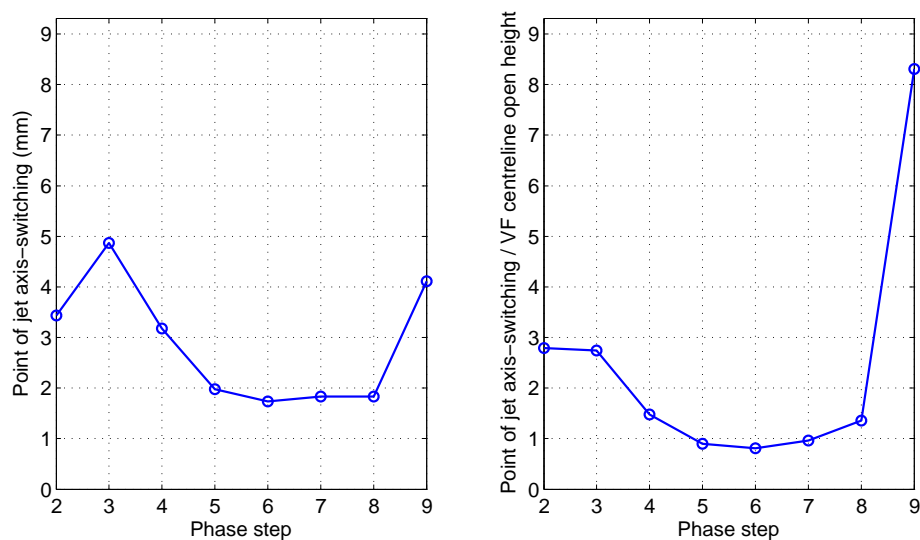


Figure 6.21: Two plots showing the distance downstream of the vocal folds whereby jet major axis-switching take place across phase steps 2 - 9 for a self-oscillating *in vitro* model of the human larynx **with rigid ventricular bands 16 mm downstream with a 3 mm separation.**

6.2. RESULTS FOR *IN VITRO* MODEL WITH RIGID VENTRICULAR BANDS

6.2.3 Summary

In this section, novel ensemble-averaged velocity magnitude, standard deviation of the velocity magnitude, vorticity, and jet major axis-switching data have been presented and discussed for the *in vitro* model with rigid ventricular bands placed 16 mm downstream and separated either by 8 mm or 3 mm. The geometry of the glottal jet was found to be the same in the cases with ventricular bands as the case without and appears to be unaffected by their presence. An increase in the average velocity magnitude was observed during the closing phase of the phonatory cycle showing a similar hysteresis-like behaviour already observed in the model without ventricular bands. However, the difference in the average velocity magnitude of the jet core between the two PIV planes investigated in the configurations including the ventricular bands was found to be less than that for the case without ventricular bands. Indeed, the average velocity magnitude of the jet core between the two PIV planes for the cases with the ventricular bands was closely comparable.

An increase in vorticity was observed for the case with ventricular bands between the shear layers and vocal tract wall on either side of the glottal jet. It was found that as the separation between the ventricular bands decreased the vorticity in these regions increased, which was attributed to the ventricular bands inhibiting the transport of the vorticity downstream. Stronger vorticity was observed during the closing phase of the phonatory cycle than the opening phase, which is consistent with observations made in [Khosla 08b] which he argues that the vortices may help with a strong vocal fold closure and hence play a role in the asymmetry observed in vocal fold oscillation. Finally, the presence of the ventricular bands was found not to have an effect on the point of jet major axis-switching.

*"Gardens are not made by singing
'Oh, how beautiful,' and sitting in the
shade."*

(Rudyard Kipling)



Conclusions and Future Work

7.1 Conclusions

Our voices and the uncountable variety of sounds that can be made with them are a truly remarkable facet of both our nature and individuality. There is not a day that goes by when I am not reminded of how complex and varied this thing is, which we take for granted as being so simple and resilient. Yet, having sung all my life and thinking that I knew all there was to know about the voice, it is only over the past 4 years that the true mysteries of this fantastic instrument have unfolded.

This study has used a variety of different approaches and experiments in order to seek answers on dynamical modelling of the human larynx during phonation. Following a brief discussion introducing the relevant anatomy and physiology of the larynx, an extensive consideration of the input made by others to the study of the voice was undertaken which was important for understanding the approach taken during this study. Through the abstraction of the complex vocal fold and laryngeal anatomy it was possible to view and begin to understand the complicated dynamic processes which take place in the larynx, and the nature of the interaction between the airflow and the structures in the larynx. The following is a summary of the major findings of this study in the light of the initial aims for the work.

7.1.1 Construction of a New *In vitro* Model of the Human Larynx and PIV of the Complete Glottal Jet

The first objective of this study was to construct an *in vitro* model of the human larynx on which is it possible to perform PIV and acquire full flow-field data up to the vocal folds, thereby exposing the complete glottal jet. This aim was satisfied entirely noting the following:

- A new *in vitro* model of the larynx was constructed by adapting a pre-existing model of a brass player's lips with a new front plate, vocal fold blocks, and vocal tracts with ventricular bands designed and built (Section 3.4.2 and Appendix C). The model was scaled at two-times life-size and made it possible to measure PIV flow field data for the glottal jet as it emerges from the vocal folds.
- A new construction technique for the *in vitro* model was developed and used in order to combat difficulties faced with reliable performance (Section 3.4.2).
- Novel results were presented for PIV conducted on a simplified self-oscillating model of the human larynx where the glottal jet is visible at the point that it leaves the vocal folds (Section 5.5). Others have only been able to acquire PIV flow field measurements from 6 mm [Krebs 12] or 8 mm [Bailly 09, Newton 09] downstream of the glottal exit due to experimental constraints.
- As an improvement on the phase windowing technique discussed in [Newton 09], new hardware and software was designed and built in order to acquire image pair acquisitions which were quasi phase-locked (Section 4.3.3). A considerable amount of time was needed in order to develop the hardware and software (both acquisition and post-processing), the technique, and to make preliminary measurements.
- As the full glottal jet was visible in the flow-field data, it was possible to measure the jet centreline, using an algorithm detailed in [Erath 06, Drechsel 08], which was adapted to work with data structures used in this study (described in Section 4.4.4). In addition, it was possible to retake the same non-dimensional measures of the jet core and pre-turbulent region undertaken in [Newton 09], with expected differences noted (Section 5.5.7).

- Finally, as in [Newton 09] and others, an asymmetry in the fluid behaviour (Section 5.5.7) and vocal fold oscillation (Section 5.5.2) was noted.

7.1.2 Impact of the Ventricular Bands on the Glottal Jet in the *In-vitro* Model of the Human Larynx

The second objective of this study was to include ventricular bands suitable for PIV within the *in vitro* model of the human larynx and analyse the effect of these constrictions on the vocal folds and glottal jet. As part of the *in vitro* model static ventricular bands were successfully designed, built, and implemented. A summary of the key observations from the results in Chapter 5 is:

- All of the PIV undertaken on the *in vitro* model had two additional setups including ventricular bands placed 16 mm downstream of the vocal folds (in the vocal tract) and with a separation (measured at the point of minimum separation) of either 8 mm or 3 mm depending on the required configuration (Section 5.6).
- The configurations with ventricular bands were found to produce slower average jet core velocities than the equivalent cases without ventricular bands, which is discussed as being evidence of a pressure recovery at the ventricular bands (Sections 5.6.5 and 5.6.6).
- Novel data showed the impact of the ventricular bands on the glottal open height in an *in vitro* model of the larynx, which exhibits the same sort of behaviour as is seen in elderly patients (Section 5.6.1). The data showed that a possible reason for supraglottic hypertension discussed in [Hagen 96] was that it improved vocal fold closure, thereby improving voice quality.
- The geometry of the glottal jet was not found to change significantly when the ventricular bands were present in comparison to the configurations where they were absent (Sections 5.6.2 and 5.6.6).
- The presence of the ventricular bands, however, did occasionally produce jet flapping and adherence on to one of the walls of the vocal tract (known as the Coandă effect), which was not present in the case without ventricular bands (Section 5.6.3).

7.1.3 Investigation of the Three-dimensional Dynamical Nature of the Glottal Jet

The third objective of this study was to investigate the three-dimensional dynamical nature of the glottal jet through the analysis of flow-field data acquired on the same *in vitro* model of the human larynx. Like the other two aims, this was achieved with the key findings relating to this aim being:

- The new front plate design detailed in Section 3.4.2 made it possible to rotate the *in vitro* model and conduct PIV in the plane perpendicular to that undertaken previously, thereby exposing an aspect of the three-dimensional nature of the glottal jet.
- The geometry of the glottal jet in the rotated aspect was different to that seen in the plane perpendicular to it; rather than expanding, the jet contracted (Section 6.1).
- The ventricular bands were found not to exert any new influence on the geometry of the glottal jet in this aspect, with the shape being the same as for the case without ventricular bands (Sections 6.1 and 6.2).
- As the shape in the rotated aspect was found to be very similar to that shown in [Krebs 12], the point of jet major axis-switching was found and discussed in the light of being a possible indicator of a change in the point of flow separation (Sections 6.2.2 and 6.2).
- With the ventricular bands included as part of the configuration, increased vorticity was observed between the shear layers and the walls of the vocal tract. As the vorticity intensified as the separation between the ventricular bands reduced, this observation was attributed to the vortices becoming ‘trapped’ and the case with ventricular bands therefore being less efficient at vortex transport (Sections 6.1.1 and 6.2.1).
- A new formula to calculate the jet volume velocity was proposed and applied based on observations from preliminary data and those published in [Krebs 12]. This was then used to calculate the flow resistance and admittance (discussed within Section 4.4.5).

7.1.4 Further Develop an Existing State-of-the-art Computational Model in order to Investigate the Relationship between Jet Behaviour and Vocal Fold Oscillation

The final objective of this study was to further develop an existing state-of-the-art computational, low-order, lumped-element, physical model of the human larynx in order to investigate the relationship between jet behaviour and vocal fold oscillation. The following conclusions were formed from this work:

- The model developed and discussed in [Bailly 09] was translated from French to English and modified in order to work with the parameters from the *in vitro* model used in this study (Section 3.7).
- The physical model was further adapted so that the expansion angle for the turbulent jet hypothesis could be altered easily. This therefore meant that the width of the glottal jet could be extracted at three different points along the laryngeal ventricle and optimised in order to work more efficiently, both in terms of memory use and speed of computation.
- In order to study the impact of the jet behaviour on vocal fold oscillation, the physical model was modified in order to work with Octave and the Condor distributed computing application (Section 3.7.5).
- The physical model was found to be affected by the temporal sample rate chosen, and so for all simulations after this test the sample rate was set to 100 kHz (Section 5.7.1).
- Part of the relationship between jet behaviour and vocal fold oscillation involves the ventricular bands. It was found that the ventricular bands did affect the oscillation of the vocal folds in a simplified model of the flow (Section 5.7.2).
- Finally, it was found that the turbulent jet hypothesis, although the best candidate of the three hypotheses proposed in Chapter 3 is still not a suitably accurate model of the glottal jet across the laryngeal ventricle (Section 5.7.4).

7.2 Possible Future Work

With so many researchers across the world both in academia and in industry working on many different aspects of the voice and with a number of approaches which is greater still, this particular section of the thesis could quite easily be the largest of the entire document. With anything as complex and demanding as the human voice, there will always be many questions. I am going to be brief and restrict myself to discussing two possible areas for future research.

7.2.1 Further Work on the Ventricular Bands

This work has only begun to scratch the surface in relation to understanding the full extent to which the vocal folds and ventricular bands interact via the glottal jet. Having only used two separation distances of the ventricular bands at a fixed position, it is highly likely that only some of the impact of the ventricular bands has been explored and that a different behaviour might be observed when they are placed elsewhere. A systematic experimental study using a simplified model would be of great help here not only to those pursuing work on the human voice, but also to the field of fluid mechanics in general.

One of the most exciting papers to come out in the last few years is [Bailly 10], as this paper begins to explore the conditions under which a self-sustained simplified model (albeit computational) of the vocal folds interacts with the ventricular bands in order to achieve period doubling oscillation. I personally would like to see experimentalists include flexible ventricular bands in their simplified models of the larynx and getting some flow field data for this model in order to see what is going on. This will be very complex, but a very interesting and useful avenue down which to walk. Also, using tools like Condor may help with the increase in parameter space expected when adding another oscillating entity, by reducing the time in order to run simulations without having to buy expensive dedicated heavy compute resources.

7.2.2 Using *in vitro* Models for Pathological Comparative Studies

The *in vitro* model used in this study presents behaviour which is similar to that exhibited by elderly patients. Although there are many computational studies of the

pathological voice (wherein polyps or cysts are quite often modelled) owing to the ease to which it is possible to include a simple pathology within an existing model, some *in vitro* studies have been undertaken by experimentalists; however, most have used forced oscillation as the means of replicating the behaviour of the vocal folds. Using this method to drive the vocal folds could be considered a weakness of these studies, as the vocal folds do not self-oscillate as would be expected within a person suffering with these types of voice pathology. This may have an implication on any observed results using models employing forced oscillation, as the polyp or cyst on the vocal folds creates an obstruction which may not only disrupt the glottal airflow, but could also have an impact on the stability of vocal fold oscillation which it may not be possible to replicate using forced oscillation. It would therefore be good to see more studies of the pathological voice undertaken using models driven by self-sustained oscillation.

Bibliography

- [ACI 12] Air Control Industries Ltd. *Company website*. <http://www.aircontrolindustries.com/>, Accessed: August 2012.
- [Adachi 96] S. Adachi & M. Sato. *Trumpet sound simulation using a two-dimensional lip vibration model*. The Journal of the Acoustical Society of America, vol. 99, no. 2, pages 1200–1209, 1996.
- [Adachi 05] S. Adachi & J. Yu. *Two-dimensional model of vocal fold vibration for sound synthesis of voice and soprano singing*. The Journal of the Acoustical Society of America, vol. 117, no. 5, pages 3213–3224, 2005.
- [Adrian 93] R. J. Adrian, editor. *Selected papers on laser doppler velocimetry*. SPIE Optical Engineering Press,, Bellingham, WA :, 1993.
- [Agarwal 03] M. Agarwal, R. C. Scherer & H. Hollien. *The false vocal folds: Shape and size in frontal view during phonation based on laminagraphic tracings*. Journal of Voice, vol. 17, no. 2, pages 97–113, 2003.
- [Agarwal 04] M. Agarwal. *The false vocal folds and their effect on translaryngeal airflow resistance*. PhD thesis, Bowling Green State University, OH, 2004.
- [Alipour 95] F. Alipour & R. C. Scherer. *Pulsatile airflow during phonation: An excised larynx model*. The Journal of the Acoustical Society of America, vol. 97, no. 2, pages 1241–1248, 1995.
- [Alipour 04] F. Alipour & R. C. Scherer. *Flow separation in a computational oscillating vocal fold model*. The Journal of the Acoustical Society of America, vol. 116, no. 3, pages 1710–1719, 2004.
- [Alipour 06] F. Alipour & R. C. Scherer. *Characterizing glottal jet turbulence*. The Journal of the Acoustical Society of America, vol. 119, no. 2, pages 1063–1073, 2006.
- [Alipour 07] F. Alipour, S. Jaiswal & E. Finnegan. *Aerodynamic and acoustic effects of false vocal folds and epiglottis in excised larynx models*. The Annals Of Otology, Rhinology, And Laryngology, vol. 116, no. 2, pages 135 – 144, 2007.
- [Alipour 12] F. Alipour & R. C. Scherer. *Ventricular pressures in phonating excised larynges*. The Journal of the Acoustical Society of America, vol. 132, no. 2, pages 1017–1026, 2012.
- [Apostoli 10a] A. G. Apostoli, D. M. Campbell & C. A. Greated. *Flow field measurements in a self-oscillating in-vitro model of the vocal folds*. In proceedings of the 10ème Congrès Français d’Acoustique, Lyon, France, April 2010.

- [Apostoli 10b] A. G. Apostoli, D. M. Campbell & C. A. Greated. *Glottal jet behaviour in a self-oscillating in-vitro model of the vocal folds with downstream constrictions*. In proceedings of the International Congress on Acoustics and the International Symposium on Music Acoustics, Sydney and Katoomba, Australia, August 2010.
- [Aronson 09] A. E. Aronson & D. M. Bless. *Clinical Voice Disorders*. Thieme Medical Publishers, Inc., New York, USA, 4th edition, 2009.
- [Arthur 09] J. K. Arthur, D. W. Ruth & M. F. Tachie. *PIV measurements of flow through a model porous medium with varying boundary conditions*. *Journal of Fluid Mechanics*, vol. 629, pages 343–374, 2009.
- [Baer 75] T. Baer. *Investigation of phonation using excised larynxes*. PhD thesis, Massachusetts Institute of Technology, February 1975.
- [Bailly 06] L. Bailly, N. Ruty, A. Van Hirtum, J. Cisonni, X. Pelorson & N. Henrich. *Aerodynamic interaction between the vocal folds and the ventricular bands*. In 7th International Conference Advances in Quantitative Laryngology, Voice and Speech Research, 2006.
- [Bailly 08] L. Bailly, X. Pelorson, N. Henrich & N. Ruty. *Influence of a constriction in the near field of the vocal folds: Physical modeling and experimental validation*. *The Journal of the Acoustical Society of America*, vol. 124, no. 5, pages 3296–3308, 2008.
- [Bailly 09] L. Bailly. *Interaction entre cordes vocales et bandes ventriculaires en phonation: exploration in-vivo, modélisation physique, validation in-vitro*. PhD thesis, École Doctorale de L'Université du Maine, June 2009.
- [Bailly 10] L. Bailly, N. Henrich & X. Pelorson. *Vocal fold and ventricular fold vibration in period-doubling phonation: Physiological description and aerodynamic modeling*. *The Journal of the Acoustical Society of America*, vol. 127, no. 5, pages 3212–3222, 2010.
- [Bakke 57] P. Bakke. *An experimental investigation of a wall jet*. *Journal of Fluid Mechanics*, vol. 2, no. 5, pages 467–472, 1957.
- [Ban 12] Bruël and Kjær Sound & Vibration Measurement A/S. *Company website*. <http://www.bksv.co.uk/>, Accessed: August 2012.
- [Barney 99] A. Barney, C. H. Shadle & P. O. A. L. Davies. *Fluid flow in a dynamic mechanical model of the vocal folds and tract. i. measurements and theory*. *The Journal of the Acoustical Society of America*, vol. 105, no. 1, pages 444–455, 1999.
- [Becker 09] S. Becker, S. Kniesburges, S. Müller, A. Delgado, G. Link, M. Kaltenbacher & M. Döllinger. *Flow-structure-acoustic interaction in a human*

- voice model. The Journal of the Acoustical Society of America, vol. 125, no. 3, pages 1351–1361, 2009.
- [Berke 87] G. S. Berke, D. M. Moore, D. G. Hanson, D. R. Hantke, B. R. Gerratt & F. Burstein. *Laryngeal modeling: theoretical, in vitro, in-vivo*. Laryngoscope, vol. 97, no. 7, pages 871–881, July 1987.
- [Berke 89] G. S. Berke, D. M. Moore, P. A. Monkewitz, D. G. Hanson & B. R. Gerratt. *A preliminary study of particle velocity during phonation in an in vivo canine model*. Journal of Voice, vol. 3, no. 4, pages 306 – 313, 1989.
- [Bian 10] S. Bian, S. L. Ceccio & J. F. Driscoll. *A dual-camera cinematographic PIV measurement system at kilohertz frame rate for high-speed, unsteady flows*. Experiments in Fluids, vol. 48, no. 3, pages 487 – 495, March 2010.
- [Billauer 12] E. Billauer. *peakdet: Peak detection using matlab (non-derivative local extremum, maximum, minimum)*. <http://www.billauer.co.il/peakdet.html>, Accessed: August 2012.
- [Birkholz 11] P. Birkholz. *A survey of self-oscillating lumped-element models of the vocal folds*. In B. J. Kröger & P. Birkholz, editors, Studentexte zur Sprachkommunikation (Bd. 61): Elektronische Sprachsignalverarbeitung 2011. Tagungsband der 22. Konferenz, pages 47 – 58. TUD Press, 2011.
- [bnc 12] Berkeley Nucleonics Corporation. *Company website*. <http://www.berkeleynucleonics.com/>, Accessed: August 2012.
- [Bromage 07] S. Bromage. *Visualisation of the lip motion of brass instrument players, and investigations of an artificial mouth as a tool for comparative studies of instruments*. PhD thesis, School of Physics; University of Edinburgh, April 2007.
- [Bru 02] Bruël and Kjær. *Help documentation from PULSE LabShop 6.1.4.4*, 2002.
- [Brücker 04] C. Brücker, M. Triep & M. Kob. *Study of the vortex dynamics in a mechanical model of the vocal folds using particle image velocimetry*. In proceedings of the 4th International Conference on Voice Physiology and Biomechanics, pages 11 – 17, Marseille, France, 2004.
- [Campbell 98] D. M. Campbell & C. A. Greated. *The Musician’s Guide to Acoustics*. Oxford University Press, Oxford, 1998.
- [Campbell 99] D. M. Campbell. *Nonlinear dynamics of musical reed and brass wind instruments*. Contemporary Physics, vol. 40, pages 415–431, June 1999.
- [Campbell 00] M. Campbell, J. A. Cosgrove, C. A. Greated, S. Jack & D. Rockliff. *Review of LDA and PIV applied to the measurement of sound and acoustic streaming*. Optics and Laser Technology, vol. 32, no. 7-8, pages 629–639, 2000.

- [Campbell 04] D. M. Campbell. *Brass instruments as we know them today*. Acta Acustica united with Acustica, vol. 90, pages 600–610, July/August 2004.
- [Chein 88] R. Chein & J. N. Chung. *Simulation of particle dispersion in a two-dimensional mixing layer*. AIChE Journal, vol. 34, no. 6, pages 946–954, 1988.
- [Childers 94] D. Childers & C.-F. Wong. *Measuring and modeling vocal source-tract interaction*. Biomedical Engineering, IEEE Transactions on, vol. 41, no. 7, pages 663–671, July 1994.
- [Cisonni 08a] J. Cisonni. *Modélisation et inversion d'un système complexe de production de signaux acoustiques; application à la voix et aux pathologies*. PhD thesis, Institut Polytechnique de Grenoble, November 2008.
- [Cisonni 08b] J. Cisonni, A. Van Hirtum, X. Pelorson & J. Willems. *Theoretical simulation and experimental validation of inverse quasi-one-dimensional steady and unsteady glottal flow models*. The Journal of the Acoustical Society of America, vol. 124, no. 1, pages 535–545, 2008.
- [Cisonni 10] J. Cisonni, A. Van Hirtum, X. Luo & X. Pelorson. *Experimental validation of quasi-one-dimensional and two-dimensional steady glottal flow models*. Medical and Biological Engineering and Computing, vol. 48, pages 903–910, 2010.
- [Cisonni 11] J. Cisonni, A. Van Hirtum, X. Pelorson & J. Lucero. *The influence of geometrical and mechanical input parameters on theoretical models of phonation*. Acta Acustica united with Acustica, vol. 97, pages 291–302, March/April 2011.
- [Con 12] Condor Research Project, University of Wisconsin-Madison. *Condor project homepage*. <http://research.cs.wisc.edu/condor/index.html>, Accessed: August 2012.
- [Cullen 00a] J. S. Cullen, J. Gilbert & D. M. Campbell. *Brass instruments: Linear stability analysis and experiments with an artificial mouth*. Acta Acustica united with Acustica, vol. 86, pages 704–724, July 2000.
- [Cullen 00b] J. S. Cullen. *A study of brass instrument acoustics using an artificial lip reed mechanism, laser doppler anemometry and other techniques*. PhD thesis, Department of Physics and Astronomy, University of Edinburgh, May 2000.
- [Dan 00] Dantec Dynamics A/S. *Product information: Adaptive correlation in FlowManager*, 2000.
- [Dan 09] Dantec Dynamics. *Help menu from Dantec Dynamics DynamicStudio v2.30*, 2009.

- [dan 12] Dantec Dynamics A/S. *Company website*. <http://www.dantecdynamics.com/>, Accessed: August 2012.
- [Dantec A/S 98] Dantec A/S. *Safex fog generator*. Technical Report, Dantec Measurement Technology A/S, 1998.
- [Degroot 08] A. Degroot, R. MacDonald, O. Richoux, B. Gazengel & M. Campbell. *Suitability of laser doppler velocimetry for the calibration of pressure microphones*. Applied Acoustics, vol. 69, no. 12, pages 1308 – 1317, 2008.
- [dig 12] Digitron Instrumentation Ltd. *Company website*. <http://digitron.co.uk/>, Accessed: August 2012.
- [Drechsel 07] J. S. Drechsel. *Characterization of synthetic, self-oscillating vocal fold models*. Master's thesis, Department of Mechanical Engineering; Brigham Young University, December 2007.
- [Drechsel 08] J. S. Drechsel & S. L. Thomson. *Influence of supraglottal structures on the glottal jet exiting a two-layer synthetic, self-oscillating vocal fold models*. The Journal of the Acoustical Society of America, vol. 123, no. 6, pages 4434–4445, 2008.
- [Erath 06] B. D. Erath & M. W. Plesniak. *An investigation of bimodal jet trajectory in flow through scaled models of the human vocal tract*. Experiments in Fluids, vol. 40, no. 5, pages 683–696, May 2006.
- [Erath 10a] B. D. Erath & M. W. Plesniak. *An investigation of asymmetric flow features in a scaled-up driven model of the human vocal folds*. Experiments in Fluids, vol. 49, no. 1, pages 131 – 146, July 2010.
- [Erath 10b] B. D. Erath & M. W. Plesniak. *Viscous flow features in scaled-up physical models of normal and pathological vocal phonation*. International Journal of Heat and Fluid Flow, vol. 31, no. 3, pages 468 – 481, 2010.
- [Faber 95] T. E. Faber. Fluid Dynamics for Physicists. Cambridge University Press, 1995.
- [Ferrein 46] A. Ferrein. *De la formation de la voix de l'homme*. In Suite de Memoires de Mathematique et de Physique, tires des Registres de l'Academie Royale des Sciences de l'Annee MDCCXLI, pages 409–432, 545–579. Pierre Mortier; Amsterdam, 1746.
- [Finnegan 09] E. M. Finnegan & F. Alipour. *Phonatory effects of supraglottic structures in excised canine larynges*. Journal of Voice, vol. 23, no. 1, pages 51 – 61, 2009.

- [Fuks 98] L. Fuks, B. Hammarberg & J. Sundberg. *A self-sustained vocal-ventricular phonation mode: Acoustical, aerodynamic and glottographic evidences*. Quarterly Progress and Status Report, KTH, Royal Institute of Technology, 1998.
- [Gilbert 98] J. Gilbert, S. Ponthus & J.-F. Petiot. *Artificial buzzing lips and brass instruments: Experimental results*. The Journal of the Acoustical Society of America, vol. 104, no. 3, pages 1627–1632, 1998.
- [Gray 05] C. D. Gray. *Acoustic pulse reflectometry for measurement of the vocal tract with application in voice synthesis*. PhD thesis, School of Physics; University of Edinburgh, November 2005.
- [Greated 90] C. A. Greated. *Fluid dynamics*. Lecture Notes, The University of Edinburgh, Unpublished, 1990.
- [Gutmark 99] E. J. Gutmark & F. F. Grinstein. *Flow control with noncircular jets*. Annual Review of Fluid Mechanics, vol. 31, pages 239–272, January 1999.
- [Hagen 96] P. Hagen, G. D. Lyons & D. W. Nuss. *Dysphonia in the elderly: diagnosis and management of age-related voice changes*. Southern Medical Journal, vol. 89, no. 2, pages 204–207, February 1996.
- [Hast 61] M. H. Hast. *Subglottic air pressure and neural stimulation in phonation*. Journal of Applied Physiology, vol. 16, no. 6, pages 1142–1146, November 1961.
- [Henrich 06a] N. Henrich, B. Lortat-Jacob, M. Castellengo, L. Bailly & X. Pelorson. *Period-doubling occurrences in singing: the ‘bassu’ case in traditional sardinian ‘a tenore’ singing*. In International Conference on Voice Physiology and Biomechanics, Tokyo, Jul, 2006.
- [Henrich 06b] N. Henrich. *Mirroring the voice from Garcia to the present day: Some insights into singing voice registers*. Logopedics Phoniatrics Vocology, vol. 31, no. 1, pages 3–14, 2006.
- [Hirano 87] M. Hirano, T. Yoshida & S. Kurita. *Anatomy and behaviour of the vocal process*. In T. Baer, C. Sasaki & K. Harris, editors, Laryngeal function in phonation and respiration, pages 1–13. College Hill Press; Boston, Massachusetts, 1987.
- [Hirschberg 92] A. Hirschberg. *Some fluid dynamic aspects of speech*. Bulletin de la Communication Parlée, vol. 2, pages 7–30, 1992.
- [Hirschberg 96] A. Hirschberg, X. Pelorson & J. Gilbert. *Aeroacoustics of musical instruments*. Meccanica, vol. 31, no. 2, pages 131–141, April 1996.

- [Hofmans 98] G. C. J. Hofmans. *Vortex sound in confined flows*. PhD thesis, Technical University Eindhoven, September 1998.
- [Hofmans 01] G. C. J. Hofmans, R. J. J. Boot, P. P. J. M. Durrieu, Y. Auregan & A. Hirschberg. *Aeroacoustic response of a slit-shaped diaphragm in a pipe at low helmholtz number, 1: Quasi-steady results*. *Journal of Sound and Vibration*, vol. 244, no. 1, pages 35 – 56, 2001.
- [Hofmans 03] G. C. J. Hofmans, G. Groot, M. Ranucci, G. Graziani & A. Hirschberg. *Unsteady flow through in-vitro models of the glottis*. *The Journal of the Acoustical Society of America*, vol. 113, no. 3, pages 1658–1675, 2003.
- [Holman 86] J. P. Holman. *Heat transfer*. McGraw-Hill Book Company, 6th edition, 1986.
- [HP 12] Hewlett-Packard Development Company, L.P. *Company website*. [www8.hp.com/uk/en/home.html](http://www.hp.com/uk/en/home.html), Accessed: August 2012.
- [Ishizaka 72] K. Ishizaka & J. L. Flanagan. *Synthesis of voiced sounds from a two-mass model of the vocal cords*. *Bell System Technical Journal*, vol. 51, pages 1233–1268, 1972.
- [Jensen 04] K. D. Jensen. *Flow measurements*. *Journal of the Brazilian Society of Mechanical Sciences and Engineering*, vol. 26, no. 4, pages 400–419, October-December 2004.
- [Kaburagi 11] T. Kaburagi. *Voice production model integrating boundary-layer analysis of glottal flow and source-filter coupling*. *The Journal of the Acoustical Society of America*, vol. 129, no. 3, pages 1554–1567, 2011.
- [Kähler 12] C. Kähler, S. Scharnowski & C. Cierpka. *On the uncertainty of digital piv and ptv near walls*. *Experiments in Fluids*, vol. 52, pages 1641–1656, 2012.
- [Keane 92] R. D. Keane & R. J. Adrian. *Theory of cross-correlation analysis of PIV images*. *Applied Scientific Research*, vol. 49, pages 191–215, 1992.
- [kem 12] Kemo Limited. *Company website*. <http://www.kemo.com/kemohtml/index2.html>, Accessed: August 2012.
- [Khosla 07] S. Khosla, S. Murugappan, E. Gutmark & R. Scherer. *Vortical flow field during phonation in an excised canine larynx model*. *Annals of Otology, Rhinology and Laryngology*, vol. 116, no. 3, pages 217–228, March 2007.
- [Khosla 08a] S. Khosla, S. Murugappan, R. Lakhamraju & E. Gutmark. *Using particle imaging velocimetry to measure anterior-posterior velocity gradients in the excised canine larynx model*. *Ann. Otol. Rhinol. Laryngol.*, vol. 117, no. 2, pages 134–144, Feb 2008.

- [Khosla 08b] S. Khosla, S. Murugappan & E. Gutmark. *What can vortices tell us about vocal fold vibration and voice production*. *Current Opinion in Otolaryngology and Head and Neck Surgery*, vol. 16, pages 183–187, 2008.
- [Khosla 09] S. Khosla, S. Murugappan, R. Paniello, J. Ying & E. Gutmark. *Role of vortices in voice production: Normal versus asymmetric tension*. *The Laryngoscope*, vol. 119, no. 1, pages 216–221, 2009.
- [Kinsler 00] L. E. Kinsler, A. R. Frey, A. B. Coppens & J. V. Sanders. *Fundamentals of Acoustics*. John Wiley & Sons, Inc., 4th edition, 2000.
- [Kob 02] M. Kob. *Physical modelling of the singing voice*. PhD thesis, Rheinisch-Westfälischen Technischen Hochschule Aachen, June 2002.
- [Kob 04] M. Kob. *Singing voice modelling as we know it today*. *Acta Acustica united with Acustica*, vol. 90, pages 649–661, July/August 2004.
- [Krane 05] M. H. Krane. *Aeroacoustic production of low-frequency unvoiced speech sounds*. *The Journal of the Acoustical Society of America*, vol. 118, no. 1, pages 410–427, 2005.
- [Krane 06] M. H. Krane & T. Wei. *Theoretical assessment of unsteady aerodynamic effects in phonation*. *The Journal of the Acoustical Society of America*, vol. 120, no. 3, pages 1578–1588, 2006.
- [Krane 07] M. Krane, M. Barry & T. Wei. *Unsteady behavior of flow in a scaled-up vocal folds model*. *The Journal of the Acoustical Society of America*, vol. 122, no. 6, pages 3659–3670, 2007.
- [Krane 10] M. H. Krane, M. Barry & T. Wei. *Dynamics of temporal variations in phonatory flow*. *The Journal of the Acoustical Society of America*, vol. 128, no. 1, pages 372–383, 2010.
- [Krebs 12] F. Krebs, F. Silva, D. Sciamarella & G. Artana. *A three-dimensional study of the glottal jet*. *Experiments in Fluids*, vol. 52, pages 1133–1147, 2012.
- [Kundu 02] P. K. Kundu, I. M. Cohen & H. H. Hu. *Fluid Mechanics*. Academic Press, 2nd edition, 2002.
- [Lemke 94] J. H. Lemke & H. M. Samawi. *Establishment of normal limits for speech characteristics*. In D. Wong, editor, *Proceedings of the Workshop on Acoustic Voice Analysis*, Denver, Colorado, USA, 17 - 18 February 1994. National Center for Voice and Speech.
- [Lighthill 52] M. J. Lighthill. *On sound generated aerodynamically. i. general theory*. *Proceedings of the Royal Society of London. Series A, Mathematical and Physical Sciences*, vol. 211, no. 1107, pages 564–587, 1952.

- [Lighthill 54] M. J. Lighthill. *On sound generated aerodynamically. ii. turbulence as a source of sound*. Proceedings of the Royal Society of London. Series A, Mathematical and Physical Sciences, vol. 222, no. 1148, pages 1–32, 1954.
- [Lindestad 01] P.-A. Lindestad, M. Södersten, B. Merker & S. Granqvist. *Voice source characteristics in mongolian “throat singing” studied with high-speed imaging technique, acoustic spectra, and inverse filtering*. Journal of Voice, vol. 15, no. 1, pages 78 – 85, 2001.
- [Logie 09] S. M. Logie, S. Stevenson, A. G. Apostoli, J. P. Chick & D. M. Campbell. *Transient behaviour in the motion of the brass player’s lips during a lip-slur*. In proceedings of the NAG-DAGA International Conference on Acoustics, pages 889–892, 2009.
- [Lous 98] N. J. C. Lous, R. N. J. Veldhuis & A. Hirschberg. *A symmetrical two-mass vocal-fold model coupled to vocal tract and trachea, with application to prosthesis design*. Acta Acustica, vol. 84, no. 6, pages 1135–1150, November/December 1998.
- [Lucero 09] J. C. Lucero, A. Van Hirtum, N. Ruty, J. Cisonni & X. Pelorson. *Validation of theoretical models of phonation threshold pressure with data from a vocal fold mechanical replica*. The Journal of the Acoustical Society of America, vol. 125, no. 2, pages 632–635, 2009.
- [Lucero 12] J. C. Lucero, K. G. Lourenço, N. Hermant, A. V. Hirtum & X. Pelorson. *Effect of source–tract acoustical coupling on the oscillation onset of the vocal folds*. The Journal of the Acoustical Society of America, vol. 132, no. 1, pages 403–411, 2012.
- [MacDonald 09] R. MacDonald. *A study of the undercutting of woodwind toneholes using particle image velocimetry*. PhD thesis, School of Physics and Astronomy; University of Edinburgh, 2009.
- [Massey 98] B. S. Massey. *Mechanics of Fluids*. Stanley Thornes (London) Ltd, 7th edition, 1998.
- [mat 12] The MathWorks, Inc. *Company website*. <http://www.mathworks.co.uk>, Accessed: August 2012.
- [Mattheus 11] W. Mattheus & C. Brücker. *Asymmetric glottal jet deflection: Differences of two- and three-dimensional models*. The Journal of the Acoustical Society of America, vol. 130, no. 6, pages EL373–EL379, 2011.
- [McGowan 88] R. S. McGowan. *An aeroacoustic approach to phonation*. The Journal of the Acoustical Society of America, vol. 83, no. 2, pages 696–704, 1988.

- [Mi 07] J. Mi, P. Kalt, G. Nathan & C. Wong. *PIV measurements of a turbulent jet issuing from round sharp-edged plate*. Experiments in Fluids, vol. 42, pages 625–637, 2007.
- [Mills 72] C. J. Mills. *Measurement of pulsatile flow and flow velocity*. In D. H. Bergel, editor, Cardiovascular Fluid Dynamics, volume 1, chapter 3, pages 51 – 90. Academic Press, June 1972.
- [Mongeau 97] L. Mongeau, N. Franche, C. H. Coker & R. A. Kubli. *Characteristics of a pulsating jet through a small modulated orifice, with application to voice production*. The Journal of the Acoustical Society of America, vol. 102, no. 2, pages 1121–1133, 1997.
- [Murugappan 08] S. Murugappan, E. J. Gutmark, R. R. Lakhamraju & S. Khosla. *Flow-structure interaction effects on a jet emanating from a flexible nozzle*. Physics of Fluids, vol. 20, no. 11, page 117105, 2008.
- [Nasri 96] S. Nasri, J. Jasleen, B. R. Gerratt, J. A. Sercarz, R. Wenokur & G. S. Berke. *Ventricular dysphonia: A case of false vocal fold mucosal traveling wave*. American Journal of Otolaryngology, vol. 17, no. 6, pages 427 – 431, 1996.
- [Neal 02] M. A. Neal. *A study of the brass instrument lip reed mechanism using artificial lips and lattice boltzmann flow simulations*. PhD thesis, Department of Physics and Astronomy, University of Edinburgh, September 2002.
- [Neubauer 07] J. Neubauer, Z. Zhang, R. Miraghaie & D. A. Berry. *Coherent structures of the near field flow in a self-oscillating physical model of the vocal folds*. The Journal of the Acoustical Society of America, vol. 121, no. 2, pages 1102–1118, 2007.
- [Newton 08] M. J. Newton, M. Campbell & J. Gilbert. *Mechanical response measurements of real and artificial brass players lips*. The Journal of the Acoustical Society of America, vol. 123, no. 1, pages EL14–EL20, 2008.
- [Newton 09] M. J. Newton. *Experimental mechanical and fluid mechanical investigations of the brass instrument lip-reed and the human vocal folds*. PhD thesis, School of Physics and Astronomy, University of Edinburgh, April 2009.
- [NI 12] National Instruments Corporation. *Company website*. <http://www.ni.com/>, Accessed: August 2012.
- [oxf 12] Oxford Lasers Ltd. *Company website*. <http://www.oxfordlasers.com/>, Accessed: August 2012.
- [pco 12] PCO AG. *Company website*. <http://www.pco.de/>, Accessed: August 2012.

- [Pelorson 94] X. Pelorson, A. Hirschberg, R. van Hassel, A. Wijnands & Y. Auregan. *Theoretical and experimental study of quasisteady-flow separation within the glottis during phonation. application to a modified two-mass model*. The Journal of the Acoustical Society of America, vol. 96, pages 3416–3431, 1994.
- [Pelorson 95] X. Pelorson, A. Hirschberg, A. Wijnands & H. Bailliet. *Description of the flow through in-vitro models of the glottis during phonation*. Acta Acustica, vol. 3, pages 191–202, April 1995.
- [Pelorson 96] X. Pelorson, C. Vescovi, E. Castelli, A. Hirschberg, A. Wijnands & H. Bailliet. *Description of the flow through in-vitro models of the glottis during phonation. application to voiced sounds synthesis*. Acta Acustica united with Acustica, vol. 82, no. 2, pages 358 – 361, March/April 1996.
- [Pelorson 08] X. Pelorson. *Contributions à l'étude aéro-acoustique de la voix*. HDR thesis, Institut National Polytechnique de Grenoble, 2008.
- [pho 01] Voice Centre at Eastern Virginia Medical School. *Mechanism of voice production: Air flow and vocal fold vibration*. http://www.voice-center.com/voice_mecha.html, Accessed: December 2001.
- [Raffel 07] M. Raffel, C. E. Willert, S. T. Wereley & J. Kompenhans. *Particle Image Velocimetry: A Practical Guide*. Experimental Fluid Mechanics. Springer Berlin Heidelberg, 2nd edition, 2007.
- [Richards 03] O. Richards. *Investigation of the lip reed using computational modelling and experimental studies with an artificial mouth*. PhD thesis, School of Physics, University of Edinburgh, 2003.
- [Riley 98] K. F. Riley, M. P. Hobson & S. J. Bence. *Mathematical Methods for Physics and Engineering*. Cambridge University Press, 1st edition, 1998.
- [Roubeau 09] B. Roubeau, N. Henrich & M. Castellengo. *Laryngeal vibratory mechanisms: The notion of vocal register revisited*. Journal of Voice, vol. 23, no. 4, pages 425 – 438, 2009.
- [Ruty 07a] N. Rutu. *Modèles d'interactions fluide/parois dans le conduit vocal. applications aux voix et aux pathologies*. PhD thesis, Institut National Polytechnique de Grenoble - INPG, November 2007.
- [Ruty 07b] N. Rutu, X. Pelorson, A. Van Hirtum, I. Lopez-Arteaga & A. Hirschberg. *An in vitro setup to test the relevance and the accuracy of low-order vocal folds models*. The Journal of the Acoustical Society of America, vol. 121, no. 1, pages 479–490, 2007.

- [saf 12] Günther Schaidt SAFEX-Chemie GMBH. *Company website*. <http://www.safex.de/Home/tabid/603/Default.aspx>, Accessed: August 2012.
- [Sato 60] H. Sato. *The stability and transition of a two-dimensional jet*. Journal of Fluid Mechanics, vol. 7, no. 01, pages 53–80, 1960.
- [Scherer 81] R. C. Scherer. *Laryngeal fluid mechanics: steady flow considerations using static models*. PhD thesis, University of Iowa, Iowa City, 1981.
- [Scherer 83] R. C. Scherer & I. R. Titze. *Pressure-flow relationships in a model of the laryngeal airway with a diverging glottis*. In D. M. Bless & J. H. Abbs, editors, Vocal Fold Physiology, pages 179–193. College Hill Press, San Diego, 1983.
- [Scherer 01] R. C. Scherer, D. Shinwari, K. J. D. Witt, C. Zhang, B. R. Kucinski & A. A. Afjeh. *Intraglottal pressure profiles for a symmetric and oblique glottis with a divergence angle of 10 degrees*. The Journal of the Acoustical Society of America, vol. 109, no. 4, pages 1616–1630, 2001.
- [Scherer 02] R. C. Scherer, D. Shinwari, K. J. D. Witt, C. Zhang, B. R. Kucinski & A. A. Afjeh. *Intraglottal pressure distributions for a symmetric and oblique glottis with a uniform duct (l)*. The Journal of the Acoustical Society of America, vol. 112, no. 4, pages 1253–1256, 2002.
- [Shadle 85] C. H. Shadle. *The acoustics of fricative consonants*. PhD thesis, Research Laboratory of Electronics; Massachusetts Institute of Technology, Cambridge, Massachusetts 02139, March 1985.
- [Shadle 91] C. H. Shadle, A. M. Barney & D. W. Thomas. *An investigation into the acoustics and aerodynamics of the larynx*. In J. Gauffin & B. Hammarberg, editors, Vocal Fold Physiology: Acoustic, Perceptual, and Physiological Aspects of Voice Mechanisms, pages 78–80. Singular Publishing Group, San Diego, 1991.
- [Shadle 99] C. H. Shadle, A. Barney & P. O. A. L. Davies. *Fluid flow in a dynamic mechanical model of the vocal folds and tract. ii. implications for speech production studies*. The Journal of the Acoustical Society of America, vol. 105, no. 1, pages 456–466, 1999.
- [Shearer 79] W. M. Shearer. *Illustrated Speech Anatomy*. Charles C. Thomas, Springfield, Illinois, 1979.
- [Shinneeb 12] A.-M. Shinneeb & A. Pollard. *Identification of vortical structures inside the human pharynx/larynx region from pod-reconstructed velocity fields*. Experiments in Fluids, vol. 53, pages 353–367, 2012.

- [Skulina 05] D. J. Skulina. *A study of non-linear acoustic flows at the open end of a tube using particle image velocimetry*. PhD thesis, School of Physics, University of Edinburgh, 2005.
- [Steinecke 95] I. Steinecke & H. Herzel. *Bifurcations in an asymmetric vocal-fold model*. The Journal of the Acoustical Society of America, vol. 97, no. 3, pages 1874–1884, 1995.
- [Stevens 98] K. N. Stevens. *Acoustic Phonetics*. MIT Press, 1998.
- [Stevenson 07] S. Stevenson, J. Chick, S. Bromage & D. M. Campbell. *Brass wind instruments: Transient behaviour in the lip-reed*. In proceedings of the International Symposium on Music Acoustics, Barcelona, Spain, September 2007.
- [Stevenson 09a] S. Stevenson, M. Campbell, S. Bromage, J. Chick & J. Gilbert. *Motion of the lips of brass players during extremely loud playing*. The Journal of the Acoustical Society of America, vol. 125, no. 4, pages EL152–EL157, 2009.
- [Stevenson 09b] S. D. F. Stevenson. *Experimental investigations of lip motion in brass instrument playing*. PhD thesis, School of Physics and Astronomy, University of Edinburgh, October 2009.
- [Story 95] B. H. Story & I. R. Titze. *Voice simulation with a body-cover model of the vocal folds*. The Journal of the Acoustical Society of America, vol. 97, no. 2, pages 1249–1260, 1995.
- [Sundberg 87] J. Sundberg. *The Science of the Singing Voice*. Northern Illinois University Press, 1987.
- [Sveen 04] J. K. Sveen. *An introduction to MatPIV 1.6.1*, 2004.
- [Takeuchi 05] J. Takeuchi, S. Satake, N. Morley, T. Yokomine, T. Kunugi & M. Abdou. *PIV measurements of turbulence statistics and near-wall structure of fully developed pipe flow at high Reynolds number*. In proceedings of the 6th International Symposium on Particle Image Velocimetry, Pasadena, California, USA, 21-23 September 2005.
- [Tao 09] C. Tao, J. J. Jiang & Y. Zhang. *A fluid-saturated poroelastic model of the vocal folds with hydrated tissue*. Journal of Biomechanics, vol. 42, no. 6, pages 774–780, 2009.
- [Thomson 04] S. L. Thomson. *Fluid-structure interactions within the human larynx*. PhD thesis, Purdue University, West Lafayette, Indiana, 2004.
- [Thomson 05] S. L. Thomson, L. Mongeau & S. H. Frankel. *Aerodynamic transfer of energy to the vocal folds*. The Journal of the Acoustical Society of America, vol. 118, no. 3, pages 1689–1700, 2005.

- [Titze 88] I. R. Titze. *The physics of small-amplitude oscillation of the vocal folds*. The Journal of the Acoustical Society of America, vol. 83, no. 4, pages 1536–1552, 1988.
- [Titze 92] I. R. Titze. *Phonation threshold pressure: A missing link in glottal aerodynamics*. The Journal of the Acoustical Society of America, vol. 91, no. 5, pages 2926–2935, 1992.
- [Titze 94] I. R. Titze. *Principles of Voice Production*. Prentice-Hall, 1994.
- [Titze 95] I. R. Titze, S. S. Schmidt & M. R. Titze. *Phonation threshold pressure in a physical model of the vocal fold mucosa*. The Journal of the Acoustical Society of America, vol. 97, no. 5, pages 3080–3084, 1995.
- [Titze 04] I. R. Titze. *Theory of glottal airflow and source-filter interaction in speaking and singing*. Acta Acustica united with Acustica, vol. 90, pages 641–648, July/August 2004.
- [Titze 08a] I. Titze, T. Riede & P. Popolo. *Nonlinear source-filter coupling in phonation: Vocal exercises*. The Journal of the Acoustical Society of America, vol. 123, no. 4, pages 1902–1915, 2008.
- [Titze 08b] I. R. Titze. *Nonlinear source-filter coupling in phonation: Theory*. The Journal of the Acoustical Society of America, vol. 123, no. 5, pages 2733–2749, 2008.
- [Titze 09] I. R. Titze & A. S. Worley. *Modeling source-filter interaction in belting and high-pitched operatic male singing*. The Journal of the Acoustical Society of America, vol. 126, no. 3, pages 1530–1540, 2009.
- [Triep 05] M. Triep, C. Brücker & W. Schröder. *High-speed PIV measurements of the flow downstream of a dynamic mechanical model of the human vocal folds*. Experiments in Fluids, vol. 39, no. 2, pages 232–245, 2005.
- [Triep 10] M. Triep & C. Brücker. *Three-dimensional nature of the glottal jet*. The Journal of the Acoustical Society of America, vol. 127, no. 3, pages 1537–1547, 2010.
- [Tritton 88] D. J. Tritton. *Physical Fluid Dynamics*. Oxford Science Publications; Clarendon Press, Oxford, 2nd edition, 1988.
- [Tropea 07] C. Tropea, A. Yarin & J. F. Foss, editors. *Springer Handbook of Experimental Fluid Mechanics*. Springer-Verlag Berlin Heidelberg, July 2007.
- [van den Berg 57a] J. van den Berg. *Sub-glottal pressure and vibrations of the vocal folds*. Folia Phoniatica, vol. 9, pages 65–71, 1957.

- [van den Berg 57b] J. van den Berg, J. T. Zantema & J. P. Doornenbal. *On the air resistance and the bernoulli effect of the human larynx*. The Journal of the Acoustical Society of America, vol. 29, no. 5, pages 626–631, 1957.
- [van den Berg 58] J. van den Berg. *Myoelastic-aerodynamic theory of voice production*. Journal of Speech and Hearing Research, vol. 1, pages 227–244, 1958.
- [van den Berg 60] J. van den Berg. *Vocal ligaments versus registers*. Current Problems in Phoniatrics and Logopedics, vol. 1, pages 19–34, 1960.
- [Van Hirtum 09] A. Van Hirtum, J. Cisonni & X. Pelorson. *On quasi-steady laminar flow separation in the upper airways*. Communications in Numerical Methods in Engineering, vol. 25, no. 5, pages 447–461, 2009.
- [van Hooff 12] T. van Hooff, B. Blocken, T. Defraeye, J. Carmeliet & G. van Heijst. *PIV measurements of a plane wall jet in a confined space at transitional slot reynolds numbers*. Experiments in Fluids, vol. 53, pages 499–517, 2012.
- [Vilain 02] C. E. Vilain. *Contribution à la synthèse de parole par modèle physique. application à l'étude des voix pathologiques*. PhD thesis, Institut National Polytechnique de Grenoble - INPG, 2002.
- [Vilain 04] C. E. Vilain, X. Pelorson, C. Fraysse, M. Deverge, A. Hirschberg & J. Willems. *Experimental validation of a quasi-steady theory for the flow through the glottis*. Journal of Sound and Vibration, vol. 276, no. 3-5, pages 475–490, 2004.
- [von Helmholtz 54] H. J. F. von Helmholtz. *On the Sensations of Tone as a Physiological Basis for the Theory of Music* (1877). Dover Publications, New York, 2nd English edition, 1954.
- [Šidlof 11] P. Šidlof, O. Doaré, O. Cadot & A. Chaigne. *Measurement of flow separation in a human vocal folds model*. Experiments in Fluids, vol. 51, pages 123–136, 2011.
- [Webber 68] N. B. Webber. *Fluid Mechanics for Civil Engineers*. Spon's Civil Engineering Series. E. and F. N. Spon Ltd, 2nd edition, 1968.
- [wik 12a] Wikipedia. *Larynx of horse*. http://commons.wikimedia.org/wiki/File:Kehlkopf_Pferd_2.jpg, Accessed: August 2012.
- [wik 12b] Wikipedia. *Planes of human anatomy*. http://en.wikipedia.org/wiki/File:Human_anatomy_planes.svg, Accessed: August 2012.
- [Willert 91] C. E. Willert & M. Gharib. *Digital particle image velocimetry*. Experiments in Fluids, vol. 10, pages 181–193, 1991.

- [Zaman 96] K. B. M. Q. Zaman. *Axis switching and spreading of an asymmetric jet: the role of coherent structure dynamics*. Journal of Fluid Mechanics, vol. 316, pages 1–27, 1996.
- [Zañartu 11] M. Zañartu, D. D. Mehta, J. C. Ho, G. R. Wodicka & R. E. Hillman. *Observation and analysis of in vivo vocal fold tissue instabilities produced by nonlinear source-filter coupling: A case study*. The Journal of the Acoustical Society of America, vol. 129, no. 1, pages 326–339, 2011.
- [Zemlin 68] W. R. Zemlin. *Speech and hearing science*. Prentice-Hall, Englewood Cliffs, New Jersey, 1968.
- [Zhang 02a] C. Zhang, W. Zhao, S. H. Frankel & L. Mongeau. *Computational aeroacoustics of phonation, part ii: Effects of flow parameters and ventricular folds*. The Journal of the Acoustical Society of America, vol. 112, no. 5, pages 2147–2154, 2002.
- [Zhang 02b] Z. Zhang, L. Mongeau & S. Frankel. *Broadband sound generation by confined stationary jets through circular and glottis-shaped orifices*. In proceedings of the 3rd International Conference on Voice Physiology and Biomechanics, 13-16 September 2002.
- [Zhang 06] Z. Zhang, J. Neubauer & D. A. Berry. *The influence of subglottal acoustics on laboratory models of phonation*. The Journal of the Acoustical Society of America, vol. 120, no. 3, pages 1558–1569, 2006.
- [Zhang 08] Z. Zhang. *Influence of flow separation location on phonation onset*. The Journal of the Acoustical Society of America, vol. 124, no. 3, pages 1689–1694, 2008.
- [Zheng 11] X. Zheng, R. Mittal & S. Bielamowicz. *A computational study of asymmetric glottal jet deflection during phonation*. The Journal of the Acoustical Society of America, vol. 129, no. 4, pages 2133–2143, 2011.



Published Papers

A.1 Conference Papers

- Adam G. Apostoli, D. Murray Campbell, and Clive A. Greated, ‘The influence of the ventricular bands and their impact on the expansion of the glottal jet’ in *proceedings of Forum Acusticum 2011*, Aalborg; Denmark, (2011).
- Alan G. Woolley, D. Murray Campbell, and Adam G. Apostoli, ‘An investigation into the airflow through pipe organ pallet valve openings using particle image velocimetry.’ in *proceedings of Forum Acusticum 2011*, Aalborg; Denmark, (2011).
- Adam G. Apostoli, D. Murray Campbell, and Clive A. Greated, ‘Glottal jet behaviour in a self-oscillating *in vitro* model of the vocal folds with downstream constrictions’ in *proceedings of the International Symposium on Musical Acoustics*, Sydney and Katoomba; Australia, (2010).
- Adam G. Apostoli, D. Murray Campbell, and Clive A. Greated, ‘Flow field measurements in a self-oscillating *in vitro* model of the vocal folds’ in *proceedings of the 10ème Congrès Français d’Acoustique*, Lyon; France, (2010).
- Adam G. Apostoli, Shona M. Logie, Arnold Myers, Jonathan A. Kemp, John P. Chick, and Alastair C. P. Braden, ‘Reconstructing the Lituus: a reassessment of impedance, harmonicity, and playability’ in *proceedings of the NAG-DAGA International Conference on Acoustics*, Rotterdam; The Netherlands, (2009).
- Shona M. Logie, Samuel Stevenson, Adam G. Apostoli, John P. Chick, and D. Murray Campbell, ‘Transient behaviour in the motion of the brass player’s lips during a lip-slur’ in *proceedings of the NAG-DAGA International Conference on Acoustics*, Rotterdam; The Netherlands, (2009).

B

Additional Results

B.1 Vorticity Flow Field Data

As in Sections 5.5.4, 6.1.1, and 6.2.1 the colour in each of the vorticity flow fields represents the amount of rotation within the flow, with a negative vorticity representing rotation of the flow in the clockwise direction and a positive vorticity representing rotation of the flow in the anti-clockwise direction. The intensity and direction of the rotation is shown by the colour scheme in both figures.

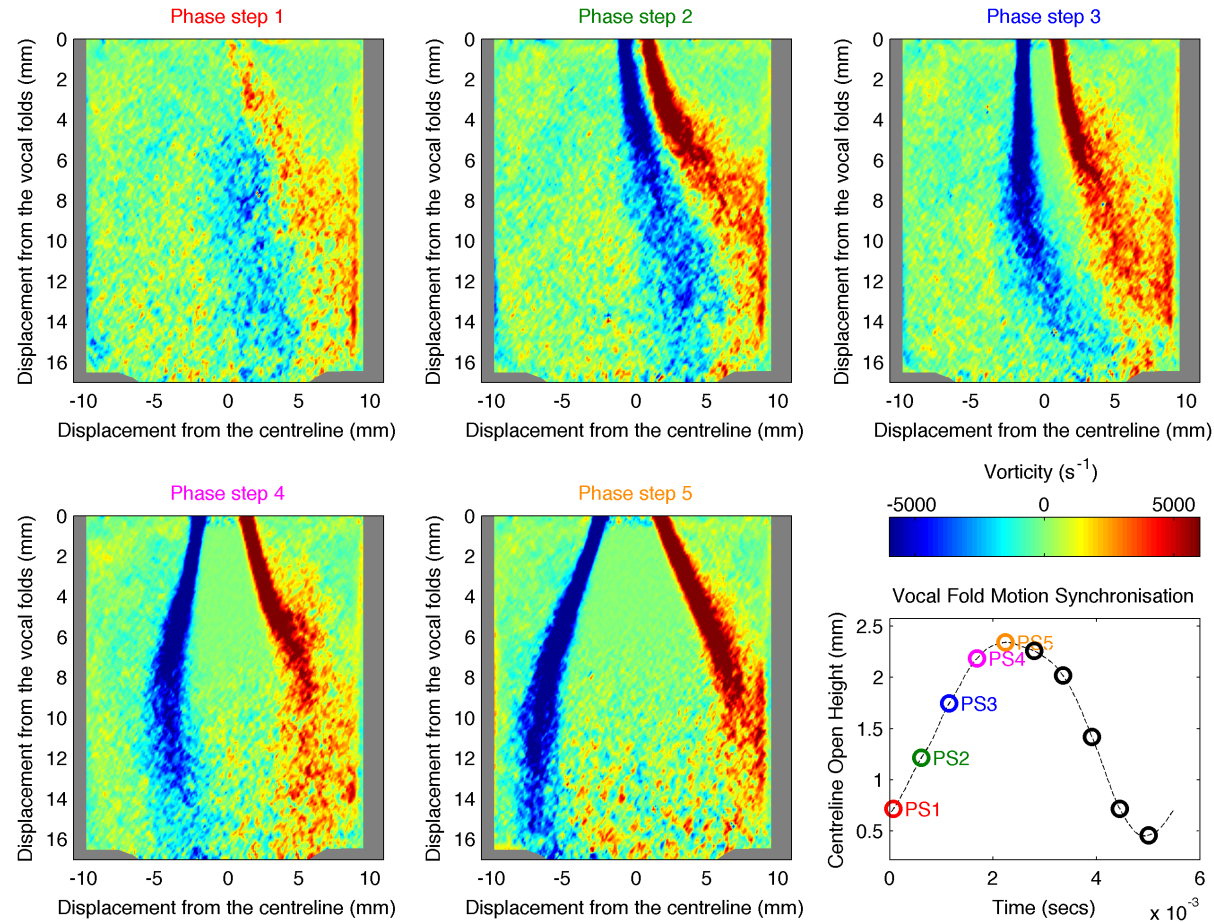


Figure B.1: Vorticity ensemble-averaged PIV data for phase steps 1 - 5 on an *in vitro* model of the human larynx **with rigid ventricular bands placed 16 mm downstream of the vocal folds with an 8 mm separation**. The positions of the phase steps in relation to the normalised open area of the vocal fold model are included. $P_{sub} = 802 \text{ Pa}$. Only the top of the ventricular bands are shown in these plots, the reported separation is the minimum constriction formed by the bands further downstream.

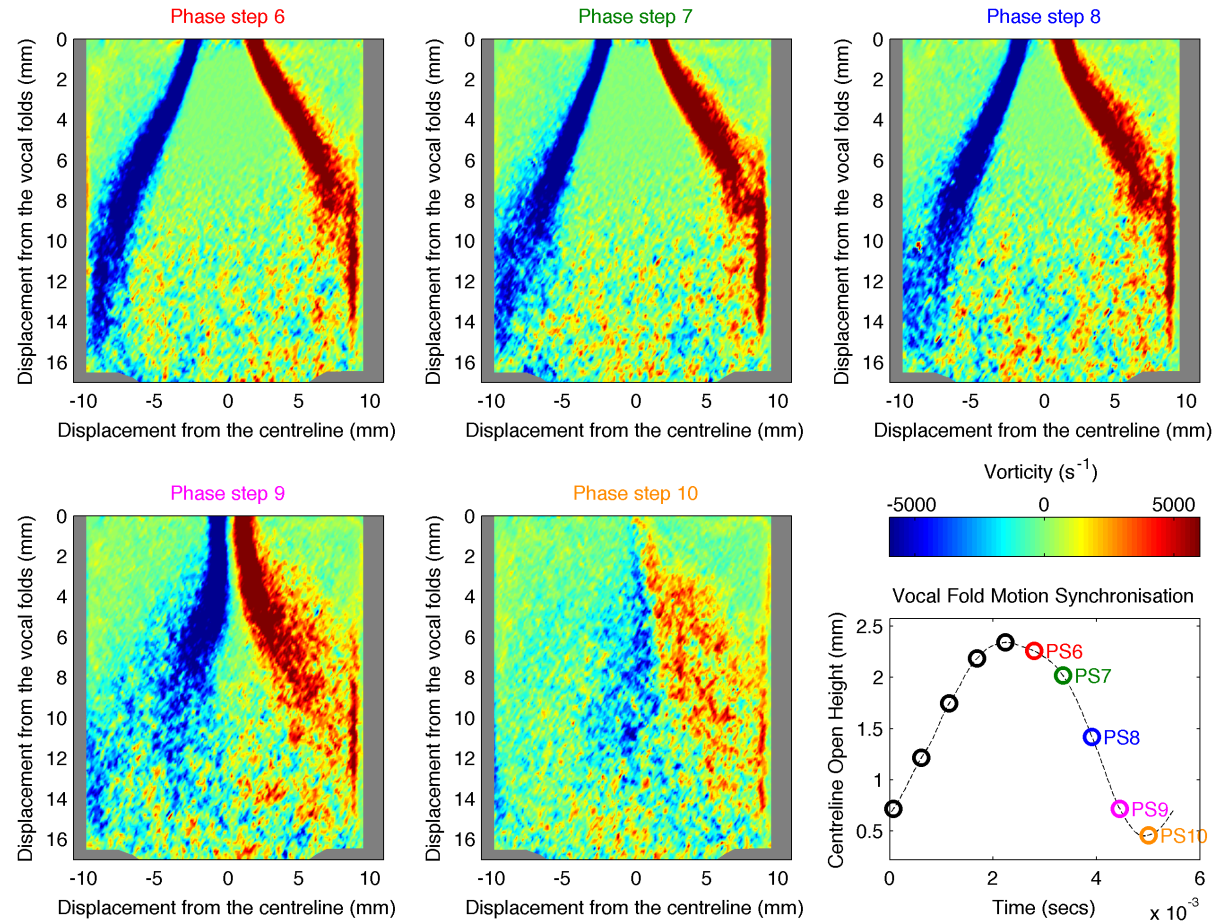


Figure B.2: Vorticity ensemble-averaged PIV data for phase steps 6 - 10 on an *in vitro* model of the human larynx **with rigid ventricular bands placed 16 mm downstream of the vocal folds with an 8 mm separation**. The positions of the phase steps in relation to the normalised open area of the vocal fold model are included. $P_{sub} = 802$ Pa. Only the top of the ventricular bands are shown in these plots, the reported separation is the minimum constriction formed by the bands further downstream.

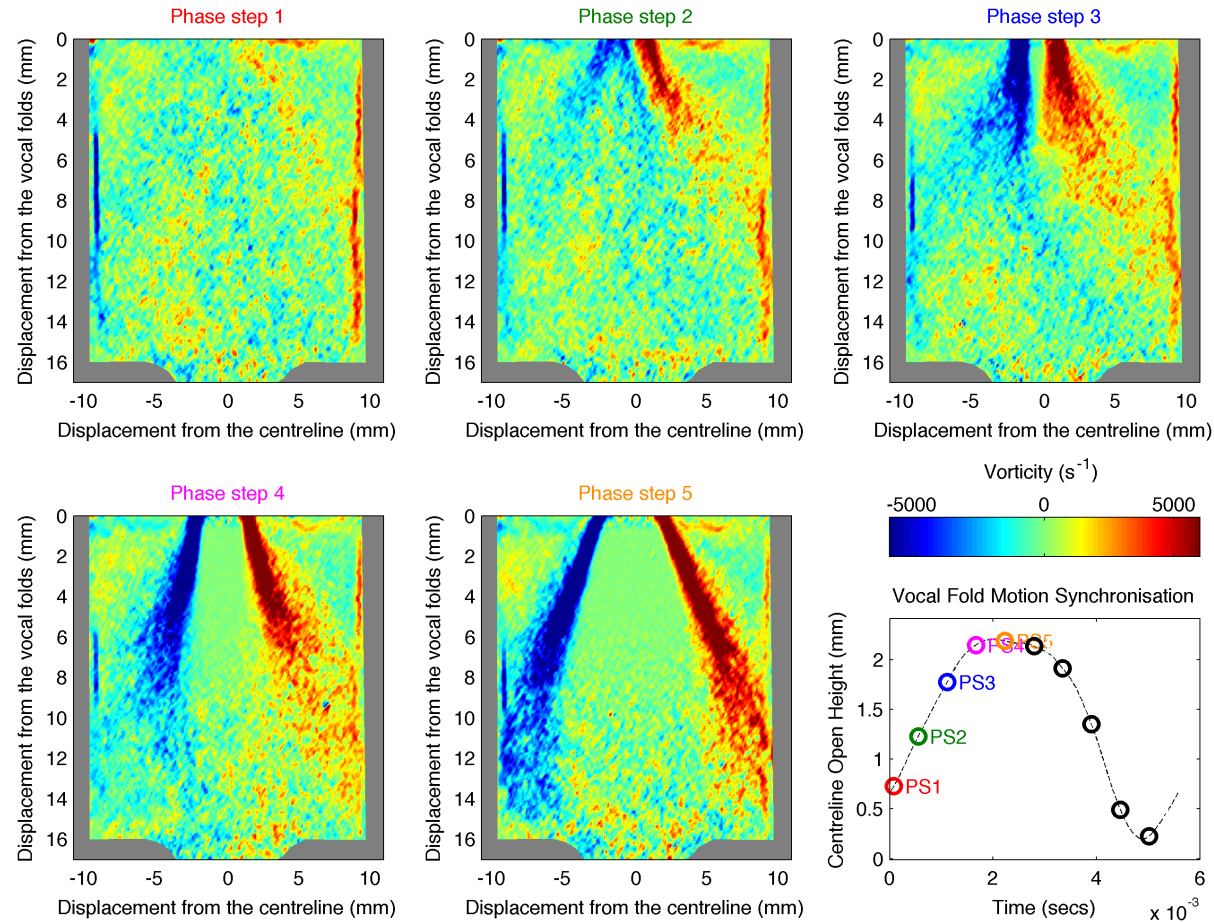


Figure B.3: Vorticity ensemble-averaged PIV data for phase steps 1 - 5 on an *in vitro* model of the human larynx **with rigid ventricular bands placed 16 mm downstream of the vocal folds with a 3 mm separation**. The positions of the phase steps in relation to the normalised open area of the vocal fold model are included. $P_{sub} = 805$ Pa. Only the top of the ventricular bands are shown in these plots, the reported separation is the minimum constriction formed by the bands further downstream.

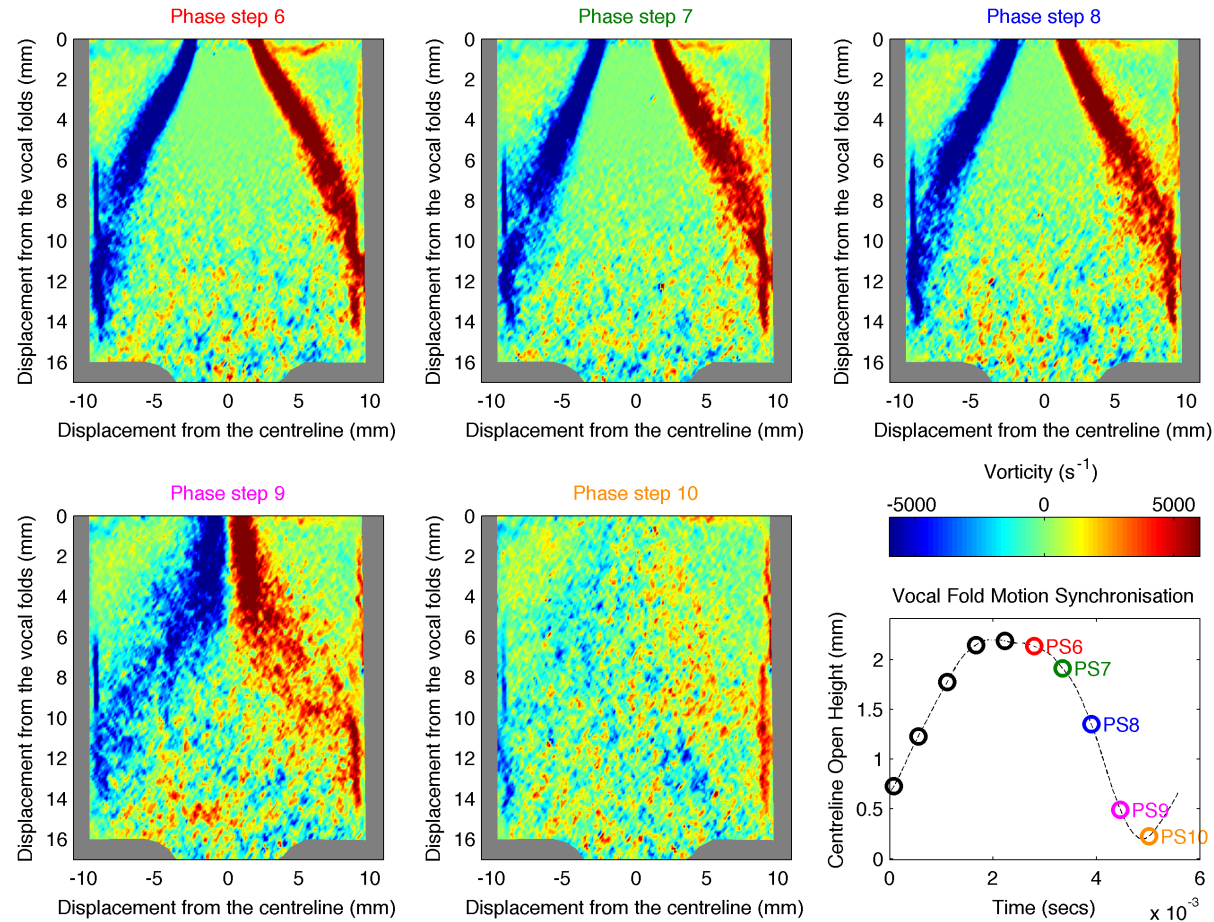


Figure B.4: Vorticity ensemble-averaged PIV data for phase steps 6 - 10 on an *in vitro* model of the human larynx **with rigid ventricular bands placed 16 mm downstream of the vocal folds with a 3 mm separation**. The positions of the phase steps in relation to the normalised open area of the vocal fold model are included. $P_{sub} = 805$ Pa. Only the top of the ventricular bands are shown in these plots, the reported separation is the minimum constriction formed by the bands further downstream.

B.2 Jet Major Axis-Switching

In this section, additional results for the jet major axis-switching discussed in Chapter 6 are presented. These additional results show the measured jet width in both planes (parallel and perpendicular to the glottal open width) under which PIV measurements were undertaken for all three different configurations of the *in vitro* model and for all phase steps. Where the two lines cross can be found the point of jet major axis-switching.

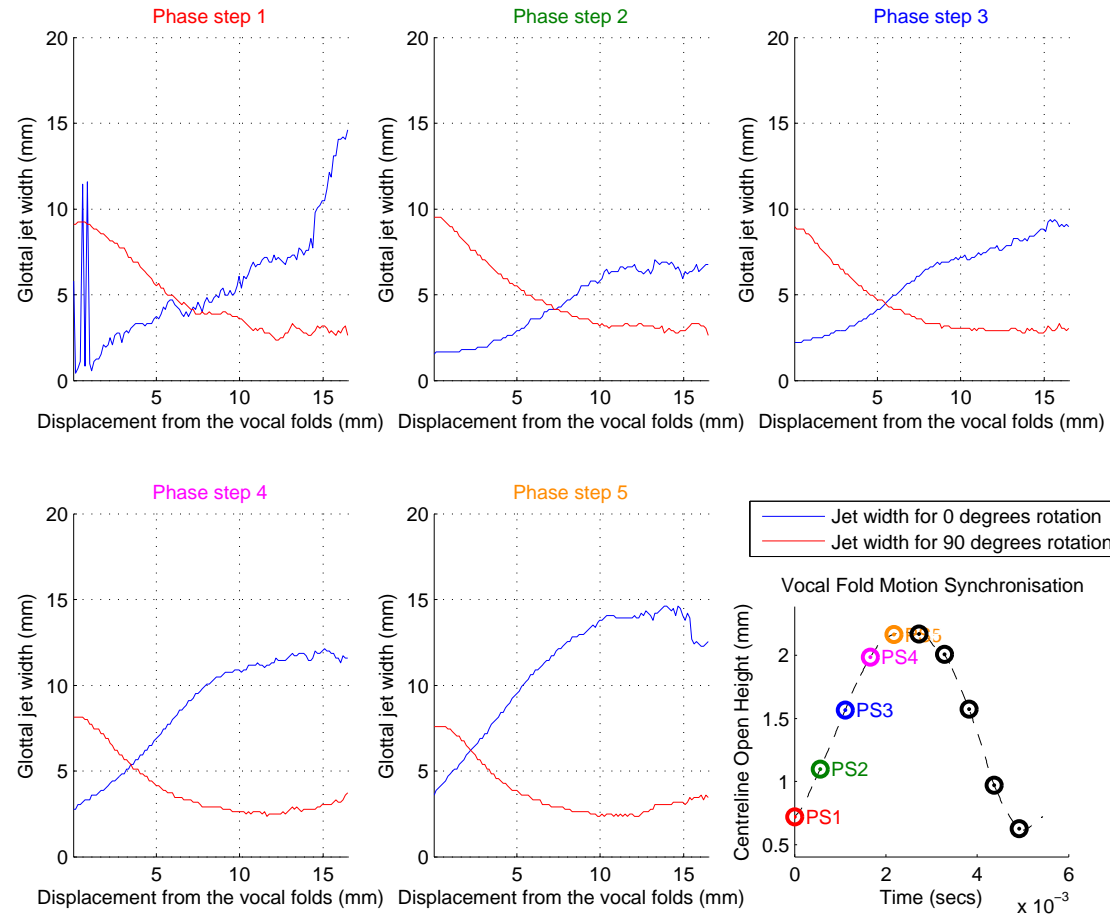


Figure B.5: Measured glottal jet widths in two perpendicular planes, signifying the point of jet major axis-switching, for phase steps 1 - 5 on an *in vitro* model of the human larynx **with no ventricular bands**. The positions of the phase steps in relation to the centreline open height of the vocal fold model are included. $P_{sub} = 813$ Pa.

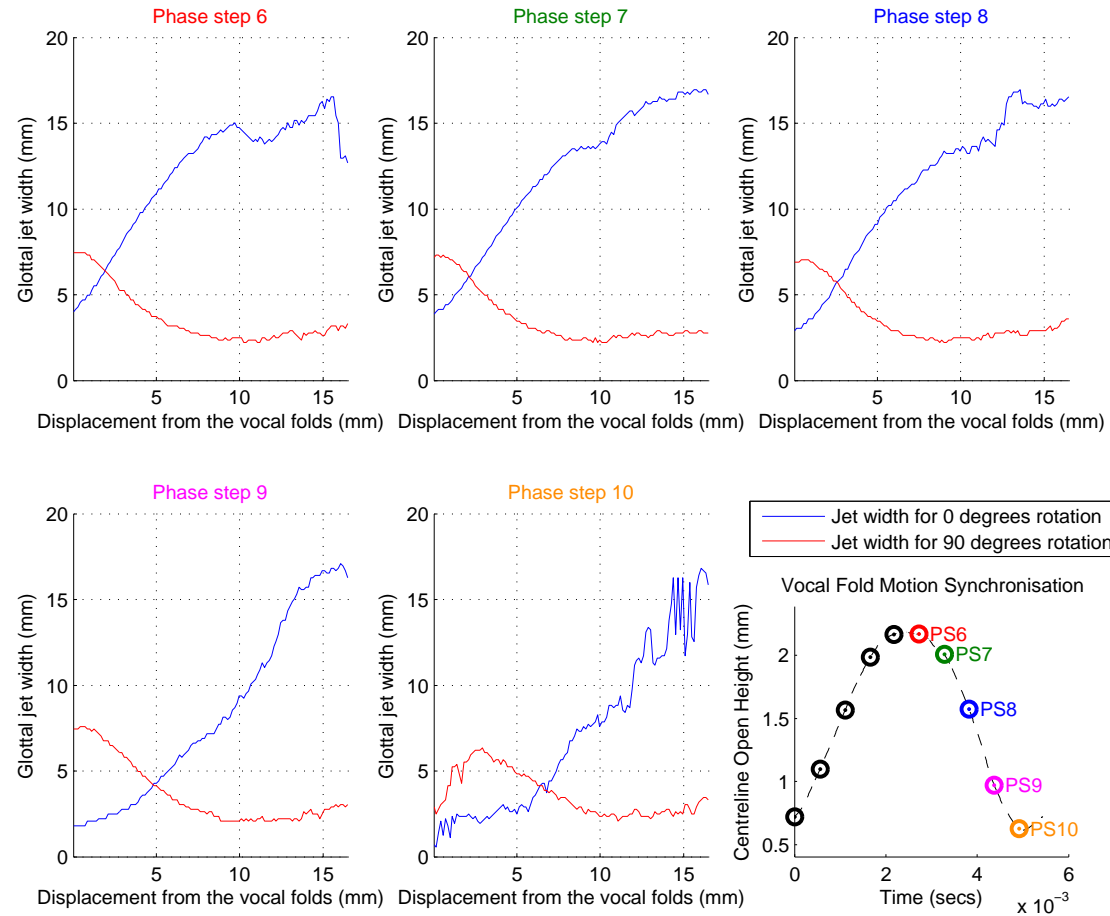


Figure B.6: Measured glottal jet widths in two perpendicular planes, signifying the point of jet major axis-switching, for phase steps 6 - 10 on an *in vitro* model of the human larynx **with no ventricular bands**. The positions of the phase steps in relation to the centreline open height of the vocal fold model are included. $P_{sub} = 813$ Pa.

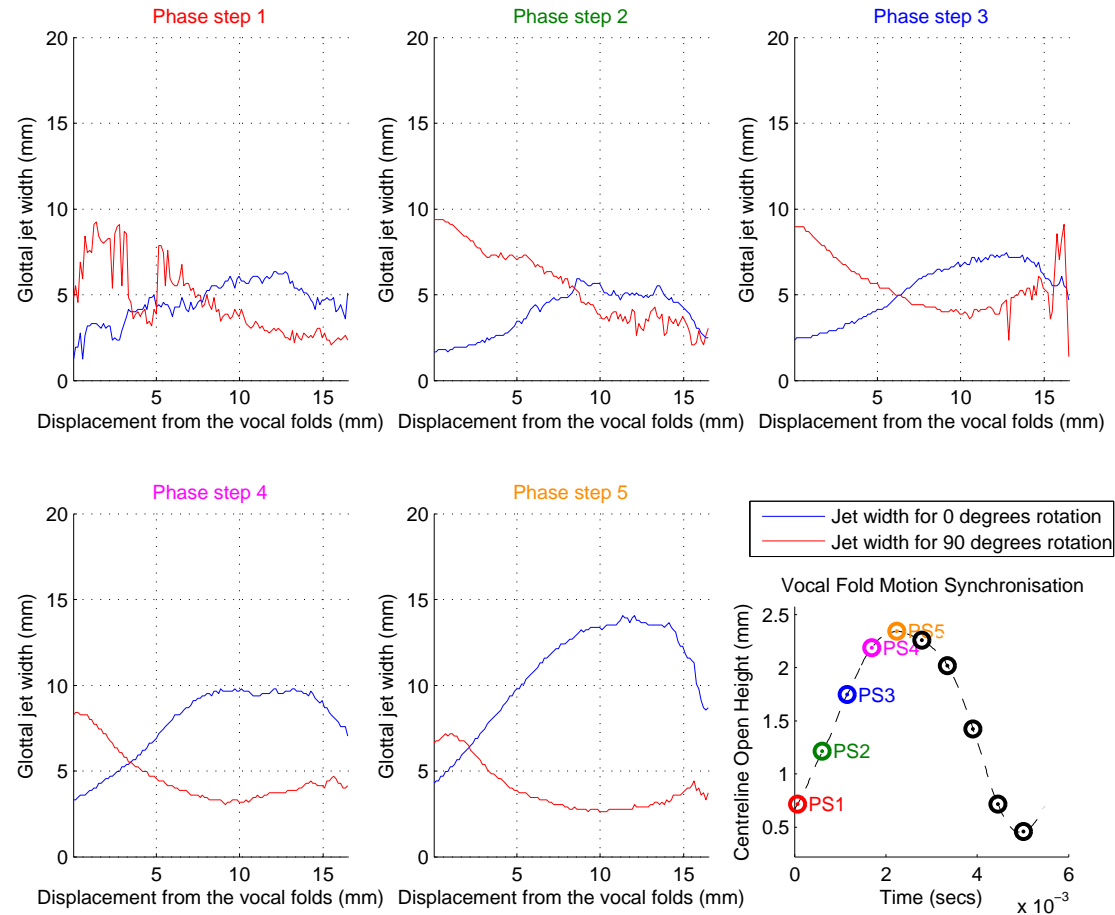


Figure B.7: Measured glottal jet widths in two perpendicular planes, signifying the point of jet major axis-switching, for phase steps 1 - 5 on an *in vitro* model of the human larynx **with rigid ventricular bands placed 16 mm downstream of the vocal folds with an 8 mm separation**. The positions of the phase steps in relation to the centreline open height of the vocal fold model are included. $P_{sub} = 802$ Pa.

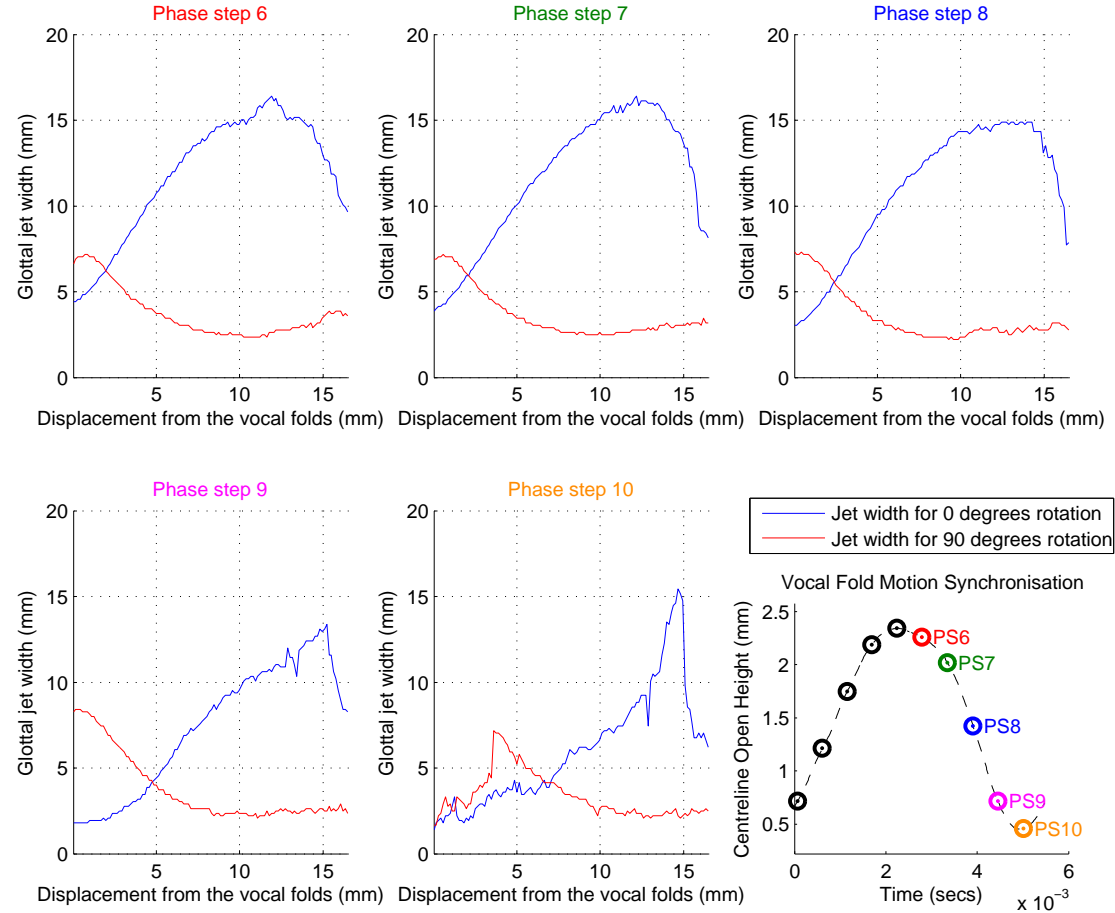


Figure B.8: Measured glottal jet widths in two perpendicular planes, signifying the point of jet major axis-switching, for phase steps 6 - 10 on an *in vitro* model of the human larynx **with rigid ventricular bands placed 16 mm downstream of the vocal folds with an 8 mm separation**. The positions of the phase steps in relation to the centreline open height of the vocal fold model are included. $P_{sub} = 802$ Pa.

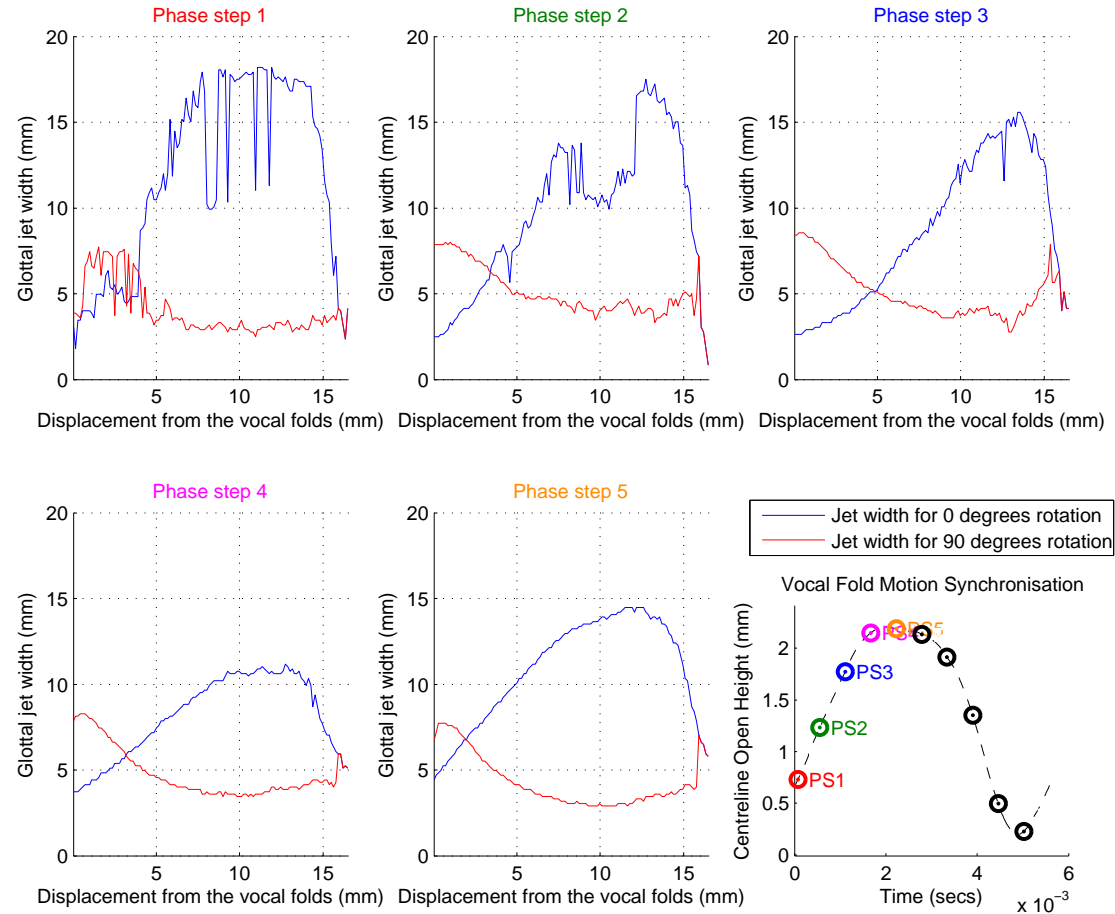


Figure B.9: Measured glottal jet widths in two perpendicular planes, signifying the point of jet major axis-switching, for phase steps 1 - 5 on an *in vitro* model of the human larynx **with rigid ventricular bands placed 16 mm downstream of the vocal folds with a 3 mm separation**. The positions of the phase steps in relation to the centreline open height of the vocal fold model are included. $P_{sub} = 805$ Pa.

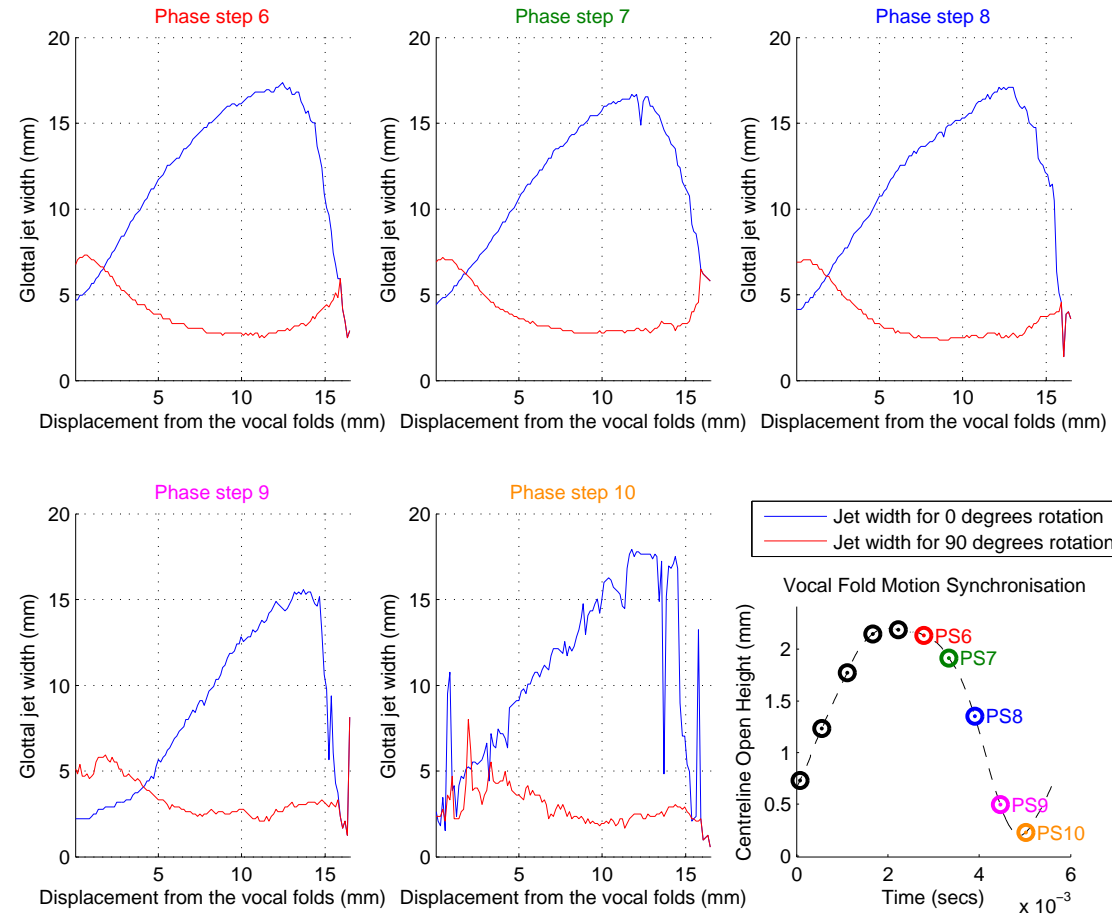
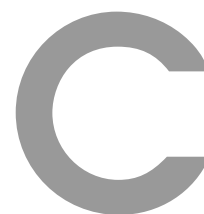
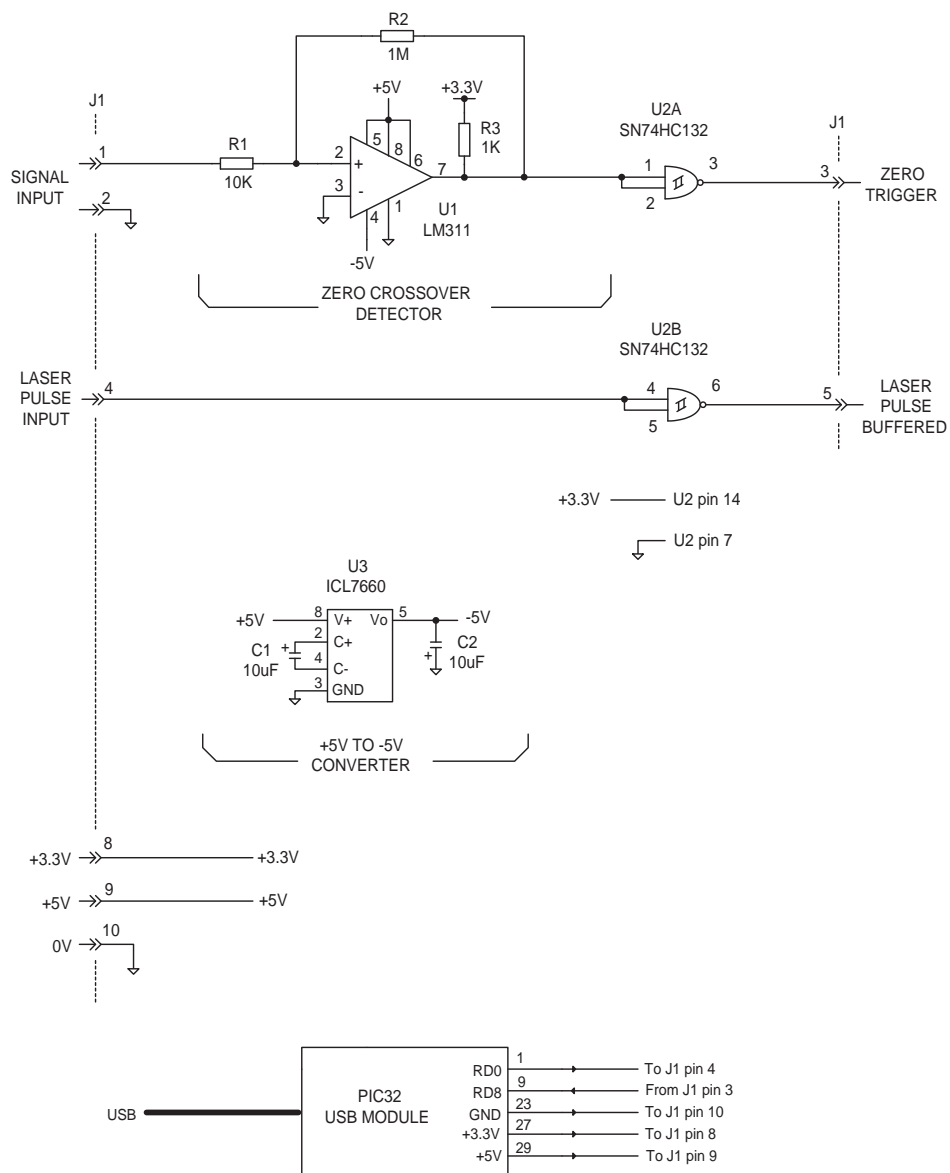


Figure B.10: Measured glottal jet widths in two perpendicular planes, signifying the point of jet major axis-switching, for phase steps 6 - 10 on an *in vitro* model of the human larynx **with rigid ventricular bands placed 16 mm downstream of the vocal folds with a 3 mm separation**. The positions of the phase steps in relation to the centreline open height of the vocal fold model are included. $P_{sub} = 805$ Pa.



Experimental Drawings



ZERO TRIGGER
 010210

Figure C.1: Schematic drawing for zero-triggering device developed at the University of Edinburgh (drawing created by R. Taylor)

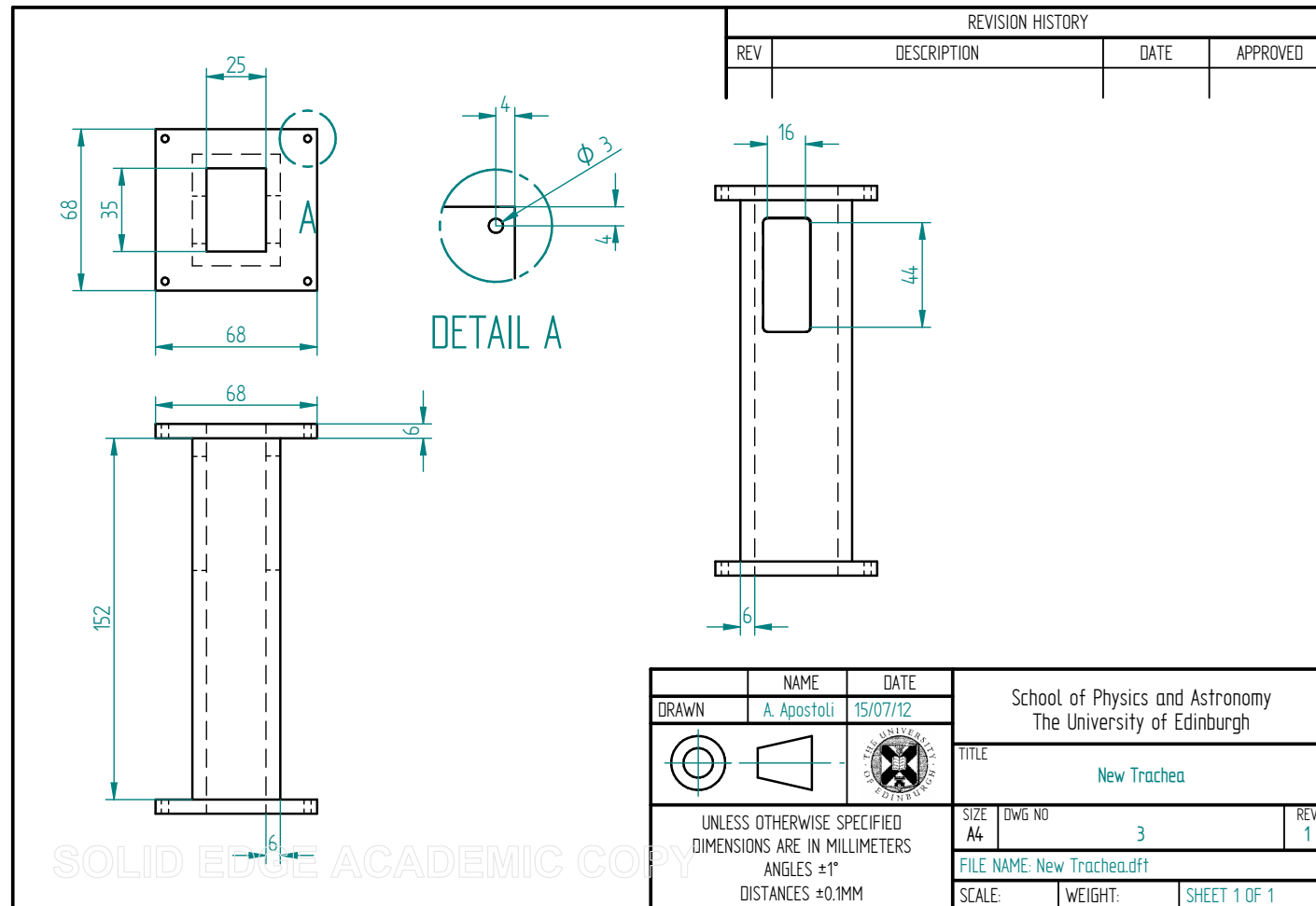


Figure C.2: Technical drawing for the trachea used in the *in vitro* model of the human larynx.

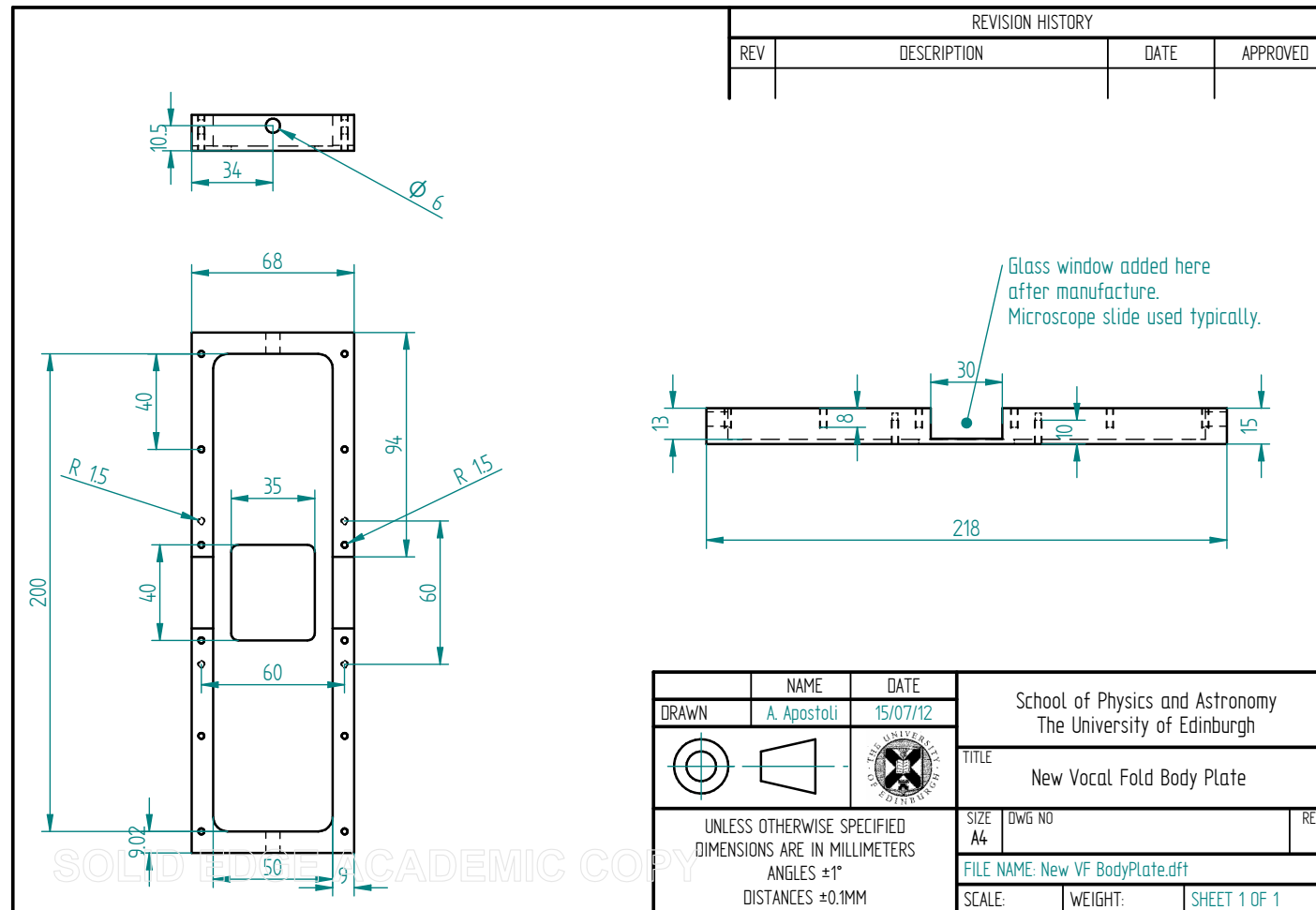


Figure C.3: Technical drawing for the body plate used in the *in vitro* model of the human larynx.

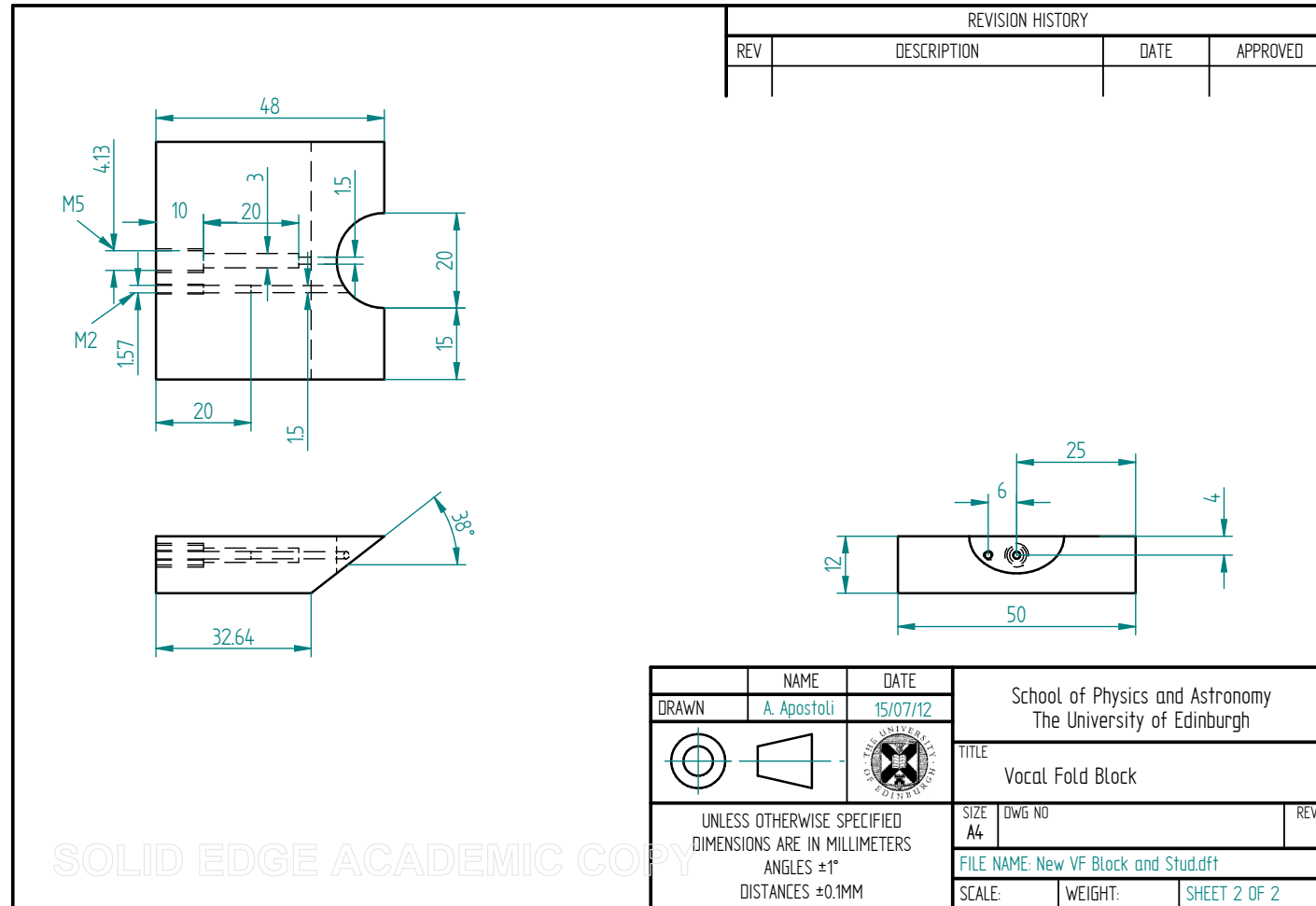


Figure C.4: Technical drawing for the block of the vocal fold assembly used in the *in vitro* model of the human larynx.

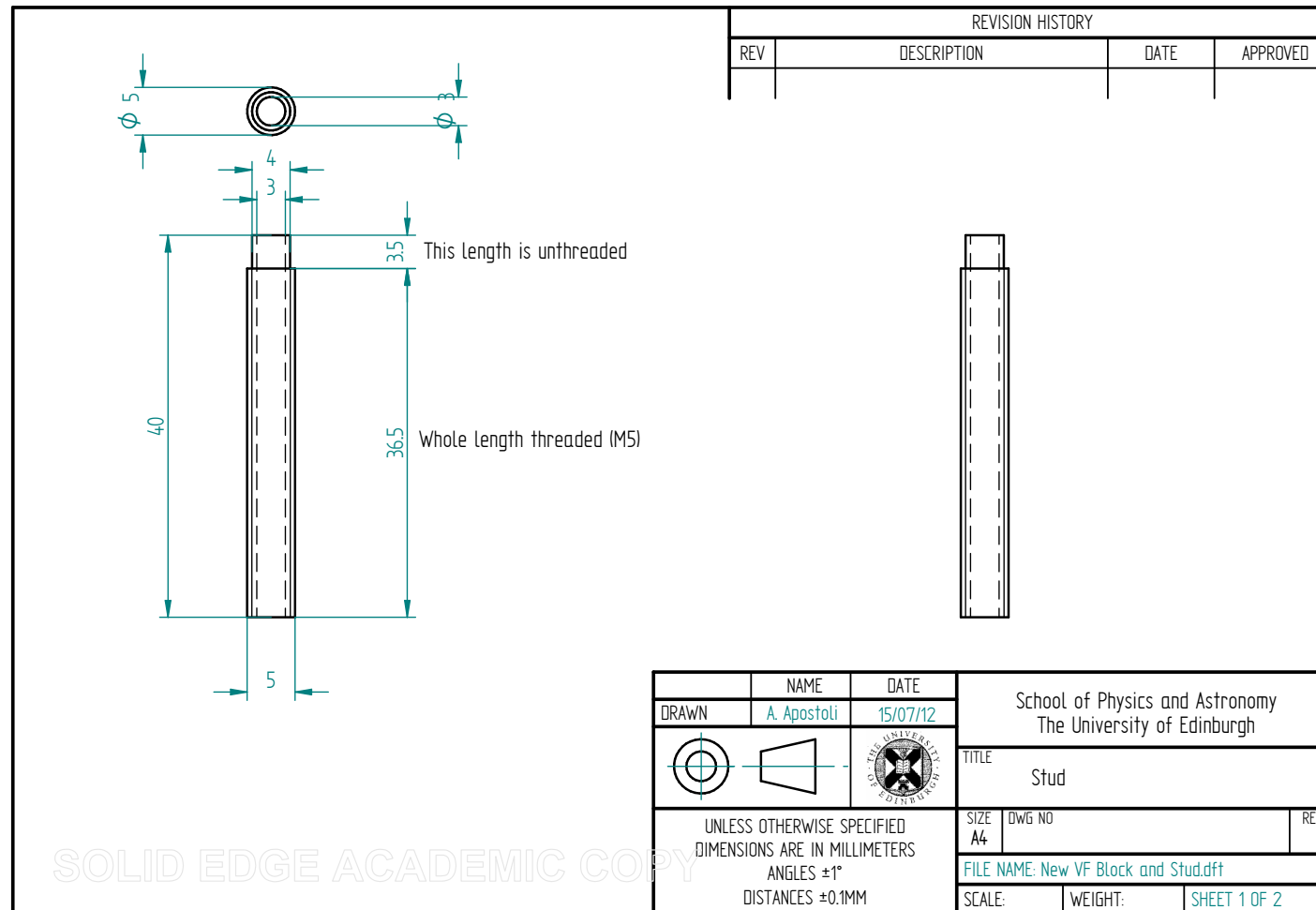


Figure C.5: Technical drawing for the stud of the vocal fold assembly used in the *in vitro* model of the human larynx.

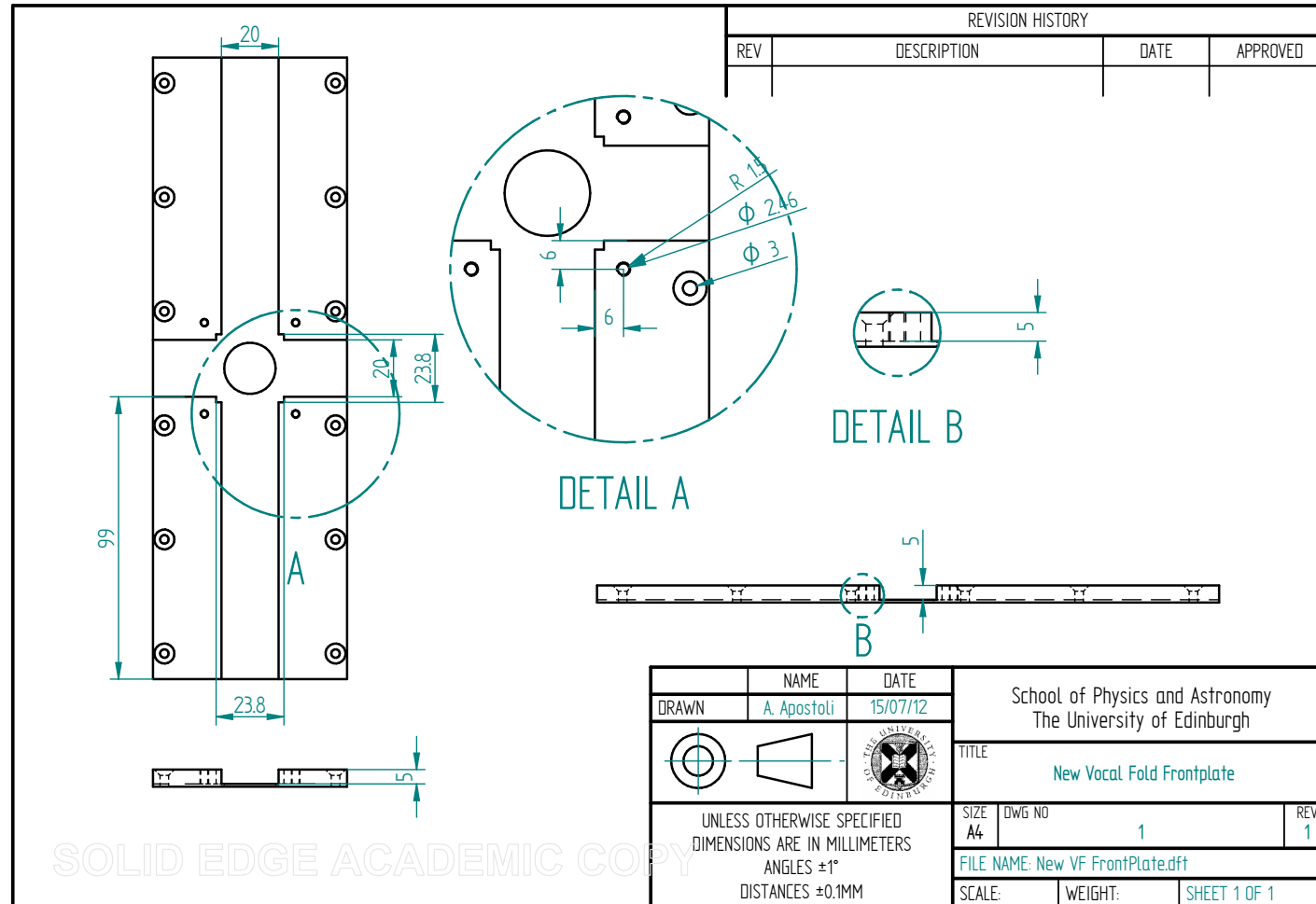


Figure C.6: Technical drawing for the front plate used in the *in vitro* model of the human larynx.

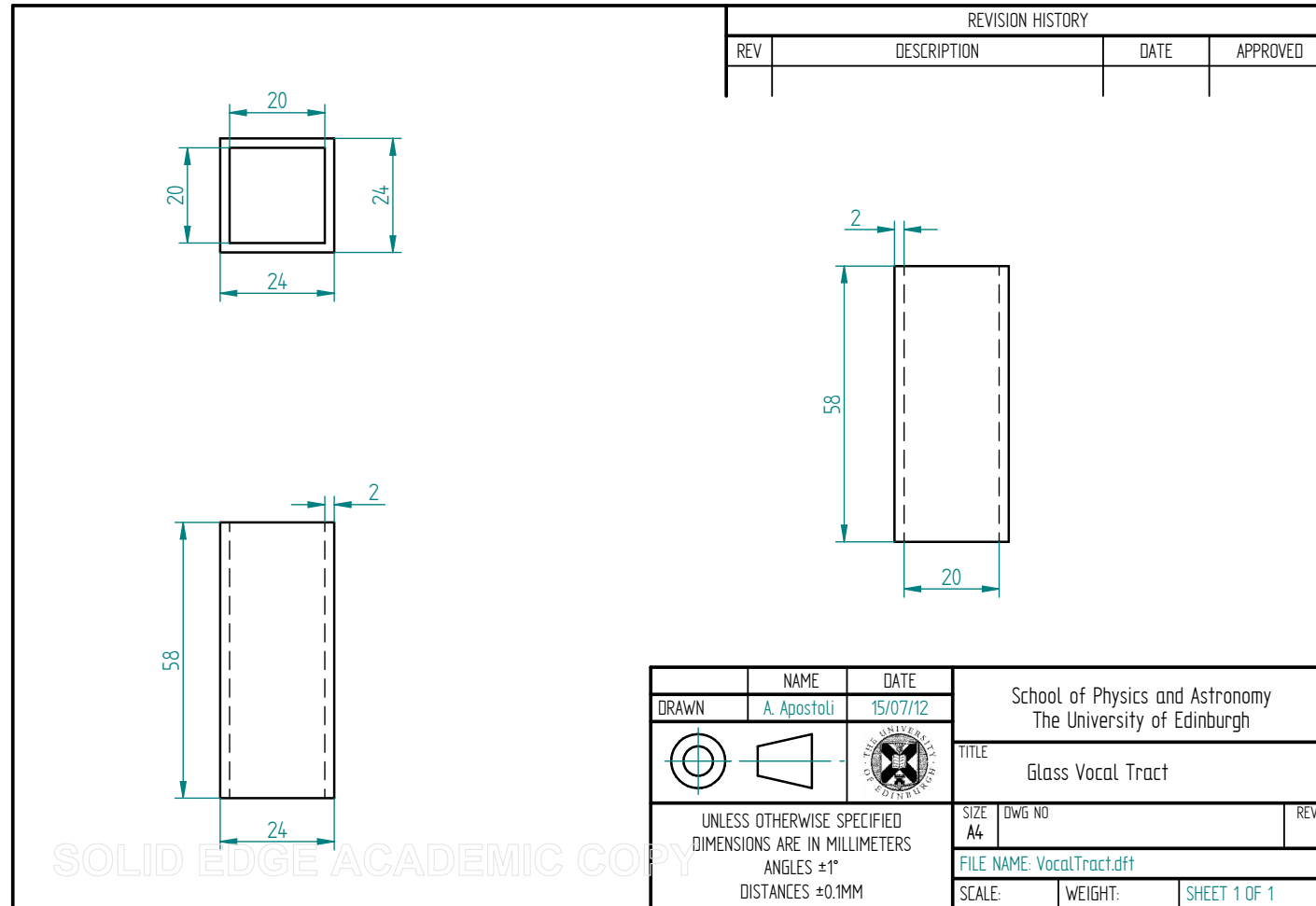


Figure C.7: Technical drawing for the glass vocal tract used in the *in vitro* model of the human larynx.

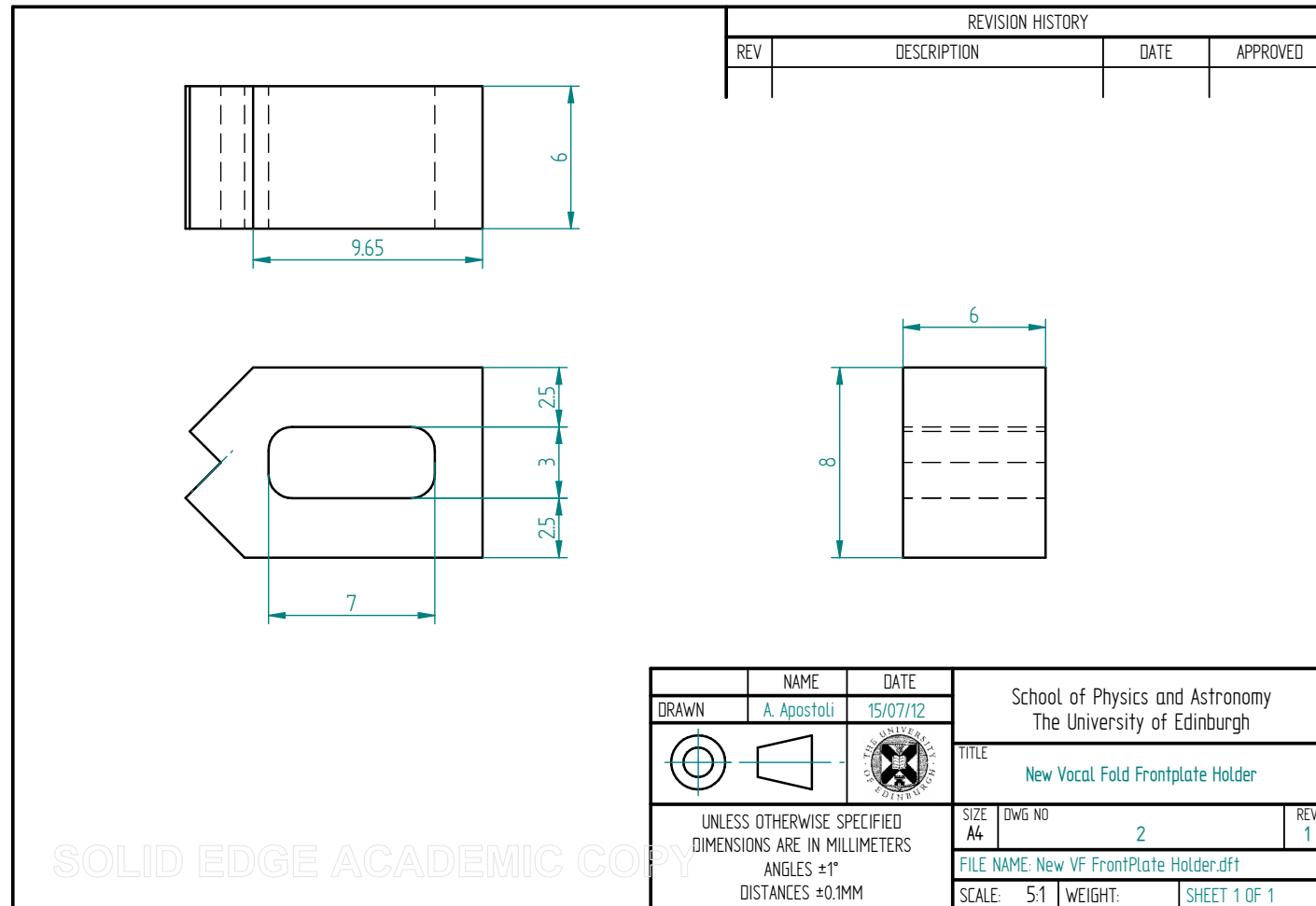


Figure C.8: Technical drawing for the holder used to secure the glass vocal tract in place in the *in vitro* model of the human larynx.

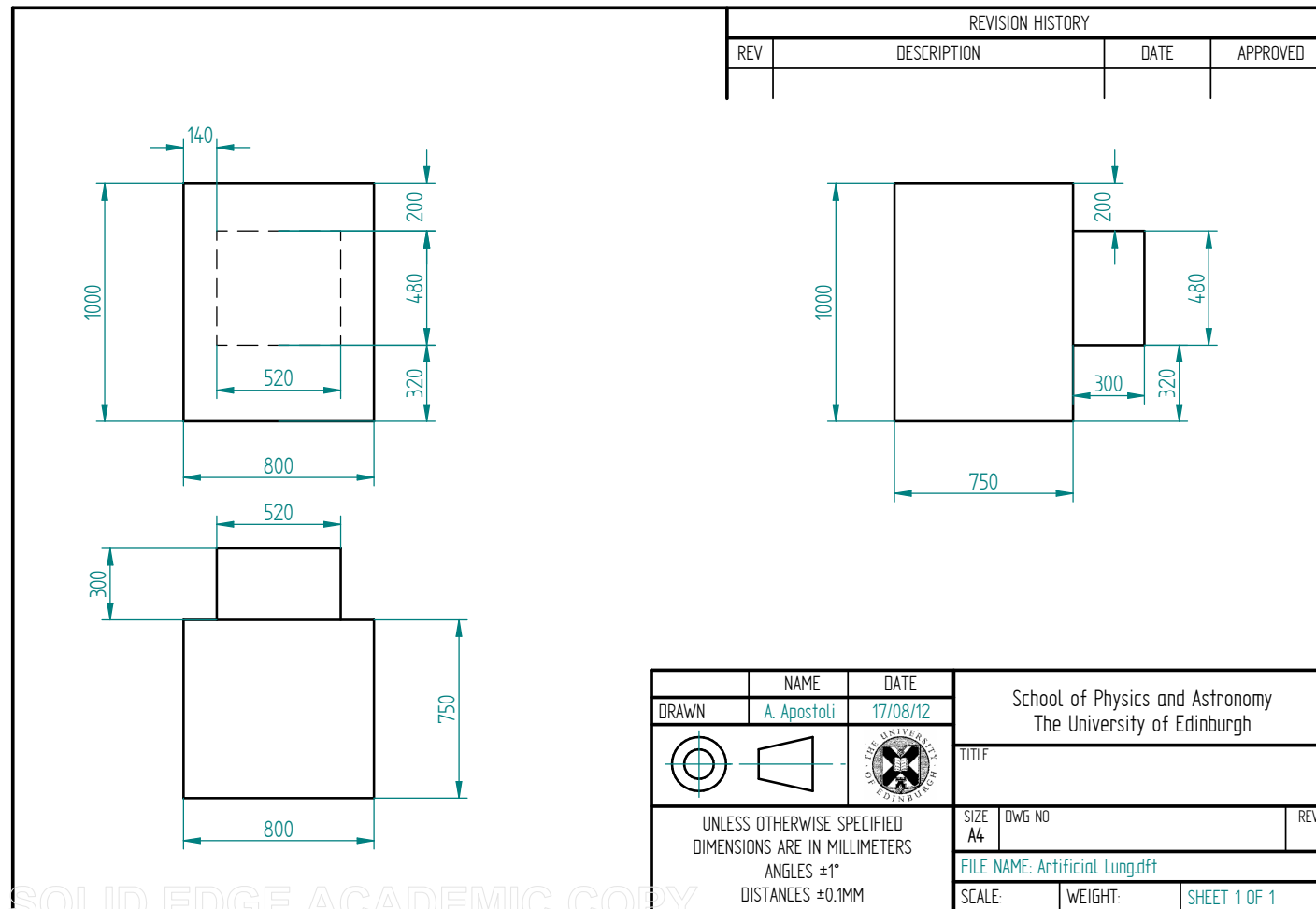


Figure C.9: Technical drawing for the artificial 'lung' replica used in the *in vitro* model of the human larynx.